UNIVERSITÀ
DEGLI STUDI
DI TRIESTE

Università degli Studi di Trieste

XXXV ciclo del Dottorato di Ricerca in Fisica

Understanding the production mechanisms of particles with strangeness in pp collisions with the ALICE experiment at the LHC

Settore scientifico-disciplinare: FIS/01

DOTTORANDA:
CHIARA DE MARTIN

COORDINATORE:
PROF. FRANCESCO LONGO

SUPERVISORE DI TESI:
DOTT.SSA RAMONA LEA

CO-SUPERVISORE DI TESI:
PROF. PAOLO CAMERINI

Anno Accademico 2021 - 2022

Abstract

Heavy-ion collisions are a unique tool to study the quark-gluon plasma (QGP), a state of matter in which quarks and gluons are not bound within hadrons by the strong force. QGP is expected to form when high energy density and temperature conditions are reached, as in heavy-ion collisions. One proposed signature of QGP formation is the strangeness enhancement effect, which consists in an increase of the ratio of strange to non-strange hadron yields in Pb–Pb collisions with respect to minimum bias pp collisions. This effect has been further investigated within the ALICE collaboration by studying its dependence on the multiplicity of charged particles produced in different collision systems. Results show that the ratios of different strange hadron yields to pion yields increase with the multiplicity of charged particles, revealing a smooth transition between different collision systems, from low multiplicity proton-proton (pp) collisions to high multiplicity central Pb–Pb collisions. This behaviour is striking as different particle production mechanisms are expected to be involved in the different collision systems. The results also show that the strangeness enhancement with multiplicity does not depend on the collision energy at the LHC energies (∼TeV) and that it is larger for hadrons with larger strangeness content.

The work presented in this thesis addresses the strangeness enhancement effect observed in proton-proton collisions, focusing on the production of the strange meson K^0_S and of the strange baryon $\Xi^\pm$ in jets and out of jets in pp collisions at $\sqrt{s} = 5.02$ TeV and at $\sqrt{s} = 13$ TeV. The data were collected by the ALICE experiment during the Run 2 data taking (2015-2018). The aim of this work is to evaluate the contribution to the strangeness enhancement effect given by the mechanisms associated to hadron production in jets (hard processes) and out of jets.

For the purpose of separating K^0_S ($\Xi^\pm$) produced in jets from the ones produced out of jets, the angular correlation between the charged particle with the highest transverse momentum p_T and with $p_\mathrm{T} > 3$ GeV/c (*trigger* particle) and the K^0_S ($\Xi^\pm$) produced in the same collision is evaluated. K^0_S and $\Xi^\pm$ are identified by applying topological and kinematic selections to the variables describing their decay into charged hadrons. The trigger particle is considered as a proxy for the jet axis: K^0_S ($\Xi^\pm$) produced in the leading jet are found in an angular region centred in the direction of the trigger particle (*toward-leading* production), whereas K^0_S ($\Xi^\pm$) produced in an angular region transverse to the trigger particle direction are associated to out-of-jet (*transverse-to-leading*) production.

The toward-leading and the transverse-to-leading yields of K^0_S ($\Xi^\pm$) are calculated as a function of the multiplicity of charged particles produced in the events with a trigger particle. For both K^0_S and $\Xi^\pm$, the transverse-to-leading yield increases with the multiplicity of charged particles faster than the toward-leading one, suggesting that the relative contribution of transverse-to-leading processes with respect to toward-leading processes increases with the multiplicity of charged particles produced in the collision. The ratio between the $\Xi^\pm$ and the K^0_S yields provides insight into the strangeness enhancement effect, since the strangeness content of the $\Xi^\pm$ ($|S|$=2) is larger than the K^0_S one ($|S|$=1). Both the transverse-to-leading

and the toward-leading $\Xi^{\pm}/K^0_S$ yield ratios increase with the multiplicity of charged particles. The transverse-to-leading ratio is larger than the toward-leading one, suggesting that the relative production of $\Xi^{\pm}$ with respect to K^0_S is favoured in transverse-to-leading processes.

The results as a function of the charged particle multiplicity are compared with the predictions of different phenomenological models, namely EPOS LHC and two different implementations of PYTHIA 8.

The results presented in this thesis were approved by the ALICE collaboration and presented in several international conferences. The paper which contains the results presented in this thesis is in preparation.

In the last part of this thesis the further developments of this work which will be possible thanks to the large amount of pp collisions which will be collected during the Run 3 data taking are also discussed.

Contents

Chapter 1

QCD and ultra-relativistic heavy-ion collisions

The nucleus-nucleus collisions at ultra-relativistic energies provided by the Large Hadron Collider (LHC) are a unique tool to study the strongly interacting matter described by the Quantum Chromodynamics (QCD) field theory. The high temperature and energy density conditions reached in heavy-ion collisions at the LHC energies determine the formation of the quark-gluon plasma (QGP), a state of matter in which the elementary constituents of the hadrons, i.e. quarks and gluons, are deconfined. In this chapter, after a brief introduction to QCD (Section 1.1), the main characteristics of heavy-ion collisions and of their space-time evolution are delineated (Section 1.2), and the key experimental probes which allow for the investigation of the QGP properties are described (Section 1.3). In recent times, many of the features interpreted as signatures of QGP formation in heavy-ion collisions have also been observed in smaller collision systems, such as p–Pb and pp collisions at the LHC energies. These observations, which challenge the current understanding of particle production mechanisms, are presented at the end of this chapter in Section 1.4.

1.1 A brief introduction to QCD

Quantum Chromodynamics (QCD) [1, 2] is the quantum field theory of the strong interaction of quarks and gluons. Its underlying symmetry is the invariance under SU(3) local phase transformations:

$$\psi(x) \rightarrow \psi'(x) = \exp\left[ig_S \boldsymbol{\alpha}(\boldsymbol{x}) \cdot \hat{\boldsymbol{T}}\right] \psi(x), \tag{1.1}$$

where $\psi(x)$ is the space-time dependent wave function, g_S is a constant, $\boldsymbol{\alpha}(\boldsymbol{x}) = \alpha^a(x)$ are eight functions of the space-time coordinate x, and $\hat{\mathbf{T}} = \{T^a\}$ are the eight generators of the SU(3) symmetry group which are related to the Gell-Mann matrices λ^a by $T^a = \frac{1}{2}\lambda^a$. Since the Gell-Mann matrices are 3×3 matrices, the wave function ψ must include an additional degree of freedom, called *colour*, represented by a 3 dimensional vector. From now on the SU(3) symmetry will be called $\mathrm{SU(3)_C}$ to underline that it is related to the colour degree of freedom.

The $\mathrm{SU(3)_C}$ gauge invariance can only be obtained by introducing eight fields $G^a_\mu(x)$, where the index a relates them to the eight generators of $\mathrm{SU(3)_C}$ and μ is the Lorentz index. These eight fields represent the eight massless and coloured gluons, which are the mediator of the QCD interaction, in the same way as the massless photon is the mediator of the QED

interaction. Gauge invariance is satisfied providing that the eight fields transform as:

$$G_{\mu}^{k} \rightarrow G_{\mu'}^{k} = G_{\mu}^{k} - \partial_{\mu}\alpha_{k} - g_{S} f_{ijk} \alpha_{i} G_{\mu}^{j}, \tag{1.2}$$

where f_{ijk} are the structure constants of the $\mathrm{SU(3)_C}$ group, defined by the commutation relations $[\lambda_i, \lambda_j] = 2if_{ijk}$. Since the $\mathrm{SU(3)_C}$ generators do not commute, QCD is a non-Abelian gauge theory and the third therm in equation 1.2 gives rise to gluon self-interactions.

The Lagrangian of QCD is given by

$$\mathscr{L} = \sum_{f}^{N_f} \bar{\psi}_f \left(i\gamma_{\mu} D\mu - m_f \right) \psi_f - \frac{1}{4} G_{k}^{\mu\nu} G_{\mu\nu}^{k}, \tag{1.3}$$

where $N_f = 6$ is the number of quark flavours, m_f is the mass of the quark of flavour f, γ_μ are the Dirac matrices, $G_{\mu\nu}^{k}$ is the QCD field tensor defined by

$$G_{\mu\nu}^{k} = \partial_{\mu} G_{\nu}^{k} - \partial_{\nu} G_{\mu}^{k} + g_{S} f_{kij} G_{\mu}^{i} G_{\nu}^{j}, \tag{1.4}$$

and D_μ is the covariant derivative

$$iD_{\mu}\psi = \left(i\partial_{\mu} + \frac{1}{2} g_{S} G_{\mu}^{k} \lambda^{k} \right) \psi. \tag{1.5}$$

The first term in equation 1.3 includes the interaction between quarks and gluons, while the second term describes the gluons self-interactions, i.e. the triple and quartic gluon vertices. The three corresponding Feynman diagrams are displayed in Figure 1.1.

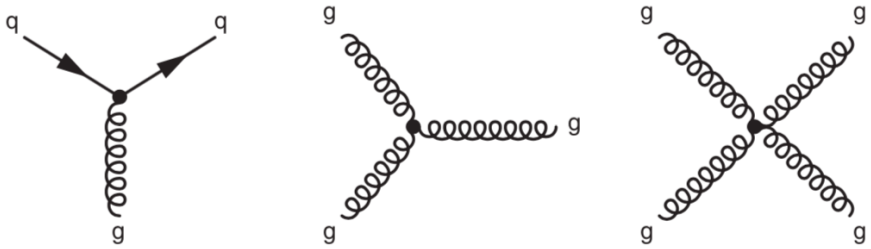

Figure 1.1: The QCD interaction vertices resulting from the requirement of SU(3) local gauge invariance. Figure taken from [1].

If quarks were massless, the QCD Lagrangian would not only be invariant under $\mathrm{SU(3)_C}$ local phase transformations but it would also be invariant under chiral flavour symmetry $\mathrm{SU}(N_f)_\mathrm{R} \times \mathrm{SU}(N_f)_\mathrm{L}$, where L and R stand for left-handed and right-handed, respectively, and $N_f = 6$ is the number of quark flavours. In nature, however, quarks have masses and the quark mass term introduces an explicit chiral symmetry breaking in the QCD Lagrangian.

In hadronic matter the chiral symmetry is spontaneously broken. As a consequence, light quarks *bare* masses ($m_u \simeq m_d \simeq 4$ MeV$/c^2, m_s \simeq 94$ MeV$/c^2$ [3]), which appear in the QCD Lagrangian, are different from light quarks *constituent* masses ($m_u \simeq m_d \simeq 350$ MeV$/c^2, m_s \simeq 500$ MeV$/c^2$ [4]), which result from the spontaneous chiral symmetry breaking and are only defined within a specific hadronic model [4, 5].

1.1.1 The running coupling constant α_S

The strength of the interaction between the quarks and the gluons is determined by the coupling at the corresponding QCD vertex. For each QCD vertex in a Feynman diagram, there is a infinite set of higher order corrections which, with the process of *renormalisation*, can be absorbed into the definition of the coupling strength g_S. As a consequence, the QCD fine structure constant $\alpha_S = g_S^2/4\pi$ depends on the energy scale Q considered:

$$\alpha_S(Q^2) = \frac{\alpha_S(\mu^2)}{1 + B\alpha_S(\mu^2)\ln(Q^2/\mu^2)} \,, \tag{1.6}$$

where $B = \frac{11N_C - 2N_f}{12\pi}$, $N_C = 3$ colours, $N_f = 6$ quark flavours and μ is the energy scale of renormalisation. Since B is positive, α_S decreases with increasing Q^2, as shown in Figure 1.2, implying that the interaction between quark and gluons, i.e. the partons, becomes weaker with increasing momentum exchange.

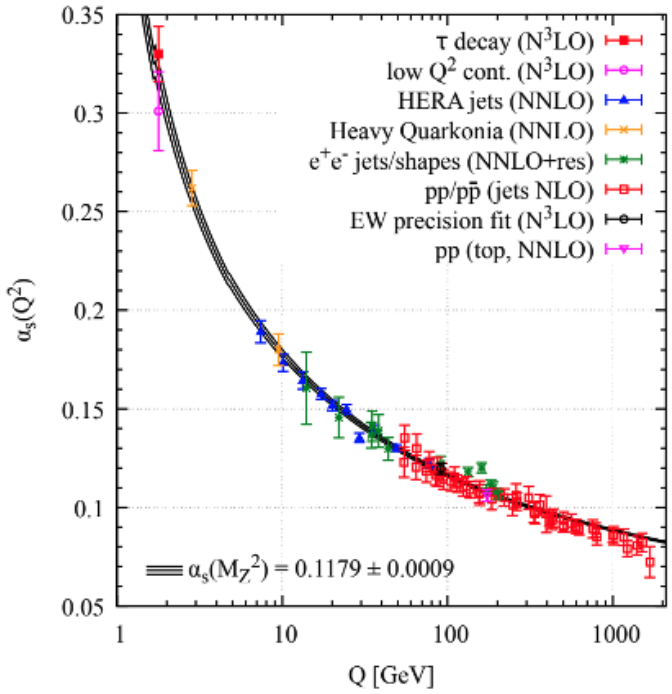

Figure 1.2: Summary of α_S measurements as a function of the energy scale Q. Different colours indicate different measurements used to extract the α_S values. The degree of QCD perturbation theory used to extract α_S is indicated in parentheses. Figure taken from [4].

For $Q > 100$ GeV, $\alpha_S \sim 0.1$ and therefore a perturbative approach (pQCD) can be used to investigate processes characterised by a large momentum transfer between partons. The behaviour in this regime is called *asymptotic freedom* [6, 7] and implies, for example, that in inelastic scattering experiments with high values of transferred momenta, quarks can be treated as free particles instead of being considered strongly bound inside the protons.

For $Q \sim 1$ GeV, α_S is $O(1)$ and perturbation theory cannot be applied. Calculations can be performed using other theoretical approaches such as the computational technique of lattice QCD [4], which consists in the evaluation of quantum-mechanical properties on a discrete lattice of space-time points. In this regime, the so called *confinement* [8] is observed: it consists in the fact that all colour charges, i.e. quarks and gluons, are bound within

colourless hadrons. This implies that quarks and gluons cannot be isolated and observed directly. This property originates from the gluon-gluon self interactions and can be described using an effective potential $V(\mathbf{r})$:

$$V(\mathbf{r}) = -\frac{4}{3}\frac{\alpha_S}{r} + \kappa r \ , \tag{1.7}$$

where $\kappa \sim 1$ GeV/fm and r is the distance from the colour charge generating the colour field. At relatively large distance this effective potential increases linearly, implying an analogous increase of the energy stored in the colour field between two colour charges. The energy required to separate two quarks to infinity is therefore infinite and for this reason quarks arrange themselves into colourless hadrons.

1.1.2 The QCD phase diagram

The QCD Lagrangian predicts a transition from a state in which quarks and gluons are confined and chiral symmetry is spontaneously broken (the *hadron gas* phase) to a state in which quarks and gluons are deconfined and, as a consequence of the restoration of the spontaneously broken chiral symmetry, acquire their *bare* masses. This state is called quark-gluon plasma (QGP) [9].

Figure 1.3 displays the phase diagram of strongly interacting matter as a function of the temperature T and of the baryochemical potential μ_{B}, which corresponds to the energy needed to increase the baryon number of the system by one unit at fixed volume and entropy, and is proportional to the net baryon density of the system.

The point at T = 0 MeV and $\mu_{\mathrm{B}} = 0$ MeV corresponds to the QCD vacuum, while the point at $T \approx 0$ MeV and $\mu_{\mathrm{B}} \approx 1000$ MeV corresponds to ordinary nuclear matter. Heavy-nuclei collisions at different centre-of-mass energies are a tool to probe the phase transition from the hadron gas to the QGP at different μ_{B} values. For example, at the LHC energies the region at $\mu_{\mathrm{B}} \approx 0$ is investigated, while the phase transition at larger values of μ_{B} can be studied at smaller centre-of-mass energies. At small values of T and large values of μ_{B} a transition to a Colour Superconductor phase is expected: this state of the matter may be present in the core of the neutron stars [10].

According to lattice QCD calculations, which can be performed for $\mu_{\mathrm{B}} \lesssim 300$ MeV, the phase transition from the hadron gas to the QGP is a smooth crossover occurring, at $\mu_{\mathrm{B}} \approx 0$ MeV, at a critical temperature of $T_C = (156 \pm 1.5)$ MeV [11]. At larger values of μ_{B}, approximate methods for the calculation of thermodynamic quantities predict a first-order phase transition ending in a critical point when decreasing μ_{B} [12, 13]. This region of the phase diagram has been recently probed by the RHIC BES-II programme [14] and will be studied by forthcoming experiments at the NICA [15, 16], FAIR [17] and SPS facilities [18].

1.2 Heavy-ion collisions

Soon after the discovery of QCD and the understanding that it implies the existence of a state of matter made of free quarks and gluons, the idea of colliding heavy-ions to create the quark-gluon plasma was conceived. First experiments colliding non-relativistic nuclei began in the mid-seventies at the Bevalac facility at LBNL [20]. Later, experiments in the relativistic regime began at the Brookhaven AGS and at the CERN SPS in 1986 [21]. The SPS accelerated ^{16}O and ^{32}S at an energy of 200 GeV per nucleon, and ^{208}Pb at 158 GeV

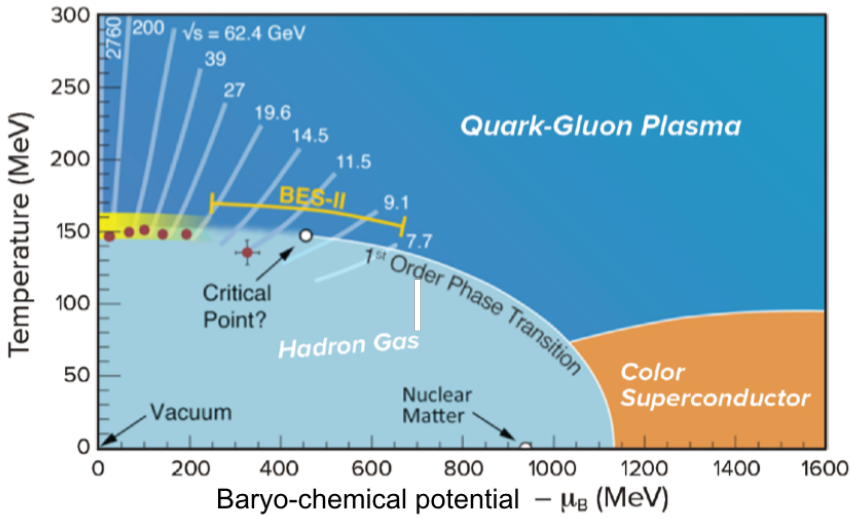

Figure 1.3: The QCD phase diagram. The baryochemical potential μ_B and the temperature T are indicated on the x and the y axes, respectively. Picture adapted from [19].

per nucleon. The first Pb–Pb collisions were provided by the SPS in 1996 and reached the centre-of-mass energy per nucleon pair $\sqrt{s_{NN}} = 17.2$ GeV.

The experiments carried out at the SPS led to the CERN announcement of QGP discovery in 2000 [21]. Five years later, the discovery was confirmed by experiments at the Relativistic Heavy Ion Collider (RHIC) at Brookhaven National Laboratory which, providing Au–Au collisions up to $\sqrt{s_{NN}} = 200$ GeV, marked the beginning of the current era of heavy-ion collisions. Finally, in 2009 the LHC at CERN began to collide ^{208}Pb nuclei at approximately ten times the energy of RHIC, confirming several of its main results.

In the following, the space-time evolution of a heavy-ion collisions is described. Then, the main geometrical parameters of a heavy-ion collision are introduced, together with the Monte Carlo Glauber model, which links the geometrical parameters to observable quantities. In the last sections the main observables used to probe the QGP are discussed.

1.2.1 Space-time evolution of heavy-ion collisions

The evolution of a heavy-ion collision follows a sequence of stages, from the collision itself to the production of hadrons, which are described in detail in the following and are summarised in Figure 1.4.

- The collision of the two nuclei takes place at the time $t = 0$ fm/c. The nuclei are Lorentz contracted along the beam direction by a factor γ, which for lead nuclei accelerated by LHC at $\sqrt{s_{NN}} = 5.02$ TeV is approximately 2500. The crossing time of the two nuclei is therefore $2R/\gamma \sim 0.01$ fm/c, where R is the radius of the nucleus ($R \simeq 7$ fm for large nuclei such as Pb and Au). The nucleons which undergo inelastic interactions are called *participant* nucleons. Their number N_{part} is inversely proportional to the impact parameter b, which measures the distance between the centres of the two colliding nuclei. The *spectator* nucleons, i.e. the ones not participating in the interaction, continue to travel along the beam direction.

- For $t < 1$ fm/c matter is out of equilibrium: this stage is called *pre-equilibrium stage*. When the two nuclei collide, most of the interactions between partons involve small mo-

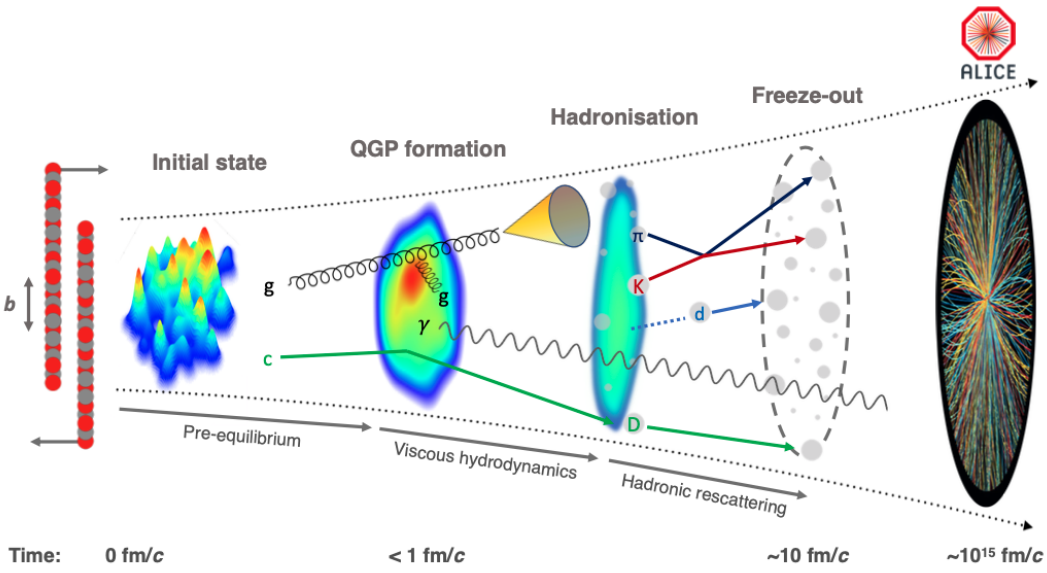

Figure 1.4: Evolution of a heavy-ion collision. Figure taken from [22].

mentum exchange (*soft* interactions). These interactions determine the initial density profile of the system, whose lumpiness depends on the nuclear fluctuations inside the colliding nuclei. A small fraction of partons undergoes hard perturbative interactions, which enable the creation of high momentum quarks and gluons and heavy quarks, such as the *charm* and the *bottom* quarks.

- If sufficiently high energy density and temperature conditions are reached, QGP forms. The initial temperature of QGP, according to hydrodynamic simulations, exceeds 450 MeV at the LHC energies [21]. According to lattice QCD calculations [23], the energy density of matter in thermal equilibrium at 300 MeV is approximately 12.7 GeV/fm^3, about twenty times the energy density of a hadron: in these conditions, quarks and gluons cannot be described as a collection of hadrons, but rather as the degrees of freedom of a deconfined medium. After its formation, QGP expands under pressure-driven forces and can be described using viscous hydrodynamic models [24] based on an equation of state calculated from lattice QCD. The hydrodynamic expansion is influenced by the QGP bulk and shear viscosities, which measure its resistance to volume growth and fluid deformation, respectively. In this phase, high-momentum partons interact with the QGP via radiative and elastic processes, loosing energy.

- When the QGP temperature falls below the critical value $T_c = (156 \pm 1.5)$ MeV [11], hadronization occurs, i.e. there is a phase transition from QGP to a hadron-resonance gas. Hard partons hadronize into jets, i.e. collimated sprays of particles, in the same way as in elementary collisions, while lower momenta partons can combine with other partons close in their phase space to form hadrons via coalescence.

- When $T \simeq T_{\mathrm{chem}}$ inelastic interactions among hadrons stop and henceforth particle yields are fixed. This process is called *chemical freeze-out* and the temperature at which it occurs can be extracted by fitting hadron yields with a thermal statistical model, as described in more detail in Section 1.3. In the region of the QCD phase diagram where $\mu_{\mathrm{B}} \sim 0$, the chemical freeze-out is placed close to the phase boundary between QGP and the hadron gas.

- After the *chemical freeze-out* hadrons can still interact via elastic scattering, until the *kinetic freeze-out* temperature is reached at $t \approx 10$ fm/c. Afterwords, particle momenta are fixed and hadrons stream freely, until they reach the detector at approximately 10^{15} fm/c after the collision [22].

Since the QGP cannot be directly detected, as its size is approximately 10 fm at the LHC energies, QGP properties have to be studied by measuring physical quantities which are affected by the QGP evolution. Information about different stages of the evolution can be obtained from different key observables, as described in Section 1.3.

1.2.2 The Glauber model

As anticipated in Section 1.2.1, a heavy-ion collision can be characterised by the impact parameter vector $\vec{b}$, defined as the vector connecting the centres of the two colliding nuclei. Other parameters useful to characterise the collision are the number of participant nucleons N_{part}, i.e. the nucleons which undergo at least one inelastic nucleon-nucleon collision, and the number of binary collisions N_{coll}.

The Glauber model [25] relates N_{part} and N_{coll} to the impact parameter $|\vec{b}|$. The model treats the collision of two nuclei as a superposition of individual nucleon-nucleon interactions and is based on the following assumptions, known as *optical limit*:

- The nucleons inside the nuclei travel on straight lines and are not deflected by the collisions.
- The nucleons interact only via strong interactions: protons and neutrons are therefore indistinguishable.
- The inelastic nucleon-nucleon cross-section does not depend on the number of collisions a nucleon has already undergone.

The experimental inputs to the Glauber model are the nuclear density ρ, usually parametrized with a Woods-Saxon function, and the inelastic nucleon-nucleon cross section $\sigma_{\text{inel}}^{\text{NN}}$.

The Glauber model is implemented in Monte Carlo simulations. In the simulations, the nucleons within each colliding nucleus are distributed in the three-dimensional space according to the nuclear density distribution. In the simplest implementation of the model, two nucleons are assumed to interact inelastically if their distance d in the plane transverse to the beam axis satisfies the condition:

$$d \leq \sqrt{\sigma_{\text{inel}}^{\text{NN}}/\pi}. \tag{1.8}$$

The average number of participating nucleons and binary nucleon-nucleon collisions are determined by simulating many nucleus-nucleus collisions. Figure 1.5 shows a Glauber Monte Carlo event as seen in the transverse plane (left plot) and along the direction of the beam (central plot). The nucleons are represented by circles: the dark ones are the participant nucleons, the light ones are the spectators, i.e. those which do not undergo any inelastic collision. The right plot shows the calculated values of N_{part} and N_{coll} as a function of the impact parameter: both variables decrease with increasing impact parameter, as expected.

The Glauber model, implemented in Monte Carlo simulations in conjunction with particle production models, provides a way to relate the impact parameter to the multiplicity of particles produced in the collision, a variable which can be experimentally measured. Indeed, the impact parameter $|\vec{b}|$, N_{part} and N_{coll} cannot be measured directly.

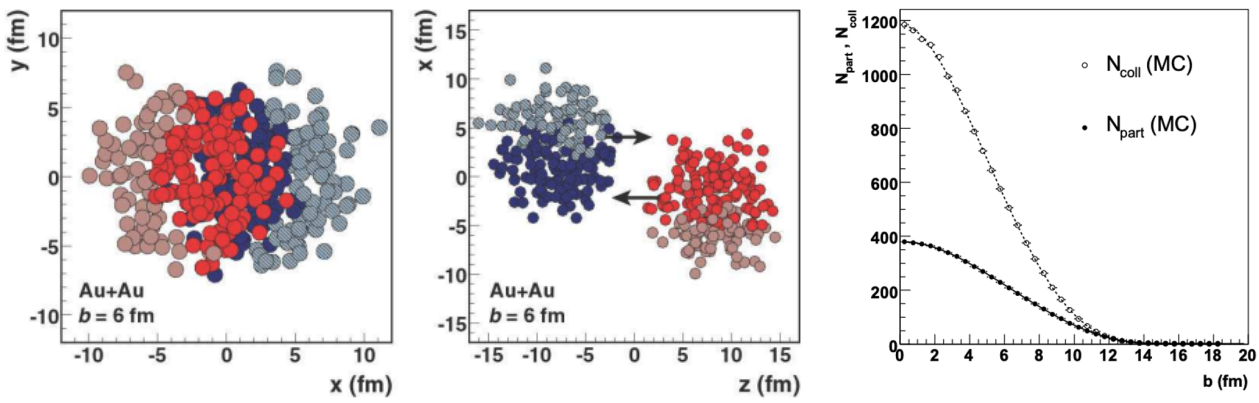

Figure 1.5: Au–Au collisions with impact parameter $|\vec{b}| = 6$ fm simulated with a Glauber Monte Carlo. The simulated collision is shown in the plane perpendicular to the beam axis (left plot) and in the direction of the incoming nuclei (central plot). Dark and light circles represent the participant nucleons and the spectator ones, respectively. (right plot) $N_{\rm part}$ and $N_{\rm coll}$ as a function of the impact parameter $|\vec{b}|$. The figures are adapted from [25].

1.2.3 Centrality selections in Pb–Pb collisions

Events in heavy-ion collisions are typically divided into event classes according to their centrality. The centrality of the collision is closely related to the impact parameter: collisions with $|\vec{b}| \sim 0$ are called *central*, while collisions with $|\vec{b}| \sim 2R$ are called *peripheral*. The centrality classes are commonly defined starting from the distribution of the signal amplitudes measured by scintillators placed at forward rapidity, that is close to the beam axis. The signal amplitudes are proportional to the multiplicity of particles produced in the collision; the multiplicity, in turn, is proportional to the centrality of the collision. Consequently, the signal amplitude distribution can be used to define the centrality classes.

For example, in the ALICE experiment (see Chapter 3) the centrality classes are defined starting from the distribution of the sum of the signal amplitudes measured by the V0 scintillators[1]. An example of the distribution is shown in Figure 1.6. The 0-5% centrality class corresponds for example to the 5% of events with the highest V0 amplitude, and the same principle applies to the more peripheral classes. Centrality classes are therefore expressed via a percentage of the total hadronic interaction cross section. The red curve is a fit performed using the Glauber model together with a particle production model that assumes there are $fN_{\rm part} + (1-f)N_{\rm coll}$ particle sources, each one producing particles distributed according to a negative binomial distribution (NBD). The parameter $f \sim 0.8$ represents the contribution of soft processes, whose rate is driven by $N_{\rm part}$. On the contrary, the rate of hard scattering processes is driven by $N_{\rm coll}$. The fit allows for the extraction of the average $N_{\rm part}$ and $N_{\rm coll}$ for each centrality class.

Also in pp collisions events can be divided into classes starting from the distribution of the sum of the signal amplitudes measured by the V0 scintillators. These classes are not denominated *centrality classes*, since the concept of centrality is not well defined in pp collisions, but are instead called *multiplicity classes*, since, as already pointed out, the sum of the signal amplitudes measured by the V0 scintillators is proportional to the multiplicity

[1]The V0 detector [26] consists in two arrays of scintillation counters, called V0A and V0C, placed close to the beam axis on opposite sides of the interaction point.

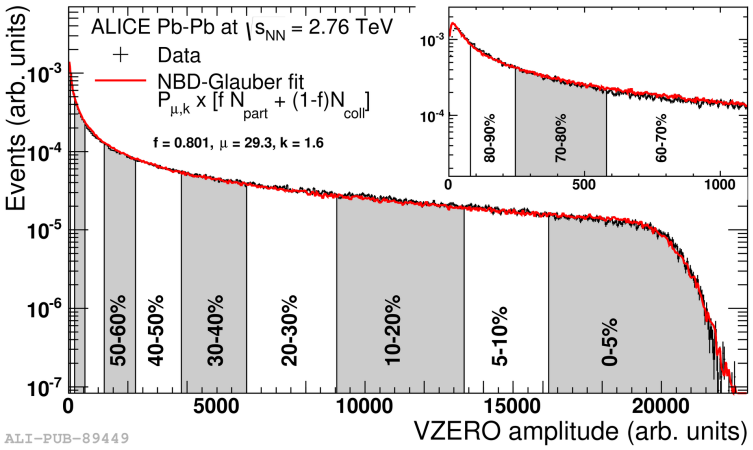

Figure 1.6: Distribution of the sum of the signal amplitudes measured in the V0 detectors in Pb–Pb collisions at $\sqrt{s_{NN}} = 2.76$ TeV. Centrality classes are defined starting from this distribution, as illustrated. Figure taken from [27].

of particles produced in the collision. A detail description of multiplicity determination in pp collisions is provided in Section 3.7.

1.3 QGP experimental probes

This section provides a description of several experimental observables which can be used to probe the QGP formation in order to extract its properties and understand its space-time evolution.

1.3.1 Charged particle multiplicity

The average multiplicity of charged particles produced at midrapidity $\langle dN/d\eta \rangle_{|\eta|<0.5}$[2] provides information on the initial energy density of the system. The $\langle dN/d\eta \rangle_{|\eta|<0.5}$ values measured in different centrality classes are divided by the average number of participant nucleon pairs $\langle N_{part} \rangle/2$ in order to allow for the comparison between different collision systems. Figure 1.7 shows $\frac{2}{\langle N_{part} \rangle} \langle dN_{ch}/d\eta \rangle_{|\eta|<0.5}$ as a function of $\langle N_{part} \rangle$ (left plot) and as a function of the centre-of-mass energy $\sqrt{s_{NN}}$ (right plot). The results obtained in heavy-ion collisions are compared to pp and p–A ones. The charged particle multiplicity per participant nucleon pair increases with $\langle N_{part} \rangle$ and with $\sqrt{s_{NN}}$. At the same centre-of-mass energy, $\frac{2}{\langle N_{part} \rangle} \langle dN_{ch}/d\eta \rangle_{|\eta|<0.5}$ is larger for A–A collisions with respect to pp and p–A collisions, indicating that heavy-ion collisions are more efficient than pp and p–A collisions in transferring the initial energy into particle production at midrapidity. The two series of points can be described by power low functions of the form $\alpha \times s^{\beta}$, with $\beta = 0.155 \pm 0.004$ for central Pb–Pb collisions and $\beta = 0.103 \pm 0.002$ for pp and p–A collisions. It is worth noting that p–A results follow the same trend of pp results, indicating that the strong rise observed for Pb–Pb collisions does not only depend on the multiple collisions undergone by the participant nucleons, since also in p–A collisions the proton encounters multiple nucleons.

[2]The pseudorapidity η is defined as $\eta = -\ln(\tan(\theta/2))$, where θ is the polar angle of the particle in the reference frame whose z axis lies along the beam direction.

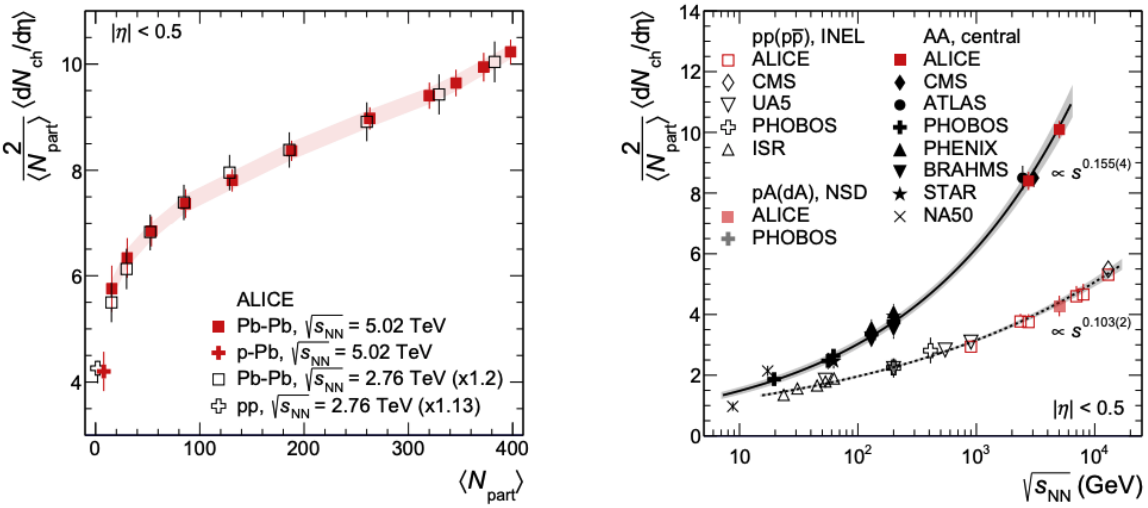

Figure 1.7: Charged particle multiplicity at midrapidity per participating nucleon pair $\frac{2}{\langle N_{\rm part}\rangle}\langle {\rm d}N_{\rm ch}/d\eta\rangle_{|\eta|<0.5}$ as a function of the average number of participating nucleons $\langle N_{\rm part}\rangle$ (left) and of the centre-of-mass energy $\sqrt{s_{\rm NN}}$ (right plot). In the left panel, the error bars show the centrality-dependent uncertainties, whereas the shaded band represents the uncertainties correlated across centrality. Figures taken from [28].

1.3.2 Identified particle yields and chemical freeze-out temperature

Hadron yields measured at midrapidity in heavy-ion collisions are well described by a statistical hadronisation model (SHM) based on the assumption that QGP equilibrates both chemically and thermally. The SHM model contains three main parameters: the temperature $T_{\rm chem}$ at the chemical freeze-out, the baryochemical potential $\mu_{\rm B}$ which takes into account baryon number conservation, and the volume V of the hadron and resonance gas (HRG) which is produced at the chemical freeze-out. The values of these parameters can be obtained by fitting the particle yields.

Figure 1.8 shows the yields of different hadron species containing only light quarks (u, d, s) measured in central (0-10%) Pb–Pb collisions at $\sqrt{\rm s_{NN}} = 2.76$ TeV, together with the fit results from four different implementations of the thermal model (THERMUS [29], SHARE [30], Thermal-FIST [31] and GSI-Heidleberg [32]). Since matter and antimatter are observed to be produced in equal amounts at the LHC energies [33], the baryochemical potential was fixed to zero in all models but the GSI-Heidelberg one, where $\mu_{\rm B}$ was considered as a free parameter of the fit and was determined to be compatible with zero within uncertainties. The chemical freeze-out temperature obtained from the fits is $T_{\rm chem} \approx 156$ MeV, with uncertainties of about 2-3 MeV for all the four models. It should be noted that $T_{\rm chem}$ is very close to the critical temperature predicted by lattice QCD calculations for the transition between QGP and hadron gas at $\mu_{\rm B} = 0$ ($T_C = (156 \pm 1.5)$ MeV [11]).

The statistical hadronisation model fits to the pion, kaon and proton yields in Pb–Pb collisions at $\sqrt{\rm s_{NN}} = 5.02$ TeV [34] provide a chemical freeze-out temperature compatible with the one obtained at $\sqrt{\rm s_{NN}} = 2.76$ TeV. This result is consistent with the observation that $T_{\rm chem}$ increases with the centre-of-mass energy, reaching a saturation value of about 155-160 MeV for $\sqrt{\rm s_{NN}} \gtrsim 20$ GeV [32]. On the contrary, the baryochemical potential is observed to decrease with the collision energy [32], reaching values compatible with zero at the LHC

energies.

Overall, the SHM model is successful in describing the hadron yields over nine orders of magnitude.

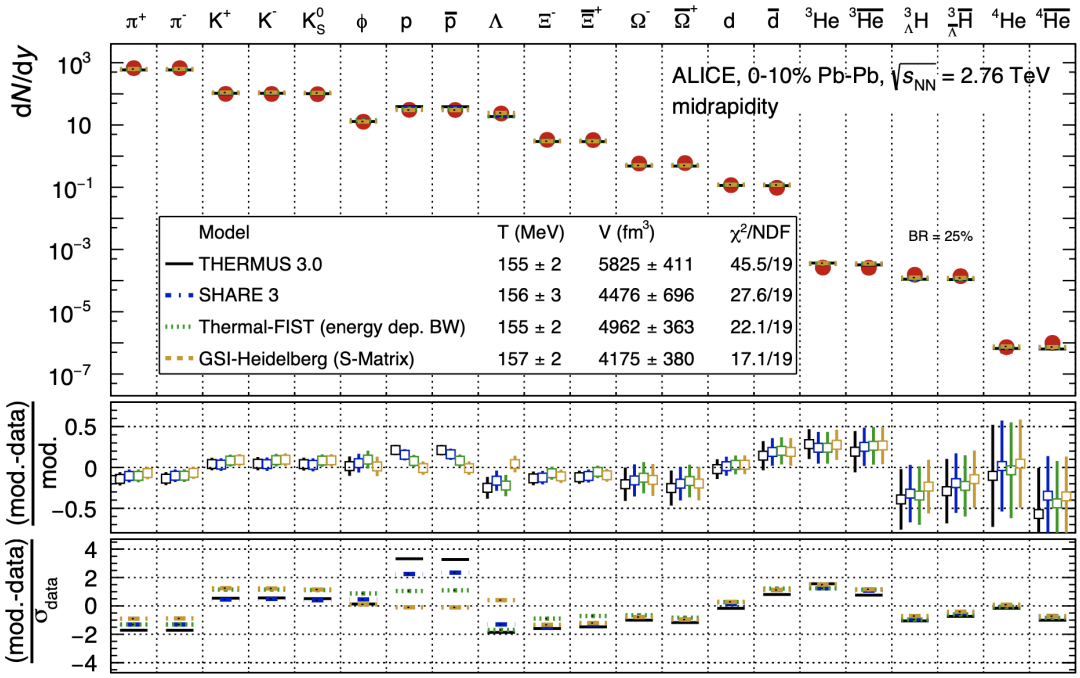

Figure 1.8: Measured yields per unit of rapidity of light flavour hadrons and nuclei in central (0-10%) Pb–Pb collisions at $\sqrt{s_{NN}} = 2.76$ TeV. Results from four different implementations of the statistical hadronisation model are shown (THERMUS [29], SHARE [30], Thermal-FIST [31], GSI-Heidleberg [32]). The middle panel shows the difference between the models and the data normalised by the model values and the lower panel shows the difference between model and data divided by the experimental uncertainties. Figure taken from [22].

1.3.3 Kinetic freeze-out temperature and radial flow

Particle production in heavy-ion collisions exhibits a collective behaviour known as collective flow. This phenomenon is a consequence of the pressure-driven expansion of QGP, which is described by hydrodynamic models, and consists in a correlation between particle momenta and position. The isotropic component of the collective flow is called radial flow and it is related to the fact that the pressure at the centre of the QGP fireball is larger than at its outskirts. As a consequence, hadrons acquire an additional transverse momentum given by the product of their mass and the common radial flow velocity.

Figure 1.9 shows the p_{T} spectra of different hadron species in central (0-5%) and peripheral (80-90%) Pb–Pb collisions at $\sqrt{s_{NN}} = 2.76$ TeV. The spectra become harder with increasing centrality, i.e. their maxima are located at higher transverse momenta in central collisions with respect to peripheral ones. This is consistent with the expected increase of radial flow with centrality. Moreover, the flattening of the spectra in the low-p_{T} region is more pronounced for heavier particles, as a consequence of the fact that the radial flow has a stronger effect on more massive particles.

The radial flow can be quantified by fitting the transverse momentum spectra with the function based on the Blast-Wave model [35], which assumes that particles are produced

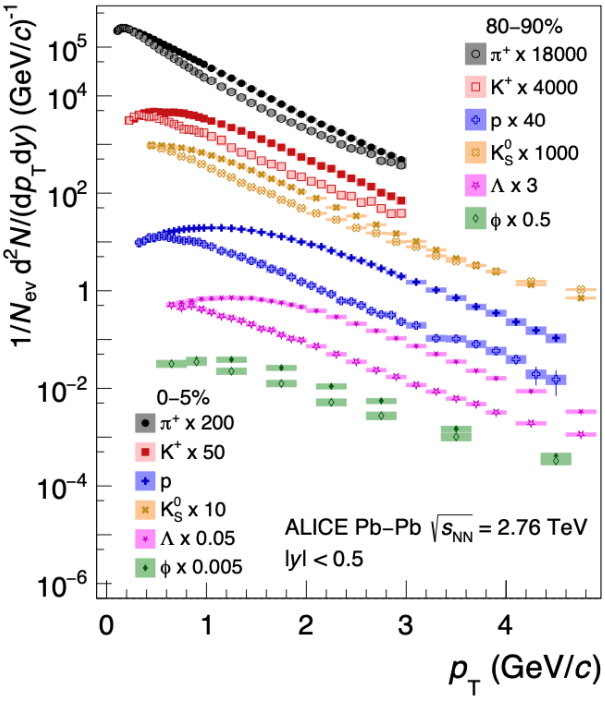

Figure 1.9: Transverse momentum distributions of different hadron species in central (0-15%) and peripheral (80-90%) Pb–Pb collisions at $\sqrt{s_{\rm NN}} = 2.76$ TeV. Figure taken from [22].

by a locally thermalised medium expanding collectively in a hydrodynamic way and then undergoing an instantaneous freeze-out at a temperature $T_{\rm kin}$. In the simplest implementation of the model, the expansion of the medium is radial and is described by a common transverse velocity $\beta_{\rm T}$ which depends on the radial distance r from the centre of the expanding fireball:

$$\beta_{\rm T}(r) = \beta_s(r/R)^n, \tag{1.9}$$

where β_s is the transverse velocity at the surface of the expanding medium, R is the radius of the expanding system and n determines the shape of the velocity profile.

Simultaneous fit to transverse momentum distributions of different particles leads to $T_k = 90$ MeV and $\beta_T = 0.65$ for the most central collisions and $T_k = 150$ MeV and $\beta_T = 0.35$ for the most peripheral ones [36]. These results suggest a more rapid expansion of the fireball with increasing centrality, and an earlier kinetic freeze-out in peripheral collisions with respect to central ones.

1.3.4 Azimuthal anisotropy

In non-central heavy-ion collisions the overlap region of the colliding nuclei is non-isotropic and the QGP fireball has an almond shape. This causes an azimuthal anisotropy in the pressure gradients which is converted in a transverse momentum azimuthal anisotropy during the expansion of the fireball. This effect can be quantified by studying the azimuthal distribution of particles $\mathrm{d}N/\mathrm{d}\varphi$, which can be expressed in terms of a Fourier expansion [37]:

$$\frac{\mathrm{d}N}{\mathrm{d}\varphi} \propto 1 + \sum_n 2v_n(p_{\rm T})\cos\left[\mathrm{n}(\varphi - \Psi_{\rm n})\right] ,$$

where φ is the azimuthal angle of the particles, $\Psi_{\rm n}$ is the $\mathrm{n}^{\rm th}$-harmonic symmetry plane angle (in the case of $\mathrm{n} = 2$ it corresponds to the orientation of the plane spanned by the beam

axis and the impact parameter vector), and v_n are the Fourier coefficients, respectively called directed, elliptic, triangular for n = 1, 2, 3. While v_2 is related to the almond shaped overlap region of the two colliding nuclei, the higher order coefficients are related to the fluctuations in the initial distributions of nucleons in the overlap region, referred to as *initial state* density fluctuations.

A non-zero v_2 is associated to the presence of a double ridge-like structure in the angular correlation distribution of particle pairs, which is typically expressed as a function of $\Delta\varphi$ and $\Delta\eta$, where $\Delta\varphi$ and $\Delta\eta$ are the differences in azimuthal angle φ and in pseudorapidity η between the two particles. The two ridge-like structures, which elongate along $\Delta\eta$ and are centred in $\Delta\varphi = 0$ and $\Delta\varphi = \pi$, indicate a non-isotropic azimuthal distribution of particles.

Figure 1.10 shows v_2 for charged particles as a function of the transverse momentum p_{T} in different centrality intervals: the magnitude of v_2 increases with decreasing centrality, reaching its maximum in the 40-50% centrality interval, where the eccentricity of the overlap region is larger. In more peripheral collisions (50-60% and 60-70%) v_2 is smaller, suggesting that the system has a shorter lifetime which does not allow for the generation of larger v_2. In all centrality intervals v_2 increases with p_{T}, reaching a maximum at about 3-4 GeV/c. For $p_{\mathrm{T}} <$ 2-3 GeV/c, the v_2 shows a mass ordering: it is smaller for heavier particles. This is a consequence of the radial flow, which imposes an equal isotropic boost to all particles, as described in Section 1.3.3. For 3 $< p_{\mathrm{T}} <$ 8-10 GeV/c, the v_2 depends on the number of constituent quarks: baryons have larger v_2 than mesons. This observation supports the hypothesis of particle production via quark coalescence [38]. For $p_{\mathrm{T}} >$ 10 GeV/c, where the v_2 originates from the path-length dependence of the in-medium energy loss of hard partons, the v_2 of different particles species are compatible within uncertainties and depend only weakly on the transverse momentum.

The elliptic flow is very sensitive to the specific shear viscosity of the medium, i.e. the ratio of the shear viscosity to the entropy: large values of specific shear viscosity suppress the collective flow and reduce the magnitude of v_2. Therefore, the comparison between the experimental measurements of v_2 and of higher order anisotropic coefficients to the output of hydrodynamic model calculations provides an estimate of the specific shear viscosity, which at the critical temperature is found to be compatible with the theoretical lower limit of $1/4\pi$ [39], suggesting that the QGP behaves as a perfect fluid [40].

1.3.5 Strangeness enhancement

Strange hadron production in heavy-nuclei collisions is enhanced with respect to minimum bias pp collisions. This phenomenon, called *strangeness enhancement*, is considered a pivotal signature of QGP formation [21]. Its origin lies in the fact that $s\bar{s}$ quark pairs are easily produced in the QGP since their bare mass is well below the QGP temperature. The high density of strangeness at hadronisation results in an enhanced production of strange baryons, in particular of multi-strange ones, with respect to minimum bias pp collisions. The topic of strangeness enhancement will be covered in greater detail in Chapter 2.

1.3.6 Energy loss in the QGP

As already pointed out, hard perturbative interactions occur in the very initial stage of the collision, before QGP is created. These processes enable the creation of heavy quarks and high-p_{T} partons which experience the full QGP evolution and, while traversing the fireball, interact with it. The interaction with the QGP can occur via inelastic processes (medium

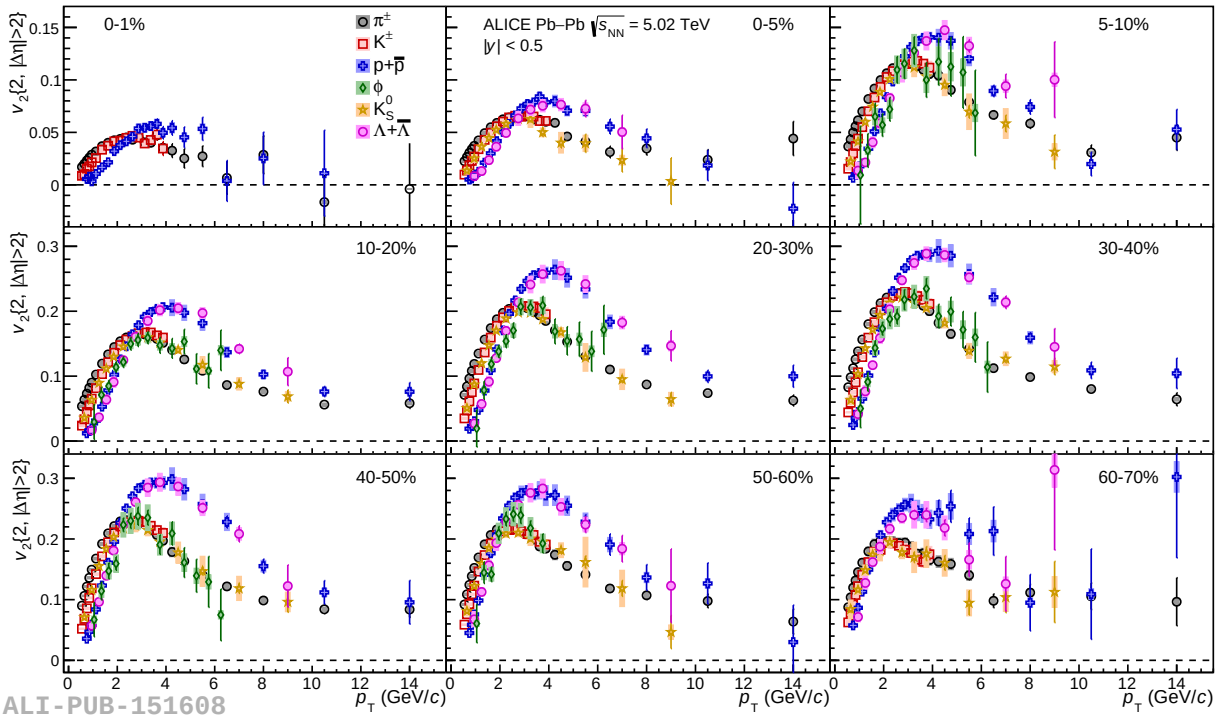

Figure 1.10: Elliptic flow coefficient v_2 for different hadron species as a function of the transverse momentum p_{T} in different centrality intervals of Pb–Pb collisions at $\sqrt{s_{\mathrm{NN}}} = 5.02$ TeV [41].

induced gluon radiation), which are dominant for high energy partons, and elastic (collisional) processes, which contribute at lower energy. The amount of lost energy depends on the path traversed by the parton in the QGP and provides information on the transport properties of the medium.

The effect of energy loss in the QGP can be quantified by the nuclear modification factor R_{AA}, defined as the ratio between the p_{T}-differential yield of a particle measured in nucleus-nucleus collisions and the same observable measured in pp collisions at the same centre-of-mass energy per nucleon pair, scaled by the average number of binary collisions $\langle N_{\mathrm{coll}} \rangle$:

$$R_{\mathrm{AA}} = \frac{\mathrm{d}N_{\mathrm{AA}}/\mathrm{d}p_{\mathrm{T}}}{\langle N_{\mathrm{coll}} \rangle \mathrm{d}N_{\mathrm{pp}}/\mathrm{d}p_{\mathrm{T}}} \,. \tag{1.10}$$

If a nucleus-nucleus collision were a simple superposition of $\langle N_{\mathrm{coll}} \rangle$ independent collisions, the nuclear modification factor would be equal to one.

Figure 1.11 shows the $\mathrm{R_{PbPb}}$ of charged particles measured by the ALICE experiment (red markers) and by the CMS experiment (magenta markers) in central (0-5%) Pb–Pb collisions as a function of the transverse momentum [42, 43]. The results, compatible within experimental uncertainties, show a clear deviation from one, indicating the presence of medium effects. Moreover, the suppression is observed to be stronger for the most central collisions, where the QGP fireball has a larger volume [42]: the parton energy loss depends in fact on the traversed path length in the medium. Figure 1.11 also reports the R_{pPb} measured in p–Pb collisions at $\sqrt{s_{\mathrm{NN}}} = 5.02$ TeV by the ALICE experiment (blue circles) [44]. For $p_{\mathrm{T}} > 2$ GeV/c, R_{pPb} is compatible with unity, showing no nuclear matter modification of hadron production at high p_{T}. It should be noted that particle production at low p_{T} ($p_{\mathrm{T}} \lesssim 2$ GeV/c) is governed by soft processes, for which the scaling from pp to AA is driven by $\langle N_{\mathrm{part}} \rangle$ rather than $\langle N_{\mathrm{coll}} \rangle$, leading

naturally to an R_{AA} below unity in that p_{T} region. The plot also shows that the R_{PbPb} of the photon (green markers) and of the Z and $\mathrm{W}^{\pm}$ bosons (blue triangle and empty marker, respectively) [45–47] is compatible with one, as expected from the fact that they are colour-neutral probes and therefore do not interact with the medium created in the heavy-nuclei collisions.

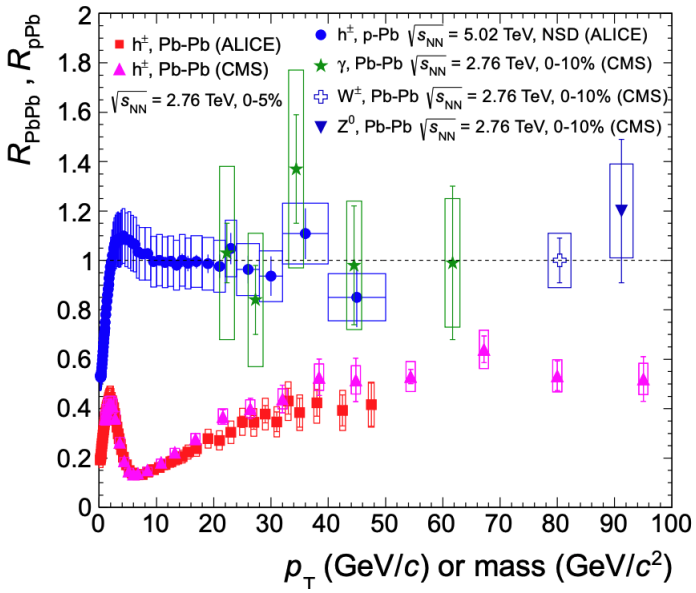

Figure 1.11: The nuclear modification factor R_{AA} for charged particles as a function of p_{T} in Pb–Pb collisions (red and magenta markers) and in p–Pb collisions (blue circular markers). The $\mathrm{R_{PbPb}}$ of photons (green markers) and of Z and $\mathrm{W}^{\pm}$ bosons (blue triangle and empty marker, respectively) are also shown. Figure taken from [44].

1.3.7 Quarkonia suppression

Quarkonia are bound states of quark-antiquark pairs ($q\overline{q}$), where q is either a charm quark ($c\overline{c}$ or *charmonium*, whose ground state is the J/Ψ particle) or a bottom quark ($b\overline{b}$ or *bottomonium*, whose ground state is the Υ hadron).

The QGP determines a colour-screening effect which can dissociate the quarkonia, causing the so-called *quarkonia suppression*. This phenomenon can be quantified by the nuclear modification factor R_{AA}. The left panel of Figure 1.12 shows the R_{AA} of the J/Ψ particle measured in heavy-ion collisions at different centre-of-mass energies as a function of the multiplicity of charged particles produced in the collision. The R_{AA} measured by NA50 (green markers) [48] and STAR (light blue markers) [49] clearly decreases with the multiplicity of charged particles, as a consequence of the larger volume of the created fireball. At the LHC energy the J/Ψ suppression is less pronounced and its multiplicity dependence is reduced, as shown by the ALICE measurement in Pb–Pb collisions at $\sqrt{\mathrm{s_{NN}}} = 5.02$ TeV. Indeed, at higher energies the cross-section for heavy-quark production is higher and thus more heavy quarks are produced: as a consequence the recombination of a quark from a dissociated $q\overline{q}$ pair with an anti-quark from another dissociated $q\overline{q}$ pair is more likely to happen. This phenomenon is called *quarkonia regeneration* [22] and is expected to be stronger for charmonia than for bottomonia states, since it is driven by the number of heavy-quark pairs produced in the collisions, which is much smaller for bottom than for charm.

Since the binding energy of excited $c\bar{c}$ and $b\bar{b}$ states is lower than that of the ground states, a sequential suppression depending on the binding energy is expected and was indeed observed for both charmonia [50, 51] and bottomonia states [52, 53]. The sequential suppression of charmonia states is displayed in the right plot of Figure 1.12: the R_{PbPb} of the excited $c\bar{c}$ state $\Psi(2S)$ (red and orange markers) is smaller than the J/Ψ one (blue and green markers) in the whole p_{T} interval where the measurement was performed ($p_{\mathrm{T}} < 30$ GeV/c). The sequential suppression can in principle be exploited to measure the temperature of the QGP, since the binding energy is tightly connected to the temperature at which the quarkonia dissociation takes place.

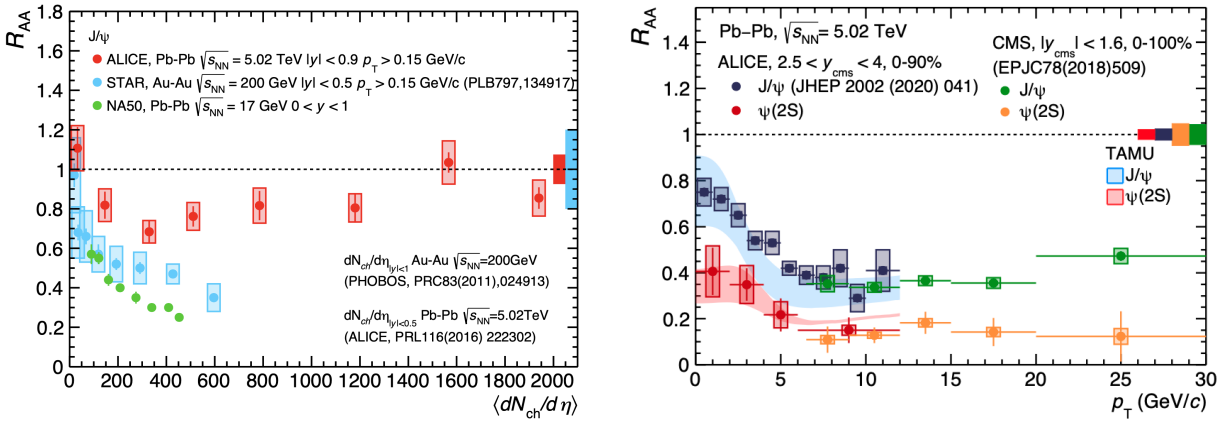

Figure 1.12: (left) J/Ψ R_{AA} as a function of the charged particle multiplicity. The results of NA50 (SPS) [48], STAR (RHIC) [49] and ALICE (LHC) [22] are compared. (right) J/Ψ and $\Psi(2S)$ R_{AA} as a function of the transverse momentum p_{T} in Pb–Pb collisions at $\sqrt{s_{\mathrm{NN}}} =$ 5.02 TeV [50, 51]. Figures taken from [22].

1.3.8 Jet quenching

The *jet quenching* effect is a consequence of the parton energy loss in the QGP medium. Jets are usually produced in a back-to-back configuration due to momentum conservation. The two back-to-back parent partons from which the jets originate might traverse different path lengths in the QGP and therefore undergo different energy loss. This results in a dijet asymmetry, an example of which is shown in the left plot in Figure 1.13, where the energy deposited in the ATLAS calorimeters by the leading jet at $(\eta, \varphi) \simeq (0, \pi/2)$ is not fully balanced by the energy of the recoil jet at $(\eta, \varphi) \simeq (0, -\pi/2)$. The dijet asymmetry can be quantified by the ratio between the transverse momentum of the sub-leading jet and the one of the leading jet $x_{\mathrm{J}} = p_{\mathrm{T}}^{jet1}/p_{\mathrm{T}}^{jet2}$. The distributions of x_{J} measured in Pb–Pb collisions in the 0-10% and 10-20% centrality intervals are compared to those measured in pp collisions in the central and right plots of Figure 1.13, respectively. The Pb–Pb distributions are characterised by smaller average values of x_{J} with respect to the pp one, indicating a higher dijet asymmetry in Pb–Pb than in pp collisions. The dijet asymmetry is observed to decrease at decreasing centrality, as expected from the path length dependence of the energy loss.

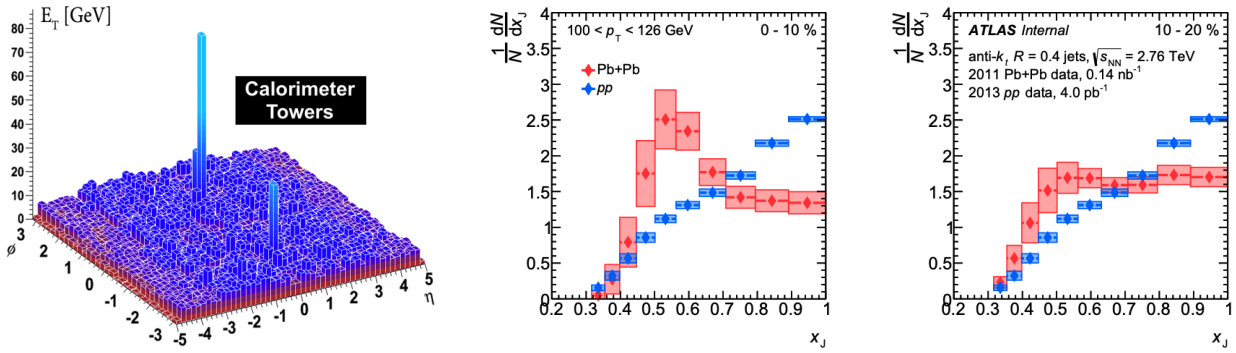

Figure 1.13: (left) Transverse energy deposited in the ATLAS calorimeters as a function of the azimuthal angle φ and of the pseudorapidity η. The leading jet is seen at $(\eta, \varphi) \simeq (0, \pi/2)$. Its energy is not fully balanced by the energy of the back-to-back jet seen at $(\eta, \varphi) \simeq (0, -\pi/2)$, as a consequence of the *jet quenching* effect. Figure taken from [54]. (centre and right) Distributions of the dijet asymmetry, quantified by the variable $x_J = p_T^{jet1}/p_T^{jet2}$, in Pb–Pb collisions (blue markers) in the centrality classes 0-10% (centre) and 10-20% (right) compared to the one measured in pp collisions (red markers). Figure taken from [55].

1.4 Small systems collectivity

Before the start of the LHC heavy-ion programme, small collision systems such as pp and p–Pb collisions were considered as plain references for heavy-ion collisions, i.e. as systems in which the conditions to form the QGP could not be reached. The measurements performed during the LHC Run 1 and Run 2 have challenged this paradigm: indeed, emblematic signatures of QGP formation have also been observed in pp and p–Pb collisions characterised by charged particle multiplicities similar to those reached in peripheral heavy-ion collisions. These features include the strangeness enhancement effect, the *double-ridge* in the two-particle correlation distributions, the mass dependent hardening of identified particle p_T spectra, and the enhancement of the ratio between baryon and meson yields at intermediate p_T values. These effects will be described in the following.

These observations, which are suggestive of a collective behaviour, raise the question as to whether their origin lies in the formation of a deconfined state of matter or rather if they are caused by initial state effects or by final state effects different from the QGP formation. The ongoing effort in the heavy-ion community to further investigate these features in a multi-differential way will help improve the current understanding of particle production mechanisms both in small and large collision systems.

Enhanced production of strange hadrons

As introduced in Section 1.3.5, the ratio of strange to non-strange hadron yields in Pb–Pb collisions is larger than in minimum bias pp collisions. This effect, called strangeness enhancement, was further investigated by studying its dependence on the multiplicity of charged particles produced in the collision [36, 56–59]. The results show that the ratios of different strange hadron yields to pion yields increase with the multiplicity of charged particles, revealing a smooth transition between different collision systems, and reaching in high-multiplicity pp collisions values comparable to those measured in peripheral Pb–Pb collisions. This behaviour is striking as different particle production mechanisms are expected to be involved

in the different collision systems. Indeed, the enhanced production of strange hadrons in Pb–Pb collisions with respect to minimum bias pp collisions was historically interpreted as a signature of QGP formation. Since the analysis presented in this thesis focuses on the strangeness enhancement effect in pp collisions, this topic will be described in greater detail in Chapter 2.

The double ridge in the two-particle correlation distribution

The two-particle angular correlation distributions are defined as a function of $\Delta\eta$ and $\Delta\varphi$, where $\Delta\eta$ is the difference of the pseudorapidity of the two particles and $\Delta\varphi$ is the difference of their azimuthal angles. Figure 1.14 displays the two-particle angular correlation measured by the ATLAS experiment in pp collisions at $\sqrt{s} = 13$ TeV for two intervals of charged particles multiplicity (left: $0 < N_{ch} < 20$, right: $N_{ch} > 120$) [60]. The peak centred in $(\Delta\eta, \Delta\varphi) = (0, 0)$ is related to particles produced in the same jet or coming from the decay of the same hadron, while the long-range ridge at $\Delta\varphi \sim \pi$ is related to the dijet partner and in general to momentum conservation. The highest multiplicity interval (right plot) shows a long-range near-side ridge at $\Delta\varphi \sim 0$ similar to the one observed in heavy-ion collisions. Similar observations were also evidenced by the ALICE collaboration in high-multiplicity pp and p–Pb collisions [61–64]. Tho origin of this flow-like behaviour, which in heavy-ion collisions results from anisotropic flow, is still not fully understood [37].

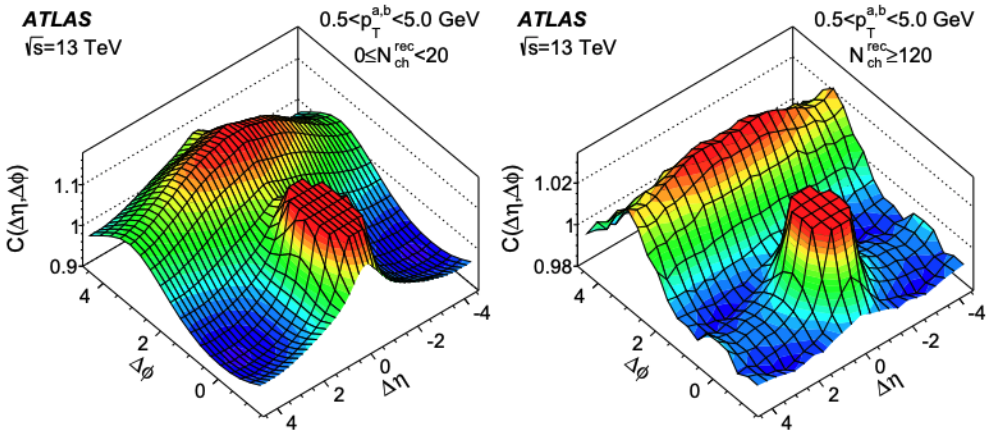

Figure 1.14: Two-particle correlation function in pp collisions at $\sqrt{s} = 13$ TeV in two intervals of charged particles multiplicity (left: $0 < N_{ch} < 20$, right: $N_{ch} > 120$). A long-range ridge structure at $\Delta\varphi \sim 0$ is visible in the highest multiplicity interval (right panel). Figure taken from [60].

Hardening of the p_{T} spectra with increasing multiplicity

In heavy-ion collisions the average transverse momentum $\langle p_{\mathrm{T}} \rangle$ increases with the centrality of the collision, as a consequence of the radial flow imparted by the fireball expansion (see Section 1.3.3). The same effect has been observed in p–Pb and pp collisions [65] as a function of the multiplicity of charged particles produced in the collision, as shown in Figure 1.15.

In heavy-ion collisions, as well as in pp and p–Pb collisions, the average transverse momentum of heavier particles is larger than the one of lighter particles. In heavy-ion collisions this mass-ordering is commonly attributed to the radial flow, which boosts the momenta of

the particle with a common velocity field. Further studies are needed to understand if the hardening of the spectra can only be attributed to the radial flow or if different mechanisms can explain the mass-dependent increase of $\langle p_{\mathrm{T}} \rangle$ in the different collision systems.

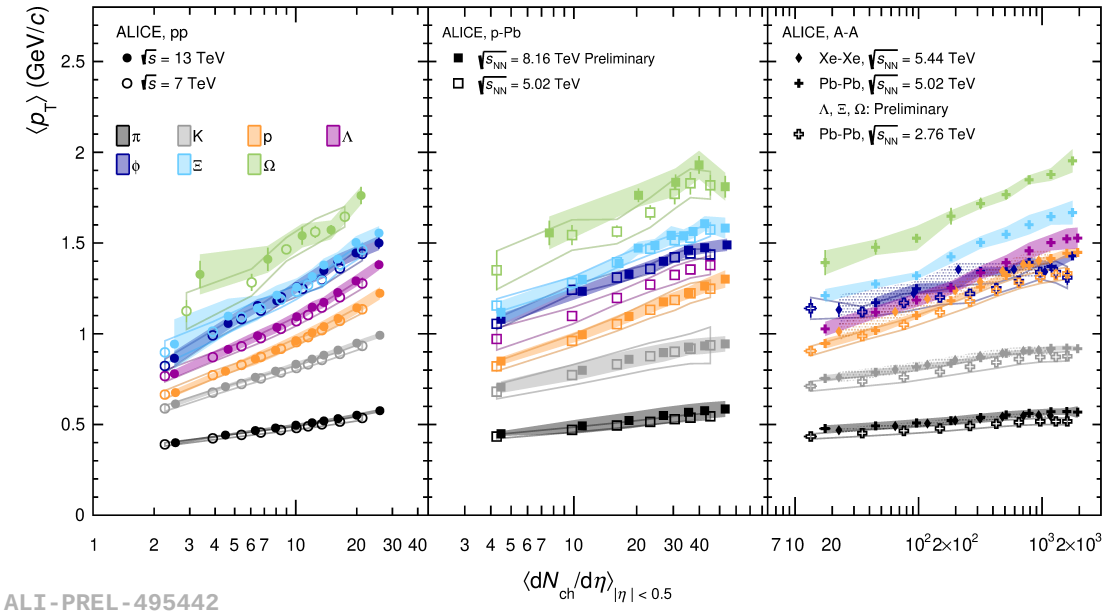

Figure 1.15: Average transverse momentum $\langle p_{\mathrm{T}} \rangle$ as a function of the charged-particle multiplicity at midrapidity $\langle \mathrm{d}N/\mathrm{d}\eta \rangle_{|\eta|<0.5}$ in pp (left panel), p–Pb (central panel) and Pb–Pb and Xe–Xe (right panel) collisions. Different colours refer to different particle species, as indicated in the legend. Figure taken from the ALICE repository.

Baryon over meson enhancement

Further insight into the spectral shape dependence on the charged-particle multiplicity can be gained by studying the p_{T}-differential ratio between baryon and meson yields. An example is provided by the $\Lambda/\mathrm{K}^0_{\mathrm{S}}$ ratio, which is displayed in Figure 1.16 for pp (left), p–Pb (centre) and Pb–Pb (right) collisions as a function of the transverse momentum [66]. In all collision systems the ratios exhibit an enhancement at intermediate p_{T} values ($p_{\mathrm{T}} \simeq 3$ GeV/c) which is observed to increase with the charged-particle multiplicity. Similar observations were made for the ratio between protons and pions [66]. The enhancement observed in heavy-ion collisions is interpreted within the hydrodynamic picture as consequence of the radial flow, which, having a stronger impact on heavier particles, causes an enhancement at intermediate p_{T} and a corresponding depletion at low p_{T}. If studied as a function of the charged-particle multiplicity, the $\Lambda/\mathrm{K}^0_{\mathrm{S}}$ ratio shows a smooth evolution across different collision system, as highlighted in Figure 1.17 for three different p_{T} intervals. These results show that the production of identified particles is strongly correlated with the final-state charged-particle multiplicity and is independent of the colliding system and collision energy at the LHC.

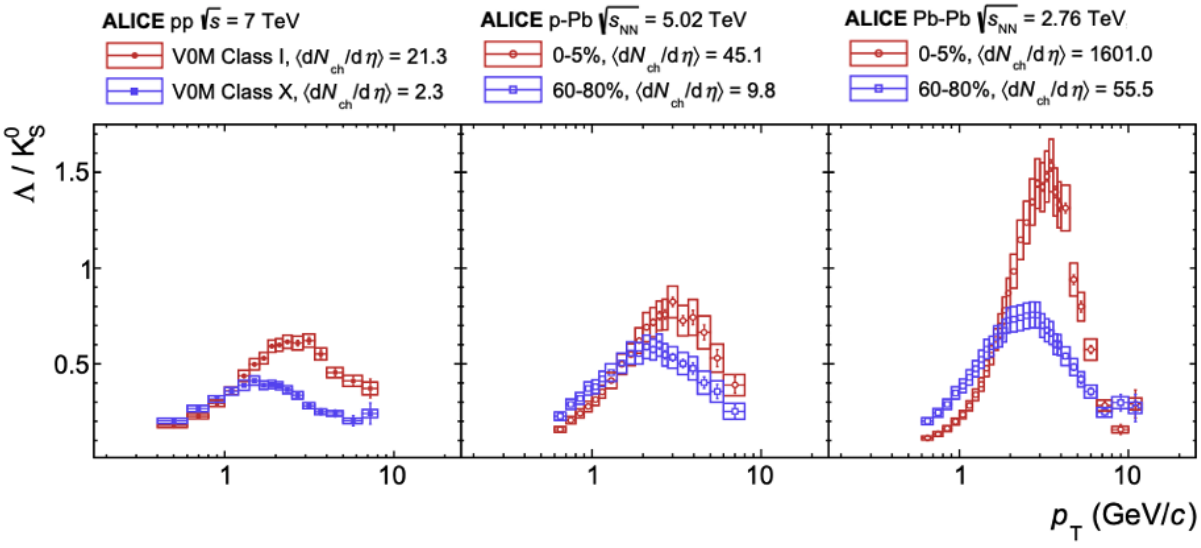

Figure 1.16: Transverse momentum dependence of the $\Lambda/\mathrm{K}^0_\mathrm{S}$ ratio in pp (left), p–Pb (centre) and Pb–Pb (right) collisions. The red markers refer to events characterised by larger charged-particle multiplicity than the blue ones. Figure adapted from [66].

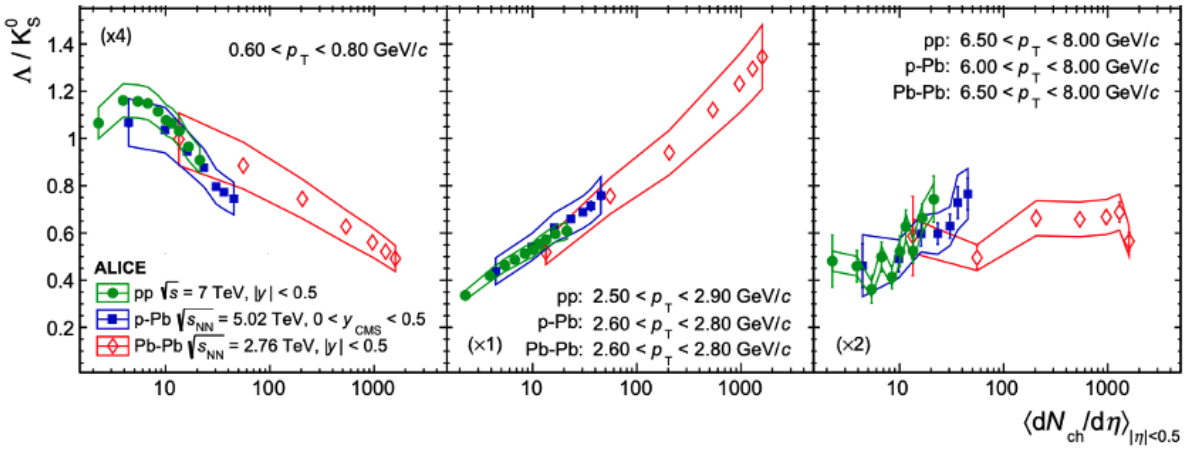

Figure 1.17: Charged-particle multiplicity dependence of the $\Lambda/\mathrm{K}^0_\mathrm{S}$ ratio at low (left), mid (centre) and high p_T (right). Different colours refer to different collision systems, as indicated in the legend. Figure adapted from [66].

Chapter 2

Strangeness production in high energy hadronic collisions

The enhancement of strange hadron production in heavy-ion collisions with respect to minimum bias pp collisions was one of the first predicted signatures of QGP formation [67–69]. Strangeness enhancement was discovered for the first time in 1988 by the CERN fixed-target experiment NA35 [70] by comparing S–S collisions to p–S ones. It was then observed by other fixed target experiments at the CERN SPS [71–76] by comparing Pb–Pb to p–Pb and p–Be collisions at beam momenta of 158 GeV/c and 40 GeV/c per nucleon, and at RHIC [77–79] by comparing Au–Au to pp collisions at $\sqrt{s_{\mathrm{NN}}} = 130$ GeV and $\sqrt{s_{\mathrm{NN}}} = 200$ GeV. In more recent times, the ALICE experiment has studied strangeness enhancement in ultra-relativistic Pb–Pb collisions [59].

The ALICE experiment has also studied the production of strange hadrons in small collision systems, namely p–Pb [36, 58] and pp collisions [56, 57, 66, 80, 81]. In order to compare the strange hadron yields measured in the different collision systems, their evolution was studied as a function of the multiplicity of charged particles produced in the collisions. The results show that the ratio of (multi-)strange to non-strange hadron yields increases with the charged-particle multiplicity, revealing a smooth transition across the different collision systems, and reaches in high-multiplicity pp collisions values comparable to those measured in peripheral Pb–Pb collisions. This behaviour is particularly striking, as different particle production mechanisms are expected to be involved in the different collision systems.

To understand the origin of this behaviour, which suggests the presence of collective effects in small collision systems, multi-differential studies are being carried out within the ALICE collaboration. The analysis presented in this thesis focuses on the contributions to strange hadron production in pp collisions given by the mechanisms associated to hadron production in jets (hard processes) and out of jets.

In the following, an overview of the strangeness production measurements performed by the ALICE experiment is presented, and the theoretical models which aim at describing strange hadron production in the different collision systems are introduced. Finally, Section 2.4 will introduce the topic of strange hadron production in and out of jets.

2.1 Strangeness production in heavy-ion collisions

Strange quark production in the QGP is expected to be favoured with respect to pp collisions because of chiral symmetry restoration, as a consequence of which light quarks acquire their bare mass. Since the bare mass of the s quark ($m_S \simeq 94$ MeV/c^2 [3]) is smaller than the QCD

deconfinement temperature $T_C = (156 \pm 1.5)$ MeV [11], thermal production of s quarks is allowed. In the QGP, in lowest order perturbative QCD $s\bar{s}$ pair creation occurs via collisions of two gluons and via annihilation of u and d quarks. These processes compete with the annihilation of $s\bar{s}$ pairs, and a saturation density of $s\bar{s}$ pairs is reached for temperatures of the system greater than 160 MeV after a time corresponding approximately to the typical lifetime of the QGP (t $\sim 10^{-23}$s) [67]. The high density of strangeness at the time of QGP hadronisation determines an enhancement of (multi-)strange hadrons as compared to pp collisions [21]. Under the assumption of thermal equilibration of $s\bar{s}$ pairs in the QGP, the yields of strange particles can be predicted using a thermal statistical model.

The ALICE experimental results on multi-strange particle production in Pb–Pb collisions at $\sqrt{s_{\rm NN}} = 2.76$ TeV [59] are presented in Figure 2.1, together with the comparison to lower energy measurements and the predictions from the thermal statistical model. The left and the middle panels display the ratios between the $\Xi^{\pm}$ and $\Omega^{\pm}$ yields measured in heavy-ion collisions and the ones measured in pp (or p–A) collisions at the same centre-of-mass energy, both normalised by the average number of participant nucleons $\langle N_{\rm part}\rangle$. The ratios, called from now on *strangeness enhancement factors*, are shown as a function of $\langle N_{\rm part}\rangle$. The results obtained by ALICE are compare to those obtained at different centre-of-mass energies by the NA57 experiment (Pb–Pb and p–Pb at $\sqrt{s_{\rm NN}} = 17.2$ GeV) and by the STAR experiment (Au–Au collisions at $\sqrt{s_{\rm NN}} = 200$ GeV).

For all the considered values of energy, the strangeness enhancement factor is larger than unity and increases with $\langle N_{\rm part}\rangle$, reaching at the LHC energies a saturation value for $\langle N_{\rm part}\rangle >$ 150-200. The increase of the strangeness enhancement factor with $\langle N_{\rm part}\rangle$ is larger for the triple-strange $\Omega^{\pm}$ baryon than for the double-strange $\Xi^{\pm}$ baryon (see central panel of Figure 2.1), consistently with the picture of $s\bar{s}$ pair production in a deconfined medium. Moreover, the strangeness enhancement factor is observed to increase with decreasing centre-of-mass energy, as a consequence of the fact that the production of strange hadrons in minimum bias pp collisions is larger at higher centre-of-mass energies.

The right panel in Figure 2.1 shows the ratio between the hyperon and the pion yields as a function of $\langle N_{\rm part}\rangle$ for different collision systems at both LHC and RHIC energies. The hyperon-to-pion ratios from pp to A–A collisions increase by a factor ∼1.6 and ∼3.3 for $\Xi^{\pm}$ and $\Omega^{\pm}$, respectively, and do not show any centre-of-mass energy dependence. The saturation value observed for $\langle N_{\rm part}\rangle > 150$ is correctly predicted by the thermal statistical models described in Ref. [32] (full line, with chemical freeze-out temperature $T_{\rm chem} = 164$ MeV) and in Ref. [82] (dashed line, with $T_{\rm chem} = 170$ MeV). These models are based on the grand canonical ensemble, in which conservation of a given quantum number is required on average and is controlled by the related chemical potential. This approach can only be applied if the number of particles carrying the considered quantum number is large enough, like in central ultra-relativistic heavy-ion collisions.

2.2 Strangeness production in small collision systems: p–Pb and pp collisions

The ALICE experiment has also studied the strange hadron production in p–Pb collisions at $\sqrt{s_{\rm NN}} = 5.02$ TeV [36, 58] and in pp collisions at $\sqrt{s} = 7$ TeV [56, 66] and $\sqrt{s} = 13$ TeV [57, 80, 81]. The plot in Figure 2.2 shows the average yields of $\rm K^0_S$, Λ, $\Xi^{\pm}$ and $\Omega^{\pm}$ per unit of rapidity $\langle {\rm d}N/{\rm d}y\rangle$ as a function of the average multiplicity of charged particles produced at midrapidity $\langle {\rm d}N/{\rm d}\eta\rangle_{|\eta|<0.5}$ in pp collisions at $\sqrt{s} = 13$ TeV (red markers) and $\sqrt{s} = 7$ TeV (blue

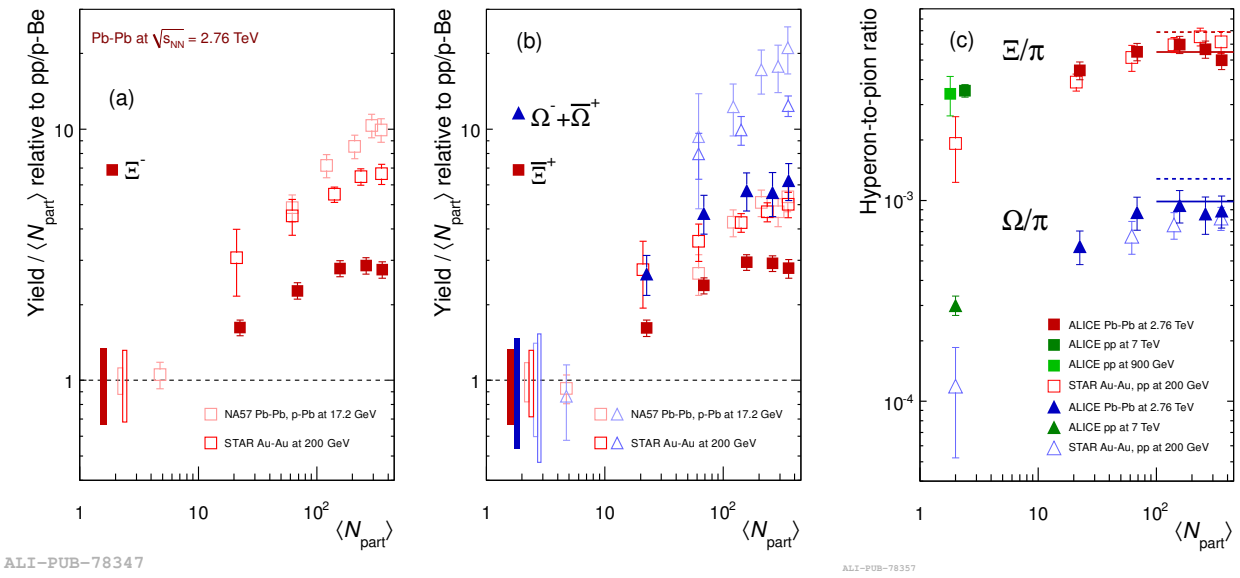

Figure 2.1: (left and middle panels) Strangeness enhancement factors for the $\Xi^{\pm}$ and the $\Omega^{\pm}$ hyperons as a function of the average number of participants $\langle N_{\rm part}\rangle$. The results are obtained at different centre-of-mass energies, as indicated in the legend. The ALICE data points are shown with full markers. Boxes on the horizontal dashed lines indicate statistical and systematic uncertainties of the pp or p–Be reference values. (right panel) Hyperon-to-pion ratio as a function of $\langle N_{\rm part}\rangle$ in A–A collisions and pp collisions at LHC and RHIC energies. The lines are predictions from statistical hadronisation models with chemical freeout temperature $T_{\rm chem}$ = 164 MeV (full line [32]) and $T_{\rm chem}$ = 170 MeV (dashed line [82]). Figure taken from [59].

markers). The yields increase with $\langle \mathrm{d}N/\mathrm{d}\eta \rangle_{|\eta|<0.5}$ and do not shown any dependence on the centre-of-mass energy. Moreover, the yield increase with $\langle \mathrm{d}N/\mathrm{d}\eta \rangle_{|\eta|<0.5}$ is larger for particles with larger strangeness content ($|S|_{\Omega^{\pm}} > |S|_{\Xi^{\pm}} > |S|_{\Lambda} > |S|_{\mathrm{K}^0_{\mathrm{S}}}$).

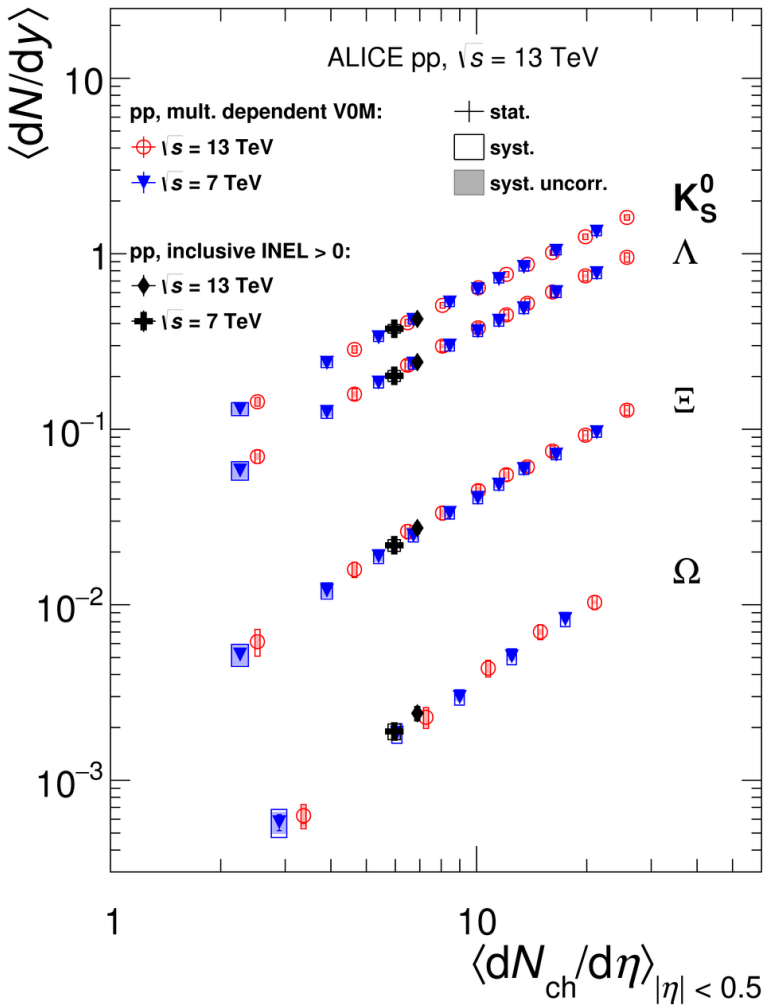

Figure 2.2: Average strange hadron yields per unit of rapidity as a function of charged particle multiplicity at midrapidity in pp collisions at $\sqrt{s} = 7$ TeV (blue markers) and at $\sqrt{s} = 13$ TeV (red markers). The black markers refer to yields measured in the inclusive sample, i.e. in the 0-100% multiplicity class. Figure taken from [57].

The evolution of strange hadron production in different collision systems, namely pp, p–Pb, Xe–Xe and Pb–Pb, is shown in Figure 2.3, which displays the ratios between (multi-)strange hadron and pion yields as a function of the charged particle multiplicity measured at midrapidity $\langle \mathrm{d}N/\mathrm{d}\eta \rangle_{|\eta|<0.5}$. The ratios increase with $\langle \mathrm{d}N/\mathrm{d}\eta \rangle_{|\eta|<0.5}$, reaching in high-multiplicity pp collisions values comparable to those measured in peripheral Pb–Pb collisions. This effect is commonly referred to as *strangeness enhancement*. The smooth transition observed across different collision systems is striking since different particle production mechanisms are expected to be involved in the different collision systems. Indeed, the larger ratio measured in central Pb–Pb collisions with respect to minimum bias pp collisions is interpreted as a signature of the formation of QGP, which however is not expected to form in smaller collision systems. It is worth noting that the ratio between the yields of protons and pions (purple markers) decreases with multiplicity for $\langle \mathrm{d}N/\mathrm{d}\eta \rangle_{|\eta|<0.5} \gtrsim 20$, indicating that the increase of strange hadrons to pions yields is not related to mass differences but it

is related to the strangeness content.

Results also show that the strangeness enhancement effect is larger for particles with larger strangeness content, as already observed when describing strange hadron production in Pb–Pb collisions in Section 2.1. The dependence on the strangeness content can be more clearly observed in Figure 2.4, which shows the strange-hadron to pion yields measured in pp collisions at $\sqrt{s} = 7$ TeV and in p–Pb collisions at $\sqrt{s_{\rm NN}} = 5.02$ TeV, divided by the values measured in the inclusive pp sample [56]. A steeper increase with multiplicity for particles with larger strangeness content is clearly seen.

Finally, the ratios do not show any dependence on the centre-of-mass energy at the energy scale of the LHC (∼TeV). These observations indicate a strong correlation between strange hadron production and the multiplicity of charged particles produced in the final state of the collisions.

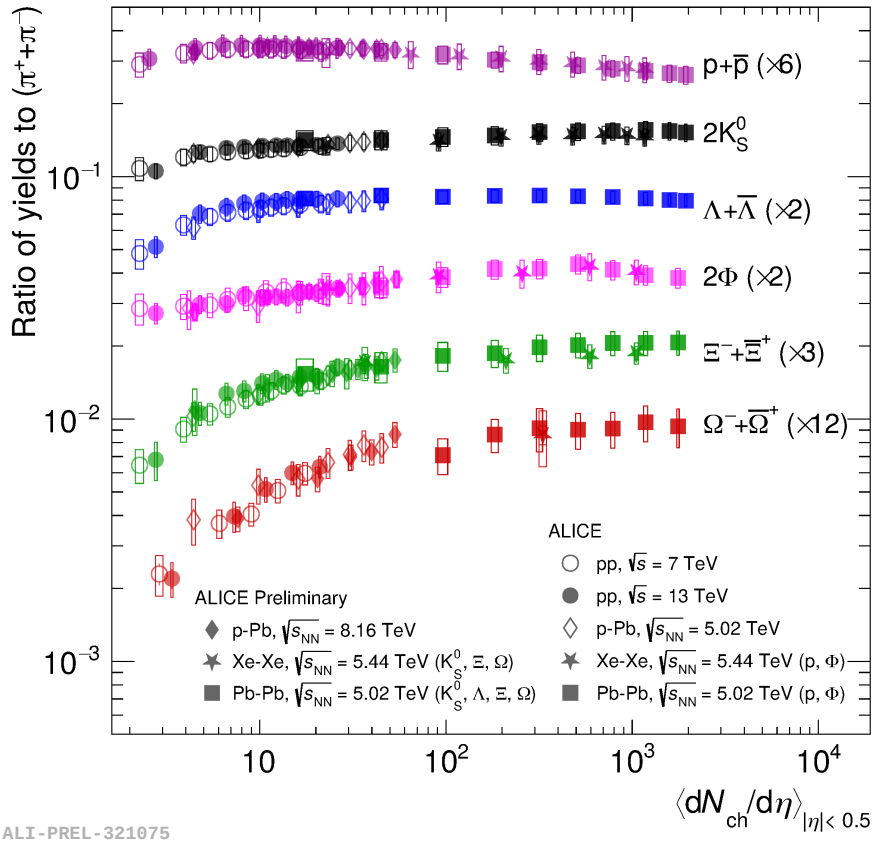

Figure 2.3: Ratios of different hadron yields to pions as a function of the charged particles multiplicity measured at midrapidity. The data shown are from pp [56, 57], p–Pb [36, 58], Xe–Xe [83] and Pb–Pb [59] collisions. Different colours refer to different hadron species, as indicated in the plot. Figure taken from the ALICE repository.

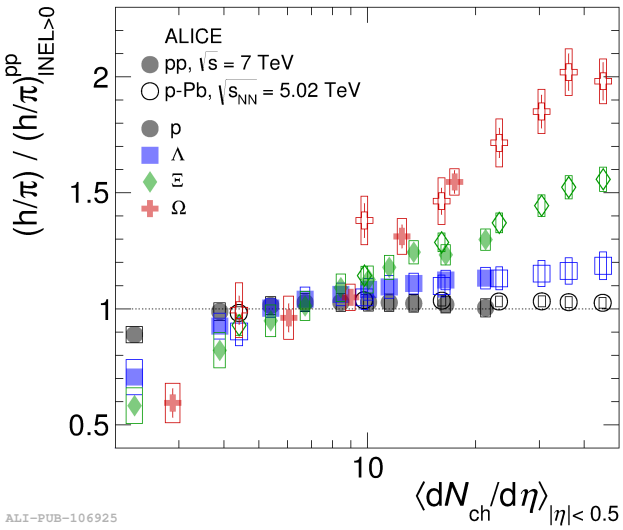

Figure 2.4: Ratios of strange hadron yields to pions measured in pp collisions at $\sqrt{s} = 7$ TeV and in p–Pb collisions at $\sqrt{s_{\rm NN}} = 5.02$ TeV, normalised by the values measured in the minimum bias pp sample. The different colours refer to different (multi-)strange hadrons. Figure taken from [56].

2.3 Model description of strange hadron production

To shed light on the origin of the strangeness enhancement in small collision systems, the experimental results are compared to the predictions of different models. In Section 2.3.1, the strange hadron to pion yield ratios measured in pp collisions are compared to the predictions of Monte Carlo simulations implementing different microscopic models commonly used to describe particle production in pp collisions, namely PYTHIA8 [84] and HERWIG [85, 86]. Then, in Section 2.3.2, the *core-corona* model is introduced, and the predictions of the event generator EPOS LHC [87], which implements this model, are discussed, together with the results obtained with the recently developed *Dynamical Core-Corona Initialisation* (DCCI [88, 89]) framework. Finally, in Section 2.3.3, the predictions of a statistical hadronisation model based on the strangeness canonical approach are presented. This model aims at describing the strangeness enhancement with multiplicity as an effect of strangeness suppression in small collision systems.

2.3.1 Monte Carlo models for pp collisions: PYTHIA and HERWIG

In pp collisions s quarks are produced in the early stages of the collisions in hard perturbative scattering processes via flavour creation ($gg \rightarrow s\bar{s}$, $q\bar{q} \rightarrow s\bar{s}$) and flavour excitation ($gs \rightarrow gs$, $qs \rightarrow qs$), and during the subsequent partonic evolution by gluon splitting ($g \rightarrow s\bar{s}$). These processes dominate at high $p_{\rm T}$. At low $p_{\rm T}$, $s\bar{s}$ pairs are instead created via non-perturbative processes like string fragmentation. In these processes strange hadron production is suppressed with respect to hadrons containing only u and d quarks, since s quarks are heavier [56].

String fragmentation is at the base of the PYTHIA event generator [84, 90], which is the most commonly used event generator in pp collisions. PYTHIA is based on the Lund string hadronization model [91], according to which the colour field between two quarks can

be treated in a similar way to a classical spring. When it becomes energetically convenient for the string to break, a new $q\overline{q}$ pair forms through quantum mechanical tunnelling.

This model cannot describe the strangeness enhancement with multiplicity, as shown in Figure 2.5, where the $\langle \mathrm{d}N/\mathrm{d}\eta \rangle_{|\eta|<0.5}$ evolution of the (multi-)strange hadron to pion yields is compared with the predictions of different phenomenological models for pp collisions at $\sqrt{s} = 13$ TeV. Indeed, the predictions of PYTHIA 8.2 [84] (Monash tune 2013 [92]) underestimate the ratios and show no dependence with multiplicity. The description worsens with increasing strangeness content, and no significant differences are observed if colour reconnection (CR) [93] between partons is allowed to occur.

An improvement of the description provided by PYTHIA8 is achieved if overlapping strings are allowed to interact with each other, forming the so-called "color ropes". The implementation of colour ropes results in a higher effective string tension, which determines the enhancement of strange and diquark production, giving rise to larger rates of strange hadrons and baryons. PYTHIA8 with colour ropes can qualitatively describe the strangeness enhancement with multiplicity (see Figure 2.5). The main differences to the data are observed for the Ω/π ratio, which is overestimated especially at low multiplicity, and for the Λ/π ratio, which is overestimated in the highest multiplicity pp collisions ($\langle \mathrm{d}N/\mathrm{d}\eta \rangle_{|\eta|<0.5} \sim 20$). While providing a good qualitative description of strangeness enhancement, PYTHIA8 with ropes is not able to predict the multiplicity evolution of the ratio between proton and pion yields, as shown in Figure 2.6. Indeed, it overestimates the ratio and predicts an increase with multiplicity which is not observed in the data.

The enhancement of strange hadrons is also predicted by HERWIG7 [85, 86], a model which implements hadronisation in a clustering approach. The implementation used for the comparison presented in Figure 2.5 includes the baryonic ropes, a reconnection scheme which increases the probability to form baryons [86]. HERWIG7 shows a larger deviation from the data than PYTHIA8 with ropes, in particular for the Ξ/π ratio at low $\langle \mathrm{d}N/\mathrm{d}\eta \rangle_{|\eta|<0.5}$. Moreover, it underestimates the Ω/π ratio in the whole multiplicity interval ($\langle \mathrm{d}N/\mathrm{d}\eta \rangle_{|\eta|<0.5} \lesssim 20$) and it overestimates the $\mathrm{K}^0_\mathrm{S}/\pi$ ratio in the lowest multiplicity intervals ($\langle \mathrm{d}N/\mathrm{d}\eta \rangle_{|\eta|<0.5} \lesssim 3$). However, in contrast to all the shown implementations of PYTHIA8, it can correctly predict the p/π ratio (see Figure 2.6).

Overall, none of the presented Monte Carlo generators are able to provide a consistent quantitative description of the multiplicity dependence of the hadron-to-pion ratios, indicating that the current understanding of particle production in pp collisions is not complete, and that the microscopic origin of strangeness enhancement in small collisions systems is still an open problem.

2.3.2 Core-corona model

The core-corona model was first developed to describe heavy-nuclei collisions [94]. This model assumes that the system produced in a heavy-ion collision is divided in two parts: a *core* region, characterised by high energy density and by the formation of a deconfined medium, and a *corona*, a more peripheral region with lower density, where nucleon-nucleon collisions occur. Hadron production in the core occurs in a thermal way, while particle production in the corona occurs through string breaking as in pp collisions. The evolution of particle production with multiplicity depends on the variation of the relative contribution of core and corona: as multiplicity increases, the core region is supposed to become larger and, a consequence, the final hadron yields become dominated by the hadrons produced from thermalised matter. Since in the core strange particle production is favoured due to the

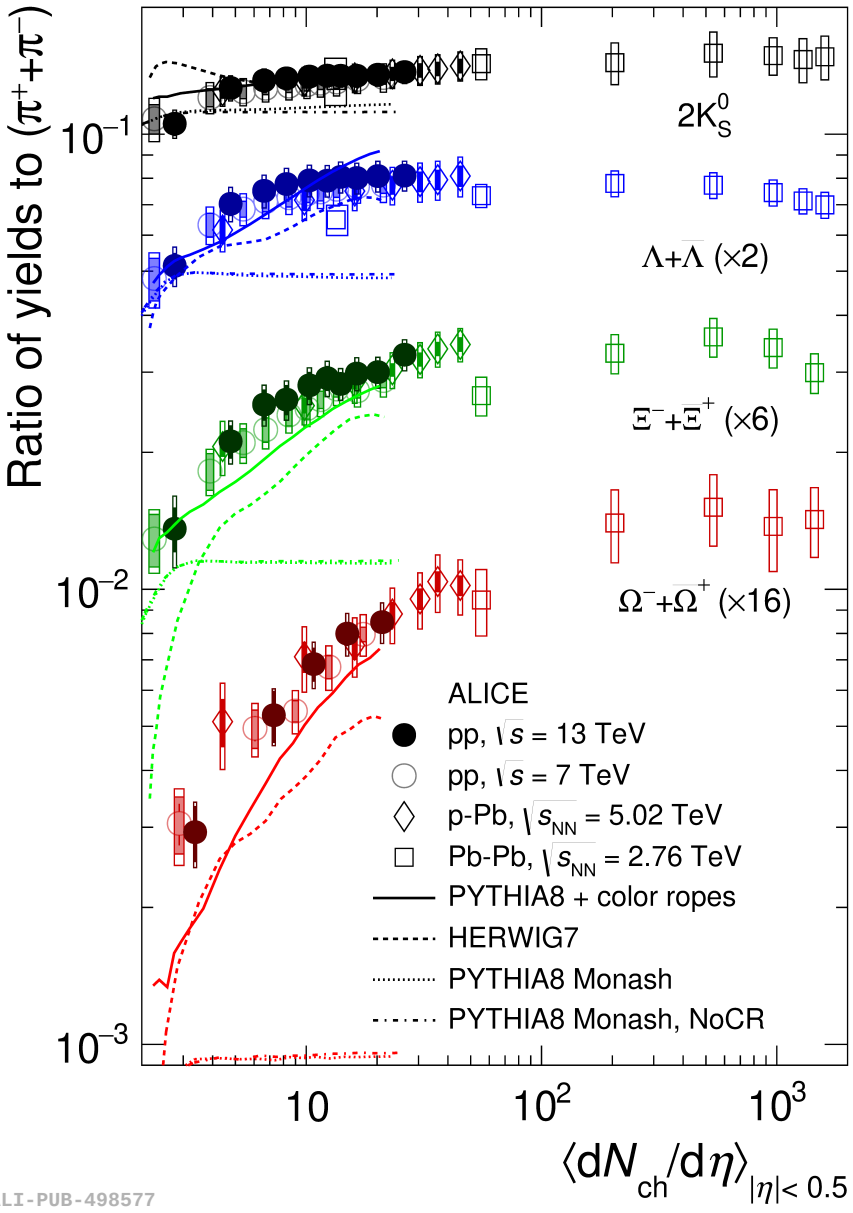

Figure 2.5: Ratios of (multi-)strange hadron yields to pions as a function of the charged particles multiplicity measured at midrapidity. The data shown are from pp [56, 57], p–Pb [36, 58] and Pb–Pb [59] collisions. The open (shaded) boxes represent full (multiplicity uncorrelated) systematic uncertainties. Different lines represent predictions of different MC generators for pp collisions at $\sqrt{s} = 13$ TeV. Figure taken from [80].

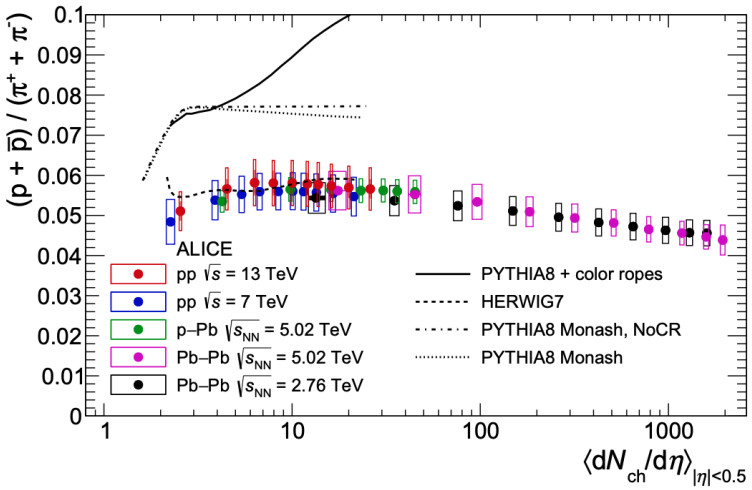

Figure 2.6: Proton-to-pion yield ratio as a function of the charged particles multiplicity measured at midrapidity. The data shown are from pp [56], p–Pb [36, 58] and Pb–Pb [59] collisions. The open (shaded) boxes represent full (multiplicity uncorrelated) systematic uncertainties. Different lines represent predictions of different MC generators for pp collisions at $\sqrt{s} = 13$ TeV. Figure taken from the [80].

presence of a deconfined medium, the variation with centrality of the relative contribution of core and corona can explain the centrality dependence of the strangeness enhancement factor discussed in Section 2.1. Indeed, in Ref. [95] it is shown that the Monte Carlo event generator EPOS [94], which implements the core-corona model, can describe the centrality dependence of the strangeness enhancement factor in Au–Au and Cu–Cu collisions at $\sqrt{s_{\rm NN}} = 200$ GeV, $\sqrt{s_{\rm NN}} = 62$ GeV and $\sqrt{s_{\rm NN}} = 17.2$ GeV.

The core-corona model has also been implemented for smaller collision systems, such as p–Pb and pp collisions, in the EPOS LHC [87] event generator. In small collision systems, strings in a low density area form the corona and hadronize normally, while strings in a high density area form the core and undergo collective hadronization. As shown in Ref. [56], EPOS LHC can fairly well describe the $\rm K^0_S/\pi$ ratio, while it overestimates the strangeness enhancement with multiplicity for the Λ, $\Xi^{\pm}$ and $\Omega^{\pm}$ baryons, whose ratios to pions are overestimated at low multiplicity, i.e. for $\langle {\rm d}N/{\rm d}\eta \rangle_{|\eta|<0.5} \lesssim 20$, 15, and 7, respectively.

Recently, the core-corona model has been implemented in the *Dynamical Core-Corona Initialisation* framework (DCCI, [88, 89]), a multi-stage dynamical model which can be applied to the description of high energy collisions, from pp to A–A. In this model, the initial partons are generated using PYTHIA8 or its heavy-ion implementation, PYTHIA8 Angantyr [96]. Partons which experience sufficient interactions with other partons are likely to form matter in thermal equilibrium, while those which undergo few interactions do not equilibrate and their hadronisation is modelled by the string fragmentation implemented in PYTHIA8. The comparison between the measured multiplicity dependence of the Ξ/π ratios and the predictions of the DCCI model [88] in pp, p–Pb and Pb–Pb collisions are shown in Figure 2.7. The model predicts an increase of the ratio with multiplicity until a saturation value is reached for $\langle {\rm d}N/{\rm d}\eta \rangle_{|\eta|<0.5} \gtrsim 100$, showing very good agreement with the data. Good agreement is also observed for other strange hadrons, namely the Λ and the ϕ, as shown in Ref. [97]. The proton-to-pion ratio predicted by the model, however, does not describe the decreasing trend with multiplicity observed in the data for $\langle {\rm d}N/{\rm d}\eta \rangle_{|\eta|<0.5} \gtrsim 50$. In this multiplicity region the model overestimates the data points by up to 50%. In Ref. [97] it is argued that further

developments of the DCCI framework will address this issue.

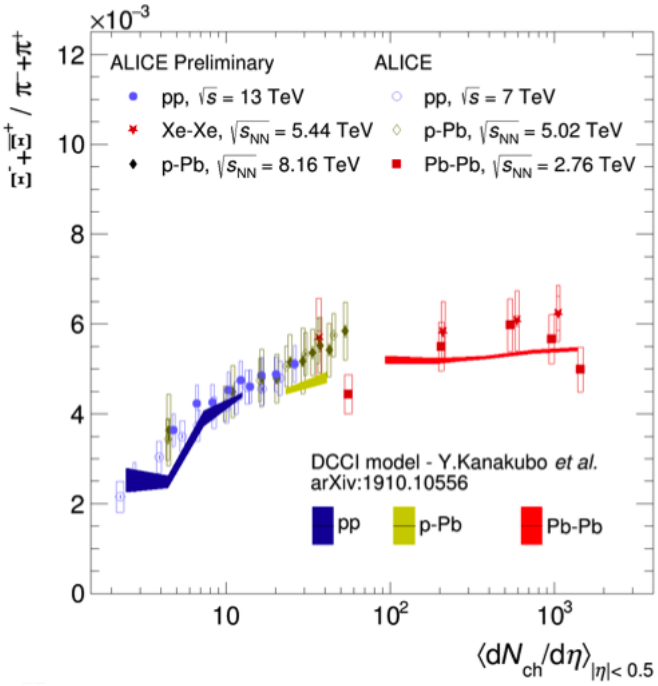

Figure 2.7: Ratios between $\Xi^{\pm}$ and charged pion yields as a function of the charged-particle multiplicity in pp, p–Pb, Xe–Xe and Pb–Pb collisions[56–59, 83]. The coloured bands represent the prediction of the DCCI model [88]. Figure taken from the ALICE repository.

2.3.3 Strangeness Canonical model

As shown in Section 2.1, strange hadron production in central ultra-relativistic heavy-ion collisions is successfully described by statistical hadronisation models based on a grand canonical ensemble. This ensemble is not suitable for the description of strange hadron production in peripheral Pb–Pb collisions and in smaller collision systems, such as pp and p–Pb collisions, since it does not require event-by-event strangeness conservation. Indeed, the grand canonical strangeness conservation condition is:

$$\langle N_s \rangle - \langle N_{\bar{s}} \rangle = 0, \tag{2.1}$$

where N_s is the number of strange quarks, $N_{\bar{s}}$ the number of strange anti-quarks produced in the collision, and the average is performed over the ensemble of physical systems, i.e. over independent collisions.

The strangeness conservation law, however, requires the exact strangeness conservation in each collision:

$$N_s - N_{\bar{s}} = 0. \tag{2.2}$$

Only in very large systems, such as central heavy-ion collisions, the grand-canonical conservation condition is satisfied, since the relative violation of the strangeness conservation low vanishes like $1/\sqrt{N_s}$ [98].

A statistical hadronisation model based on the grand canonical conservation of the baryonic quantum number and on the canonical conservation of strangeness is able to reproduce the basic features of the strangeness enhancement factor, as described in Ref.[99] and

Ref.[100]. This model depends on three main parameters: the chemical freeze-out temperature $T_{\rm chem}$ of the system, the baryochemical potential $\mu_{\rm B}$, and the correlation volume $V_{\rm c}$, i.e. the volume in which strangeness is exactly conserved. In addition to these parameters, the strangeness undersaturation parameter γ_s can be used to model any deviation from strangeness chemical equilibrium. Within this model, the decrease of the strangeness enhancement factor with decreasing $\langle N_{\rm part}\rangle$ is interpreted as a suppression related to the canonical conservation of strangeness. The saturation value obtained at large $\langle N_{\rm part}\rangle$ indicates that the thermodynamic limit, i.e. the limit in which a grand canonical ensemble can be used, has been reached. In this scenario, the energy dependence and the strangeness content dependence of the strangeness enhancement factor are mainly related to the suppression of the thermal phase space available for strangeness production in pp collisions, which increases with decreasing collision energy and with increasing strangeness content.

The strangeness canonical description has also been applied to describe the ratios of strange hadron to pion yields as a function of the charged-particle multiplicity across different collision systems, as shown in Figure 2.8 for the Λ and the $\Xi^{\pm}$ baryons. The model predictions shown in the plots are obtained with the THERMUS 3.0 code [29], setting the baryochemical potential to zero and varying $T_{\rm chem}$ from 146 to 166 MeV, according to recent results from lattice QCD calculation and from fits to Pb–Pb experimental data [66]. The correlation volume $V_{\rm c}$ is imposed to be equal to the total volume V of the system, and the strangeness undersaturation parameter γ_S is fixed to one, assuming that the system reaches thermal and chemical equilibrium. All ratios are normalised to the high multiplicity limit, i.e. the mean ratio in the 0-60% most central Pb–Pb collisions for the data and the grand canonical saturation value for the model, in order to cancel the influence of the freeze-out temperature and to isolate the dependence on the volume. The theoretical curves show good agreement with data, as all data points can be described within 1-2 standard deviations, considering the sum in quadrature of statistical and systematic uncertainties.

Good agreement between the strangeness canonical model and the data is also observed for the $\Omega^{\pm}$ ratio, as shown in the left panel of Figure 2.9: the model predictions differ from most of the data points by less than 2σ, where σ represents one standard deviation of the statistical and systematic uncertainties summed in quadrature. The model predictions displayed in this plot implement exact conservation of strangeness and of baryonic number and electric charge, and are obtained with the Thermal FIST package [31, 101] (solid lines) and with the THERMUS code [102] (dashed lines, restricted to pp). The strangeness canonical model implemented in the Thermal FIST package is also able to qualitatively reproduce the multiplicity dependence of the proton to pion yield ratio, as shown in the right plot of Figure 2.9. However, the proton yield is overestimated by about 20% to 30%, depending on the charged-particle multiplicity interval. A better agreement with the data is shown by the THERMUS predictions, which are however limited to $\langle {\rm d}N/{\rm d}\eta\rangle_{|\eta|<0.5}<20$.

Overall, the strangeness canonical model provides a way to describe the strangeness enhancement with multiplicity across the different collision systems. However, a quantitative description of the proton over pion yield ratios across different collisions system is not achieved, indicating that a comprehensive description of all particle ratios is still a theoretical challenge.

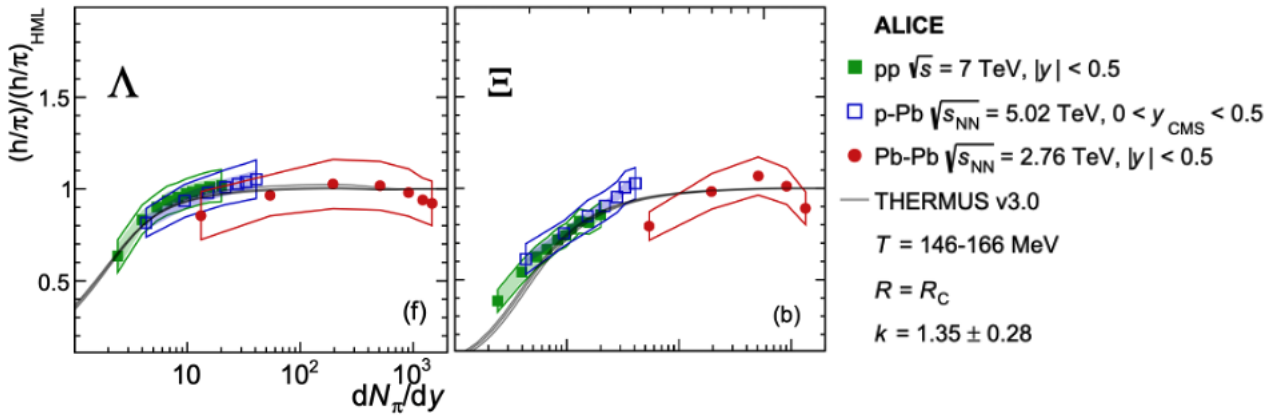

Figure 2.8: Ratios of strange hadron yields to pion yields as a function of the charged-particle multiplicity measured at midrapidity in pp, p–Pb and Pb–Pb collisions. The lines are the predictions of the strangeness canonical model implemented in THERMUS [102]. All values are normalised to the high multiplicity limit (see text for details). Figures adapted from [66].

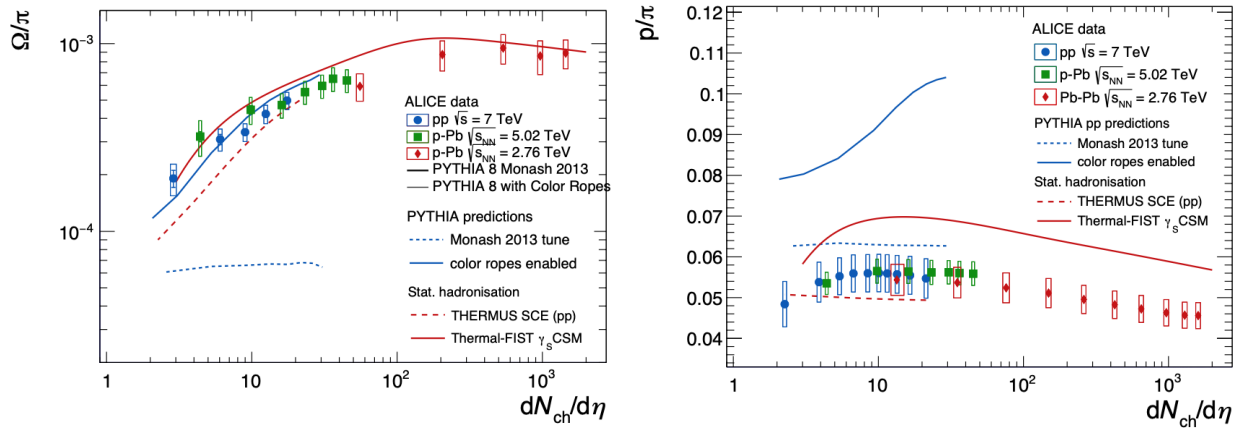

Figure 2.9: Ratios between $\Omega^{\pm}$ and pion yields (left panel) and between proton and pion yields (right panel) as a function of the charged-particle multiplicity measured at midrapidity in pp (blue markers), p–Pb (green markers) and Pb–Pb (red markers) collisions. The red lines are predictions of the canonical statistical model implemented in the Thermal FIST package [31, 101] (solid line) and in the THERMUS code [102] (dashed line). The blue lines are predictions of PYTHIA8.2 with Monash 2013 tune (dotted lines) and with colour ropes (solid line). Figures taken from [22].

2.4 Strange hadron production in jets and out of jets

A way to investigate the origin of strangeness enhancement in small collision systems consists in studying the strange hadron production associated to hard scattering processes and to the underlying event. Hard scattering processes are associated to the production of jets, sprays of particles originating from a single parton produced in a hard scattering interaction and undergoing subsequent parton fragmentation and hadronization. The underlying event (UE) consists instead of all the processes different from the hardest partonic interaction [103]. These processes are:

- Initial and final state radiation (ISR/FSR): partons undergoing a scattering process can radiate gluons before the interaction (ISR) or after the interaction (FSR).
- Multiple Parton Interaction: it consists in partonic scattering processes different from the hardest one.
- Beam remnants: they are the remnants of the beam which do not undergo any partonic scattering process.

A method which allows to separate the strange hadrons associated to hard processes from those produced in the UE makes use of jet finding algorithms. This method has been applied by the ALICE collaboration in order to study the production of different strange hadron yields (K^0_S , Λ, $\Xi^\pm$, $\Omega^\pm$) in jets and in the underlying event in minimum bias pp collisions at $\sqrt{s}$ = 7 TeV and $\sqrt{s}$ = 13 TeV and in p–Pb at $\sqrt{s_\mathrm{NN}}$ = 5.02 TeV [104, 105]. The reconstruction of jets is performed with the anti-k_T algorithm [106, 107], taking in input charged tracks and applying a jet resolution parameter R_res = 0.4. In addition, jets are required to have a transverse momentum $p^\mathrm{ch}_\mathrm{T,jet} > 10$ GeV/c.

Strange hadrons are considered to be located inside a jet cone if their distance to the jet axis in the $\eta - \varphi$ plane

$$\mathrm{R(particle, jet)} = \sqrt{(\eta_\mathrm{particle} - \eta_\mathrm{jet\ axis})^2 + (\varphi_\mathrm{particle} - \varphi_\mathrm{jet\ axis})^2} \tag{2.3}$$

is smaller than R_cut, which is chosen equal to the jet resolution parameter. Strange hadrons not associated with hard scatterings, i.e. produced in the UE, are extracted from a cone perpendicular to the jet one with radius $R = R_\mathrm{cut} = 0.4$. The yield of strange hadrons produced in jets N_jet is obtained by subtracting the underlying event contribution N_UE to the yield measured in the jet cone N_JC:

$$N_\mathrm{jet} = N_\mathrm{JC} - N_\mathrm{UE}. \tag{2.4}$$

Figure 2.10 shows the K^0_S density yields, i.e. the yields normalised by the jet area $A = \pi R^2_\mathrm{cut}$, measured in the jet cone (green markers), in the perpendicular cone (empty markers) and in jets (red markers) as a function of the transverse momentum p_T in pp collisions at $\sqrt{s}$ = 7 TeV. The plot also displays the inclusive K^0_S spectrum, i.e. the spectrum measured in all events, and not only in those containing a reconstructed jet. The spectrum of K^0_S produced in jets (red markers) is harder than the one measured in the perpendicular cone (empty markers), as expected from the fact that the jet is associated to hard scattering processes. Moreover, it is compatible with the one measured in the jet cone (green markers) for $p_\mathrm{T} \gtrsim 2$ GeV/c, indicating that contribution of the underlying event to the jet cone becomes less important with increasing p_T. Similar findings are observed for the Λ, $\Xi^\pm$ and $\Omega^\pm$ baryons [104, 105].

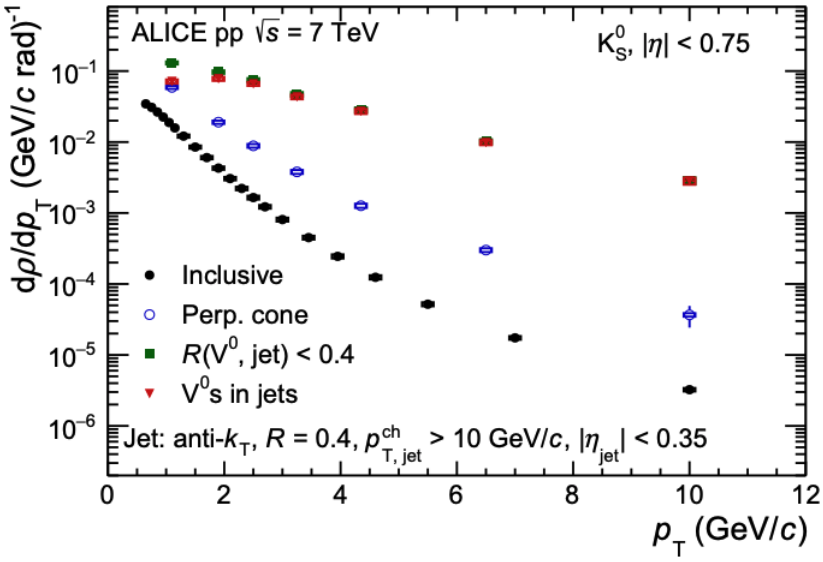

Figure 2.10: K^0_S density spectra $d\rho/dp_T$ as a function of the transverse momentum of the K^0_S in pp collisions at $\sqrt{s} = 7$ TeV. The density spectra are shown for inclusive K^0_S produced in minimum bias events (black markers), for K^0_S associated with the underlying event (empty markers), for K^0_S produced in the jet cone (green markers) and for K^0_S produced in jets after the subtraction of the contribution from the underlying event (red markers). Figure taken from [104].

The baryon-over-meson enhancement observed in pp collisions at intermediate p_T values (see Section 1.4) is investigated by looking at the ratio between Λ and K^0_S yields (Figure 2.11). The Λ/K^0_S yield ratio measured in the perpendicular cone (empty markers) shows an enhancement at $p_T \sim 3$ GeV/c compatible with the one displayed by the inclusive yield ratio (black markers). On the contrary, the ratio between the spectra of Λ and K^0_S produced in jets (red markers) does not show such an enhancement. A similar behaviour is also shown by the $\Xi^{\pm}/K^0_S$ ratio.

These results indicate that jet fragmentation alone is not sufficient to describe strange particle production in hadronic collisions at the LHC energies, and suggest that the increase with multiplicity of the baryon-over-meson yield ratio at intermediate p_T values (see Section 1.4) might be driven by particle production in the underlying event.

These results do not provide any information about the multiplicity dependence of in-jet and out-of-jet strange particle production in pp collisions. The analysis presented in this thesis, instead, focuses on the study of p_T-integrated yields of strange hadrons produced in jets and out of jets as a function of the multiplicity of charged particles produced at midrapidity in pp collisions, in order to shed light on the origin of the strangeness enhancement with multiplicity. The separation of strange hadron produced in jets from those produced out of jets is performed with a method based on the angular correlation between high-p_T particles, which are considered as a proxy for the jet axis, and strange hadrons. This method will be described in detail in Section 4.6.

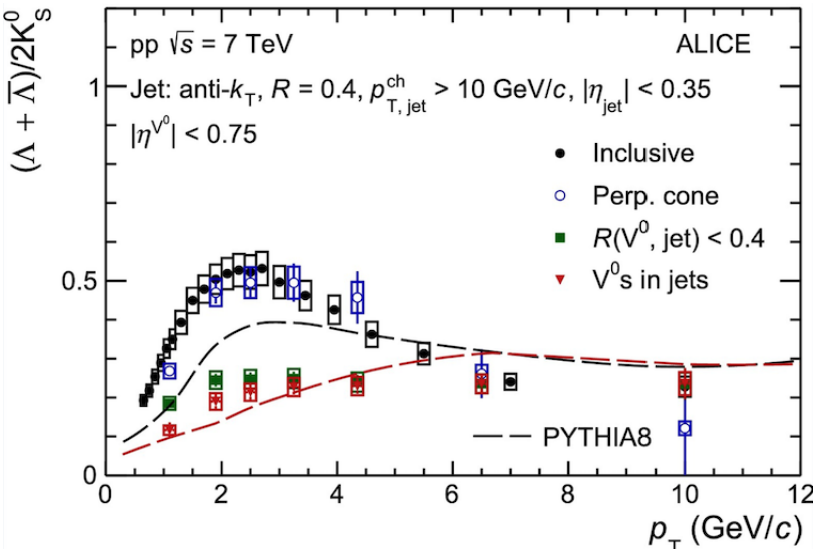

Figure 2.11: $(\Lambda + \bar{\Lambda})/2\mathrm{K}^0_\mathrm{S}$ ratio in pp collisions at $\sqrt{s} = 7$ TeV as a function of the transverse momentum p_T of the K^0_S. The meaning of the different markers is described in Figure 2.10.

Chapter 3

ALICE: A Large Ion Collider Experiment

The LHC (Large Hadron Collider) [108] is the most powerful particle collider in the world. It is located at CERN (the European Centre for Nuclear Research), on the border between France and Switzerland, close to the city of Geneva.

The LHC is placed in the 26.7 km long tunnel built for the CERN LEP [109] (Large Electron-Positron collider) machine. It is designed to collide protons at a centre-of-mass energy up to 14 TeV and at a maximum peak luminosity of 10^{34} cm^{-2}s^{-1}, and it can also provide heavy nuclei collisions (so far, Pb–Pb and Xe–Xe) and proton-nucleus (p–Pb) collisions.

Four main experiments are located along the LHC ring, in correspondence of four interaction points: ATLAS (*A Toroidal Lhc ApparatuS)* [110], CMS (*Compact Muon Solenoid*) [111], ALICE (*A Large Ion Collider Experiment*) [112] and LHCb (*Large Hadron Collider beauty*) [113]. ATLAS and CMS are general-purpose detectors which allowed for the discovery of the Higgs boson in 2012 [114, 115]. They are now used for precision tests of the Standard Model and to search for new physics beyond it. ALICE is specifically designed to study heavy-ion collisions, with the purpose of characterising the properties of the quark-gluon plasma which is formed in such collisions. Finally, LHCb focuses on precision measurements of CP violation.

The CERN complex of accelerators and the LHC are described in more detail in Section 3.1, while the ALICE experiment is presented in Section 3.2 and in the following ones.

3.1 The Large Hadron Collider

The LHC is the last step of the CERN accelerator complex (Figure 3.1), a series of machines which accelerate particles to increasingly high energies: each machine boosts the energy of the particles before injecting them into the next accelerator of the sequence. At intermediate stages of acceleration, particle beams can be extracted in order to carry out low energy experiments.

The proton acceleration chain starts from the ionisation of hydrogen atoms with an electric field. Protons are then accelerated to the energy of 50 MeV by the *Linear Accelerator 2* (Linac 2 [117]). In 2020, Linac 2 was replaced by Linac 4 [118], which accelerates protons to the energy of 160 MeV. The proton beam is then injected into the *Proton Synchrotron Booster* (PSB [119]), where protons are accelerated up to the energy of 1.4 GeV, and into the *Proton Synchrotron* (PS [120]), in which they reach an energy of 25 GeV. Afterwards, they are accelerated in the *Super Proton Synchrotron* (SPS [121]) and finally, with an energy of 450 GeV, they are sent to the LHC. In the LHC each proton beam consists of up to 2808

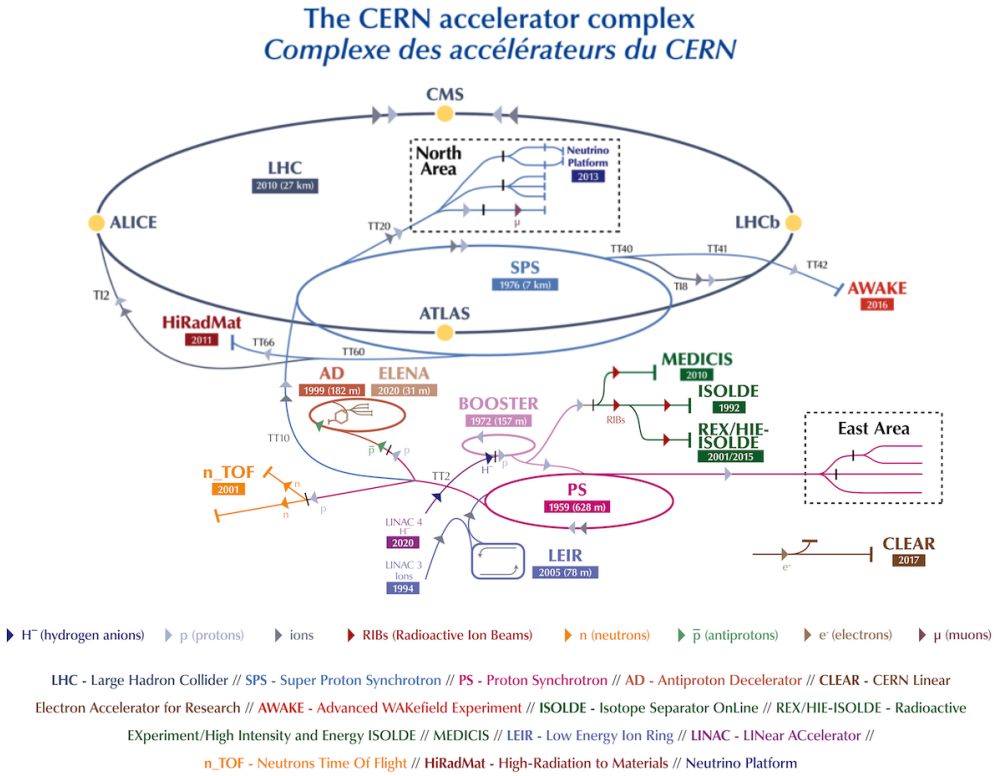

Figure 3.1: The CERN accelerator complex. Figure taken from [116].

bunches of protons, with a nominal bunch separation of 25 ns and containing approximately 10^{11} protons each.

Lead ions are produced starting with the vaporization of a ^{208}Pb source and the subsequent selection of $^{208}Pb^{27+}$ ions, which are then accelerated in the *Linear Accelerator 3* (Linac 3 [122]) and subsequently stripped to $^{208}Pb^{54+}$, before being sent to the *Low Energy Ion Ring* (LEIR [123]), in which they are accelerated from 4.2 to 72 MeV per nucleon. The lead ions are then accelerated in the PS, stripped to their bare nuclei of $^{208}Pb^{82+}$ and accelerated again in the SPS. Finally, they are sent to the LHC. Each lead beam consists of up to 592 bunches of approximately 10^8 lead ions.

LHC delivered the first pp collisions in 2009. During the first data taking period (Run 1), taking place from 2009 to 2013, protons were accelerated up to $\sqrt{s} = 8$ TeV, Pb–Pb collisions were delivered at $\sqrt{s_{NN}} = 2.76$ TeV, and p–Pb collisions at $\sqrt{s_{NN}} = 5.02$ TeV [124]. After the first Long Shutdown (LS1) LHC began the second data taking period (Run 2, 2015-2018), during which it collided protons up to $\sqrt{s} = 13$ TeV, p–Pb collisions up to $\sqrt{s_{NN}} = 8.16$ TeV and Pb–Pb collisions at $\sqrt{s_{NN}} = 5.02$ TeV. During Run 2, LHC also provided Xe–Xe collisions at $\sqrt{s_{NN}} = 5.44$ TeV. During the third data taking period (Run 3), which officially started in July 2022 after the second Long Shutdown (LS2), pp collisions are delivered at $\sqrt{s} = 13.6$ TeV and lead ions at $\sqrt{s_{NN}} = 5.5$ TeV. After Run 3, during the third Long Shutdown, LHC will be upgraded to High Luminosity LHC (HL-LHC [125]), which will deliver proton collisions at a peak luminosity 5 to 7 times larger the present nominal value of 10^{34} cm^{-2}s^{-1}. Afterwards, in 2029, the Run 4 data taking period is expected to start.

3.2 The ALICE experiment

ALICE (A Large Ion Collider Experiment) [112] is a general-purpose heavy-ion detector designed to address the physics of strongly interacting matter and the quark-gluon plasma, a state of matter formed in the high energy density and temperature conditions produced in heavy-ion collisions. The ALICE physics programme not only includes heavy-ion collisions (mainly Pb–Pb), but also proton-proton collisions and proton-nucleus collisions, which produce a final state of intermediate size between the former two.

The ALICE detector was optimised in order to have excellent tracking and particle identification capabilities in a high-multiplicity environment such as the one produced in heavy-ion collisions, where the number of charged particles produced at midrapidity $\langle \mathrm{d}N/\mathrm{d}\eta \rangle_{|\eta|<0.5}$ spans the range 1500-4000, reaching values more than two orders of magnitude larger than in a typical pp collision at the same energy.

The ALICE detector is located 44 m underground, its total weight is 10^7 kg and its overall dimensions are $16 \times 16 \times 26$ m^3. The layout of the ALICE detector during Run 2 is displayed in figure 3.2. The experiment is divided into two main parts:

- A central barrel which measures hadrons, electrons and photons. From the inside out, the central barrel consists of an Inner Tracking System (ITS) of six layers of silicon detectors, a Time Projection Chamber (TPC), a Transition Radiation Detector (TRD), a Time Of Flight detector (TOF), a Ring Imaging Cherenkov detector (HMPID) and two electromagnetic calorimeters (PHOS and EMCal). All detectors but HMPID, PHOS and EMCal cover the full azimuthal angle. The central barrel is embedded in a large solenoid magnet which produces a magnetic field of 0.5 T used to bend the charge particles trajectories in order to measure their momenta.

- A forward muon spectrometer consisting of an absorber, a dipole magnet with a nominal magnetic field of 0.67 T used to bend the muons trajectories, ten planes of tracking chambers and four planes of triggering chambers used to trigger on events with muons.

In addition to that, several small detectors (ZDC, PMD, FMD, T0, V0A and V0C) located in the forward direction, i.e. at small polar angles, are used for global events characterisation and for triggering purposes. Finally, an array of scintillators (ACORDE) positioned on top of the solenoid magnet is used to trigger on cosmic rays.

During the Long Shutdown 2 (2019-2021), the ALICE detector was majorly upgraded in order to improve and extend its physics capabilities for the Run 3 and Run 4 data taking periods [126, 127]. The upgrades made the detector able to record collisions at higher interaction rates, up to 50 kHz for Pb–Pb collisions and 4 MHz for pp collisions.

This will allow for an increase of the integrated luminosity to 200 pb^{-1} for pp collisions and to 13 nb^{-1} for Pb–Pb collisions, enlarging the size of the data samples by one to almost three orders of magnitude, depending on the physics observable. This large amount of data, together with the improvement in vertexing and tracking efficiency and resolution, will allow for detailed studies of rare probes at low and high p_{T} and for multi-dimensional analyses of these probes. On the detector side the main upgrade involved the ITS, which was substituted with a new Inner Tracking System (ITS2) consisting of seven layers of silicon pixel detectors, as described in more detail in Section 3.2.1. Another important upgrade involved the Time Projection Chamber, whose readout chambers were substituted in order to increase the readout rate (see Section 3.2.2). In addition to that, the V0 and T0 detectors were substituted with the Fast Interaction Trigger (FIT), a system of forward detectors used for triggering and event selection, and the muon arm was complemented with the Muon Forward Tracker

(MFT), which improves the pointing resolution of muon tracks in order to better discriminate between primary and secondary $q\bar{q}$ states (quarkonia). All the other detectors were involved in the maintenance and improvement of the readout chain.

In the following, the detectors used for the analysis presented in this thesis are described in detail. For each detector, the first part of the description refers to the Run 2 configuration, during which the data used for the analysis work presented in this thesis were collected, while the second part provides some details about the upgraded detector, i.e. the one which is currently being used for the Run 3 data taking campaign.

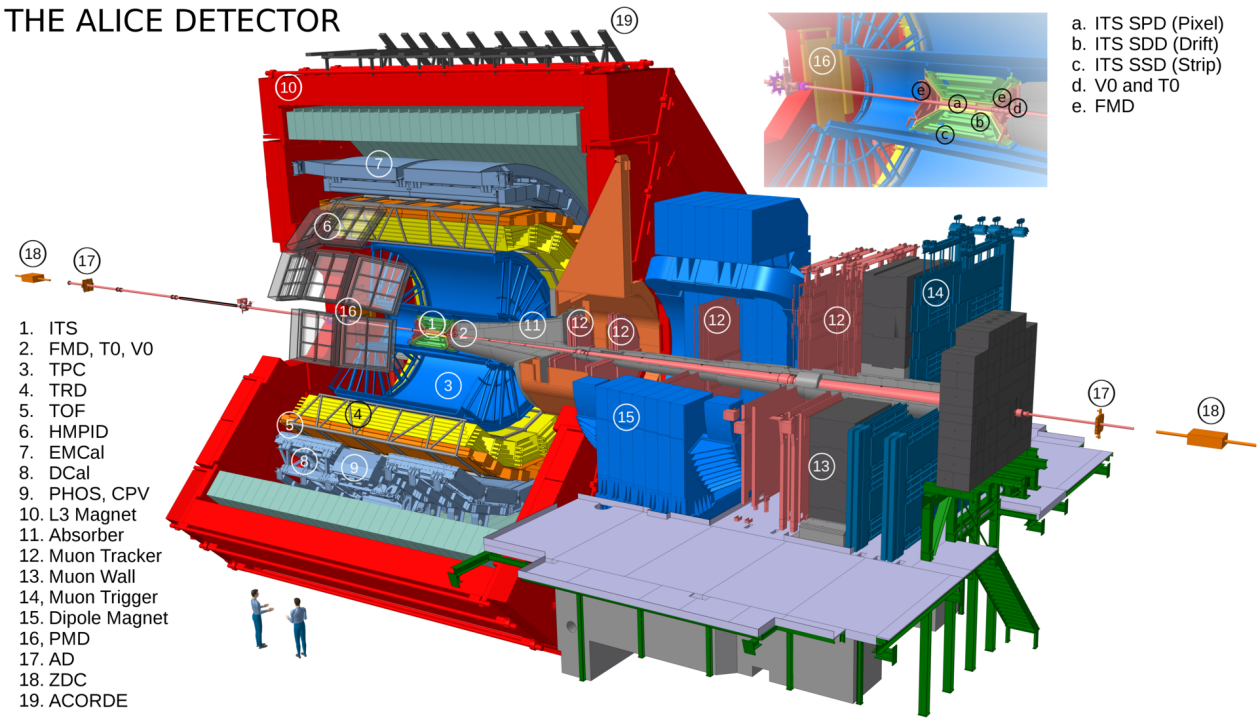

Figure 3.2: Schematic view of the ALICE detector in the Run 2 configuration (2015-2018). Figure taken from the ALICE figure repository.

3.2.1 Inner Tracking System

The Inner Tracking System (ITS) [128] was the innermost detector of the central barrel (Figure 3.3). The ITS covered the pseudorapidity range of $|\eta| < 0.9$ and consisted of six cylindrical layers of silicon detectors placed around the beam pipe at radii between 3.9 cm and 43.0 cm.

The main tasks of the ITS were:

- The determination of the primary vertex, i.e. the point where the interaction between the colliding protons or nuclei occur. The primary vertex can be determined with a resolution better than 100 μm in the plane perpendicular to the beam axis.

- The reconstruction of the secondary vertices from the weak decays of hyperons and B and D mesons. This task requires a high impact parameter resolution (i.e. the resolution of the distance of closest approach of a track to the primary vertex) in order to discriminate between primary tracks coming from the collision vertex and secondary tracks produced by weak decays.

- The tracking and identification of particles with momentum smaller than 200 MeV/c. The identification is performed measuring the specific ionisation energy loss $\mathrm{d}E/\mathrm{d}x$ in the material of the four outer layers, which have analogue readout. This is particularly useful for low-p_{T} tracks which cannot be tracked with the TPC (see Section 3.5).
- The momentum resolution improvement for particles reconstructed by TPC, as shown in Section 3.5.

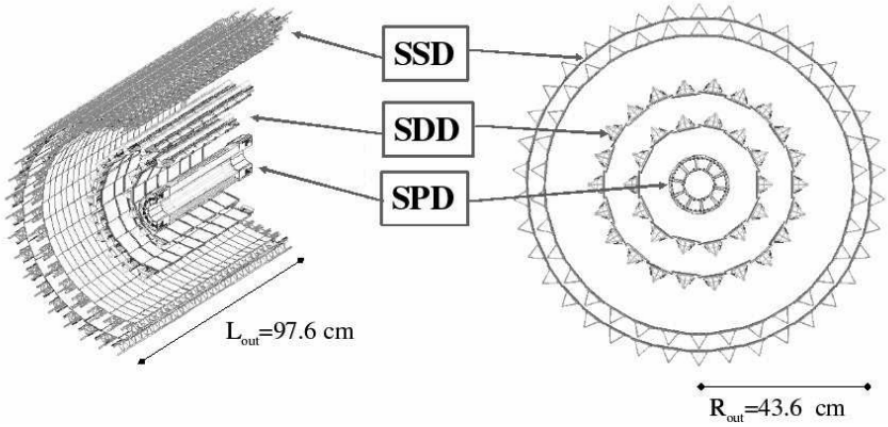

Figure 3.3: Layout of the Inner Tracking System. Figure taken from [112].

The two innermost layers of the ITS consisted of Silicon Pixel Detectors (SPD) which allowed for the operation in relatively high radiation levels and provided the high spatial resolution required in an environment characterised by a high track density (more than 50 tracks/cm^2). In particular the spatial resolution was 100 μm along the z direction, i.e. in the direction of the beam, and 12 μm in the transverse plane (rφ plane). The first layer was positioned as close as possible to the beam pipe, in order to maximise the impact parameter resolution. The two following layers, which operated in an environment with a charged particle density up to 7 tracks/cm^2, were equipped with Silicon Drift Detectors (SDD), which provided a resolution of 35 μm in the rφ plane and 25 μm along the z axis. Finally, the two outer layers, placed at a distance from the interaction point such that the charged track density was below 1 particle per cm^2, consisted of Silicon Strip Detectors (SSD), which allowed for the coverage of larger areas. They provided a resolution of 20 μm in the rφ plane and 830 μm along the z axis. The position of the last layer was determined by the necessity to match the ITS tracks with those reconstructed in the TPC (see Section 3.5 for a description of the track reconstruction procedure). The SDD and SSD layers had analogue readout and could therefore be used for particle identification via the measurement of the specific ionisation energy loss $\mathrm{d}E/\mathrm{d}x$.

Since the momentum and impact parameter resolution are dominated by multiple scattering effects, the amount of material used for the detector was minimised: the detectors effective thickness was equal to 0.4% of one radiation length X_0 and, considering all the additional material in the active volume (support structures, cooling systems, cabling), the total material traversed by a track perpendicular to the detector surface amounted to approximately 7.2% of X_0.

The main characteristics of the ITS layers are summarised in Table 3.1.

Layer	Type	r (cm)	Acceptance	Material budget (%X_0)	Resolution $r\varphi \times z$ (μm^2)
1	pixel	3.9	$\|\eta\| < 2.0$	1.14	12×100
2	pixel	7.6	$\|\eta\| < 1.4$	1.14	12×100
3	drift	15.0	$\|\eta\| < 0.9$	1.13	35×25
4	drift	23.9	$\|\eta\| < 0.9$	1.26	35×25
5	strip	38.0	$\|\eta\| < 0.97$	0.83	20×830
6	strip	43.0	$\|\eta\| < 0.97$	0.86	20×830

Table 3.1: Main characteristics of the ITS layers [27].

Upgrade of the Inner Tracking System

During the Long Shutdown 2 the ITS was replaced by a new upgraded Inner Tracking System (ITS2)[129]. The ITS2 consists of seven layers of Silicon Pixel Detector (see Figure 3.4) based on Monolithic Active Pixel Sensors (MAPS). It has a better impact parameter resolution, improved by a factor 3 in the rφ plane and by a factor 5 in the z direction for tracks with $p_{\mathrm{T}} \sim 500$ MeV/c [130]. This improvement was achieved by reducing the pixel size and by positioning the first layer closer to the interaction point, at 22.4 mm from it. For this purpose, a new beam pipe with smaller diameter was developed and installed. Another key element to improve the impact parameter resolution was the reduction of the material budget of the detector, which amounts to 0.35%X_0 per layer. These improvements also increased the tracking efficiency and the momentum resolution at low p_{T}, and will allow for a very precise reconstruction of secondary vertices from the decays of charm and beauty hadrons.

Finally, the readout rate was increased from 1 kHz to 100(200) kHz in Pb–Pb(pp) collisions, allowing for an increase of the data taking rate and, consequently, of the total amount of recorded collisions in Run 3 with respect to the previous data taking campaigns.

Thanks to the expected large amount of recorded data and to the improvement of tracking efficiency and impact parameter resolution, it will be possible to study for the first time charm baryons and beauty hadrons in central Pb–Pb collisions, and to measure charm mesons with transverse momentum smaller than 1 GeV/c.

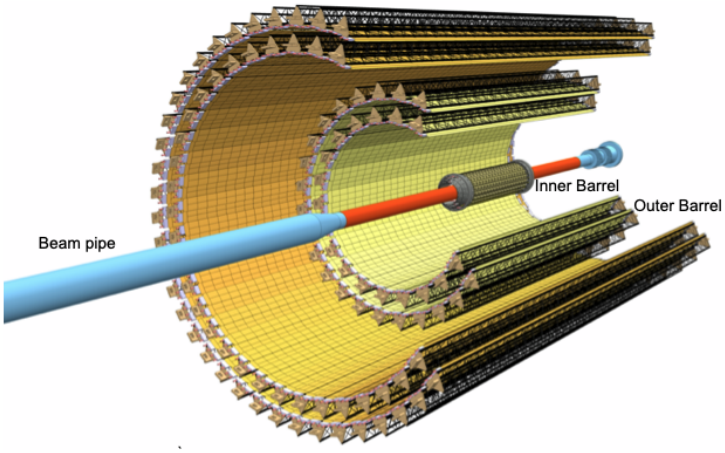

Figure 3.4: Layout of the new Inner Tracking System (ITS2). Figure taken from [126].

3.2.2 Time Projection Chamber (TPC)

The Time Projection Chamber (TPC) [131] is the main tracking detector of the central barrel and is used for the identification of charged particles via the measurement of the specific ionisation energy loss $\mathrm{d}E/\mathrm{d}x$. The TPC has a cylindrical shape (see Figure 3.5) with an inner radius of 85 cm, an outer radius of 250 cm and an overall length along the beam direction of 5 m. It covers the pseudorapidity region of $|\eta| < 0.9$ for tracks with full radial length and provides full azimuthal acceptance.

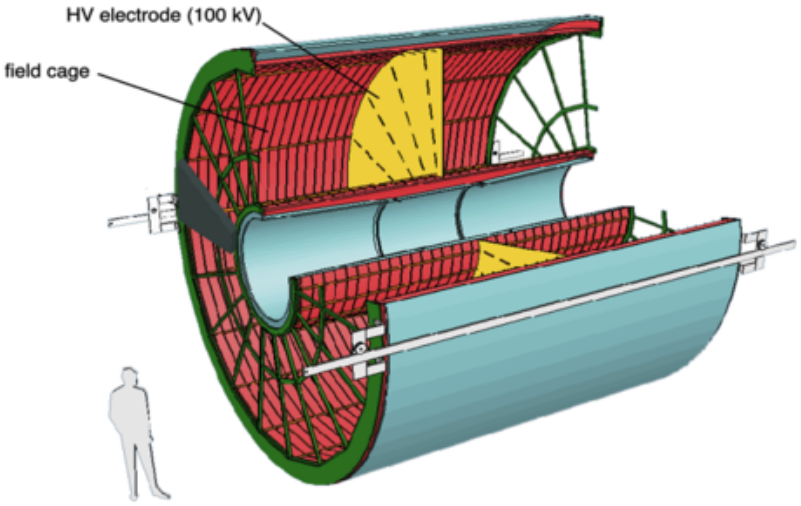

Figure 3.5: Layout of the Time Projection Chamber (TPC). Figure taken from [132].

The TPC is a field cage filled with 90 m^3 of gas mixture, which consisted primarily of Ne and CO_2 or of Ar and CO_2, depending on the data taking period. A central high voltage electrode and two opposite end-plates are used to create a highly uniform electric field of 400 V/cm in the gas volume. Each end-plate is segmented into 18 trapezoidal sectors which during Run 2 were instrumented with multi-wire proportional chambers (MWPCs) with cathode pad readout.

When a charged particle traverses the gas volume, it ionises the gas molecules. The ionisation electrons drift in the electric field to the end-plates, with a drift velocity of 2.7 cm/μs and a maximum drift time of 92 μs. The electrons are then detected using the MWPCs, in order to reconstruct the projection of the track on the rφ plane. The z-coordinate of the track, i.e. the coordinate along the beam axis, is calculated from the drift time of the ionisation electrons. Since each trapezoidal sector of the end-plate is segmented into 159 pad rows, a track with full radial length can ideally be reconstructed from 159 three-dimensional points. The TPC is capable of tracking particles with transverse momentum in the interval $0.15 < p_{\mathrm{T}} < 100$ GeV/c, with a track finding efficiency which saturates at about 80-85% for $p_{\mathrm{T}} > 1$ GeV/c (see Figure 3.8). More details abouth the tracking in the TPC are provided in Section 3.5, while a detailed description of particle identification with the TPC is given in Section 3.6.

Upgrade of the TPC

During the Long Shutdown 2, the TPC underwent a major upgrade [133] which made it able to cope with the higher interaction rates of Run 3 and Run 4. For this purpose, the MWPCs

were replaced by gas electron multiplier (GEM) chambers. The use of MWPCs required to suppress the ion backflow into the drift region by using a gating grid technique, which limited the readout rate. The GEMs, instead, feature intrinsic ion blocking capabilities that avoid massive charge accumulation in the drift volume, and can thus be operated without the use of a gating grid. Consequently, the TPC can now readout all the collision events in a continuous way, without the use of a trigger. More details about the continuous readout are given in Section 3.3.

3.2.3 Time Of Flight detector (TOF)

The ALICE Time of Flight (TOF) detector [134] is an array of multigap resistive plate chambers (MRPCs) which covers the pseudorapidity range of $|\eta| \lesssim 0.9$ and has full azimuthal acceptance. It is positioned within a cylindrical shell with internal radius of 370 cm and external radius of 399 cm, and it is segmented into 18 azimuthal sectors, called supermodules, each of which is segmented into 5 modules along the z direction. Its main purpose is the identification of particles with intermediate momentum via the measurement of their time of flight, as described in Section 3.6. In the analysis described in this thesis the time resolution of TOF is exploited to reject strange hadrons produced in out-of-bunch pile-up events, as will be described in detail in Section 4.5.

In preparation of Run 3 the TOF underwent an important upgrade which mainly involved its readout electronics, with the purpose to accomplish the continuous readout of data.

3.2.4 V0 detector

The V0 detector [26] consists in two arrays of scintillation counters, called V0A and V0C, placed at forward rapidity. The V0A is located at 340 cm from the interaction point and covers the pseudorapidity range of $2.8 < |\eta| < 5.1$, whereas the V0C is placed on the opposite side at 90 cm from the interaction point and covers the pseudorapidity range of $-3.7 < |\eta| < -1.7$.

The V0 detector provides the minimum bias trigger in pp, p–Pb and Pb–Pb collisions. It is also used to determine the centrality of p–Pb and Pb–Pb collisions via the measurement of the multiplicity of produced charged particles, and it is used to classify pp collisions in multiplicity classes, as described in Section 3.7. It also participates to the determination of the luminosity in pp collisions.

During the Long Shutdown 2, the V0 detectors were substituted by the FV0 detector, an azimuthally segmented scintillator disk positioned at 320 cm from the interaction point and covering the pseudorapidity range of $2.2 < |\eta| < 5.1$. The FV0 is part of the new Fast Interaction Trigger (FIT) detector [135], which is the main triggering detector of ALICE in Run 3.

3.3 The ALICE trigger and data acquisition

The main tasks of the ALICE trigger and data acquisition (DAQ) systems [136] are the selection of interesting physics events and the permanent storage of data for later analysis. The ALICE Trigger system used during Run 2 was constituted by a low-level hardware trigger, called Central Trigger Processor (CTP), and a High-Level software Trigger (HLT). The CTP generated the trigger decision by combining the information from the different detectors. Since the detectors have different sensitive periods and readout times, the trigger system was divided into three levels (L0, L1 and L2) with the following characteristics:

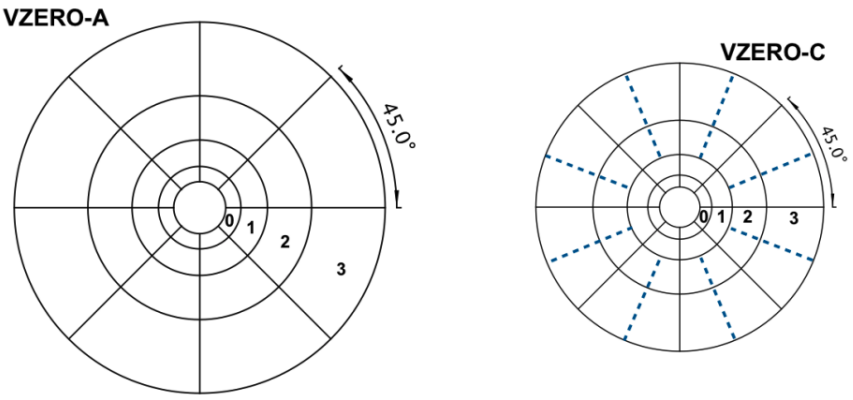

Figure 3.6: Schematic view of V0A and V0C arrays showing their azimuthal segmentation. Figure taken from [26].

- L0 level: the L0 decision was based on the information acquired from the fast detectors (e.g., the V0 and T0 detectors) and was made about 900 ns after the collision takes place. Events accepted at the L0 level were further evaluated at the L1 level.
- L1 level: the L1 decision was based on the information obtained from the detectors which require a longer time to respond and was made 6.5 μs after the L0 one. The L1 decision was delivered to the detectors in order to trigger the buffering of the event data.
- L2 level: the L2 decision was taken after about 90 μs, which corresponds to the drift time in the TPC. The L2 level implemented the *past-future protection*, which was used to discard events spoilt by the pile-up, a condition which occurs when multiple events fall within the sensitive time of the detector. This is a fundamental task since, for example, pile-up between two central Pb–Pb events leads to an unreconstructable set of tracks. The L2 decision triggered the sending of the event data to the DAQ system and to the HLT.

The ALICE DAQ system manages the dataflow from the detector to the data storage. During Run 2, the data were first sent to front-end machines called Local Data Concentrators (LDCs), where the event fragments were assembled into sub-events, which were then shipped to a farm of machines called Global Data Collectors (GDCs). In the GDCs the whole event was built. The DAQ was interfaced to the HLT which performed a fast reconstruction of each event, decided to accept or reject it, and reduced its size without loosing physics information by applying compression algorithms. This was necessary in order to cope with the DAQ archiving rate, which was about 1 GB/s. Finally, events were permanently stored in the CERN computing centre.

Upgrade of the trigger and data acquisition system

The ALICE trigger and data acquisition systems have been majorly upgraded in order to cope with the 50 kHz interaction rate at which Pb–Pb collisions will be provided during Run 3 [137]. At this rate, an average of five pile-up events occur within the sensitive time of the TPC detector, making the triggered operations of the TPC meaningless. To deal with the increased interaction rate, a continuous data-taking mode has been implemented.

Within this mode, the readout of the detectors is not based on a trigger decision but it is done continuously. The unit of information is a ∼11.4 ms long snapshot of the data, called timeframe (TF), containing the information of approximately 570 collisions when the interaction rate is 50 kHz.

The raw data from the detectors are sent to the First Level Processors (FLP), where they are assembled into sub-time frames (STF). Each sub-time frame consists in a ∼11.4 ms snapshot of the data coming from a specific sub-detector. Sub-time frames are sent to the Event Processing Nodes (EPN), where the information from different detectors is assembled into timeframes and a first synchronous (i.e., online) reconstruction of the events is performed. In the EPNs, data are compressed into the compressed timeframes (CTF), which are written to a disk buffer and are archived on mass storage systems. The data throughput from raw data to compressed timeframes is reduced from 3.5 PB/s to 100 GB/s, in order to cope with the available computing resources. The output of the synchronous reconstruction of events performed in the EPNs is used for the subsequent asynchronous reconstruction, which is performed after improving the calibration of the detectors.

The whole data processing is performed using the new computing software framework developed for Run 3, called Online-Offline computing system (O^2) [137]. The new framework provides a unified and coherent computing environment from data taking through data reconstruction and up to data analysis.

3.4 The ALICE offline framework

The huge amount of data collected by the ALICE experiment requires an infrastructure able to process and analyse the events.

Data processing is distributed in several computing centres located worldwide and coordinated by the Worldwide LHC Computing Grid (WLCG) project [138]. The WLCG is a highly hierarchical computing infrastructure developed on three levels: the largest computing centre is located at CERN and is called Tier-0. Regional computing centres, called Tier-1, are logically clustered around the Tier-0 and contribute to the storage of events, which at present relies on magnetic tapes. Tier-2 centres are smaller centres logically clustered around Tier-1 centres. The grid infrastructure is not only used to store the data but also for the data processing, which includes calibration, reconstruction, simulation and analysis. The ALICE collaboration has developed a service, called AliEn (ALICE Environment) [139] that allows the collaboration to easily access the data on the Grid.

The analysis of the data collected in Run 1 and Run 2 is performed using the ALICE software environment called AliRoot [140]. AliRoot is based on ROOT, a data analysis framework mainly written in C++, and is used for simulations, calibrations, visualisations and analysis of experimental data. The AliRoot framework is also interfaced to different Monte Carlo event generators, like for example PYTHIA [90], and different transport codes which simulate the detector response like GEANT 3 [141], GEANT 4 [142] and FLUKA [143]. The analysis code is collected in a data repository called AliPhysics [144].

The analyses of data collected in Run 3 are performed within the new computing software framework O^2 [145], which fully replaces the AliRoot framework. The code for Run 3 physics analyses is collected in a data repository called O2Physics [146].

3.5 Tracking of charged particles and reconstruction of the interaction vertex

The procedure followed to track charged particles in the central barrel and to determine the position of the interaction vertex consists of several steps.

First of all, the data collected with each detector are converted into "clusters" characterised by space-time information. Then, a preliminary determination of the primary vertex is performed using the SPD tracklets, defined as lines connecting two clusters found in the two SPD layers of the ITS. The vertex is defined as the space point to which a maximum number of tracklets converge.

Afterwards, track finding and fitting is performed using ITS and TPC clusters and applying the Kalman filter technique [147]. The fitting procedure consists of three stages and follows an inward-outward-inward scheme, schematically shown in Figure 3.7.

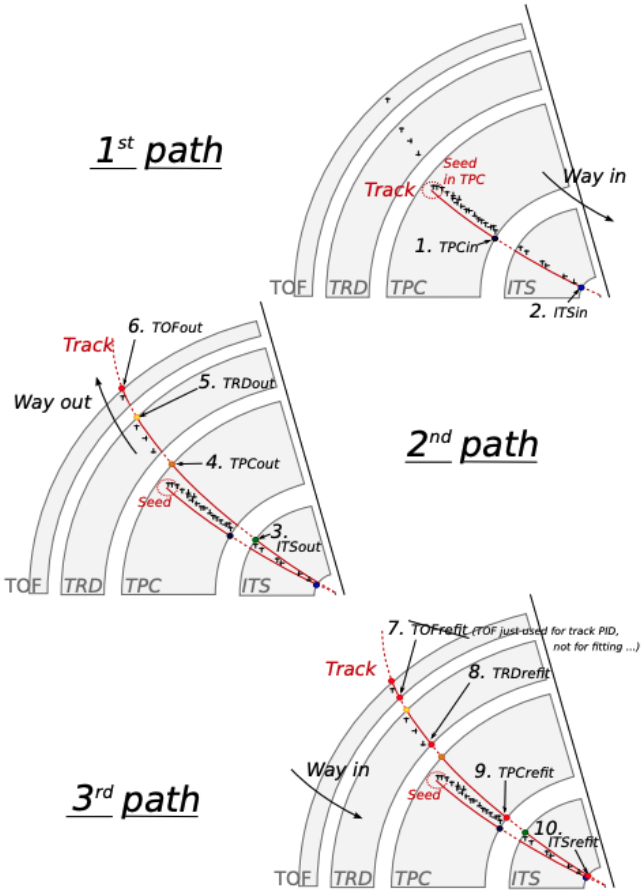

Figure 3.7: Schematic description of the three stages of track reconstruction in an event recorded by ALICE. Figure taken from [148].

The first inward stage starts by building track seeds from TPC clusters at large radii. The track seeds are then propagated inward and, at each step, they are updated with the nearest cluster, if it passes some proximity selections. Only tracks with a minimum of 20 clusters out of an ideal maximum of 159 clusters (each corresponding to one pad row) are accepted. Moreover, tracks are rejected if they miss more than 50% of the clusters that for geometrical reasons are expected to be found. The TPC track finding efficiency, computed with a Monte Carlo simulation and defined as the ratio between the reconstructed tracks

and the generated primary particles, is shown in the left panel of Figure 3.8 as a function of the transverse momentum p_{T}. The efficiency saturates at about 80-85% for $p_{\mathrm{T}} > 1$ GeV/c, while for $p_{\mathrm{T}} < 500$ MeV/c it rapidly decreases because of the energy loss and the multiple scattering in the detector material. The TPC tracks are propagated to the outermost layer of the ITS and become the seeds for the track reconstruction in the ITS, which follows an inward propagation similar to the one described for the TPC. The TPC track prolongation efficiency to the ITS, also called ITS–TPC matching efficiency, is show in the right plot of Figure 3.8. The efficiency is close to one when two hits in the ITS are required, whereas it decreases to approximately 85% when the track is required to have at least one hit in the SPD. Since the track finding efficiency with the TPC is approximately zero for $p_{\mathrm{T}} < 200$ GeV/c, a standalone ITS reconstruction is performed taking into account those clusters not used to build ITS–TPC tracks, in order to allow for the tracking of particles with transverse momenta down to 80 MeV/c.

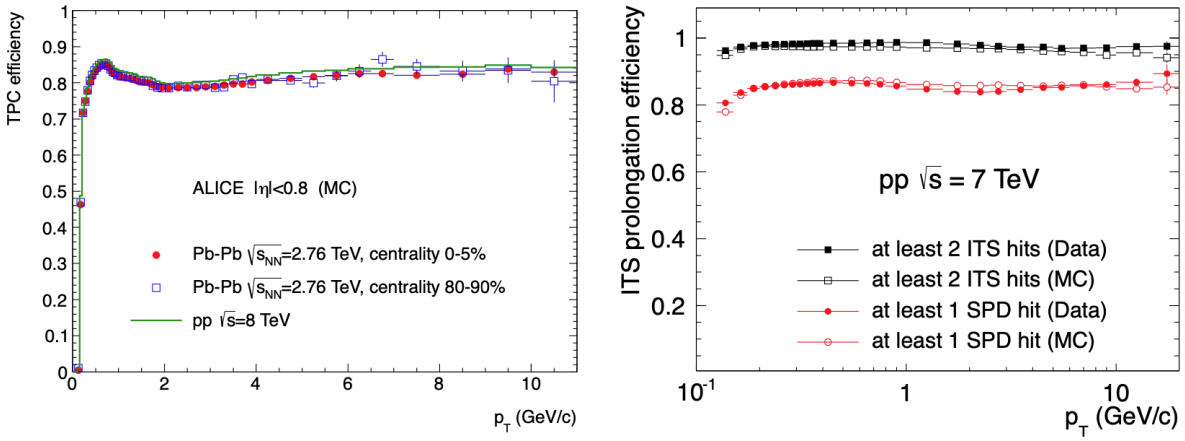

Figure 3.8: (left) TPC track finding efficiency for primary particles in pp and Pb–Pb collisions. (right) ITS–TPC matching efficiency in pp collisions. Figures taken from [27].

The second tracking stage starts once the track reconstruction in the ITS is completed. The tracks are refitted by the Kalman filter in the outward direction using the clusters previously found, and they are matched to TRD hits in the six TRD layers and to TOF clusters. The information from these two detectors is not used to update the kinematic properties of the tracks, but is used for particle identification purposes.

Finally, the last tracking stage consists in the inward refitting of tracks using the clusters previously found in the ITS and the TPC. The final track properties are computed at this point.

The inverse-p_{T} resolution of the ITS–TPC matched tracks and of the standalone TPC tracks (i.e., tracks reconstructed using only TPC clusters) is shown in Figure 3.9. The ITS–TPC tracks (green and blue markers) show better resolution than standalone TPC tracks (black markers), whose resolution can be improved by constraining them to the position of the primary vertex (red markers). Since the ITS–TPC tracks suffer from gaps in the ITS acceptance caused by inefficiencies of the SPD layers, standalone TPC tracks constrained to the primary vertex can be used in the analyses which require a uniform detector response.

Finally, ITS–TPC matched tracks are used to determine the primary vertex position with a resolution up to 2.5 times better than with SPD tracklets, with the improvement depending on the number of contributing tracks (see Figure 3.10).

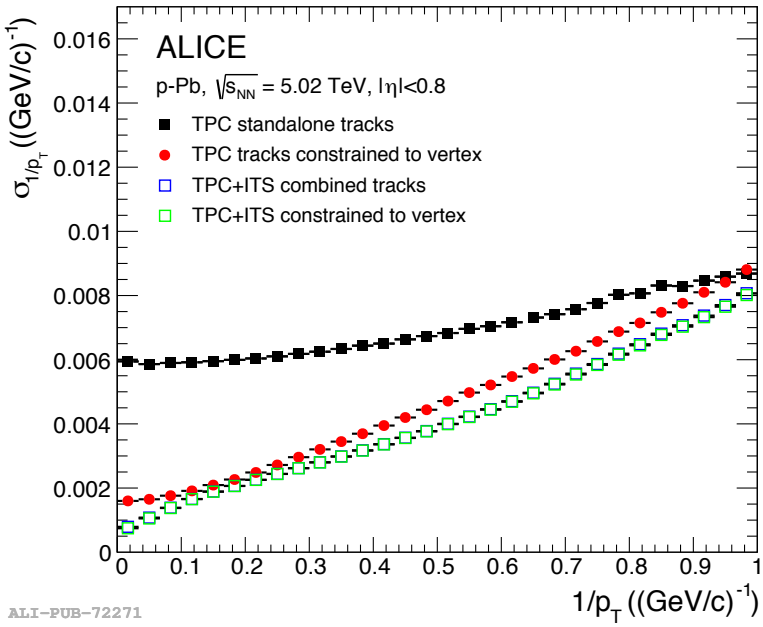

Figure 3.9: Inverse-p_{T} resolution of standalone TPC tracks (solid markers) and ITS–TPC matched tracks (empty markers) with and without constraint to the primary vertex. The vertex constrain improves the resolution of TPC standalone tracks, whereas it has no effect on ITS–TPC tracks. Figure taken from [27].

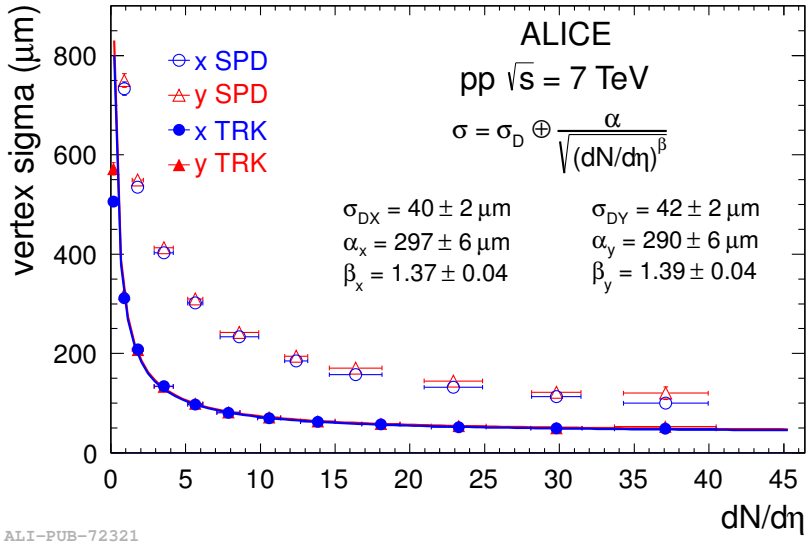

Figure 3.10: Transverse resolution of the primary vertex found with SPD tracklets (open markers) and with ITS–TPC matched tracks (solid markers) as a function of the number of contributing tracks. Figure taken from [27].

3.6 Particle identification

The ALICE detector has unique particle identification capabilities, thanks to the several techniques exploited by the different sub-detectors.

The main detector for particle identification over a wide momentum range is the TPC, which identifies particles via the measurement of their specific energy loss $\mathrm{d}E/\mathrm{d}x$ in the gas volume. The energy loss is described by the Bethe-Block formula [149] and in ALICE is parametrized by the function:

$$f(\beta\gamma) = \frac{P_1}{\beta^{P_4}} \left(P_2 - \beta^{P_4} - ln \left(P_3 + \frac{1}{(\beta\gamma)^{P_5}} \right) \right), \tag{3.1}$$

where β is the particle velocity, γ is the Lorentz factor, and P_i are fit parameters [27]. The distribution of the specific energy loss $\mathrm{d}E/\mathrm{d}x$ in the TPC as a function of the particle momentum in pp collisions at $\sqrt{s} = 13$ TeV is shown in Figure 3.11. The black lines represent the energy loss parametrizations. At low momenta ($p_\mathrm{T} \lesssim 1$ GeV/c) particles can be separated on a track-by-track basis. The separation power, i.e. the distance between the mean values of the $\mathrm{d}E/\mathrm{d}x$ distributions for two different particles divided by the width of one of the two distributions, is greater than 2 up to 1 GeV/c for π–K and up to 1.5 GeV for p–K. In the relativistic rise region ($2 \lesssim p_\mathrm{T} \lesssim 20$ GeV/c) particles can be separated on a statistical basis via multi-Gaussian fits. Indeed, in this region the $\mathrm{d}E/\mathrm{d}x$ shows a nearly constant separation for the different particle species. Currently, the main limitation to particle identification at larger momenta is the statistical precision: with Run 3 data the measurement is expected to be extendable up to about 50 GeV/c.

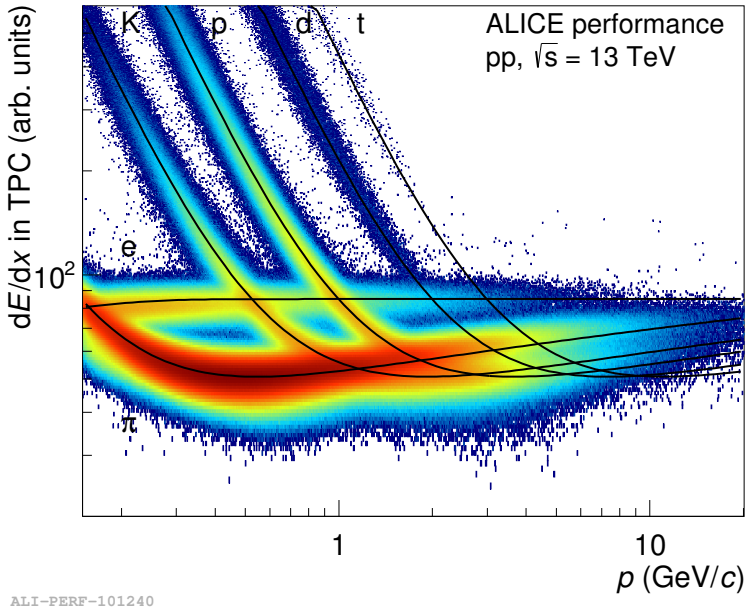

Figure 3.11: The specific ionisation energy loss $\mathrm{d}E/\mathrm{d}x$ as a function of the momentum p for different particles produced in pp collisions at $\sqrt{s} = 13$ TeV. The coloured points are measurements performed with the TPC, the black lines represent the parametrizations of the energy loss with the formula 3.1. Figure taken from the ALICE figure repository.

Particle identification via the measurement of $\mathrm{d}E/\mathrm{d}x$ can also be performed with the four outer layers of the ITS, which have analogue readout. This is particularly useful for low-p_T particles which cannot be tracked with the TPC.

Another technique applied for particle identification purposes is the measurement of the time of flight of particles using the TOF detector, which can determine the arrival time of particles with a resolution better than 80 ps. The start time for the time of flight measurement is provided by the T0 detectors, two arrays of Cherenkov counters which are placed at forward rapidities on both sides of the interaction point and measure the collision time. The TOF provides a separation power of more than 3σ between kaons and pions up to 2.5 GeV/c, and between kaons and protons up to 4 GeV/c. The distribution of the velocity β measured by the TOF detector in p–Pb collisions at $\sqrt{s_{NN}} = 5.02$ TeV is shown in Figure 3.12 as a function of the particle momentum.

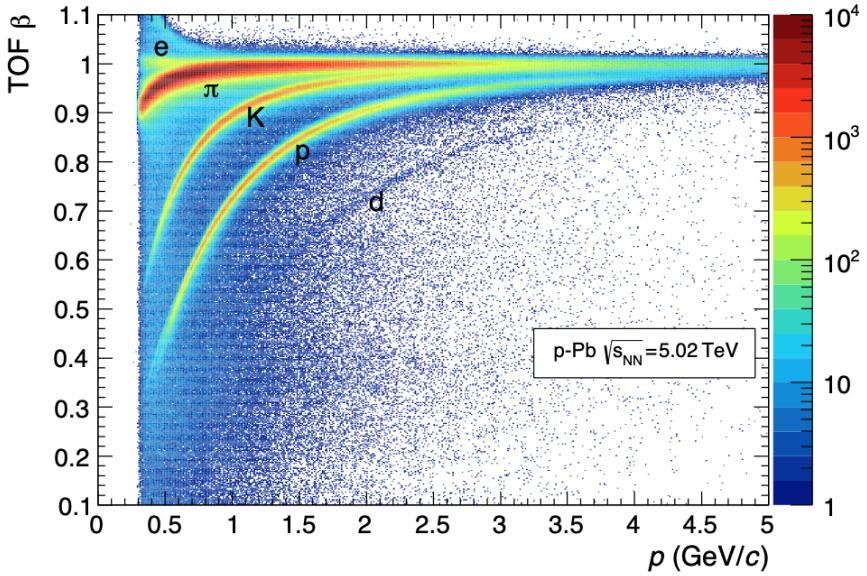

Figure 3.12: Distribution of the velocity β measured by the TOF detector in p–Pb collisions at $\sqrt{s_{NN}} = 5.02$ TeV as a function of the particle momentum. Figure taken from [27].

At higher momenta, particle identification can be performed via the measurement of the Cherenkov angle of the rings produced by charged particles in the ring-imaging Cherenkov (RICH) detectors which constitute the High Momentum Particle IDentification Detector (HMPID) [150]. The HMPID provides a separation power of more than 3σ between kaons and pions up to 3 GeV/c, and between kaons and protons up to 5 GeV/c.

The measurements with the different techniques and detectors can be combined to improve the separation between the different hadron species. Finally, electron identification is performed using dedicated detectors like the TRD [151], the EMCal [152] and the PHOS [153].

3.7 Multiplicity determination

The multiplicity of charged particles produced at midrapidity ($|\eta| < 0.5$) in the collision is a key observable for the classification of events.

Proton-proton collisions can be classified in multiplicity classes based on the sum of the signal amplitudes measured in the two forward V0 detectors. The signal amplitude measured by the V0 detectors is indeed proportional to the multiplicity of charged particles produced at midrapidity in the collision. An example of self-normalised distribution of the V0 signal amplitude measured in pp collisions at $\sqrt{s} = 13$ TeV is shown in Figure 3.13. The distribution is divided into percentile classes, called V0M percentile (or multiplicity) classes: the 0-5%

class corresponds for example to the 5% of events with the highest V0 amplitude, while the 70-100% class correspond to the 30% of events with the smallest signal amplitude. For each V0M percentile class, an average number of charged particles produced at midrapidity $\langle \mathrm{d}N/\mathrm{d}\eta \rangle_{|\eta|<0.5}$ can be computed. The $\langle \mathrm{d}N/\mathrm{d}\eta \rangle_{|\eta|<0.5}$ values are obtained by measuring the number of charged particles produced at midrapidity and by correcting it for the tracking efficiency of charged particles, computed with a Monte Carlo simulation.

The signal amplitude measured in the V0 detectors also allows one to divide heavy-ion collisions in centrality classes, as described in Section 1.2.2.

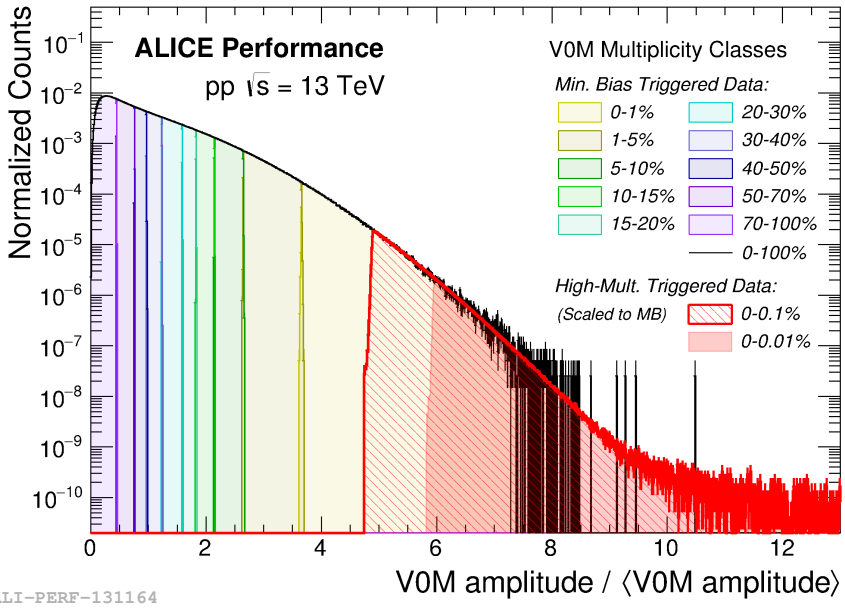

Figure 3.13: Distribution of the self-normalised sum of the signal amplitudes measured in the V0 detector in pp collisions at $\sqrt{s} = 13$ TeV. V0M multiplicity classes are defined starting from this distribution, as illustrated. Figure taken from the ALICE figure repository.

Chapter 4

Angular correlation techniques for in-jet and out-of-jet strangeness production studies

The work presented in this thesis focuses on the production of the strange meson K^0_S and of the strange baryon $\Xi^\pm$ in jets and out of jets in pp collisions at $\sqrt{\mathrm{s}} = 5.02$ TeV and at $\sqrt{\mathrm{s}} = 13$ TeV collected by the ALICE experiment during the Run 2 data taking campaign. The aim of this work is to evaluate the contribution to the strangeness enhancement effect given by the mechanisms associated to hadron production in jets (*hard* processes) and out of jets.

For the purpose of separating K^0_S ($\Xi^\pm$) produced in jets from the ones produced out of jets, the angular correlation between the highest-p_T primary charged particles with $p_\mathrm{T} > 3$ GeV/c (*trigger* particle –"h") and the K^0_S ($\Xi^\pm$) produced in the same collision is exploited.

This chapter provides the description of the analysis procedure applied to obtain the h-K^0_S and the h-$\Xi^\pm$ angular correlation distributions and to compute the in-jet and out-of-jet p_T-spectra and p_T-integrated yields of K^0_S and $\Xi^\pm$ as a function of the charged particle multiplicity. The main steps of the analysis procedure are also briefly summarised in the following Section 4.1.

4.1 Analysis strategy

The first step of the analysis consists in the selection of pp collisions (*events*) of good quality. A detailed description of all the selections applied for this purpose are provided in Section 4.3. The good-quality events which are selected are divided into several multiplicity classes starting from the distribution of the sum of the signal amplitudes measured with the two V0 detectors (see Section 3.7).

The second step of the analysis consists in the selection of the trigger particle, which is considered as a proxy for the jet axis. The trigger particle is defined as the highest-p_T charged particle found in the event, and is required to have $p_\mathrm{T} > 3$ GeV/c. The minimum p_T threshold is applied in order to select particles originating from the hadronization of a hard scattering process. The trigger particle is required to be produced at midrapidity ($|\eta| < 0.8$) and to satisfy the track-quality selection criteria described in detail in Section 4.4.

The third step of the analysis consists in the identification of K^0_S and $\Xi^\pm$ hadrons, which is performed by exploiting their weak decays into charged hadrons, as described in Section 4.5. All the steps of the analysis are performed by separating K^0_S ($\Xi^\pm$) in nine (seven) intervals according to their transverse momentum p_T.

The fourth step consists in the calculation of the raw angular correlation between trigger particles and K^0_S ($\Xi^\pm$), from now on called *associated* particles:

$$\Delta\varphi = \varphi_{trigg} - \varphi_{assoc} \ , \ \Delta\eta = \eta_{trigg} - \eta_{assoc} \ , \tag{4.1}$$

where φ is the azimuthal angle and η is the pseudorapidity, defined as $\eta = -\ln(\tan(\theta/2))$, with θ denoting the polar angle. Azimuthal and polar angles are defined according to the convention in the reference frame whose z axis lies along the beam axis.
The angular separation between associated particles produced in the leading jet and the leading particle of the jet itself (i.e., the trigger particle) is expected to be small, and therefore a region in the angular correlation distribution centred in $(\Delta\varphi, \Delta\eta) = (0, 0)$ is associated to K^0_S ($\Xi^\pm$) produced in the leading jet (*toward-leading* production). A region at larger values of $\Delta\eta$ and centred at $\Delta\varphi \sim \pi/2$ allows instead to select K^0_S ($\Xi^\pm$) produced out of jets (*transverse-to-leading* production).

The raw angular correlation distributions must be corrected by several factors. First of all, the distributions are corrected by the efficiency of reconstruction of K^0_S ($\Xi^\pm$). The efficiency is obtained from MC simulation and is given by the ratio between the number of reconstructed K^0_S ($\Xi^\pm$) and the number of generated K^0_S ($\Xi^\pm$). The details of the efficiency correction procedure are provided in Section 4.6.1. The raw angular correlation distributions are also corrected by the trigger-associated particle pair acceptance, in order to eliminate the angular correlations related to the acceptance of the detector and to the η and φ distributions of trigger and associated particles, and to retain only the physical correlations. The correction by the pair acceptance is described in Section 4.6.2.

The corrected angular correlation distributions are projected along the $\Delta\varphi$ axis in the $\Delta\eta$ regions chosen to extract the toward-leading and the transverse-to-leading production. The projections in the whole $\Delta\eta$ interval are also obtained, in order to extract the total production yield, from now on called *full* yield. The projections are scaled by the width of the $\Delta\eta$ region from which they are obtained and by the number of trigger particles N_{trigg}.

Further correction factors must be applied to the $\Delta\varphi$ projections. The first correction is applied in order to take into account the presence of fake K^0_S ($\Xi^\pm$) in the sample of selected K^0_S ($\Xi^\pm$) candidates. This contribution is computed from the data, as described in Section 4.5. The correction procedure is described in Section 4.6.4. The second correction takes into account the contribution from K^0_S ($\Xi^\pm$) which are not primary, i.e. are not produced at the primary interaction point but are produced from the decay of more massive particles or from the interaction of particles with the material of the detector. This contribution is evaluated using MC simulations, as described in Section 4.5.3.

Once all the corrections are applied, the full, transverse-to-leading and toward-leading yields are computed by performing the integrals of the corresponding $\Delta\varphi$ projections in specific $\Delta\varphi$ regions: the full yield is extracted from the whole $\Delta\varphi$ region ($-\pi/2 < \Delta\varphi < 3/2\pi$), the toward-leading yield from a region centred at $\Delta\varphi \sim 0$, and the transverse-to-leading

yield from a region centred at $\Delta\varphi \sim \pi/2$. The details of the yield extraction procedure are reported in Section 4.6.6.

The full, transverse-to-leading and toward-leading yields are studied as a function of the transverse momentum p_{T} of the associated particles in the different multiplicity classes in which the events were divided. The p_{T} spectra are further corrected by a factor which takes into account the efficiency with which events with a trigger particle are selected (see Section 4.8) . Finally, the fully corrected p_{T}-spectra are interpolated with fit functions in order to extract the yields in the low p_{T} intervals where they cannot be measured, due to inefficiencies. The toward-leading, transverse-to-leading and full p_{T}-integrated yields are studied as a function of the multiplicity of charged particles produced in events containing a trigger particle.

4.2 Data and Monte Carlo samples

The work presented in this thesis is performed using the pp collisions at $\sqrt{\mathrm{s}} = 5.02$ TeV and at $\sqrt{\mathrm{s}} = 13$ TeV collected by the ALICE experiment during the Run 2 data taking campaign (2015-2018).

Two different samples of pp collisions at $\sqrt{\mathrm{s}} = 13$ TeV are used for the analysis: one collected with the minimum bias (MB) trigger, the other collected with the high multiplicity (HM) trigger. The MB trigger is provided by the logic AND between the V0A and V0C signals (see Section 3.2.4). The HM trigger is activated when the amplitude of the signal in the V0 detectors is above a predefined threshold, and allows for the selection of events characterised by a larger average charged particle multiplicity at midrapidity ($\langle \mathrm{d}N/\mathrm{d}\eta \rangle_{|\eta|<0.5} \sim$ 30) than MB ones ($\langle \mathrm{d}N/\mathrm{d}\eta \rangle_{|\eta|<0.5} \sim$ 7). Both samples are used to perform the analysis in a multiplicity range as wide as possible, reaching multiplicity values comparable to those measured in peripheral Pb–Pb collisions. For the h-$\mathrm{K}^0_{\mathrm{S}}$ correlation analysis, the MB events at $\sqrt{\mathrm{s}} = 13$ TeV collected in 2016 and 2017 are used. The total number of events passing the event quality selections described in the next section (Section 4.3) is about 1×10^9. For the h-$\Xi^{\pm}$correlation analysis, all the MB events at $\sqrt{\mathrm{s}} = 13$ TeV collected in 2016, 2017 and 2018 are used. The total number of selected events is 1.6×10^9. The sample of HM events at $\sqrt{\mathrm{s}} = 13$ TeV consists of 4×10^8 selected events, which were collected in 2016, 2017 and 2018. The sample of pp collisions at $\sqrt{\mathrm{s}} = 5.02$ TeV was collected with the MB trigger in 2017 and consists of 9×10^8 good quality events.

Monte Carlo (MC) simulations are needed to compute the efficiency of reconstruction of $\mathrm{K}^0_{\mathrm{S}}$ and $\Xi^{\pm}$, and to calculate the correction factors applied to the p_{T}-spectra (see Section 4.28). The MC samples used for this work were generated with the PYTHIA 8.2 [84] event generator, and use GEANT4 [142] to describe the propagation of particles through the material of the detector. The MC simulations are *anchored* to the data samples, that is they reproduce the configuration of the detector during the data acquisition. The MC simulation anchored to the MB events at $\sqrt{\mathrm{s}} = 13$ TeV consists of 9×10^8 events, the one anchored to the HM events at $\sqrt{\mathrm{s}} = 13$ TeV consists of 6×10^7 events, and the one anchored to the MB events at $\sqrt{\mathrm{s}} = 5.02$ TeV consists of 2×10^8 events.

4.3 Event selection

In order to select good-quality events, the following selections are applied:

- The z coordinate of the primary vertex is required to lie within 10 cm from the nominal interaction point, in order to guarantee the desired uniformity in the detector acceptance. The primary vertex is determined using the tracks reconstructed in the TPC and in the ITS.

- Events tagged as pile-up are rejected. Pile-up occurs when two or more collisions happen in the same bunch crossing (*in-bunch* pile-up) or when one or more collisions happen in a bunch crossing different from the one which triggered the acquisition but within the sensitive time of the detector (*out-of-bunch* pile-up). There are different tools for pile-up removal: in the present analysis events are rejected if more than one primary vertex is found using the tracks in the SPD layers of the ITS. In this way not only the in-bunch pile up is removed, but also the out-of-bunch pile-up which occurs within the SPD readout window (300 ns [112]).

Minimum bias events at $\sqrt{s} = 13$ TeV are divided into five multiplicity classes (0-5%, 5-10%, 10-30%, 30-50%, 50-100%) starting from the distribution of the sum of the signal amplitudes measured with the two V0 detectors, as described in 3.7. As a reminder, the multiplicity class 0-5% consists of the 5% of events characterised by the highest V0 amplitude, and the same applies to the other multiplicity classes.
Minimum bias events at $\sqrt{s} = 5.02$ TeV are divided into two multiplicity classes (0-10%, 10-100%). The number of events available at this centre-of-mass energy is not enough to perform the analysis in a larger number of multiplicity classes: indeed, the average multiplicity of $\sqrt{s} = 5.02$ TeV events is smaller than the one measured in $\sqrt{s} = 13$ TeV events and, consequently, the average strange hadron yields per event are smaller at $\sqrt{s} = 5.02$ TeV. For both samples, the analysis is also performed in the 0-100% multiplicity class for comparison purposes.
High Multiplicity events at $\sqrt{s} = 13$ TeV are selected in the multiplicity range 0-0.1%. By definition, this range includes the 0.1% of the minimum bias events characterised by the highest V0 amplitude. Events in the multiplicity class 0-0.1% are divided into three multiplicity classes: 0-0.1%, 0.01-0.05% and 0.05-0.1%.

4.4 Trigger particle identification

For the purpose of separating K^0_S ($\Xi^{\pm}$) produced in jets from the ones produced out of jets, the trigger particles used in the angular correlation must be the leading particles of the jets. In a jet, the leading particle is the one characterised by the highest p_T and, as such, its energy and direction are strongly correlated to those of the parent parton, which is one of the two high p_T partons that have undergone the initial hard scattering process [154] (see Section 2.4).

In this analysis, a trigger particle is defined as the highest-p_T charged particle in a given event coming from the primary interaction vertex and having $p_T > 3$ GeV/c. The minimum p_T threshold is applied in order to select particles originating from the hadronization of a hard scattering process. The threshold value of 3 GeV/c is chosen as a trade-off between two effects: on one hand, a further increase of the threshold value would allow for the reduction of the contamination from particles not originating from hard scattering processes, on the

other hand it would reduce the number of events containing a trigger particle, limiting the possibility to perform a multiplicity dependent measurement of the in-jet and out-of-jet yields of the $\Xi^{\pm}$, which is approximately fifteen times less abundant than the K^0_S.

The trigger particles are selected starting from all the tracks reconstructed using the TPC and constrained to the primary vertex, and requiring them to pass the following selections:

- Track quality selection: tracks reconstructed with the TPC can consist of a maximum of 159 points, each corresponding to one crossed pad row (see Section 3.2.2). To ensure a good track reconstruction quality, only tracks which cross more than 80 TPC pad rows are selected. Moreover, the track is required to be formed by more than 70 clusters, where a cluster is the signal induced by the passage of the particle in a crossed pad row. Due to detector inefficiencies, the number of clusters can be smaller than the number of crossed pad rows. In addition to that, the ratio of crossed pad rows over findable clusters is required to be greater than 0.8. The number of findable clusters is the total number of clusters which for geometrical reasons should be produced, assuming the TPC has no dead sectors and is fully efficient. This selection is applied in order not to have large gaps in the number of expected tracking points in the radial direction. Finally, the χ^2/ndf of the track fit in the TPC is required to be smaller than 4. The number of degrees of freedom (ndf) of the fitting procedure corresponds to the number of clusters from which the track is built.

- Good p_{T} resolution selection: the p_{T} of the trigger particle is required to be smaller than 15 GeV/c. Tracks which satisfy this selection have a p_{T} resolution better than 2%. Moreover, the radial length of the track is required to be greater than 90 cm, and the ratio between the number of crossed pad rows and the radial track length is required to be greater than 0.8 cm^{-1}. This allows for the rejection of the low resolution tracks which pass through the edges of the TPC sectors.

- Primary particle selection: to select only the charged particles coming from the primary interaction vertex and reject the ones coming from the weak decay of hadrons or the interaction with the material of the detector, a selection on the distance of closest approach (DCA) of the track to the primary vertex is applied both along the z direction ($\mathrm{DCA_z}$) and in the perpendicular plane ($\mathrm{DCA_{xy}}$). The selection applied for this purpose is the following:

$$|\mathrm{DCA_z}| < 0.04 \text{ cm} \ , \ |\mathrm{DCA_{xy}}| < \left(0.0105 + \frac{0.035}{[p_{\mathrm{T}}/(\mathrm{GeV}/c)]^{1.1}}\right) \text{ cm}. \tag{4.2}$$

  The p_{T}-dependent selection applied to the $\mathrm{DCA_{xy}}$ allows to select tracks within 7σ from the position of the interaction vertex on the transverse plane, where σ is the resolution with which the $\mathrm{DCA_{xy}}$ is measured.

- Detector acceptance selection: trigger particles are required to have $|\eta| < 0.8$ in order to use the geometrical region in which the detector can provide full track reconstruction.

- Leading particle selection: in each event only the highest-p_{T} particle with transverse momentum larger than 3 GeV/c is selected.

A schematic list of all the selections applied to identify trigger particles is reported in Table 4.1. If an event contains a trigger particle, the search for K^0_S and Ξ is performed, as described in Section 4.5.

Trigger particle selections	
Number of TPC clusters	> 70
χ^2/ndf	< 4
Number of TPC crossed pad rows	> 80
Number of TPC crossed pad rows over findable clusters	> 0.8
Track length in the TPC	> 90 cm
Number of crossed pad rows over track length in the TPC	> 0.8 cm^{-1}
$\lvert\eta\rvert$	< 0.8
$\lvert\mathrm{DCA_z}\rvert$	< 0.4 cm
$\lvert\mathrm{DCA_{xy}}\rvert$	$< (0.0105 + 0.035/p_{\mathrm{T}}^{1.1})$ cm
p_{T}	> 3 GeV/c

Table 4.1: Selections applied to identify trigger particles. The meaning of the variables is explained in the text.

4.4.1 Trigger particle efficiency

To evaluate the effect of the track quality selections listed above, the efficiency ε with which trigger particles are selected is calculated from the MC as follows:

$$\varepsilon = \frac{\text{N. primary particles (selected)}}{\text{N. primary particles (generated)}} , \tag{4.3}$$

where both the selected and the generated trigger particles are required to have $|\eta| < 0.8$.

The top plot of Figure 4.1 shows ε as a function of p_{T} for the different multiplicity classes in which the minimum bias events at $\sqrt{s} = 13$ TeV are divided. The efficiency is calculated before applying the selection $p_{\mathrm{T}} > 3$ GeV/c. The η and φ dependence of the efficiency is shown in the bottom left and right plots, respectively. These efficiencies are obtained after applying the selection $p_{\mathrm{T}} > 3$ GeV/c.

For $p_{\mathrm{T}} > 3$ GeV/c, the efficiency is independent of p_{T} within 5%. The efficiency is independent of η, while its distribution as a function of φ shows periodic gaps, which are related to the boundaries between TPC sectors. The efficiency for $p_{\mathrm{T}} > 3$ GeV/c is independent of the multiplicity class within 1%. The same features are observed in the high multiplicity sample and in the minimum bias sample of pp collisions at $\sqrt{s} = 5.02$ TeV.

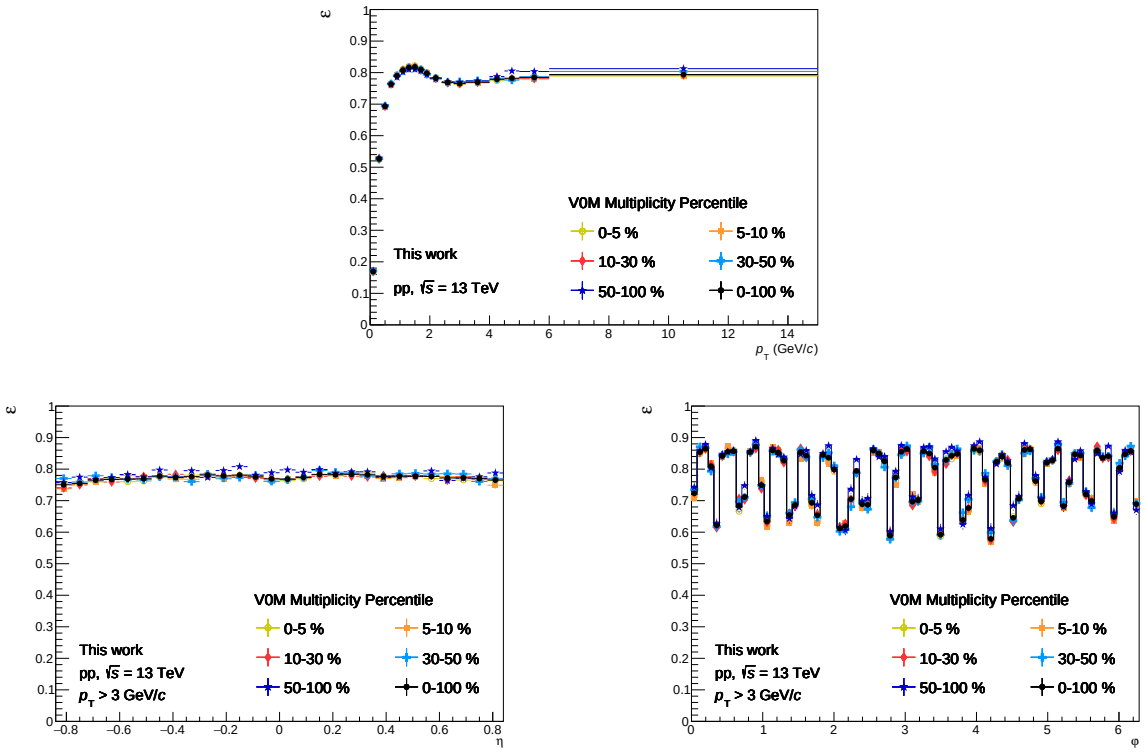

Figure 4.1: Efficiency of trigger particle selection ε as a function of p_{T} (top), η (bottom left) and φ (bottom right) in minimum bias pp collisions at $\sqrt{\mathrm{s}} = 13$ TeV. The efficiencies are calculated as specified in 4.4.1. Different colours refer to different V0M multiplicity classes, as indicated in the legend. Error bars represent statistical uncertainties.

4.4.2 Fraction of non-primary trigger particles

The selections applied to the DCA of the charged tracks to the primary vertex (see equation 4.2) are optimised in order to minimise the fraction of the selected trigger particles which are not primary but come from the weak decay of hadrons or from the interaction with the material of the detector. The ratio between the selected non-primary trigger particles and the totality of selected trigger particles is called *fraction of non-primary trigger particles* ($F_{trigg,NP}$) and is calculated using the MC:

$$F_{trigg,NP} = \frac{\text{N. non-primary selected trigger particles}}{\text{N. selected trigger particles}} \,. \tag{4.4}$$

As can be seen in Figure 4.2, the fraction of non-primary trigger particles is independent of the multiplicity class within statistical uncertainties and lies between 0.5% and 0.6%. No dependence on the centre-of-mass energy is observed.

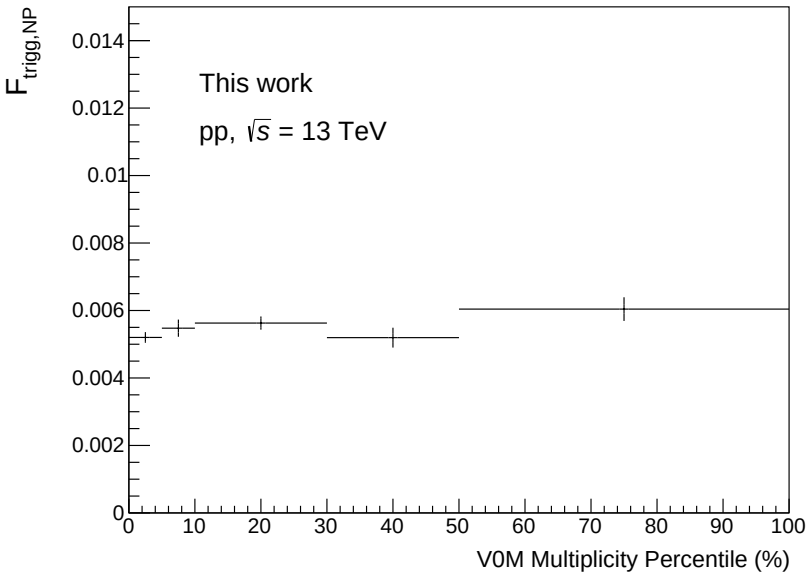

Figure 4.2: Fraction of non-primary trigger particles ($F_{trigg,NP}$) as a function of the V0M percentile classes in which the analysis of minimum bias pp collisions at $\sqrt{s}$ = 13 TeV is performed. $F_{trigg,NP}$ is defined in equation 4.4.

4.4.3 Fraction of events with a trigger particle

The fraction of good-quality events which contain a trigger particle is shown in Figure 4.3 as a function of the average multiplicity of charged particles $\langle dN/d\eta \rangle_{|\eta|<0.5}$ produced in the event. The fraction increases with the multiplicity, since it is more likely to find a high-p_T track in events characterised by a large multiplicity of charged particles. Consequently, as can be observed in Figure 4.4, the V0M multiplicity percentile distribution of events with a trigger particle (right plot) is peaked at large values of multiplicities (i.e., at low V0M percentile values), whereas the distribution of all good-quality events (left plot) has a flat shape, as expected from the definition of V0M percentiles. Figure 4.3 also shows that the fraction of events which contain a trigger particle is slightly larger in pp collisions at $\sqrt{s}$ = 13 TeV than in pp collisions at $\sqrt{s}$ = 5.02 TeV with similar values of charged particle multiplicities. This

is due to the fact that at larger centre-of-mass energy the average p_{T} of tracks is larger, and therefore the probability to find a high-p_{T} track is increased.

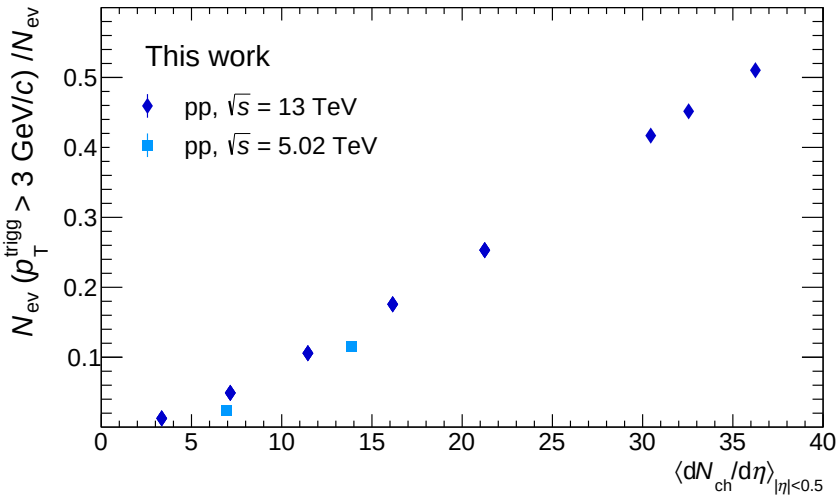

Figure 4.3: Fraction of good-quality events which contain a trigger particle defined as in 4.4 as a function of the average multiplicity of charged particles produced at midrapidity in the event.

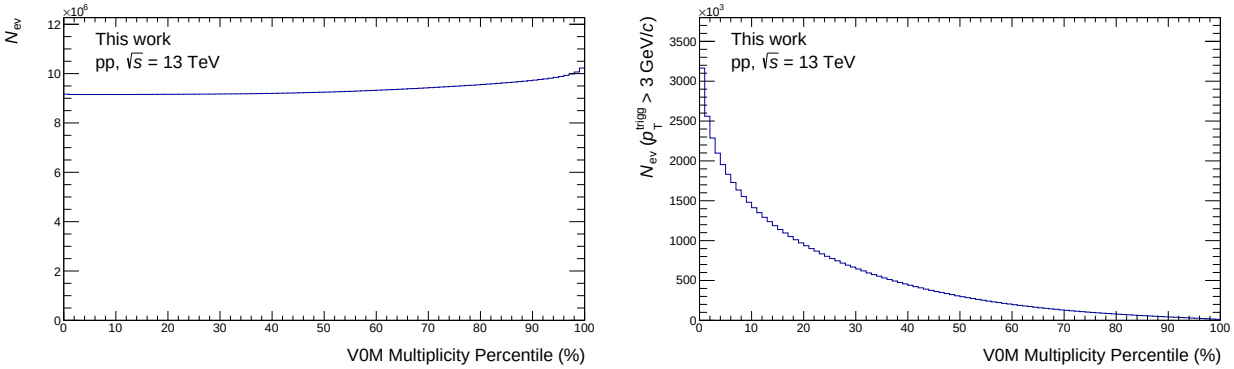

Figure 4.4: (left) Multiplicity percentile distribution of good-quality events satisfying the selections listed in Section 4.3. (right) Multiplicity percentile distribution of events containing a trigger particle defined according to the selections described in Section 4.4.

4.4.4 Computation of the average charged particle multiplicity in events with a trigger particle

For each of the multiplicity classes in which the analysis is performed, the average multiplicity of charged particles produced at midrapidity in events containing a trigger particle $\langle \mathrm{d}N/\mathrm{d}\eta \rangle_{|\eta|<0.5,\ p_{\mathrm{T,trigg}}>3\ \mathrm{GeV}/c}$ is computed by measuring the number of charged particles produced at midrapidity and by correcting it for the efficiency of charged particles, computed with a MC simulation.

The $\langle \mathrm{d}N/\mathrm{d}\eta \rangle_{|\eta|<0.5,\ p_{\mathrm{T,trigg}}>3\ \mathrm{GeV}/c}$ values associated to each of the multiplicity classes in which the analysis is performed are reported in Table 4.2 and Table 4.3 for the analysis of

pp collisions at $\sqrt{s} = 13$ TeV and $\sqrt{s} = 5.02$ TeV, respectively. The error associated to each value represents the systematic uncertainty.

To compute the systematic uncertainty, different sets of selections are applied to tracks and events, and the $\langle dN/d\eta \rangle_{|\eta|<0.5,\ p_{T,trigg}>3\ GeV/c}$ values are recalculated. For example, the selection applied to the z coordinate of the primary vertex PV_z is varied from its default value $|PV_z| < 10$ cm by taking tighter selections within this interval. Another source of systematic uncertainty is associated to the track selections: to evaluate this contribution, systematic variations are applied to the selections on the DCA_{xy} and the DCA_z of the tracks, on the minimum number of crossed pad rows, and on the χ^2/ndf of the track fit in the TPC. In addition to that, the primary and secondary particle composition in the MC is varied: this has an impact on the track finding efficiency, as it is particle dependent. The $\langle dN/d\eta \rangle_{|\eta|<0.5,\ p_{T,trigg}>3\ GeV/c}$ values obtained by varying the above mentioned selections are compared to the default ones, and the maximum difference is assigned as a systematic uncertainty.

pp collisions at $\sqrt{s} = 13$ TeV	
Multiplicity classes	$\langle dN/d\eta \rangle_{\|\eta\|<0.5,\ p_{T,trigg}>3\ GeV/c}$
0-0.01 %	$37.60^{+0.75}_{-1.03}$
0.01-0.05 %	$34.06^{+0.54}_{-0.62}$
0.05-0.1 %	$32.05^{+0.48}_{-0.57}$
0-0.1 %	$33.48^{+0.49}_{-0.58}$
0-5 %	$24.04^{+0.27}_{-0.22}$
5-10 %	$18.93^{+0.23}_{-0.26}$
10-30 %	$14.80^{+0.18}_{-0.21}$
30-50 %	$10.70^{+0.17}_{-0.18}$
50-100 %	$7.40^{+0.17}_{-0.14}$
0-100 %	$15.85^{+0.19}_{-0.2}$

Table 4.2: Average multiplicity of charged particles produced at midrapidity $\langle dN/d\eta \rangle_{|\eta|<0.5,\ p_{T,trigg}>3\ GeV/c}$ in events with a trigger particle for each of the multiplicity classes in which the analysis of pp collisions at $\sqrt{s} = 13$ TeV was performed. The values are reported together with their systematic uncertainties.

pp collisions at $\sqrt{s} = 5.02$ TeV	
Multiplicity classes	$\langle dN/d\eta \rangle_{\|\eta\|<0.5,\ p_{T,trigg}>3\ GeV/c}$
0-10 %	$16.96^{+0.20}_{-0.29}$
10-100 %	$10.23^{+0.14}_{-0.17}$
0-100 %	$12.53^{+0.16}_{-0.21}$

Table 4.3: Average multiplicity of charged particles produced at midrapidity $\langle dN/d\eta \rangle_{|\eta|<0.5,\ p_{T,trigg}>3\ GeV/c}$ in events with a trigger particle for each of the multiplicity classes in which the analysis of pp collisions at $\sqrt{s} = 5.02$ TeV was performed. The values are reported together with their systematic uncertainties.

4.5 K^0_S and $\Xi^{\pm}$ identification

Both K^0_S and $\Xi^{\pm}$ are identified performing an invariant mass analysis after the application of topological and kinematic selections to the variables describing their weak decay into charged hadrons. In particular, K^0_S are identified via the decay into two charged pions ($K^0_S \rightarrow \pi^+\pi^-$), which has a branching ratio B.R. = $(69.20 \pm 0.05)\%$ [155]. $\Xi^{\pm}$ are instead identified via their decay $\Xi^- \rightarrow \pi^-\Lambda(\rightarrow p\pi^-)$ and its charged conjugate. This decay has a branching ratio B.R. = $(99.89 \pm 0.04)\%$ [155] .

A pictorial representation of the K^0_S and $\Xi^{\pm}$ decays is shown in Figure 4.5. Since the two daughter pions of the K^0_S form a V-like shape, the K^0_S is a so-called "V^0 particle". The $\Xi^{\pm}$ is instead a so-called "cascade" particle, because the decay vertex of the daughter (anti-)Λ is displaced with respect to the decay vertex of the $\Xi^{\pm}$ itself. The charged pion coming from the decay of the $\Xi^{\pm}$ is called "bachelor" to distinguish it from the charged pion coming from the displaced decay of the (anti-)Λ.

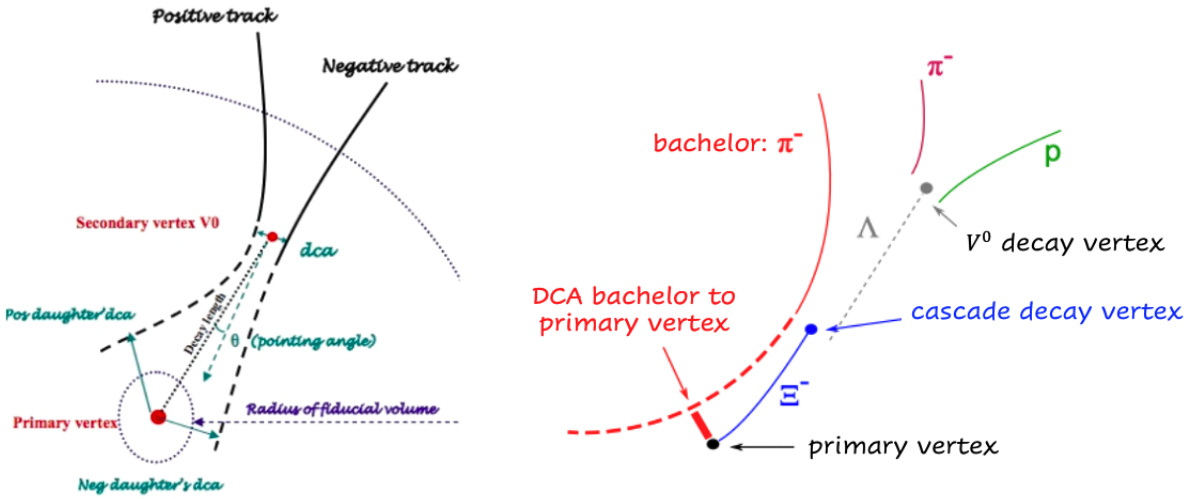

Figure 4.5: Pictorial representation of the decay of a V^0 particle (left) and of a cascade particle (right). The right figure is taken from Ref. [148] and adapted.

V0 decay vertices are reconstructed by the ALICE offline reconstruction algorithms by pairing tracks of particles with opposite charges and satisfying basic topological criteria. For example, it is required that the distance of closest approach (DCA) of the charged tracks should be smaller than a predefined value, in order to reject all particle pairs which do not come from the decay of the same particle but constitute the so-called *combinatorial background*. $\Xi^\pm$ candidates are reconstructed by the ALICE offline reconstruction algorithms by pairing V0 decay vertices to charged pions. Also in this case basic topological criteria are applied. Further topological and kinematic selections are applied to V0 and cascade candidates in order to reduce the combinatorial background and obtain a sample of K^0_S and $\Xi^\pm$ candidates as pure as possible. These selections are described in the following and are listed in Table 4.4 and 4.5 for K^0_S and $\Xi^\pm$, respectively. The term "daughter track" will be used to refer to the charged tracks produced in the decay.

- The daughter tracks are required to satisfy the same track quality criteria applied for the trigger particle selection (number of TPC clusters > 70, $\chi^2/\mathrm{ndf} < 4$, number of crossed pad rows > 80, ratio of crossed pad rows over findable clusters > 0.8, radial track length > 90 cm, ratio of crossed pad rows over track length > 0.8 cm^{-1}).

- The daughter tracks are required not to be associated with a "kink topology", which is characteristic of the decay of charged kaons.

- The daughter tracks are required to be properly identified using the specific ionization energy loss $\mathrm{d}E/\mathrm{d}x$ in the TPC. For example, to identify K^0_S the two daughter tracks of the V^0 are required to be identified as pions. For this purpose, the measured $\mathrm{d}E/\mathrm{d}x$ associated to a daughter track of given momentum is required to be compatible within 3σ with the expected theoretical value. The σ is related to the resolution with which $\mathrm{d}E/\mathrm{d}x$ is measured.

- $|\eta_\pi| < 0.8$: the daughter tracks of K^0_S and $\Xi^\pm$ candidates are selected in the pseudorapidity range where full track reconstruction is provided.

- $|\eta_{V^0}| < 0.8$ and $|\eta_{\Xi^\pm}| < 0.8$: also K^0_S and $\Xi^\pm$ candidates are selected in the same pseudorapidity range.

- To reduce the out-of-bunch pileup background, it is required that at least one daughter track has a hit on the TOF or the SPD. These detectors have a better time resolution than the TPC and allow therefore for the rejection of tracks not related to the collision under consideration, but produced in a collision occurring in a different bunch crossing.

- The distance of closest approach (DCA) of the daughter tracks to the primary vertex is required to be greater than a predefined value (see Tables 4.4 and 4.5), in order to reject particles coming from the primary vertex and not from a secondary decay vertex.

- To select pion pairs coming from the decay of the same K^0_S, the DCA between the V^0 daughter tracks is required to be smaller than 1σ, where the σ is related to the resolution with which the DCA is measured. The same kind of selection is applied to the daughter tracks of the (anti-)Λ produced in the $\Xi^\pm$ decay. In this case, taking into account the different decay topology, the DCA is required to be smaller than 1.5σ.

- To select bachelor-V^0 pairs coming from the decay of the same $\Xi^\pm$, the DCA between the bachelor track and the V^0 daughter is required to be smaller than 0.8 cm.

- To reject V^0 and cascade candidates not coming from the primary vertex, a selection on the cosine of the pointing angle θ_P is applied. θ_P is defined as the angle between the direction of the reconstructed momentum $\vec{p}$ of the V^0 or cascade candidate and the line connecting the primary to the secondary vertex. To identify K^0_S ($\Xi^\pm$) the selection $\cos(\theta_P) > 0.995$ is applied to V^0 (cascade) candidates.

- For $\Xi^\pm$ identification a selection on the cosine of pointing angle of the V^0 daughter of the cascade is also applied. In this case the pointing angle is computed as the angle between the direction of the reconstructed momentum $\vec{p}$ of the V^0 and the line connecting the V^0 decay vertex to the cascade decay vertex. The selection $\cos(\theta_P) > 0.97$ allows for the rejection of V^0 candidates not coming from the decay of a $\Xi^\pm$.

- To identify K^0_S, the DCA of the V^0 to the primary vertex is required to be smaller than 0.5 cm, to further discard V^0 candidates which are not primary. On the contrary, to identify $\Xi^\pm$, the DCA of the V^0 daughter to the primary vertex is required to be greater than 0.06 cm, to reject (anti-)Λ coming from the primary vertex and not from the decay of a $\Xi^\pm$.

- A selection on the decay radius, that is the radial distance of the secondary vertex from the primary one, is applied to V^0 and cascade candidates in order to reject daughter tracks coming from the primary interaction vertex and not from the decay of a V^0 or a cascade.

- A selection on the proper lifetime τ of V^0 and cascade candidates is applied to further reject the background. The proper lifetime is calculated as $\tau = \frac{d \cdot m}{|\vec{p}|}$, where m is the nominal mass of the considered particle, $|\vec{p}|$ is the magnitude of the reconstructed momentum and d is the distance of the secondary vertex from the primary one. V0 (cascade) candidates with $\tau > 7.5\langle\tau\rangle_{K^0_S}$ ($\tau > 3\langle\tau\rangle_{\Xi^\pm}$) are rejected. A tighter selection is applied to the cascade candidates since the background associated to the cascade topology is larger.

- In order to identify K^0_S, a selection to reject the background of (anti-)Λ in the V^0 sample is applied. For this purpose, the invariant mass calculated assuming that one of the daughter tracks is a (anti-)proton is required to differ from the nominal mass value of the (anti-)Λ by more than 5 MeV/c^2. The chosen rejection window depends on the invariant mass resolution of the (anti-)Λ. This background is caused by misidentification of protons.

- Similarly, in order to identify $\Xi^\pm$, a selection to reject the background of $\Omega^\pm$ in the cascade sample is applied. For this purpose, the invariant mass calculated assuming that the bachelor is a charged kaon is required to differ from the nominal mass value of the $\Omega^\pm$ by more than 5 MeV/c^2. The chosen rejection window depends on the invariant mass resolution of the $\Omega^\pm$. This background is caused by misidentification of charged kaons.

- In order to identify $\Xi^\pm$, the invariant mass of the daughter V^0 is required to differ from the nominal mass value of the Λ by less than 6 MeV/c^2.

Once these selections are applied, the K^0_S ($\Xi^\pm$) candidates are divided into nine (seven) intervals according to their transverse momentum p_T, and all the steps described in the following are performed in each p_T interval.

V^0 daughter tracks selections	
Number of TPC clusters	> 70
χ^2/ndf	< 4
Number of TPC crossed pad rows	> 80
Number of TPC crossed pad rows over findable	> 0.8
Track length in the TPC	> 90 cm
Number of crossed pad rows over track length in the TPC	> 0.8
Rejection of kink topology	Yes
$\lvert\eta_\pi\rvert$	< 0.8
$\mathrm{d}E/\mathrm{d}x$ measured in the TPC	$< 3\sigma$
At least one daughter track has a hit in the SPD or in the TOF	Yes
Topological variables selections	
DCA daughter tracks to primary vertex	> 0.06 cm
DCA between daughter tracks	$< 1\sigma$
$\cos(\theta_{\mathrm{P}})$	> 0.995
DCA V^0 to primary vertex	< 0.5 cm
V^0 decay radius	> 0.5 cm
V^0 candidates selections	
$\lvert\eta_{V^0}\rvert$	< 0.8
$\lvert\mathrm{m}_{\pi\mathrm{p}} - \mathrm{m}_\Lambda\rvert$	> 5 MeV/c^2
τ	< 20 cm/c ($\simeq 7.5\langle\tau\rangle$)

Table 4.4: Selections applied to identify K^0_S among the reconstructed V^0 . The meaning of the variables is explained in the text.

Cascade daughter tracks selections	
Number of TPC clusters	> 70
χ^2/ndf	< 4
Number of TPC crossed pad rows	> 80
Number of TPC crossed over findable pad rows	> 0.8
Track length in the TPC	> 90 cm
Number of crossed pad rows over track length in the TPC	> 0.8
Rejection of kink topology	Yes
$\lvert\eta_\pi\rvert$, $\lvert\eta_\mathrm{p}\rvert$	< 0.8
$\mathrm{d}E/\mathrm{d}x$ measured in the TPC	$< 4\sigma$
At least one daughter track has a hit in the SPD or in the TOF	Yes
Topological variables selections	
DCA meson daughter to primary vertex	> 0.04 cm
DCA baryon daughter to primary vertex	> 0.03 cm
DCA bachelor to primary vertex	> 0.04 cm
DCA between daughter tracks of the V^0	$< 1.5\sigma$
$\cos(\theta_\mathrm{P})$ (of cascade to primary vertex)	> 0.995
$\cos(\theta_\mathrm{P})$ (of V^0 to cascade decay vertex)	> 0.97
DCA between bachelor and V^0	< 0.8 cm
DCA V^0 to primary vertex	> 0.06 cm
V^0 decay radius	> 1.1 cm
Cascade decay radius	> 0.5 cm
Cascade candidates selections	
$\lvert\eta_{\Xi^{\pm}}\rvert$	< 0.8
$\lvert\mathrm{m}_{\pi\mathrm{p}} - \mathrm{m}_\Lambda\rvert$	< 6 MeV/c^2
$\lvert\mathrm{m}_{\mathrm{K}\Lambda} - \mathrm{m}_\Omega\rvert$	> 5 MeV/c^2
τ	< 14.73 cm/c $(= 3\langle\tau\rangle)$

Table 4.5: Selections applied to identify $\Xi^{\pm}$ among the reconstructed cascades. The meaning of the variables is explained in the text.

For K^0_S, the nine p_T intervals range from 0.1 GeV/c to 8 GeV/c as follows:

$$p_T^{K^0_s} \text{ intervals : } [0.1 - 0.5), [0.5 - 0.8), [0.8 - 1.2), [1.2 - 1.6), [1.6 - 2.0), [2.0 - 2.5), [2.5 - 3.0), [3.0 - 4.0), [4.0 - 8.0) \text{ GeV}/c$$

For $\Xi^{\pm}$, the following seven p_T intervals ranging from 0.5 GeV/c to 8 GeV/c are used:

$$p_T^{\Xi^{\pm}} \text{ intervals : } [0.5 - 1.0), [1.0 - 1.5), [1.5 - 2.0), [2.0 - 2.5), [2.5 - 3.0), [3.0 - 4.0), [4.0 - 8.0) \text{ GeV}/c$$

The identification of K^0_S ($\Xi^{\pm}$) cannot be performed for $p_T < 0.1(0.5)$ GeV/c, since in this interval the reconstruction efficiency is approximately zero.

The invariant mass distributions of K^0_S and $\Xi^{\pm}$ candidates in the different p_T intervals are fitted with the sum of two Gaussian functions, used to describe the signal, and a first degree polynomial, used to describe the background. The Gaussian functions are used to describe the resolution of the detector: since it receives contributions from different sources, it is better modelled by two Gaussian functions rather than one.

The polynomial fit is first performed in a region which excludes the signal peak ($0.46 < m_{\pi^+\pi^-} < 0.474$ GeV/c^2 and $0.52 < m_{\pi^+\pi^-} < 0.54$ GeV/c^2 for K^0_S, $1.3 < m_{\pi^+\pi^-} < 1.31$ GeV/c^2 and $1.334 < m_{\pi^+\pi^-} < 1.342$ GeV/c^2 for $\Xi^{\pm}$), while the fit with the two Gaussian functions is first performed in the invariant mass range which approximately corresponds to the peak region ($[0.47 - 0.53]$ GeV/c^2 and $[1.31 - 1.334]$ GeV/c^2 for K^0_S and $\Xi^{\pm}$, respectively). The parameters obtained in this way are used as input parameters for the total fit, which is performed in the $[0.46-0.54]$ GeV/c^2 invariant mass range for K^0_S, and in the $[1.3-1.342]$ GeV/c^2 for $\Xi^{\pm}$.

Figure 4.6 shows two examples of invariant mass distributions of K^0_S candidates (left plot) and $\Xi^{\pm}$ candidates (right plot) produced in pp collisions at $\sqrt{s} = 13$ TeV in the multiplicity class 0-100%. The total fit function is shown in dark blue, the two Gaussian functions in light blue and magenta, and the first degree polynomial in dark green. The sum of the Gaussian functions and of the polynomial gives the total fit function.

The average value μ of the mean values of the two Gaussian functions used to describe the signal peak of the invariant mass distribution of K^0_S candidates produced in minimum bias pp collisions at $\sqrt{s} = 13$ TeV is displayed in the top left plot of Figure 4.7 as a function of the transverse momentum p_T of the K^0_S candidates. The different colours refer to different multiplicity intervals, as described in the legend. The horizontal line shows the nominal value of the K^0_S mass ($m = 497.611$ MeV/c^2) [155]. The measured μ values differ from the nominal value by up to 1 MeV/c^2 and increase with p_T, reaching a saturation value for $p_T \gtrsim 1.5$ GeV/c. This behaviour is related to the procedure with which daughter particles are tracked.

The average width σ_G of the two Gaussian functions is shown in the top right plot: it represents the K^0_S invariant mass resolution and it depends on the p_T-resolution of the K^0_S daughter tracks. σ_G increases with the p_T of the K^0_S, as a consequence of the worsening of the p_T resolution of daughter tracks at large p_T values. Both μ and σ_G do not show any significant dependence on the multiplicity class.

The purity of the sample of selected K^0_S is displayed in the bottom panel of Figure 4.7 as a function of p_T for all the multiplicity classes. Purity is defined as the ratio between

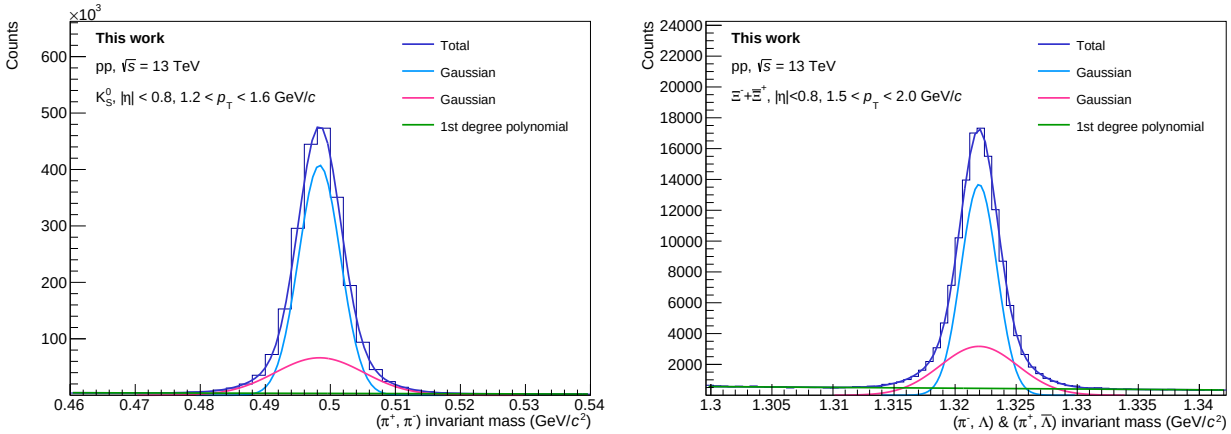

Figure 4.6: Examples of invariant mass distributions of K^0_S candidates (left) and $\Xi^{\pm}$ candidates (right) produced in pp collisions at $\sqrt{s} = 13$ TeV in the multiplicity class 0-100%. The invariant mass distribution is obtained after the application of all the selections listed in Tables 4.4 and 4.5. The global fit function is displayed in dark blue, the two Gaussian functions in light blue and magenta, and the first degree polynomial in dark green.

the amount of signal (S) and the sum of signal and background (S+B) in the invariant mass interval $\mu - 4\sigma_G < m_{\pi^+\pi^-} < \mu + 4\sigma_G$:

$$\text{Purity}_{K^0_S} = \frac{\text{S} \quad (\mu - 4\sigma_\text{G} < \text{m}_{\pi^+\pi^-} < \mu + 4\sigma_\text{G})}{\text{S} + \text{B} \ (\mu - 4\sigma_\text{G} < \text{m}_{\pi^+\pi^-} < \mu + 4\sigma_\text{G})} \ , \tag{4.5}$$

where S+B is obtained from the sum of the bin contents of the invariant mass distribution, and S is given by the difference between S+B and the integral of the background function.

Overall, the purity is larger than 0.95. It shows a decrease with p_T in the range $[0.1 - 2.0]$ GeV/c, whereas at larger p_T values it shows a slight increase with p_T. The purity decreases with the multiplicity because the combinatorial background is larger in events characterised by a larger multiplicity of charged particles. The variation across multiplicity classes is however smaller than 1%.

The average mean value μ, the average width σ_G and the purity show the same behaviour also for K^0_S candidates selected in pp collisions at $\sqrt{s} = 5.02$ TeV and in high multiplicity pp collisions at $\sqrt{s} = 13$ TeV. The purity of the K^0_S sample in high multiplicity pp collisions at $\sqrt{s} = 13$ TeV is smaller than the one observed in minimum bias collisions, as expected from the multiplicity trend observed in the bottom plot of Figure 4.7. The minimum value is observed in the highest p_T interval and is approximately 0.93.

The same plots for $\Xi^{\pm}$ candidates are shown in Figure 4.8. The purity of the $\Xi^{\pm}$ sample is defined in the same way as the K^0_S one:

$$\text{Purity}_{\Xi^{\pm}} = \frac{\text{S} \quad (\mu - 4\sigma_\text{G} < \text{m}_{(\pi^-\Lambda)\&(\pi^+\overline{\Lambda})} < \mu + 4\sigma_\text{G})}{\text{S} + \text{B} \ (\mu - 4\sigma_\text{G} < \text{m}_{(\pi^-\Lambda)\&(\pi^+\overline{\Lambda})} < \mu + 4\sigma_\text{G})} \ , \tag{4.6}$$

The μ and σ_G values and the purity of $\Xi^{\pm}$ show very similar features to the K^0_S ones. The main difference is observed in the purity, which is smaller than the K^0_S one in all p_T intervals, as a consequence of the larger combinatorial background associated to the cascade topology. The p_T dependence and the multiplicity dependence of the purity are similar to what observed for K^0_S. Another difference is observed in the invariant mass resolution, which is approximately 50% smaller than the K^0_S one.

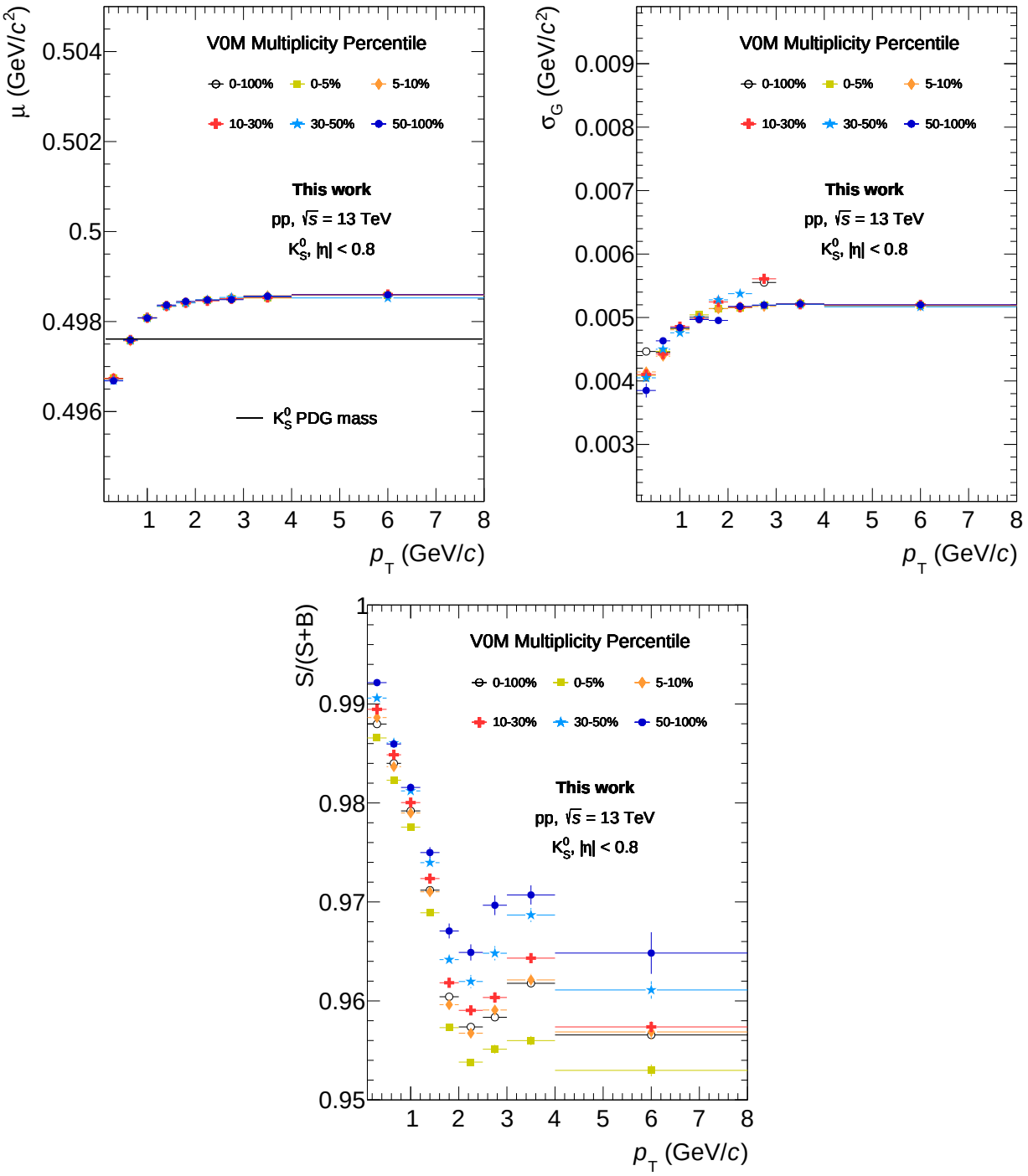

Figure 4.7: (upper panel) Average mean value μ (left) and average width σ_G (right) of the two Gaussian functions used to fit the signal peak in the invariant mass distribution of K^0_S candidates produced in pp collisions at $\sqrt{s} = 13$ TeV. In the top left plot the K^0_S nominal mass [155] is shown with a black line. (bottom panel) Purity of the sample of selected K^0_S in the invariant mass interval $\mu - 4\sigma_G < m_{\pi^+\pi^-} < \mu + 4\sigma_G$. Purity is defined as in equation 4.5. μ, σ_G and the purity are shown as a function of p_T for different multiplicity classes, as described in the legend. Statistical uncertainties are shown by error bars.

The same behaviour of μ, σ_G and the purity is observed also for $\Xi^{\pm}$ candidates selected in pp collisions at $\sqrt{s} = 5.02$ TeV and in high multiplicity pp collisions at $\sqrt{s} = 13$ TeV. As observed also for K^0_S, the purity of the $\Xi^{\pm}$ sample in high multiplicity pp collisions at $\sqrt{s} = 13$ TeV is smaller than the one observed in minimum bias collisions, and reaches the minimum of 0.87 for $p_T \simeq 2$ GeV/c.

Only K^0_S and $\Xi^{\pm}$candidates in an invariant mass interval of 4σ around the μ values are used to build the angular correlation distributions.

4.5.1 K^0_S selection efficiency

The efficiency $\varepsilon_{K^0_S}$ with which K^0_S particles are reconstructed and selected is calculated using the MC and is defined as:

$$\varepsilon_{K^0_S} = \text{reconstruction efficiency} \times \text{acceptance} \times \text{B.R.} = \frac{\text{N. primary } K^0_S \text{ (selected)}}{\text{N. primary } K^0_S \text{ (generated)}} , \quad (4.7)$$

where both the selected and generated K^0_S are required to have $|\eta| < 0.8$ and to be true K^0_S . The selections include all the requirements listed in Table 4.4.

The left panel of Figure 4.9 shows $\varepsilon_{K^0_S}$ as a function of p_T for K^0_S selected in minimum bias pp collisions at $\sqrt{s} = 13$ TeV. Different colours refer to the different multiplicity classes. The ratios of the efficiencies measured in the different multiplicity classes to the one measured in the 0-100% multiplicity class are shown in the right panel. The efficiency decreases with the multiplicity: going from the highest to the lowest multiplicity class, the decrease is about 10%, regardless of the p_T interval. The efficiency integrated in p_T is shown in Figure 4.10 as a function of η (left) and φ (right). While $\varepsilon_{K^0_S}$ is almost flat in φ, it decreases with increasing η, as a consequence of the request that both the daughter pions should have $|\eta| < 0.8$. The dependence of the efficiency on both p_T and η is shown in Figure 4.11 for the multiplicity class 0-100%.

The efficiency of K^0_S shows the same behaviour also in pp collisions at $\sqrt{s} = 5.02$ TeV and in high multiplicity pp collisions at $\sqrt{s} = 13$ TeV. In the latter data sample the efficiency is smaller than in the minimum bias one, as expected from the multiplicity dependence displayed in Figure 4.9.

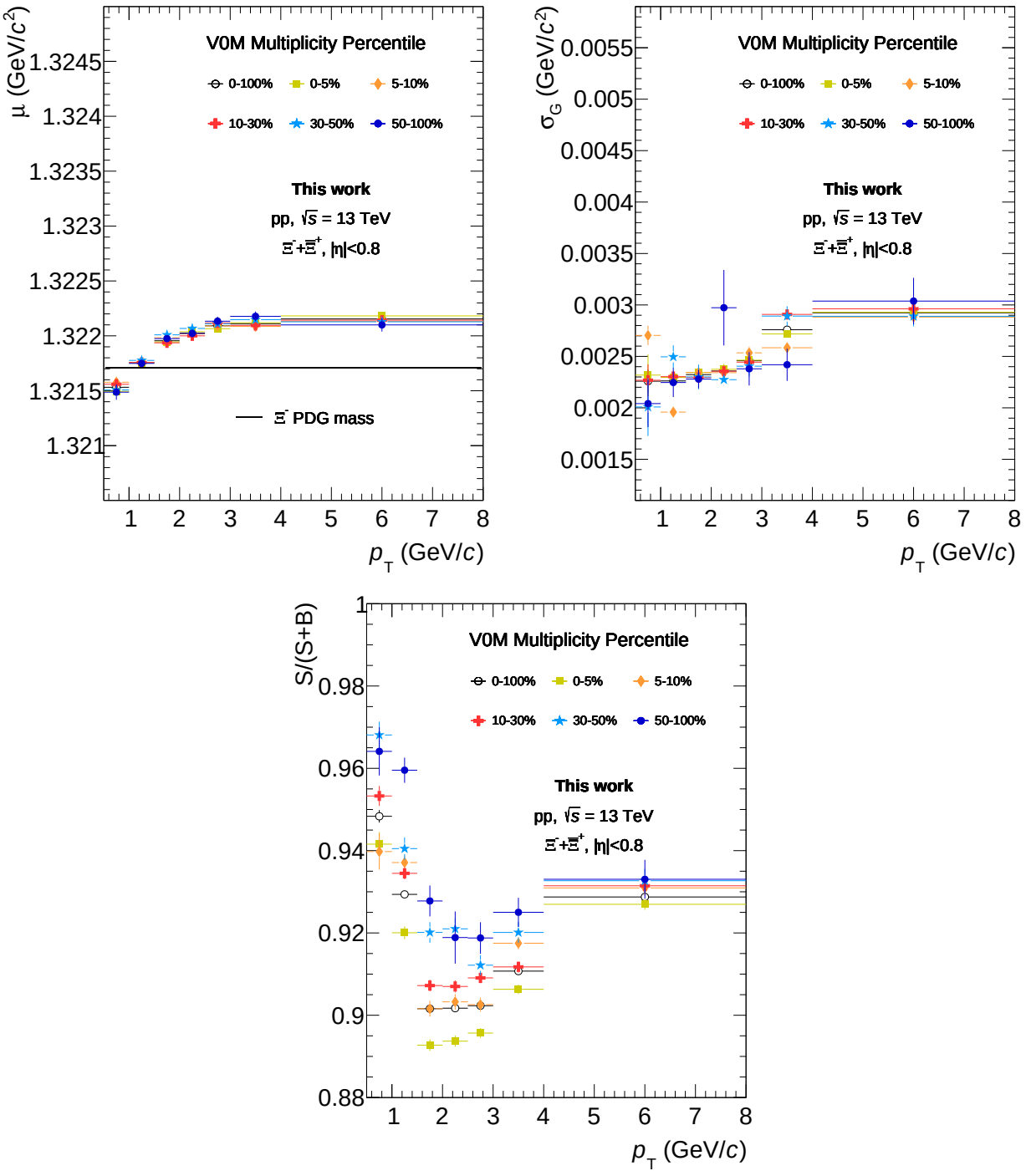

Figure 4.8: (upper panel) Average mean value μ (left) and average width σ_G (right) of the two Gaussian functions used to fit the signal peak in the invariant mass distribution of $\Xi^{\pm}$ candidates produced in pp collisions at $\sqrt{s} = 13$ TeV. In the top left plot the $\Xi^{\pm}$ nominal mass [155] is shown with a black line. (bottom panel) Purity of the sample of selected $\Xi^{\pm}$ in the invariant mass interval $\mu - 4\sigma_G < m_{\pi^+\pi^-} < \mu + 4\sigma_G$. Purity is defined as in equation 4.6. μ, σ_G and the purity are shown as a function of p_{T} for different multiplicity classes, as described in the legend. Statistical uncertainties are shown by error bars.

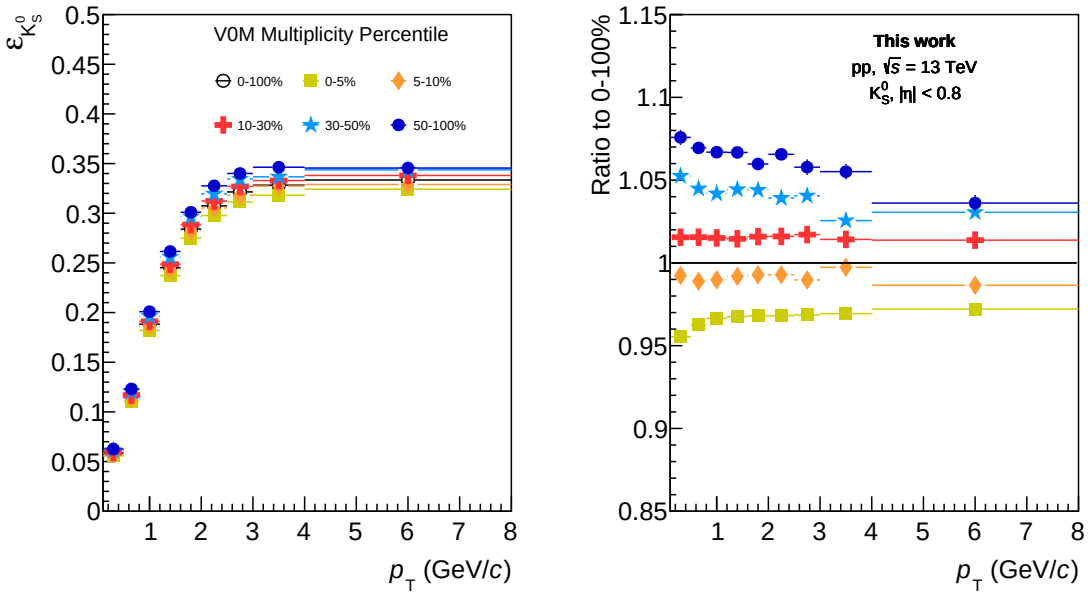

Figure 4.9: (left) Efficiency of K^0_S as a function of p_T in minimum bias pp collisions at $\sqrt{s}$ = 13 TeV. Different colours refer to different multiplicity classes, as indicated in the legend. (right) Ratio to the efficiency in the 0-100% multiplicity class.

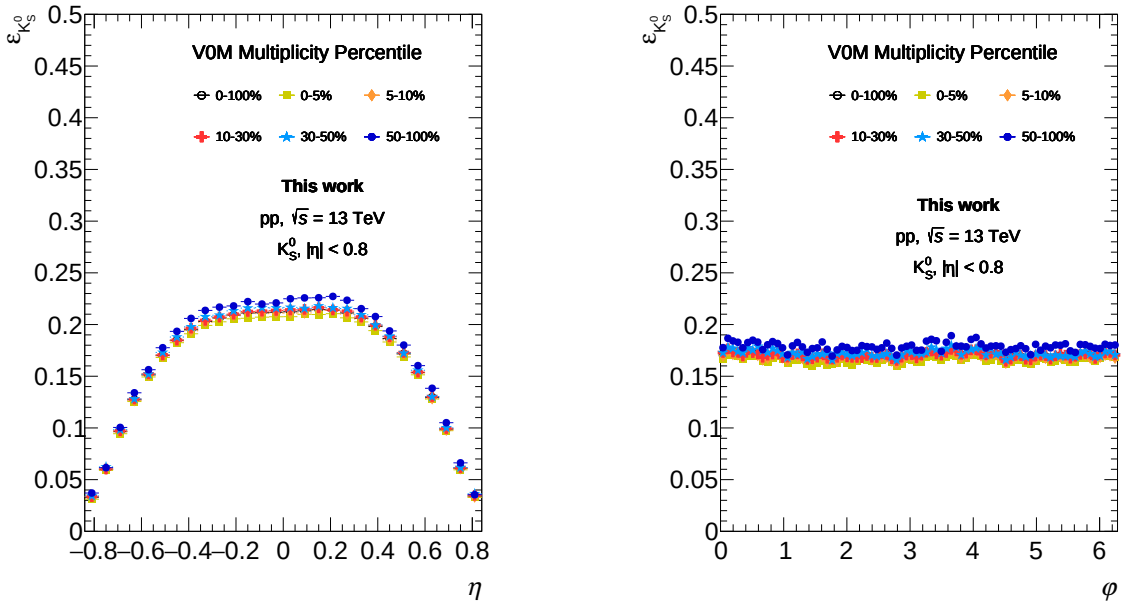

Figure 4.10: Efficiency of K^0_S as a function of η (left) and φ (right) in minimum bias pp collisions at $\sqrt{s} = 13$ TeV. Different colours refer to different multiplicity classes, as indicated in the legend.

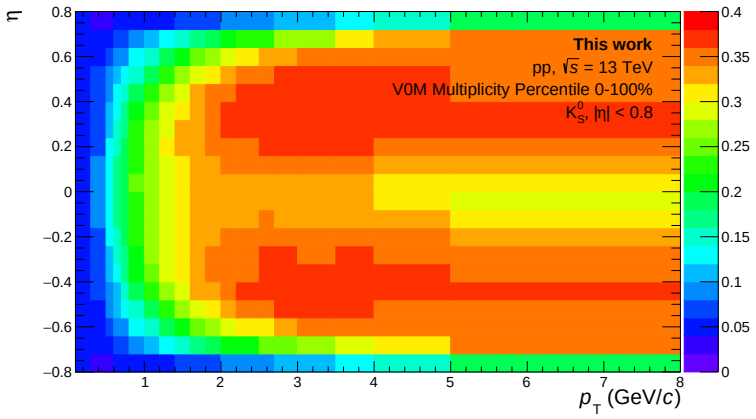

Figure 4.11: Efficiency of K^0_S as a function of η and p_T in minimum bias pp collisions at $\sqrt{s} = 13$ TeV.

4.5.2 $\Xi^{\pm}$ selection efficiency

The efficiency ε_{Ξ} with which $\Xi^{\pm}$ particles are reconstructed and selected is defined in the same way as K^0_S one:

$$\varepsilon_{\Xi} = \text{reconstruction efficiency} \times \text{acceptance} \times \text{B.R.} = \frac{\text{N. primary } \Xi^{\pm} \text{ (selected)}}{\text{N. primary } \Xi^{\pm} \text{ (generated)}} \,. \quad (4.8)$$

Figure 4.12 shows ε_{Ξ} as a function of p_T for $\Xi^{\pm}$ selected in minimum bias pp collisions at $\sqrt{s} = 13$ TeV. Different colours refer to the different multiplicity classes. Values of ε_{Ξ} are compatible within the statistical uncertainty across multiplicity classes.

The efficiency integrated in p_T is shown in Figure 4.13 as a function of η (left) and φ (right). As observed for K^0_S, ε_{Ξ} is almost flat in φ and it decreases with increasing η, as a consequence of the request that daughter tracks should have $|\eta| < 0.8$. The dependence of the efficiency on both p_T and η is shown in Figure 4.14 for the multiplicity class 0-100%.

The efficiency of $\Xi^{\pm}$ shows the same behaviour also in pp collisions at $\sqrt{s} = 5.02$ TeV and in high multiplicity pp collisions at $\sqrt{s} = 13$ TeV.

The dependence of the efficiency on both p_T and η is shown in Figure 4.14 for all the multiplicity classes considered.

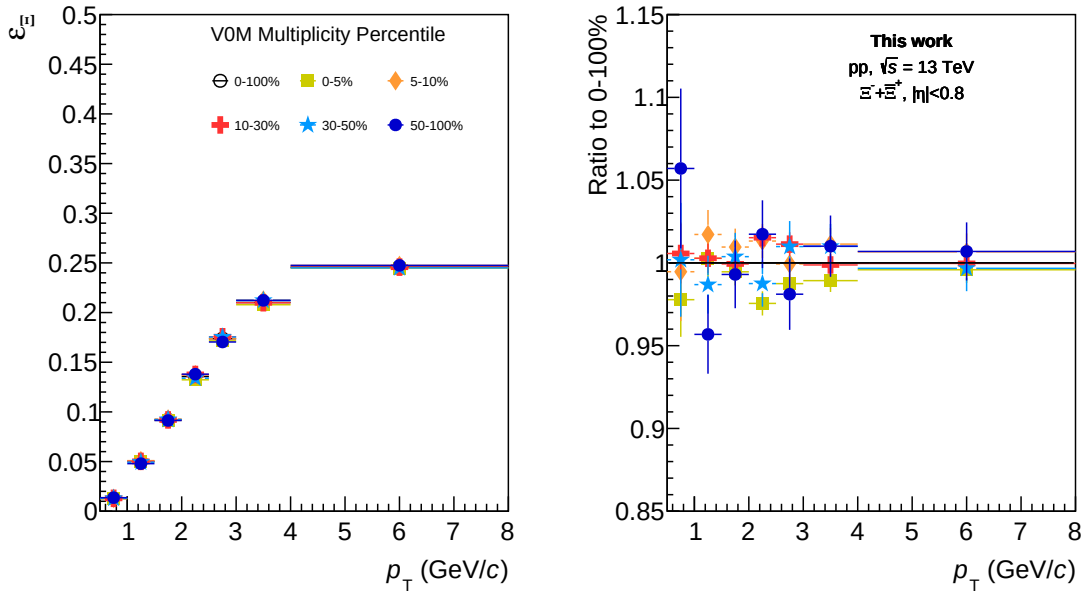

Figure 4.12: (left) Efficiency of $\Xi^{\pm}$ as a function of p_{T} in minimum bias pp collisions at $\sqrt{s}$ = 13 TeV. Different colours refer to different multiplicity classes, as indicated in the legend. (right) Ratio to the efficiency in the 0-100% multiplicity class.

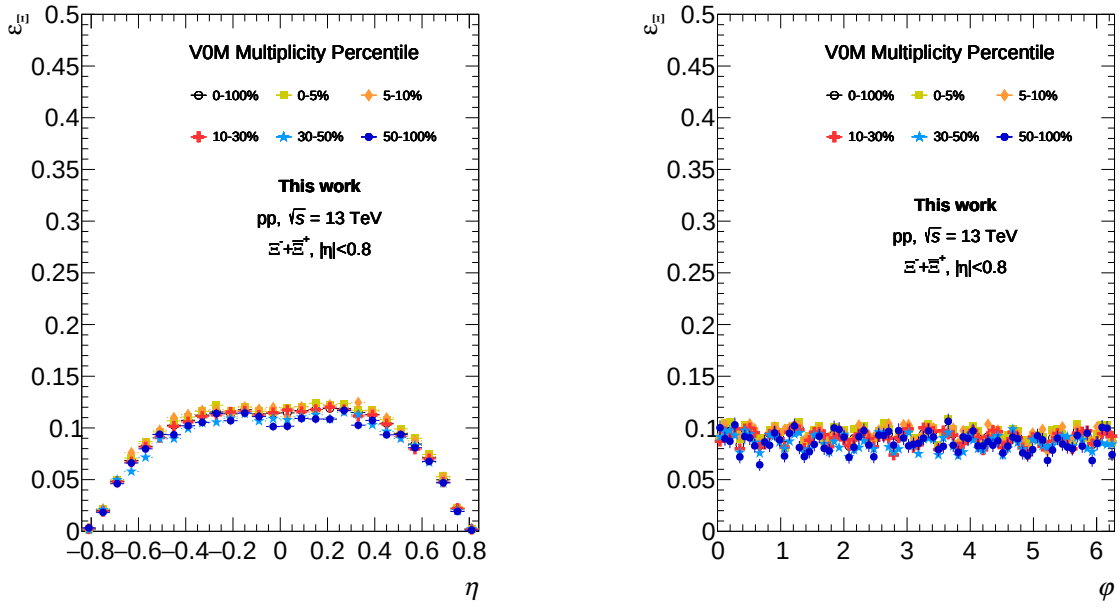

Figure 4.13: Efficiency of $\Xi^{\pm}$ as a function of η (left) and φ (right) in minimum bias pp collisions at $\sqrt{s} = 13$ TeV. Different colours refer to different multiplicity classes, as indicated in the legend.

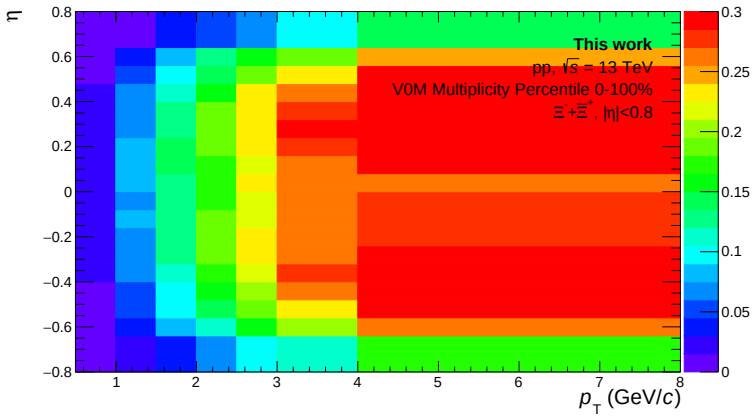

Figure 4.14: Efficiency of $\Xi^{\pm}$ as a function of η and p_{T} in minimum bias pp collisions at $\sqrt{s} = 13$ TeV.

4.5.3 Fraction of non-primary K^0_S and $\Xi^{\pm}$

A very small fraction of the selected K^0_S and $\Xi^{\pm}$ are not primary but come from the weak decay of hadrons or from the interaction with the material of the detector. The ratio between the selected non-primary K^0_S ($\Xi^{\pm}$) and the totality of selected K^0_S ($\Xi^{\pm}$) is calculated using the MC and is shown in the left (right) plot of Figure 4.15 as a function of p_{T}.

The fraction of non-primary K^0_S is smaller than 0.06% and is only due to the interaction of particles with the material of the detector. The fraction of non-primary $\Xi^{\pm}$ is approximately one order of magnitude larger, and only the 40% of it is related to the interaction with the material for the detector. For both K^0_S and $\Xi^{\pm}$, there is no dependence on the multiplicity class. Similar results are obtained for K^0_S and $\Xi^{\pm}$ selected in high multiplicity pp collisions at $\sqrt{s} = 13$ TeV and in pp collisions at $\sqrt{s} = 5.02$ TeV.

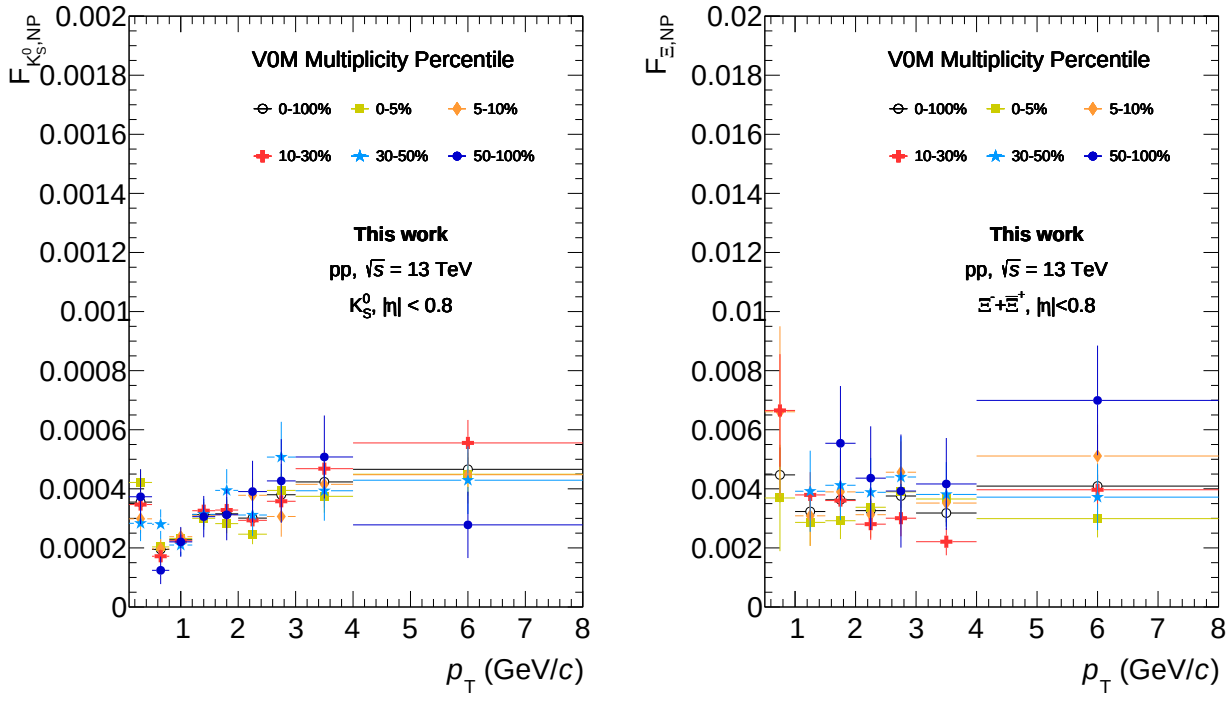

Figure 4.15: Fraction of non-primary K^0_S (left) and $\Xi^{\pm}$ (right) as a function of p_T in minimum bias pp collisions at $\sqrt{s} = 13$ TeV. Different colours refer to different multiplicity classes, as indicated in the legend.

4.6 Angular correlation distributions

4.6.1 Angular correlation distributions and efficiency corrections

As already introduced at the beginning of this chapter, the angular correlation distributions of the trigger and associated particle pairs are defined as a function of the two variables $\Delta\eta$ and $\Delta\varphi$:

$$\Delta\eta = \eta_{trigg} - \eta_{assoc} \ , \ \Delta\varphi = \varphi_{trigg} - \varphi_{assoc} \ , \tag{4.9}$$

where φ is the azimuthal angle of the particles and η is their pseudorapidity, defined as $\eta = -\ln(\tan(\theta/2))$, with θ denoting the polar angle. Azimuthal and polar angles are defined according to the convention in the reference frame whose z axis lies along the beam axis.
The angular correlation distributions are obtained in different p_{T} intervals of the associated particle, as introduced in 4.1. In the following, the procedure will be described for trigger particle-$\mathrm{K}^0_{\mathrm{S}}$ (h-$\mathrm{K}^0_{\mathrm{S}}$) correlations, but the same procedure was applied for h-$\Xi^{\pm}$ correlations as well.

Each $(\Delta\eta, \Delta\varphi)$ interval of the angular correlation distribution is filled with $N^{\mathrm{SE}}_{\mathrm{assoc}}(\Delta\eta, \Delta\varphi)$, where "SE" stands for "Same Event", to underline the fact that both the trigger particle and the associated particles are produced in the same collision:

$$N^{\mathrm{SE}}_{\mathrm{assoc}}(\Delta\eta, \Delta\varphi) = \sum_{i=1}^{N_{\mathrm{K}^0_{\mathrm{S}}}(\Delta\eta,\Delta\varphi)} \frac{1}{\epsilon_i(p_{\mathrm{T}}, \eta)}. \tag{4.10}$$

In the formula, $N_{\mathrm{K}^0_{\mathrm{S}}}(\Delta\eta, \Delta\varphi)$ is the number of selected $\mathrm{K}^0_{\mathrm{S}}$ candidates characterised by an angular distance from the trigger particle in the interval $(\Delta\eta, \Delta\varphi)$, and $\epsilon(p_{\mathrm{T}}, \eta)$ is the $\mathrm{K}^0_{\mathrm{S}}$ efficiency computed as a function of both p_{T} and η (see Figure 4.11). It is important to take into account the η dependence of the associated particle efficiency since it affects the shape of the angular correlation distribution. Only $\mathrm{K}^0_{\mathrm{S}}$ candidates with invariant mass within $4\sigma_{\mathrm{G}}$ from the mean value of the Gaussian fit function (see Section 4.5) are used to build the angular correlation distributions.

An example of angular correlation distribution of h-$\mathrm{K}^0_{\mathrm{S}}$ pairs produced in pp collisions at $\sqrt{\mathrm{s}} = 13$ TeV is shown in the left panel of Figure 4.16. The distribution shows a peak centred at $(\Delta\eta, \Delta\varphi) = (0, 0)$ which is associated to $\mathrm{K}^0_{\mathrm{S}}$ produced in the leading jet (*toward-leading* or *near-side jet* production). The distribution also shows a substructure of triangular shape in $\Delta\eta$ which is related to the geometrical acceptance of the trigger-associated particle pairs. Indeed, due to the the finite size of the detector, h-$\mathrm{K}^0_{\mathrm{S}}$ pairs with a small separation in $\Delta\eta$ are more likely to be found than those with a larger $\Delta\eta$ separation. The SE distributions have to be corrected for this effect, as described in the next section.

4.6.2 Pair acceptance correction

The acceptance of the trigger-associated particle pairs (pair acceptance) is calculated from the mixed event (ME) angular correlation distribution: it consists in the correlation between the trigger particles found in one event and the associated particles found in n different events. The ME angular correlation is therefore not related to the underlying physics but only to geometrical effects.

The number of events with which the mixing is performed is $n \simeq 5$, and these events are required to have the same characteristics, namely to lie in the same multiplicity class and to

have the z-coordinate of the primary vertex in the same interval (ten intervals of same width are defined in the [-10,10] cm range). In addition to that, all events with which the mixing is performed are required to contain a trigger particle.

Also the ME angular correlation distributions are corrected for the K^0_S efficiency computed as a function of both p_T and η. For each ($\Delta\eta$, $\Delta\varphi$) interval, the ME angular correlation distribution is therefore filled with:

$$N^{ME}_{assoc}(\Delta\eta, \Delta\varphi) = \sum_{i=1}^{N^{ME}_{K^0_S}(\Delta\eta,\Delta\varphi)} \frac{1}{\epsilon_i(p_T, \eta)}. \tag{4.11}$$

Like for the SE distributions, only K^0_S candidates with invariant mass within 4σ from the mean value of the Gaussian fit function are taken into account.

As can be observed in the central plot of Figure 4.16, the ME angular distribution has a triangular shape: no dependence on $\Delta\varphi$ is observed, as a consequence of the cylindrical symmetry of the detector, but the distribution depends on $|\Delta\eta|$, reaching a maximum for $|\Delta\eta| \simeq 0$. Assuming that all pairs at $|\Delta\eta| \simeq 0$ are accepted, the distribution is divided by the average value $\langle N^{ME}_{\Delta\eta=0}\rangle$ at $\Delta\eta = 0$ in order to obtain the pair acceptance ε_{pair}:

$$\varepsilon_{pair}(\Delta\eta, \Delta\varphi) = \frac{d^2N^{ME}_{assoc}}{d\Delta\eta d\Delta\varphi}(\Delta\eta, \Delta\varphi) \times \frac{1}{\langle N^{ME}_{\Delta\eta=0}\rangle}. \tag{4.12}$$

It should be noted that, given the applied normalisation, the K^0_S efficiency correction has the only effect of changing the shape of the ME distribution along the $\Delta\eta$ axis.

The SE angular correlation distributions are divided by the pair acceptance in order to retain only the physical correlations between trigger and associated particles:

$$\frac{d^2N_{assoc}}{d\Delta\eta d\Delta\varphi}(\Delta\eta, \Delta\varphi) = \frac{d^2N^{SE}_{assoc}}{d\Delta\eta d\Delta\varphi}(\Delta\eta, \Delta\varphi) \times \frac{1}{\varepsilon_{pair}}. \tag{4.13}$$

The right plot of Figure 4.16 shows the distribution obtained by dividing the SE distribution shown in the left panel by the pair acceptance shown in the central panel.

To check if the normalised ME distributions are able to properly correct for the acceptance of trigger-associated pairs, the corrected angular correlation distributions are projected along the $\Delta\eta$ axis in the interval $\pi/2 < \Delta\varphi < 3/2\pi$, where the contribution of the near-side jet peak is negligible. These projections are expected to be flat in $\Delta\eta$. However, a residual $\Delta\eta$ dependence is observed for h-K^0_S correlation in the region $|\Delta\eta| \gtrsim 1$, where the projections show an increase of about 5%, as shown by the violet plot in Figure 4.17. To remove the remaining $\Delta\eta$ dependence, a correction factor is applied to the pair acceptance. The correction factor is computed starting from the projections along the $\Delta\eta$ axis of the SE distributions in the interval $\pi/2 < \Delta\varphi < 3\pi/2$. These projections are divided by the $\Delta\eta$ projections of the ME distributions obtained in the 0-100% multiplicity class. Before performing the division, both projections are scaled in order to be equal to one in the interval centred at $\Delta\eta = 0$. The ratios, which differ from one up to 5% at large $\Delta\eta$ values, are applied as correction factors to the pair acceptance obtained in the 0-100% multiplicity class, which is then used as pair acceptance in all multiplicity classes, allowing for the reduction of the statistical uncertainties. It should be noted that the correction factors depend on the multiplicity class. An example of corrected angular correlation distribution projected along the $\Delta\eta$ axis in the interval $\pi/2 < \Delta\varphi < 3/2\pi$ is shown in Figure 4.17.

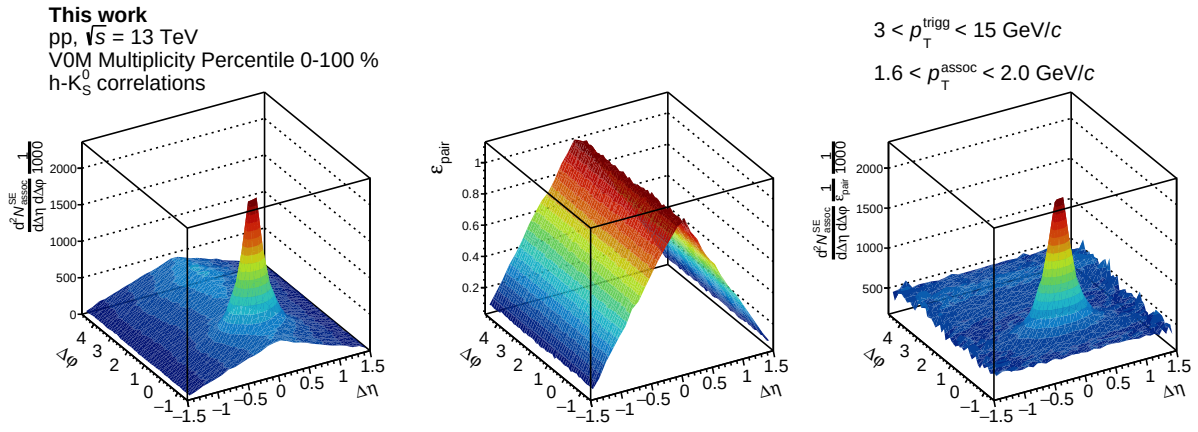

Figure 4.16: (left) Example of angular correlation distribution between trigger and K^0_S found in the same collision. (centre) Acceptance of trigger-K^0_S pairs. (right) Angular correlation distribution divided by the pair acceptance.

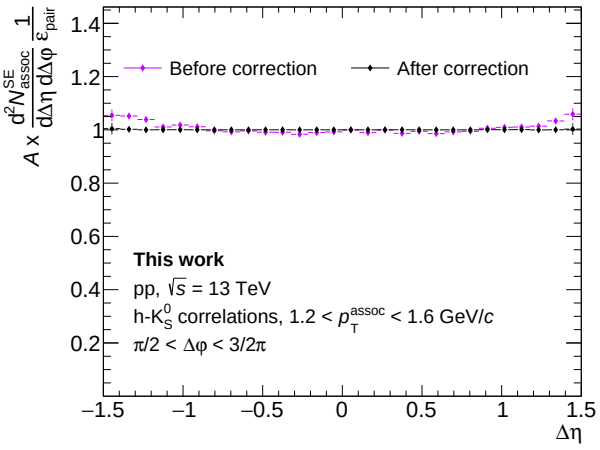

Figure 4.17: Example of angular correlation distribution projected along the $\Delta\eta$ axis in the interval $\pi/2 < \Delta\varphi < 3/2\pi$ before (violet markers) and after (black markers) applying the correction procedure described in the text. The distributions are arbitrarily normalised.

There is no need to apply this correction to h-$\Xi^{\pm}$ ME distributions, since the $\Delta\eta$ projections of the h-$\Xi^{\pm}$ corrected angular correlation distributions in the $\Delta\varphi$ interval $\pi/2 < \Delta\phi < 3/2\pi$ do not show any $\Delta\eta$ dependence. Since the h-$\Xi^{\pm}$ ME distributions do not show any multiplicity dependence within the statistical uncertainty (see Figure 4.18), the pair acceptance of the multiplicity class 0-100% is used to correct the SE distributions obtained in all the multiplicity classes, in order to reduce the statistical fluctuations. Figure 4.19 shows an example of h-$\Xi^{\pm}$ SE angular correlation distribution (left plot), the corresponding h-$\Xi^{\pm}$ pair acceptance (central plot) and the corrected angular correlation distribution (right plot).

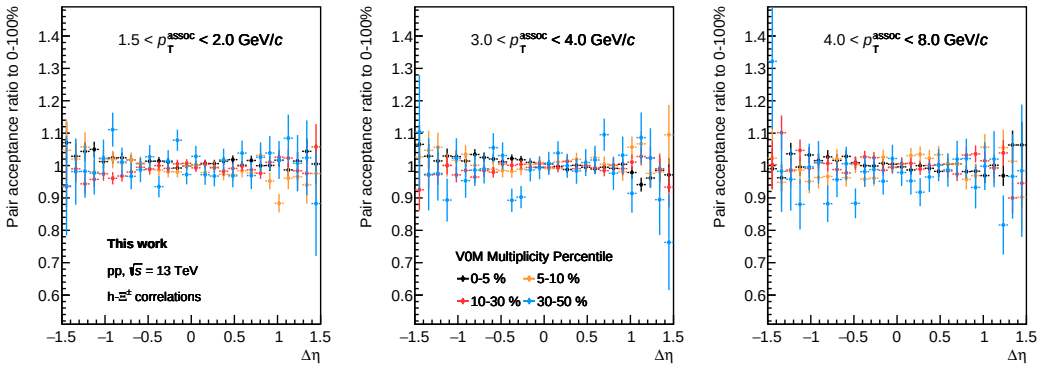

Figure 4.18: Ratios between the h-$\Xi^{\pm}$ pair acceptance projected along $\Delta\eta$ in different multiplicity classes and the one measured in the multiplicity class 0-100%. The different colours refer to different multiplicity classes, while the three different plots refer to different p_{T} intervals of the $\Xi^{\pm}$.

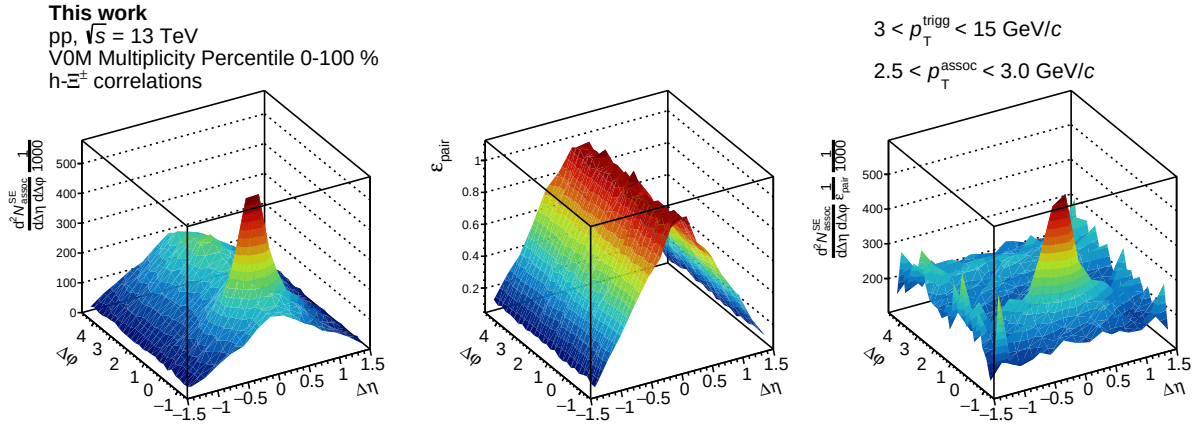

Figure 4.19: (left) Example of angular correlation distribution between trigger and $\Xi^{\pm}$ found in the same collision. (centre) Acceptance of trigger-$\Xi^{\pm}$ pairs. (right) Angular correlation distribution divided by the pair acceptance.

4.6.3 $\Delta\varphi$ projections of the pair acceptance corrected angular correlation distributions

As shown in the right plots of Figures 4.16 and 4.19, the angular correlation distributions show a peak centred at $(\Delta\eta, \Delta\varphi) = (0, 0)$ which can be associated to $\mathrm{K}^0_{\mathrm{S}}$ ($\Xi^{\pm}$) produced in the

leading jet (*toward-leading* or *near-side jet* production). A $(\Delta\eta, \Delta\varphi)$ region centred at larger values of $\Delta\eta$ and $\Delta\varphi$, where the peak contribution is negligible, can instead be associated to the production of K^0_S ($\Xi^{\pm}$) out of jets (*transverse-to-leading* production), while the region centred at $\Delta\varphi \sim \pi$ and extended over the whole $\Delta\eta$ interval includes the contribution of K^0_S ($\Xi^{\pm}$) candidates produced in the recoil jet (*away-side* production). In Figure 4.20 the $\Delta\eta\Delta\varphi$ regions used to extract the toward-leading and transverse-to-leading yields are drawn on top of an example of angular correlation distribution. The toward-leading production is extracted from the region ($|\Delta\eta| < 0.86$, $|\Delta\varphi| < 1.1$), while the transverse-to-leading production is extracted from ($0.86 < |\Delta\eta| < 1.2$, $0.96 < \Delta\varphi < 1.8$). The upper boundary of the transverse-to-leading region is chosen so to exclude the fluctuations at large $|\Delta\eta|$ due to limited statistics at the edges. The boundaries of the two regions are varied in order to estimate the associated systematic uncertainty, as described in Section 4.7. The whole $\Delta\eta\Delta\varphi$ region ($|\Delta\eta| < 1.2$, $-\pi/2 < \Delta\varphi < 3/2\pi$) is used to extract the *full* yield. In the following, the details of the procedure applied to extract the fully corrected yields are provided.

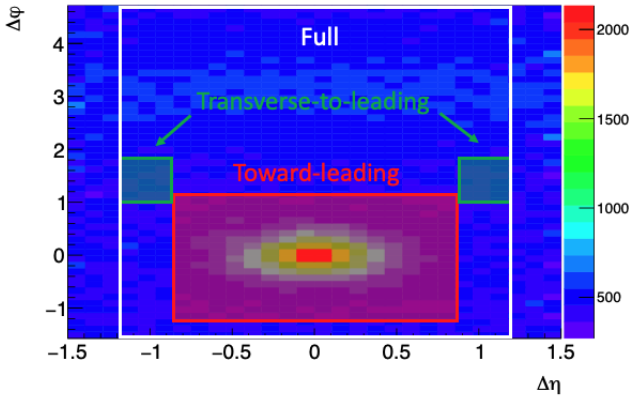

Figure 4.20: Example of pair acceptance corrected h-K^0_S correlation. The regions used to extract the toward-leading yield ($|\Delta\eta| < 0.86$, $|\Delta\varphi| < 1.1$), the transverse-to-leading yield ($0.86 < |\Delta\eta| < 1.2$, $0.96 < \Delta\varphi < 1.8$), and the full yield ($|\Delta\eta| < 1.2$, $-\pi/2 < \Delta\varphi < 3/2\pi$) are indicated by the rectangles.

The first step to extract the yields consists in projecting the angular correlation distributions along the $\Delta\varphi$ axis in the different $\Delta\eta$ regions. Figure 4.21 shows the $\Delta\varphi$ projections obtained from the three regions, normalised by the number of trigger particles N_{trigg} and by the width of the $\Delta\eta$ regions. The top plots refer to h-K^0_S correlation in different p_{T} intervals of K^0_S, the bottom plots to h-$\Xi^{\pm}$ correlation in different p_{T} intervals of $\Xi^{\pm}$.

The $\Delta\varphi$ projections obtained from $|\Delta\eta| < 0.86$ (red distributions) show a peak centred at $\Delta\varphi \simeq 0$ due to K^0_S candidates produced in the near-side jet. The less pronounced peak centred at $\Delta\varphi \simeq \pi$ (*away-side* peak) is instead related to the K^0_S ($\Xi^{\pm}$) candidates produced in the recoil jet. The *away-side* peak is less pronounced than the near-side jet peak as a consequence of the fact that the dijet partner, although approximately back to back in azimuth, can move in pseudorapidity [37]. Indeed, the *away-side* peak is also visible in the $\Delta\varphi$ projections obtained from $0.86 < |\Delta\eta| < 1.2$ (green distributions), and the projections obtained from the three different $\Delta\eta$ regions superimpose in $\pi/2 \lesssim \Delta\varphi \lesssim 3/2\pi$. It should be noted that the magnitude of the near-side jet peak differs in the projections obtained from $|\Delta\eta| < 0.86$ and from $|\Delta\eta| < 1.2$: this is a consequence of the fact that the projections are divided by the width of the two $\Delta\eta$ regions.

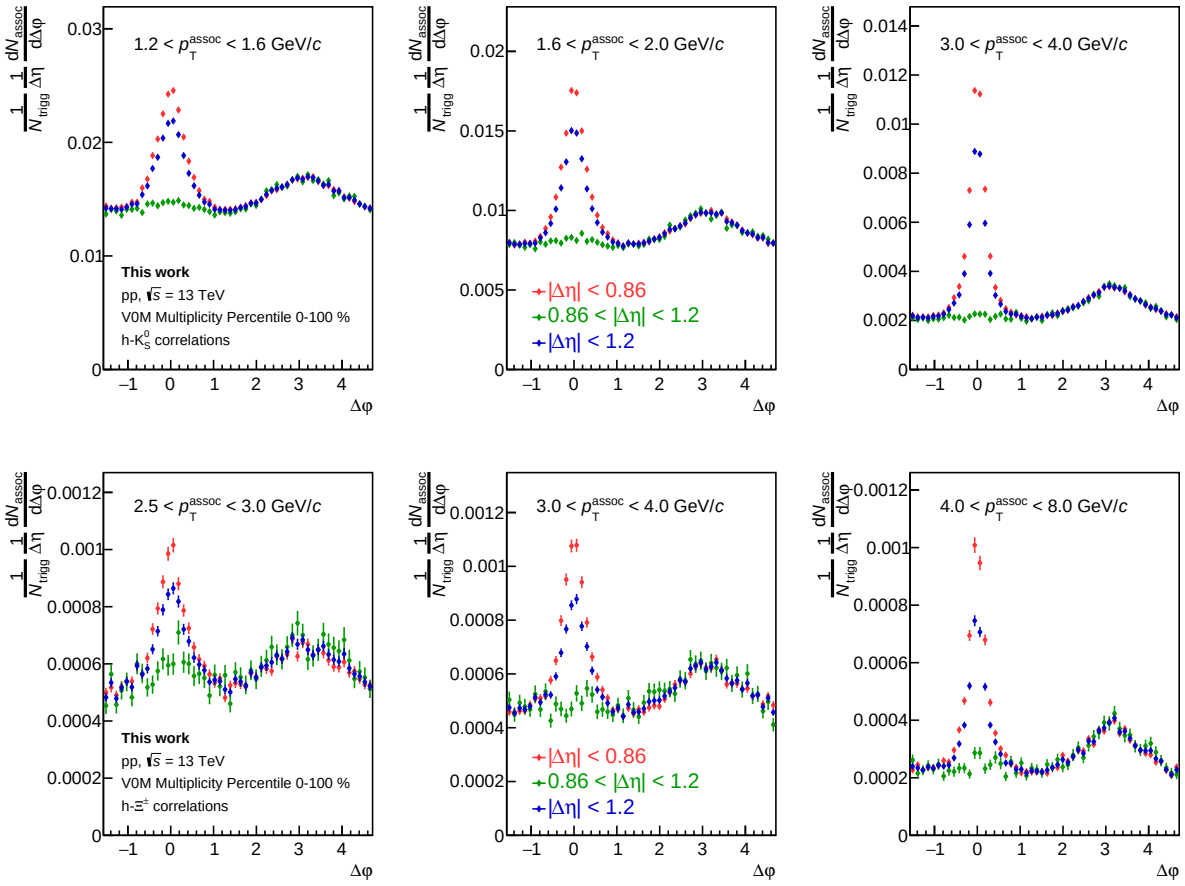

Figure 4.21: $\Delta\varphi$ projections of the angular correlation distributions obtained from $|\Delta\eta| < 0.86$ (red curves), $0.86 < |\Delta\eta| < 1.2$ (green curves), and $|\Delta\eta| < 1.2$ (blue curves).
The top plots are relative to h-K^0_S correlations in different p_T intervals of the K^0_S, the bottom ones to h-$\Xi^{\pm}$correlations in different p_T intervals of the $\Xi^{\pm}$. Error bars show the statistical uncertainty. The distributions are normalised by the number of trigger particles N_{trigg} and by the width of the $\Delta\eta$ interval chosen for the projection. The distributions are obtained by analysing minimum bias pp collisions at $\sqrt{s} = 13$ TeV in the multiplicity class 0-100%.

The plots show that the width of the near-side jet peak decreases with the p_{T} of the associated particle, suggesting that high-p_{T} strange hadrons in jets are produced closer to the leading track than low-p_{T} ones. It can also be observed that the relative contribution of toward-leading production with respect to transverse-to-leading production increases with the p_{T} of the associated particle, as strange hadrons produced in hard scattering processes are more likely to have a larger p_{T} than those produced in out-of-jet processes.

4.6.4 Subtraction of the background from fake $\mathrm{K}^0_{\mathrm{S}}$ and $\Xi^{\pm}$

The $\Delta\varphi$ projections have to be corrected for the contribution of particles misidentified as $\mathrm{K}^0_{\mathrm{S}}$ ($\Xi^{\pm}$), that is all the V0s (cascades) satisfying the criteria listed in Table 4.4 (4.5) but not being $\mathrm{K}^0_{\mathrm{S}}$ ($\Xi^{\pm}$).

For this purpose, the angular correlations obtained using V0 (cascade) candidates in the *sidebands* of the invariant mass distributions are computed. The sidebands of the $\mathrm{K}^0_{\mathrm{S}}$ invariant mass distributions are defined as the intervals $0.45 < m_{\pi^+\pi^-} < \mu - 4\sigma$ and $\mu + 4\sigma < m_{\pi^+\pi^-} < 0.55$, whereas the sidebands of the $\Xi^{\pm}$ invariant mass distribution are defined as the intervals $1.29 < m_{(\pi^-,\Lambda)\&(\pi^+,\overline{\Lambda})} < \mu - 4\sigma$ and $\mu + 4\sigma < m_{(\pi^-,\Lambda)\&(\pi^+,\overline{\Lambda})} < 1.35$.

The sideband regions are marked by blue lines in the two examples of $\mathrm{K}^0_{\mathrm{S}}$ and $\Xi^{\pm}$ invariant mass distributions shown in Figure 4.22. The small magnitude of the sidebands is related to the large purity of the $\mathrm{K}^0_{\mathrm{S}}$ and $\Xi^{\pm}$ samples, which in the p_{T} intervals shown in the two plots is about 0.96 and 0.9 for $\mathrm{K}^0_{\mathrm{S}}$ and $\Xi^{\pm}$, respectively (see Section 4.5).

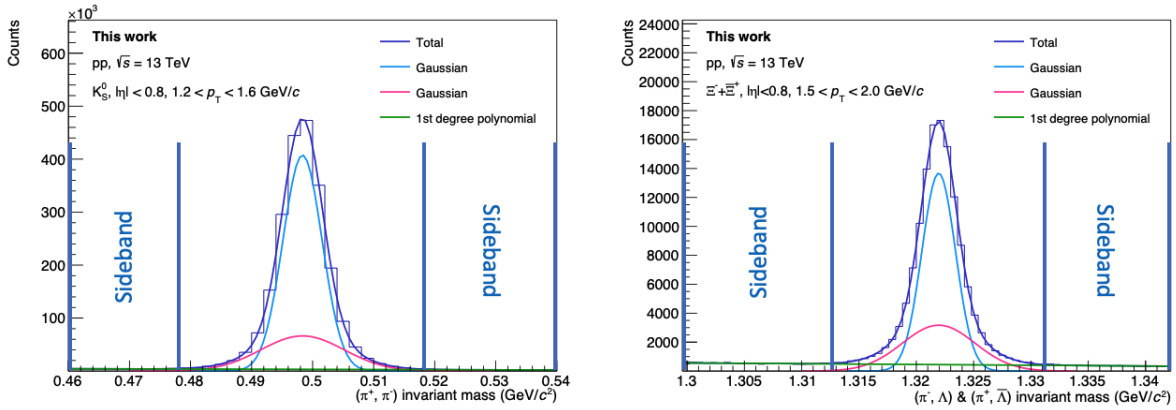

Figure 4.22: Examples of invariant mass distributions of $\mathrm{K}^0_{\mathrm{S}}$ (left) and $\Xi^{\pm}$(right) candidates. Blue lines mark the sidebands regions.

The sidebands (SB) angular correlation distributions are computed following the same procedure described in the previous Sections, but considering only candidates in the sidebands of the invariant mass distributions.

The $\Delta\varphi$ projections corrected for the contribution of particles misidentified as $\mathrm{K}^0_{\mathrm{S}}$ ($\Xi^{\pm}$) are given by:

$$\frac{\mathrm{d}N_{\mathrm{assoc}}}{\mathrm{d}\Delta\varphi} = \frac{\mathrm{d}N^{\mathrm{SB\ uncorr}}_{\mathrm{assoc}}}{\mathrm{d}\Delta\varphi} - \frac{\mathrm{d}N^{\mathrm{SB}}_{\mathrm{assoc}}}{\mathrm{d}\Delta\varphi} \times \frac{N^{\mathrm{Peak}}_{\Delta\mathrm{m}}}{N^{\mathrm{SB}}_{\Delta\mathrm{m}}}, \tag{4.14}$$

where the $\Delta\varphi$ projections $\mathrm{d}N^{\mathrm{SB}}_{\mathrm{assoc}}/\mathrm{d}\Delta\varphi$ of the SB angular correlation distributions are properly scaled by the ratio between the integral of the background fit function in the signal region $N^{\mathrm{Peak}}_{\Delta\mathrm{m}}$ and the integral of the invariant mass distribution in the sidebands region $N^{\mathrm{SB}}_{\Delta\mathrm{m}}$.

An example of $\Delta\varphi$ projections obtained from the sidebands of $\mathrm{K}^0_{\mathrm{S}}$ invariant mass distributions is shown in Figure 4.23. The $\Delta\varphi$ projections obtained from the sidebands have

similar characteristics to those obtained from candidates in the peak of the invariant mass distributions. In this case the near-side jet peak is related to pion pairs wrongly associated to a K^0_S which however are both produced in the jet defined by the trigger particle.
The plots in Figure 4.24 show the $\Delta\varphi$ projections obtained from the $|\Delta\eta| < 1.2$ region uncorrected for the contribution of fake K^0_S (dark blue curves) together with the corresponding $\Delta\varphi$ projections obtained from the sidebands and properly scaled (black curves). The differences between the two curves, that is the $\Delta\varphi$ projections corrected for the contribution of fake K^0_S, are shown in light blue.

This procedure is applied also to the h-$\Xi^{\pm}$ correlation distributions obtained by analysing the pp collisions at $\sqrt{s} = 13$ TeV collected with the high multiplicity trigger. The other data samples, namely the pp collisions at $\sqrt{s} = 13$ TeV collected with the minimum bias trigger and the pp collisions at $\sqrt{s} = 5.02$ TeV, do not contain enough events to compute the SB angular correlation distributions. In this case, to take into account the contribution of fake $\Xi^{\pm}$, the $\Delta\varphi$ projections are scaled by the purity of the sample of Ξ candidates (see bottom panel of Figure 4.8) and a systematic uncertainty is added, as described in Section 4.7.

Finally, the $\Delta\varphi$ projection are corrected for the fraction of non-primary K^0_S ($\Xi^{\pm}$). For this purpose, the distributions are multiplied by $(1 - F_{NP})$, where F_{NP} is the fraction of non-primary K^0_S ($\Xi^{\pm}$) (see Section 4.5.3). This correction has a negligible impact since $F_{NP} \sim 0.5\%$ for $\Xi^{\pm}$ and $\sim 0.05\%$ for K^0_S .

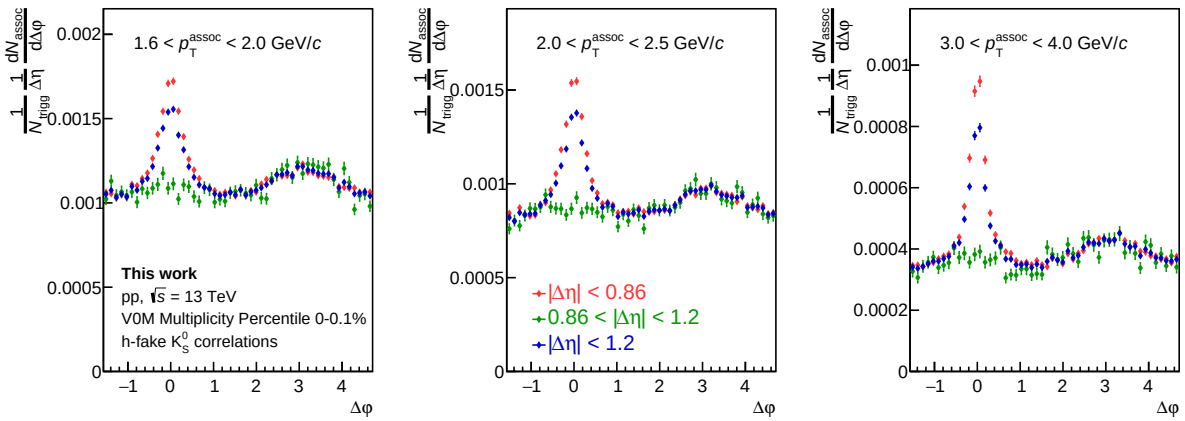

Figure 4.23: $\Delta\varphi$ projections of the angular correlation distributions obtained from the sidebands of K^0_S invariant mass distributions. Red curves are obtained from $|\Delta\eta| < 0.86$, green ones from from $0.86 < |\Delta\eta| < 1.2$, and blue ones from $|\Delta\eta| < 1.2$. Different plots refer to different p_T intervals of the K^0_S. Error bars show the statistical uncertainty. The distributions are normalised by the number of trigger particles N_{trigg} and by the width of the $\Delta\eta$ interval chosen for the projection. These distributions are obtained by analysing HM pp collisions at $\sqrt{s} = 13$ TeV in the multiplicity class 0-0.1%. It should be noted that these projections are about one order of magnitude smaller than the corresponding projections obtained from candidates in the peak region of the invariant mass distributions.

4.6.5 Subtraction of the contribution from uncorrelated pairs to the $\Delta\varphi$ projection in the jet region

As already noted in Section 4.6.3, the $\Delta\varphi$ projections obtained from the $|\Delta\eta| < 0.86$ region not only include the contribution of K^0_S ($\Xi^{\pm}$) produced in the leading jet, but also include the

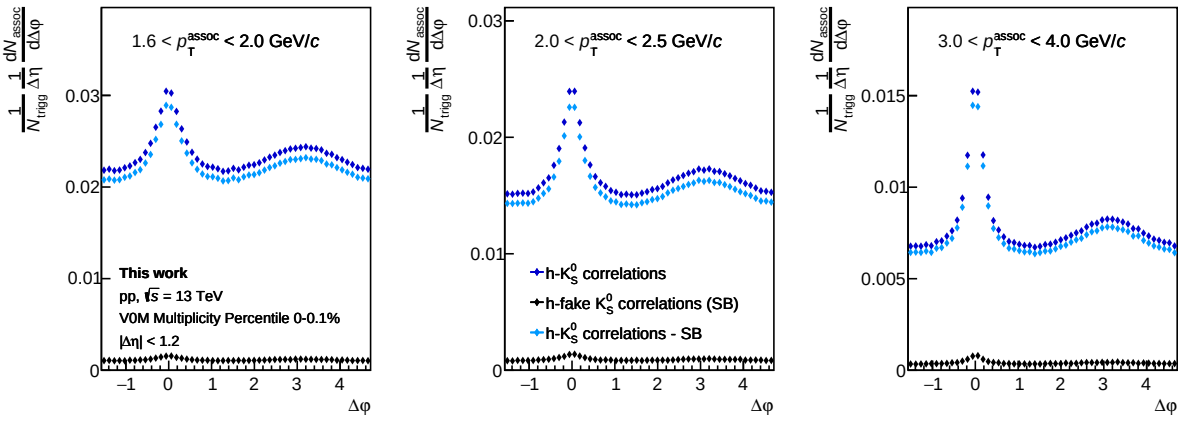

Figure 4.24: $\Delta\varphi$ projections obtained from the $|\Delta\eta| < 1.2$ region uncorrected for the contribution of fake K^0_S (dark blue curves) together with the corresponding $\Delta\varphi$ projections obtained from the sidebands and properly scaled (black curves). The differences between the two curves, that is the $\Delta\varphi$ projections corrected for the contribution of fake K^0_S, are shown in light blue. These distributions are obtained by analysing HM pp collisions at $\sqrt{s} = 13$ TeV in the multiplicity class 0-0.1%.

contribution of K^0_S ($\Xi^{\pm}$) produced in the recoil jet and out of jets. An estimate of the latter contributions is provided by the $\Delta\varphi$ projections obtained from the $0.86 < |\Delta\eta| < 1.2$ region. These distributions are subtracted to the $\Delta\varphi$ projections obtained from the $|\Delta\eta| < 0.86$ in order to extract the toward-leading distributions.

Figure 4.25 shows the K^0_S toward-leading distributions (light red curves) in three different p_T intervals for minimum bias pp collisions at $\sqrt{s} = 13$ TeV. These distributions are obtained by subtracting the fully corrected $\Delta\varphi$ projections obtained from the $0.86 < |\Delta\eta| < 1.2$ region (green curves) to the fully corrected $\Delta\varphi$ distributions obtained from the $|\Delta\eta| < 0.86$ region (dark red curves).

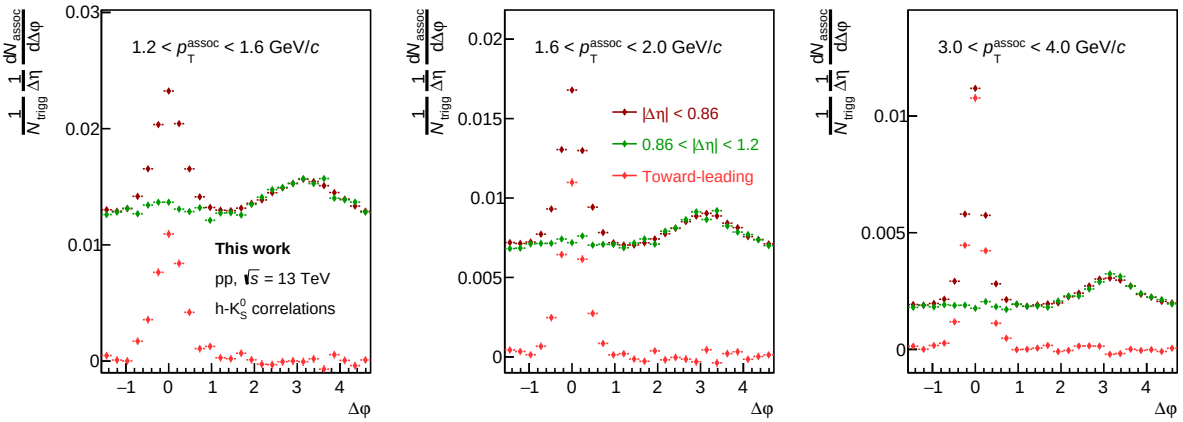

Figure 4.25: K^0_S toward-leading distributions (light red curves) in three different p_T intervals in the multiplicity class 0-100% of minimum bias pp collisions at $\sqrt{s} = 13$ TeV. These distributions are obtained by subtracting the $\Delta\varphi$ projections obtained from the $0.86 < |\Delta\eta| < 1.2$ region (green curves) to the $\Delta\varphi$ projections obtained from the $|\Delta\eta| < 0.86$ region (dark red curves). Error bars show the statistical uncertainties.

This procedure cannot be applied to extract the toward-leading yield of $\Xi^{\pm}$ at low p_{T} ($p_{\mathrm{T}} \lesssim 2$ GeV/c), as a consequence of the large statistical uncertainties which affect the $\Delta\varphi$ projections in the $0.86 < |\Delta\eta| < 1.2$ interval. In order to extract the toward-leading yield in the low-p_{T} region, the out-of-jet contribution is estimated from events which do not contain any trigger particle (*no-trigger* events). In particular, events with the highest-p_{T} charged particle in the range $0.15 < p_{\mathrm{T}} < 2.5$ GeV/c are taken into account. These events represent the 80% of all the selected events in the minimum bias sample, and therefore the angular correlation distributions obtained from them have smaller statistical uncertainties. To allow for a proper subtraction of the out-of-jet contribution, the $\Delta\varphi$ projections in the $0.86 < |\Delta\eta| < 1.2$ region obtained from *no-trigger* events are scaled to the $|\Delta\eta| < 0.86$ projections in the interval $1 \lesssim \Delta\varphi \lesssim 2$. As shown in the left panel of Figure 4.26, these distributions are compatible with the default ones, i.e. with those obtained from events with a trigger particle, and therefore can be used in their place. Moreover, the $\Delta\varphi$ distribution obtained in the 0-100% multiplicity class is compatible with the ones obtained in the other multiplicity classes (right panel of Figure 4.26), and since it has the smallest statistical uncertainties it is used to extract the toward-leading yield in all multiplicity classes.

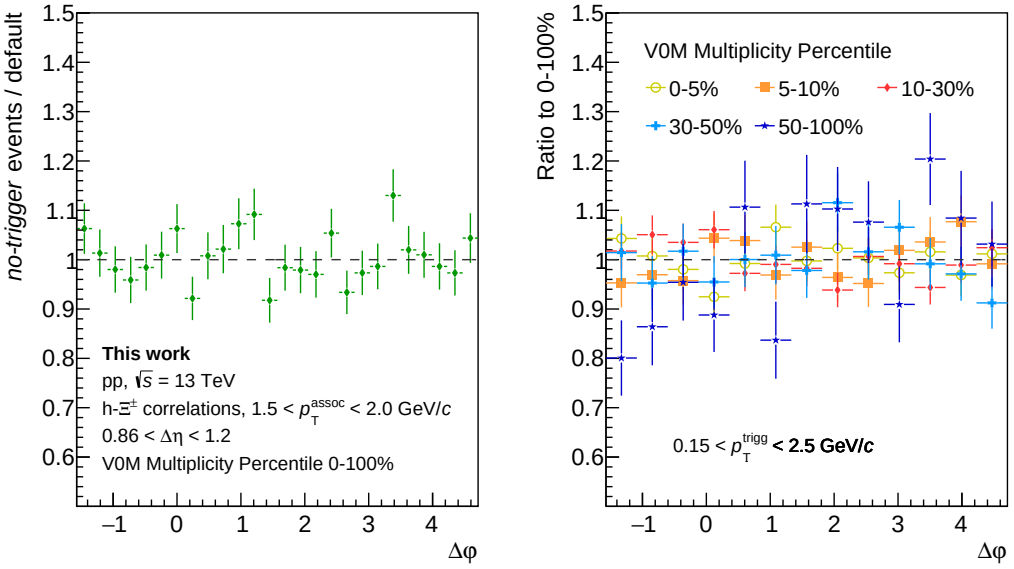

Figure 4.26: (left) Example of ratio between the h-$\Xi^{\pm}$ $\Delta\varphi$ projection in the $0.86 < |\Delta\eta| < 1.2$ region obtained from *no-trigger* events and the one obtained from events with a trigger particle. See the text for details. (right) Ratios between the h-$\Xi^{\pm}$ $\Delta\varphi$ projections in the $0.86 < |\Delta\eta| < 1.2$ region obtained from *no-trigger* events in different multiplicity classes, as indicated in the legend, and the one obtained from the 0-100% multiplicity class.

To further check the validity of this method the same procedure is applied to h-$\mathrm{K}^0_{\mathrm{S}}$ correlation, where the smaller statistical uncertainties allow for a better comparison between the default distributions and the ones obtained from *no-trigger* events. The distributions obtained with the two methods are compatible in all the p_{T} intervals considered, and those obtained from *no-trigger* events are compatible across multiplicity classes.

This method is applied to $\Xi^{\pm}$ with $p_{\mathrm{T}} < 2.5$ GeV/c and allows for the measurement of the $\Xi^{\pm}$ toward-leading yield for $p_{\mathrm{T}} > 1.0$ (1.5) GeV/c, depending on the multiplicity class. When applying the default method, instead, the measurement could only be performed for $p_{\mathrm{T}} > 1.5$ (2.0) GeV/c. In the p_{T} interval where both methods can be used, a systematic uncertainty has been evaluated, as described in section 4.7.

The approach based on *no-trigger* events is not applied in the analysis of high multiplicity pp collisions at $\sqrt{s} = 13$ TeV, since in this case events with a trigger particle already represent 40% of all the events, and consequently the angular correlation distributions obtained from *no-trigger* events do not have significantly smaller statistical uncertainties. Instead, in all multiplicity classes the out-of-jet contribution is estimated from the $\Delta\varphi$ projections in the $0.86 < |\Delta\eta| < 1.2$ region obtained in the whole multiplicity interval 0-0.1%. Before subtraction, these distributions are scaled to the $|\Delta\eta| < 0.86$ projections in the interval $1 \lesssim \Delta\varphi \lesssim 2$. These distributions are compatible within uncertainties with the default distributions in the $-\pi/2 < \Delta\varphi < \pi/2$ interval, that is the interval where the near-side jet peak lies, and therefore can be used in place of the default ones.

Figure 4.27 shows the $\Xi^{\pm}$ toward-leading distributions (light red curves) in different p_{T} intervals for minimum bias pp collisions at $\sqrt{s} = 13$ TeV. These distributions are obtained by subtracting the fully corrected $\Delta\varphi$ projections obtained from the $0.86 < |\Delta\eta| < 1.2$ region (green curves) to the fully corrected $\Delta\varphi$ distributions obtained from the $|\Delta\eta| < 0.86$ region (dark red curves). For $p_{\mathrm{T}} < 2.5$ GeV/c, the $\Delta\varphi$ projections in the $0.86 < |\Delta\eta| < 1.2$ region are those obtained from events with no trigger particles. Similar plots are shown in Figure 4.27 for high multiplicity pp collisions at $\sqrt{s} = 13$ TeV. In this case, for $p_{\mathrm{T}} < 2.5$ GeV/c the $\Delta\varphi$ projections in the $0.86 < |\Delta\eta| < 1.2$ region are taken from the multiplicity class 0-0.1% and are properly scaled to the $|\Delta\eta| < 0.86$ projections in the interval $1 \lesssim \Delta\varphi \lesssim 2$.

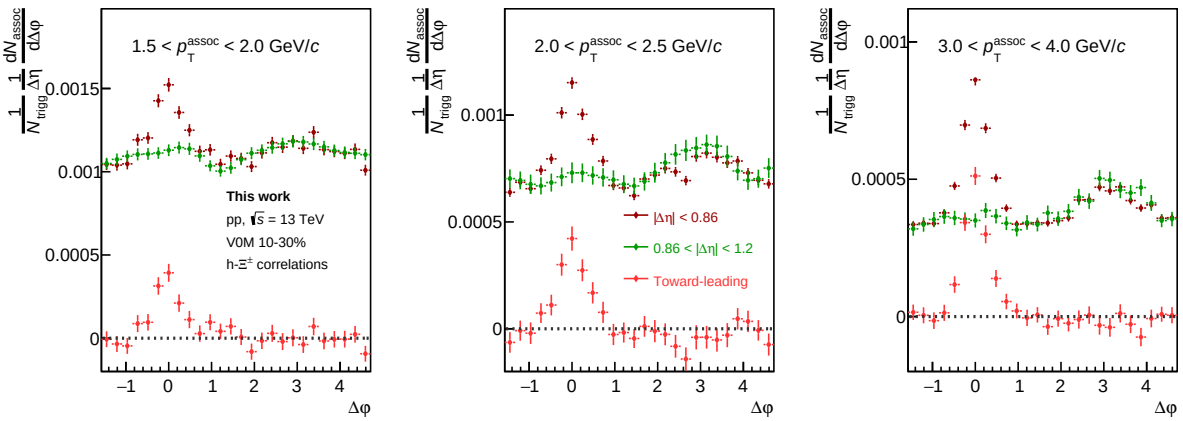

Figure 4.27: $\Xi^{\pm}$ toward-leading distributions (light red curves) in three different p_{T} intervals in the multiplicity class 30-50% of minimum bias pp collisions at $\sqrt{s} = 13$ TeV. These distributions are obtained by subtracting the $\Delta\varphi$ projections obtained from the $0.86 < |\Delta\eta| < 1.2$ region (green curves) to the $\Delta\varphi$ projections obtained from the $|\Delta\eta| < 0.86$ region (dark red curves). For $p_{\mathrm{T}} < 2.5$ GeV/c, the $\Delta\varphi$ projections in the $0.86 < |\Delta\eta| < 1.2$ region are obtained from events with no trigger particles and are scaled to the dark red distributions in the $1 \lesssim \Delta\varphi \lesssim 2$ interval. Error bars show the statistical uncertainties.

4.6.6 Computation of p_{T} spectra

Once the necessary corrections are applied to the $\Delta\varphi$ projections, the full, transverse-to-leading and toward-leading yields are computed.

The full yield of $\mathrm{K}^0_{\mathrm{S}}$ ($\Xi^{\pm}$) is obtained by integrating the $\Delta\varphi$ projections obtained from the $|\Delta\eta| < 1.2$ region over the whole $\Delta\varphi$ interval ($-\pi/2 < \Delta\varphi < 3/2\pi$). The transverse-to-leading yield is instead obtained by integrating the $\Delta\varphi$ projections obtained from the

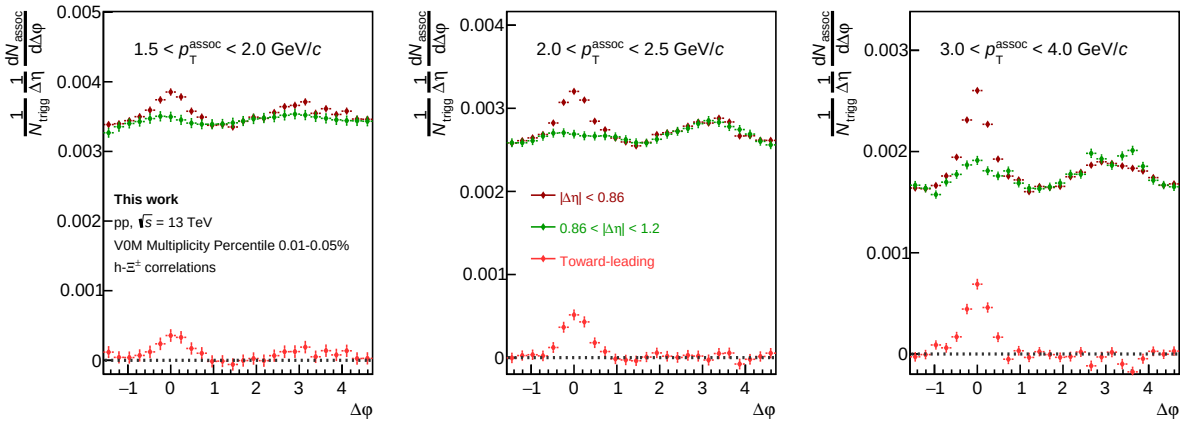

Figure 4.28: $\Xi^{\pm}$ toward-leading distributions (light red curves) in three different p_{T} intervals in the multiplicity class 0.01-0.05% of high multiplicity pp collisions at $\sqrt{s} = 13$ TeV. These distributions are obtained by subtracting the $\Delta\varphi$ projections obtained from the $0.86 < |\Delta\eta| < 1.2$ region (green curves) to the $\Delta\varphi$ projections obtained from the $|\Delta\eta| < 0.86$ region (dark red curves). For $p_{\mathrm{T}} < 2.5$ GeV/c, the $\Delta\varphi$ projections in the $0.86 < |\Delta\eta| < 1.2$ region are taken from the multiplicity class 0-0.1% and scaled to the dark red distributions in the $1 \lesssim \Delta\varphi \lesssim 2$ interval. Error bars show the statistical uncertainties.

$0.86 < |\Delta\eta| < 1.2$ region in the interval $0.85 < \Delta\varphi < 1.8$. This interval is chosen in order to exclude the away-side peak, situated around $\Delta\varphi \sim \pi$, and to exclude any possible residual near-side jet contribution in the region around $\Delta\varphi \sim 0$. Finally, to obtain the toward-leading yield, the sum of the bin contents of the toward-leading distribution is performed in the interval $|\Delta\varphi| < 1.1$.

The yields are divided by the width of the $\Delta\varphi$ interval and by the width of the p_{T} interval Δp_{T}, in order to obtain the p_{T} density spectra, from now on called p_{T} spectra (see Section 5.1):

$$\frac{1}{N_{\mathrm{trigg}}}\frac{1}{\Delta\eta\Delta\varphi}\frac{d\mathrm{N}}{\mathrm{d}p_{\mathrm{T}}} = \frac{1}{N_{\mathrm{trigg}}}\frac{1}{\Delta\eta\Delta\varphi}\frac{1}{\Delta p_{\mathrm{T}}}\int_{\Delta\varphi}\frac{\mathrm{d}N_{\mathrm{assoc}}}{\mathrm{d}\Delta\varphi}\mathrm{d}\Delta\varphi. \tag{4.15}$$

4.7 Study of the systematic effects

Several sources of systematic uncertainties affecting the measurement of the full, transverse-to-leading and toward-leading p_{T} spectra are taken into account. A detailed description of the treatment of these uncertainties is provided in this Section.

In general, to evaluate the systematic uncertainty associated to a given selection (e.g., a topological selections applied to identify associated particles), the analysis is repeated by varying that selection and the results are compared to those obtained with the default selection. For some sources of systematic uncertainties, the comparison is performed at the level of the $\Delta\varphi$ projections, as described in Section 4.7.1. The sources of systematic uncertainty which are expected to give a variation correlated across $\Delta\varphi$ are directly evaluated by comparing the $\Delta\varphi$-integrated yields, that is the p_{T} spectra, as described in Section 4.7.2.

All the considered sources of systematic uncertainties are reported in Tables 4.13 and 4.14 for h-$\mathrm{K}^0_{\mathrm{S}}$ and h-$\Xi^{\pm}$ correlation, respectively, together with the relative uncertainty associated to each of the sources at three different p_{T} values. The relative uncertainties are also shown as a function of p_{T} in Figures 4.31 and 4.32 for $\mathrm{K}^0_{\mathrm{S}}$ and $\Xi^{\pm}$, respectively. The plots refer to minimum bias pp collisions at $\sqrt{s} = 13$ TeV, but similar results are observed in all multiplicity classes and at both centre-of-mass energies.

4.7.1 Systematic effects on the fully corrected $\Delta\varphi$ projections

Three sources of systematic effects on the fully corrected $\Delta\varphi$ projections are considered: the selections applied to topological and kinematic variables for $\mathrm{K}^0_{\mathrm{S}}$ and $\Xi^{\pm}$ identification, the selection applied to the distance of closest approach of the trigger particle to the primary vertex along the z axis (DCAz), and the choice of the $\Delta\eta$ regions from which the $\Delta\varphi$ projections are obtained.

By varying the topological selections it is possible to take into account the differences between the distributions of the topological variables in the data and in the Monte Carlo (MC) simulation used to compute the $\mathrm{K}^0_{\mathrm{S}}$ and $\Xi^{\pm}$ efficiencies. For this purpose, six topological variables used for $\mathrm{K}^0_{\mathrm{S}}$ identification and five topological variables used for $\Xi^{\pm}$ identification are considered. For each topological variable a *variation range* is defined such that the lower and upper values of the range, applied together with the default selections for all the other topological variables, give a variation of the number of $\mathrm{K}^0_{\mathrm{S}}$ ($\Xi^{\pm}$) candidates of about 2%. For each of the considered topological variables, the default values and the lower and upper values of the *variation ranges* are listed in Tables 4.6 and 4.7 for $\mathrm{K}^0_{\mathrm{S}}$ and $\Xi^{\pm}$, respectively. The loose selections which do not give an increase of the number of candidates of 2% could not be further loosened since they were applied before storing the samples of $\mathrm{K}^0_{\mathrm{S}}$ and $\Xi^{\pm}$ candidates. When the loosest(tightest) selections are applied altogether, the increase(decrease) of the raw yield is about 10% for both $\mathrm{K}^0_{\mathrm{S}}$ and $\Xi^{\pm}$. For each topological variable a random number is extracted from a uniform distribution within the *variation range*, and the new set of selections is used to obtain the fully corrected $\Delta\varphi$ projections. This procedure is repeated 500 times, in order to suppress statistical fluctuations, and for each $\Delta\varphi$ interval a histogram is filled with the resulting yields. The ratio between the standard deviation and the mean value of the distribution so obtained is assigned as relative systematic uncertainty. The procedure is performed separately for the full, the toward-leading and the transverse-to-leading distributions.

Each combination of the topological selections determines a shift of the yield towards larger (or smaller) values in all $\Delta\varphi$ intervals, and therefore this source of systematic un-

certainty is considered correlated across $\Delta\varphi$. Consequently, the uncertainty applied to the p_{T} spectra is computed as the linear sum of the systematic uncertainties $\sigma_{\Delta\varphi}$ of the $\Delta\varphi$ projections in the $\Delta\varphi$ region from which the yield is extracted:

$$\sigma_{p_{\mathrm{T}}} = \sum_{\Delta\varphi} \sigma_{\Delta\varphi} \, . \tag{4.16}$$

The relative systematic uncertainty associated to topological selections is smaller than 1% (3%) for the transverse-to-leading and full p_{T} spectra of $\mathrm{K}^0_{\mathrm{S}}$ ($\Xi^{\pm}$), whereas for toward-leading production it reaches values up to 3% for $\mathrm{K}^0_{\mathrm{S}}$ spectra and up to 8% for $\Xi^{\pm}$, for which this source of uncertainty represents the dominant one. The magnitude of this uncertainty is observed to be correlated with the magnitude of the statistical uncertainty.

V^0 **selections**	**Default**	**Loose (N. candidates variation)**	**Tight (N. candidates variation)**
DCA daughter tracks to PV	> 0.06	> 0.05 (+0.5%)	> 0.09 (-2%)
$\cos(\theta_{\mathrm{P}})$	> 0.995	> 0.97 (+1.5%)	> 0.998 (-2%)
DCA V^0 to PV	< 0.5	< 0.6 (+0.7%)	< 0.4 (-2%)
$\lvert \mathrm{m}_{\pi\mathrm{p}} - \mathrm{m}_{\Lambda} \rvert$	> 5 MeV/c^2	> 0 MeV/c^2 (+3%)	> 10 MeV/c^2 (-2%)
$c\tau$	< 20 cm	< 30 cm (+1‰)	< 9.5 cm (-2%)

Table 4.6: V^0 candidates topological and kinematic variables considered for the determination of the systematic uncertainty. The default selections are listed in the second column, the loose and tight selections, representing the boundaries of the *variation ranges*, are listed in the third and fourth columns, respectively, together with the relative variation of the number of $\mathrm{K}^0_{\mathrm{S}}$ candidates. More details are given in the text.

Cascade selections	**Default**	**Loose (N. candidates variation)**	**Tight (N. candidates variation)**
$\cos(\theta_{\mathrm{P}})$ (of cascade to PV)	> 0.995	> 0.99 (+2%)	> 0.997 (-2%)
$\cos(\theta_{\mathrm{P}})$ (of V^0 to cascade)	> 0.97	> 0.95 (+2%)	> 0.995 (-2%)
DCA between bachelor and V^0	< 0.8	< 0.9 (+1%)	< 0.68 (-2%)
$\lvert \mathrm{m}_{\pi\mathrm{p}} - \mathrm{m}_{\Lambda} \rvert$	< 6 MeV/c^2	< 9 MeV/c^2 (+2%)	< 5 MeV/c^2 (-2%)
$c\tau$	$< 3 < c\tau >$	$< 5 < c\tau >$ (+2%)	$< 2.6 < c\tau >$ (-2%)

Table 4.7: Cascade candidates topological and kinematic variables considered for the determination of the systematic uncertainty. The default selections are listed in the second column, the loose and tight selections, representing the boundaries of the *variation ranges*, are listed in the third and fourth columns, respectively, together with the relative variation of the number of $\Xi^{\pm}$ candidates. More details are given in the text.

By varying the selection applied to the DCAz of the trigger particles it is possible to test the effect of a different fraction of non-primary charged particles in the sample of trigger particles. The systematic uncertainty associated to this source is estimated in the same way described above for the topological selections. In this case, a hundred different values of DCAz within the $(0, 2)$ cm range are randomly extracted. This source of uncertainty is

uncorrelated across $\Delta\varphi$, and therefore the uncertainty applied to the p_{T} spectra is computed as the sum in quadrature of the systematic uncertainties $\sigma_{\Delta\varphi}$ of the $\Delta\varphi$ projections over the $\Delta\varphi$ interval from which the yield is extracted:

$$\sigma_{p_{\mathrm{T}}} = \sqrt{\sum_{\Delta\varphi} \sigma^2_{\Delta\varphi}} \,. \tag{4.17}$$

The relative uncertainty associated to this source is smaller than 0.2% for full and transverse-to-leading production, and smaller than 0.5% for toward-leading production: it represents therefore the least important contribution to the total systematic uncertainty.

The systematic uncertainty associated to the choice of the $\Delta\eta$ region is assessed by changing the boundaries of the $\Delta\eta$ regions used in the analysis. The variations applied to the $\Delta\eta$ region from which the toward-leading yield is extracted are reported in Tables 4.8 and 4.10 for h-$\mathrm{K}^0_{\mathrm{S}}$ and h-$\Xi^{\pm}$ correlations, respectively. It should be noted that for each selection of the $\Delta\eta$ region from which for toward-leading yield is extracted, also the $\Delta\eta$ region used for the estimation of the out-of-jet contribution is varied accordingly. For h-$\mathrm{K}^0_{\mathrm{S}}$ correlation, two variations are applied: one consists in increasing the upper value of the region from where the out-of-jet contribution is estimated (Selection 1), the other in enlarging the $\Delta\eta$ region which contains the near-side jet peak and, consequently, in increasing the lower value of the region from where the out-of-jet contribution is estimated (Selection 2). Only the first variation (Selection 1) is applied to h-$\Xi^{\pm}$ correlation, since the out-of-jet contribution estimated with Selection 2 suffers from large statistical uncertainties. For both h-$\mathrm{K}^0_{\mathrm{S}}$ and h-$\Xi^{\pm}$ correlation, the upper boundaries of the $\Delta\eta$ region which contains the near-side jet peak are not decreased below the default value of 0.86 (see Figure 4.20), in order not to exclude part of the in-jet production.

The upper and lower boundaries of the $\Delta\eta$ region from which the transverse-to-leading yield is extracted are increased and decreased as reported in Tables 4.9 and 4.11 for h-$\mathrm{K}^0_{\mathrm{S}}$ and h-$\Xi^{\pm}$ correlations, respectively. For h-$\Xi^{\pm}$ correlation, the lower boundary can only be decreased, due to the aforementioned increase of statistical uncertainties at large values of $\Delta\eta$. It should be noted that the decrease of the lower boundary might determine the inclusion of near-side jet contribution in the $\Delta\varphi$ projection used to extract the transverse-to-leading yield. However, this contribution would be located around $\Delta\varphi \sim 0$, while the transverse-to-leading yield is extracted from the region $0.96 < \Delta\varphi < 1.8$.

The full yield, which by definition is obtained from the region ($|\Delta\eta| < 1.2$, $-\pi/2 < \Delta\varphi < 3/2\pi$), is not affected by this source of systematic uncertainty.

$\Delta\eta$ **region**	**Toward-leading**	**Out-of-jet contribution**
Default selection	$\lvert\Delta\eta\rvert < 0.86$	$0.86 < \lvert\Delta\eta\rvert < 1.2$
Selection 1	$\lvert\Delta\eta\rvert < 0.86$	$0.86 < \lvert\Delta\eta\rvert < 1.3$
Selection 2	$\lvert\Delta\eta\rvert < 0.96$	$0.96 < \lvert\Delta\eta\rvert < 1.3$

Table 4.8: Systematic variations of the $\Delta\eta$ region from which the $\mathrm{K}^0_{\mathrm{S}}$ toward-leading yields are extracted. The central column shows the variations of the $\Delta\eta$ range which includes the near-side jet peak, the third column shows the corresponding variation of the $\Delta\eta$ region from which the out-of-jet contribution is estimated.

$\Delta\eta$ **region**	**Transverse-to-leading**
Default selection	$0.86 < \|\Delta\eta\| < 1.2$
Selection 1	$0.86 < \|\Delta\eta\| < 1.3$
Selection 2	$0.96 < \|\Delta\eta\| < 1.3$
Selection 3	$0.75 < \|\Delta\eta\| < 1.3$

Table 4.9: Systematic variations of the $\Delta\eta$ region from which the K^0_S transverse-to-leading yields are extracted.

$\Delta\eta$ **region**	**Toward-leading**	**Out-of-jet contribution**
Default selection	$\|\Delta\eta\| < 0.86$	$0.86 < \|\Delta\eta\| < 1.2$
Selection 1	$\|\Delta\eta\| < 0.86$	$0.86 < \|\Delta\eta\| < 1.3$

Table 4.10: Systematic variations of the $\Delta\eta$ region from which the $\Xi^{\pm}$ toward-leading yields are extracted. The central column shows the variations of the $\Delta\eta$ range which includes the near-side jet peak, the third column shows the corresponding variation of the $\Delta\eta$ region from which the out-of-jet contribution is estimated.

$\Delta\eta$ **region**	**Transverse-to-leading**
Default selection	$0.86 < \|\Delta\eta\| < 1.2$
Selection 1	$0.75 < \|\Delta\eta\| < 1.2$
Selection 2	$0.75 < \|\Delta\eta\| < 1.3$
Selection 3	$0.64 < \|\Delta\eta\| < 1.2$

Table 4.11: Systematic variations of the $\Delta\eta$ region from which the $\Xi^{\pm}$ transverse-to-leading yields are extracted.

To determine if a variation of the $\Delta\eta$ region is significant, i.e. it results in a distribution which differs from the default one by more than what expected on the basis of statistical fluctuations only, the Barlow check [156] is applied. For this purpose, the Barlow variable B is defined as follows:

$$B = \frac{\Delta y}{\sqrt{|\sigma_{def}^2 - \sigma_{var}^2|}} = \frac{y_{def} - y_{var}}{\sqrt{|\sigma_{def}^2 - \sigma_{var}^2|}} \,, \tag{4.18}$$

where y_{def} is the yield obtained applying the default selection and y_{var} is the yield obtained varying the selection, and σ_{def} and σ_{var} are the statistical uncertainties associated to y_{def} and y_{var}, respectively. The same data set is used to compute both y_{def} and y_{var}, which are therefore correlated. Consequently, a good approximation of the variance of the difference Δy between y_{def} and y_{var} is given by $|\sigma_{def}^2 - \sigma_{var}^2|$.

On the assumption that y_{def} and y_{var} are normally distributed, B follows a Gaussian distribution with mean equal to zero and variance equal to one. Therefore, assuming that the considered systematic effect is not present, the probability p that $|B| > 2$ is about 5%.

The probability $P(k, n)$ that the condition $|B| > 2$ is verified for k out of n intervals of the fully corrected $\Delta\varphi$ distribution is given by the binomial distribution:

$$P(k, n) = \binom{n}{k} p^k (1-p)^{(n-k)} \,. \tag{4.19}$$

The number n of $\Delta\varphi$ intervals used to compute both the transverse-to-leading and the toward-leading yield is 10. Therefore, the effect is considered significant if $k > 3$ ($P(k > 3, n = 10) = 0.001$).

The systematic uncertainty in a given $\Delta\varphi$ interval is computed as the half-difference between the maximum and the minimum yields obtained by applying the significant $\Delta\eta$ selections:

$$\sigma_{SYS,\Delta\eta} = |y_{Max} - y_{Min}|/2. \tag{4.20}$$

For h-$\mathrm{K^0_S}$ correlation, all selections give a Barlow significant variation. For h-$\Xi^{\pm}$ correlation, the only significant variation of the transverse-to-leading $\Delta\eta$ interval is given by Selection 2, where the upper boundary of the interval is increased. This variation is significant only in the high multiplicity sample. For what concerns the $\Delta\eta$ region used to extract the $\Xi^{\pm}$ toward-leading yield, the only variation is significant at low p_{T} ($p_{\mathrm{T}} \lesssim 2.5$ GeV/c) in minimum bias pp collisions at $\sqrt{\mathrm{s}} = 13$ TeV and in all p_{T} interval in high multiplicity pp collisions at $\sqrt{\mathrm{s}} = 13$ TeV, whereas it is not significant in minimum bias pp collisions at $\sqrt{\mathrm{s}} = 5.02$ TeV.

For both h-$\mathrm{K^0_S}$ and h-$\Xi^{\pm}$ correlations, the Barlow variables B do not show any significant correlation with $\Delta\varphi$, i.e. they are observed to be randomly distributed at both positive and negative values. This behaviour indicates that the systematic uncertainties associated to the choice of $\Delta\eta$ are not correlated across $\Delta\varphi$. Therefore, the uncertainties associated to the choice of $\Delta\eta$ are propagated to the p_{T} spectra by performing the sum in quadrature of the systematic uncertainties of the $\Delta\varphi$ projections.

The total systematic uncertainty of the fully corrected $\Delta\varphi$ projections is obtained by summing in quadrature the systematic uncertainties from the three sources (topological variables selection, trigger particle DCAz selection, $\Delta\eta$ region selection), since they are uncorrelated with each other.

Figures 4.29 and 4.30 show the fully corrected $\Delta\varphi$ projections obtained in three different p_{T} intervals in the 0-100% multiplicity class of minimum bias pp collisions at $\sqrt{s} = 13$ TeV for h-$\mathrm{K}^0_{\mathrm{S}}$ and h-$\Xi^{\pm}$ correlation, respectively. Both the statistical and the systematic uncertainties are shown.

As already observed in Section 4.6.3, the near-side-jet peak becomes more visible and narrower with the increase of the p_{T} of the associated particle, whereas at low p_{T} it is wider and its relative contribution to the full yield decreases. To evaluate if in a given p_{T} interval the near-side jet peak is significant and is not just a statistical fluctuation of the out-of-jet production, the significance S of the peak is measured:

$$S = \frac{\mathrm{Y}}{\sigma_{\mathrm{Y}}} \,, \tag{4.21}$$

where Y is the toward-leading yield, that is the integral of the near-side jet peak, and σ_Y is the sum in quadrature of its statistical and systematic uncertainties uncorrelated across $\Delta\varphi$. The variations correlated across $\Delta\varphi$ are not taken into account since they do not change the shape of the peak, but they only determine a shift of the whole $\Delta\varphi$ distribution. If the significance is larger than three, the toward-leading yield is measured: the $\mathrm{K}^0_{\mathrm{S}}$ toward-leading yield is measured for $p_{\mathrm{T}} > 0.5(0.8)$ GeV/c, and the $\Xi^{\pm}$ toward-leading for $p_{\mathrm{T}} > 1.0(1.5)$ GeV/c, depending on the multiplicity class.

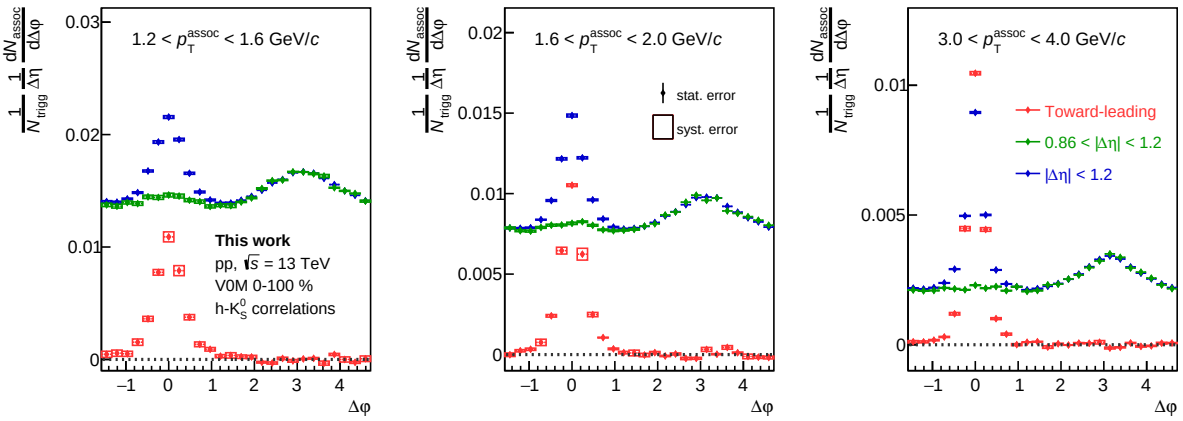

Figure 4.29: Fully corrected $\Delta\varphi$ projections in different p_{T} intervals of the $\mathrm{K}^0_{\mathrm{S}}$ in minimum bias pp collisions at $\sqrt{s} = 13$ TeV. The blue distributions are the fully corrected projections obtained from the $|\Delta\eta| < 1.2$, the green distributions are obtained from $0.86 < |\Delta\eta| < 1.2$, and the red distributions are the toward-leading distributions ($|\Delta\eta| < 0.86$), obtained as described in Section 4.6.5. Error bars and boxes show the statistical and systematic uncertainties, respectively.

4.7.2 Study of the systematic effects on the p_{T} spectra

This section provides a description of the several sources of systematic uncertainty which are evaluated by comparing the default p_{T} spectra with the ones obtained by varying the default selections, as described in the following.

One source of systematic uncertainty is related to the choice of the $\Delta\varphi$ interval where the $\Delta\varphi$ projections are integrated in order to obtain the toward-leading and transverse-to-leading yields. As for the choice of the $\Delta\eta$ region, this source does not affect the full yields, which are

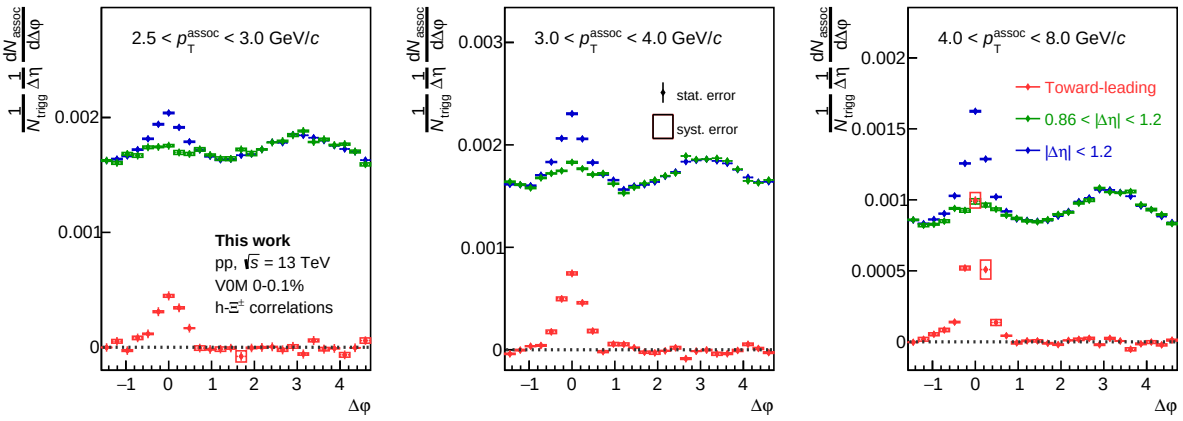

Figure 4.30: Fully corrected $\Delta\varphi$ projections in different p_{T} intervals of the $\Xi^{\pm}$ in minimum bias pp collisions at $\sqrt{s} = 13$ TeV. The blue distributions are the fully corrected projections obtained from the $|\Delta\eta| < 1.2$, the green distributions are obtained from $0.86 < |\Delta\eta| < 1.2$, and the red distributions are the toward-leading distributions, obtained as described in Section 4.6.5. Error bars and boxes show the statistical and systematic uncertainties, respectively.

obtained by definition from the whole $\Delta\varphi$ interval ($-\pi/2 < \Delta\varphi < 3/2\pi$). Two(four) regions different from the default one are chosen for the toward-leading (transverse-to-leading) yield extraction, as indicated in Table 4.12.

$\Delta\varphi$ **interval**	**Toward-leading**	**Transverse-to-leading**
Default selection	$\lvert\Delta\varphi\rvert < 1.1$	$0.96 < \lvert\Delta\varphi\rvert < 1.8$
Selection 1	$\lvert\Delta\varphi\rvert < 1.33$	$1.1 < \lvert\Delta\varphi\rvert < 1.8$
Selection 2	-	$0.96 < \lvert\Delta\varphi\rvert < 2.05$
Selection 3	-	$1.1 < \lvert\Delta\varphi\rvert < 2.05$

Table 4.12: Variations of the $\Delta\varphi$ interval in order to determine the associated systematic uncertainty.

To determine if a variation of the $\Delta\varphi$ region gives a significant variation of the yield, the Barlow check is applied. The Barlow variable B is defined as in equation 4.18.

In this case the effect is considered significant if the condition $|B| > 2$ is verified in three or more p_{T} intervals: the probability that this happens as a consequence of statistical fluctuations only is $P(k \geq 3, n = 9) = 0.008$ for $\mathrm{K}^0_{\mathrm{S}}$ and $P(k \geq 3, n = 7) = 0.004$ for $\Xi^{\pm}$.

The significant variations are taken into account to compute the systematic uncertainty in each of the p_{T} intervals:

$$\sigma_{SYS,\Delta\varphi} = |y_{Max} - y_{Min}|/2, \tag{4.22}$$

where y_{Max} and y_{Min} are the maximum and the minimum yields obtained in a given p_{T} interval by applying the different $\Delta\varphi$ selections which give a significant variation.

All the variations of the transverse-to-leading $\Delta\varphi$ interval are significant for both h-$\mathrm{K}^0_{\mathrm{S}}$ and h-$\Xi^{\pm}$ correlation. The relative uncertainty increases with p_{T} up to 2% for both particles.

The variation of the toward-leading yield is significant for K^0_S only in minimum bias pp collisions at $\sqrt{s} = 13$ TeV, while it is not significant for h-$\Xi^{\pm}$correlation. The relative uncertainty decreases with p_T from about 2% down to $\sim 0.1\%$ for $p_T > 4$ GeV/c. The Barlow variables B are observed to be correlated with p_T, as they are either positive or negative in almost all the p_T intervals. This indicates that the systematic uncertainty associated to the choice of $\Delta\varphi$ is correlated across p_T.

Another systematic effect is related to the choice of the function used to fit the background of the invariant mass distributions of K^0_S and $\Xi^{\pm}$ candidates. A variation of the background fit function translates into a difference in the purity of the sample of selected K^0_S and $\Xi^{\pm}$. It also affects the σ_G of the Gaussian functions used to fit the signal (see Section 4.5) and, consequently, the invariant mass interval within which candidates are selected. To quantify the systematic uncertainty related to this source, for both K^0_S and $\Xi^{\pm}$ candidates the fit to the background is performed with a second degree polynomial and the invariant mass interval in which the fit is performed is varied. For K^0_S, the variation of the background fit function mainly translates into a difference in the estimate of the number of fake candidates, whereas the total number of candidates, which depends on the value of the Gaussian σ, does not change significantly. Therefore, the systematic uncertainty is computed as the half-difference of the maximum variation of the purity P:

$$\sigma_{SYS,purity} = |P_{Max} - P_{Min}|/2. \tag{4.23}$$

The relative systematic uncertainty increases with p_T up to 1.5% and does not depend on the multiplicity class. For $\Xi^{\pm}$, the variation of the purity is smaller than 0.4% and decreases with p_T, while the variation of the σ determines a variation of the total number of candidates of about 0.5%. Taking into account both effects, which are correlated with one another, the resulting relative systematic uncertainty is set to 0.5% in all p_T intervals and multiplicity classes. For both K^0_S and $\Xi^{\pm}$, this source of uncertainty is observed to be correlated across p_T.

Another source of systematic uncertainty is related to the MC simulation used to calculate the K^0_S and $\Xi^{\pm}$ efficiencies. In principle, the efficiency should not depend on the MC simulation, since it is related to detector effects only and not to the event generator implemented in the simulation. However, a different multiplicity distribution of events might give a difference in the efficiency, if the latter depends on the multiplicity, as observed for K^0_S (see Section 4.5). To test this effect, the K^0_S and $\Xi^{\pm}$ efficiencies are computed using a MC simulation based on EPOS LHC [87]. Indeed, the $\Xi^{\pm}$ efficiencies computed with the two MC simulations are compatible within uncertainties, as expected since they do not show any multiplicity dependence. On the contrary, the K^0_S efficiencies differ up to 1%. Therefore, in order to take this effect into account, a 1% systematic uncertainty is added in quadrature to the K^0_S spectra.

The method used to subtract the contribution of fake $\Xi^{\pm}$represents another source of systematic uncertainty. As described in Chapter 4.6.4, the method based on the sidebands of the invariant mass distribution can only be applied in the sample of high multiplicity pp collisions at $\sqrt{s} = 13$ TeV, whereas in the two other data samples the angular correlation distributions are multiplied by the purity of the $\Xi^{\pm}$ sample. In order to assess the systematic uncertainty related to this simplified procedure, both methods are applied to the 0-100% multiplicity class of minimum bias pp collisions at $\sqrt{s} = 13$ TeV, which has enough events for this purpose. The difference between the spectra obtained with the two methods is significant according to the Barlow prescription, and their relative half-difference is assigned as a systematic un-

certainty to the spectra in all multiplicity classes. The relative uncertainty decreases with increasing p_{T}, it is smaller than 1% for full and transverse-to leading production and smaller than 3% for toward-leading production. This source of uncertainty is uncorrelated across p_{T} for transverse-to-leading production, whereas it is correlated across p_{T} for toward-leading and full production, as a consequence of the different shape at low p_{T} ($p_{\mathrm{T}} \lesssim 2.5$ GeV/c) of the near-side jet peak obtained from the sidebands and from the peak region of the invariant mass distribution.

Another source of uncertainty is related to the method applied to extract the $\Xi^{\pm}$ toward-leading yield. To evaluate the uncertainty related to the applied procedure (see Section 4.6.5), the toward-leading p_{T} spectra of $\Xi^{\pm}$ are compared to those obtained using the default procedure. The comparison is performed in the [2-2.5) GeV/c interval, where the number of $\Xi^{\pm}$ candidates is large enough to allow for the application of both methods. This systematic effect is found to be significant at high multiplicity, namely in the 0-5% multiplicity class of minimum bias pp collisions at $\sqrt{\mathrm{s}} = 13$ TeV, in the 0-10% class of minimum bias pp collisions at $\sqrt{\mathrm{s}} = 5.02$ TeV, and in all multiplicity classes of the sample of high multiplicity pp collisions at $\sqrt{\mathrm{s}} = 13$ TeV. The half-difference between the yields gives the corresponding systematic uncertainty, which is also assigned to the lower p_{T} intervals where the jet extraction procedure differs from the default one. This uncertainty amounts to 5-10%, depending on the multiplicity class, and is assumed to be correlated across p_{T}, in order to be conservative.

The imperfect reproduction of the detector material budget in the MC simulation used to compute the $\mathrm{K}^0_{\mathrm{S}}$ and $\Xi^{\pm}$ efficiencies is taken into account as a possible source of systematic uncertainty. To assess this uncertainty, the $\mathrm{K}^0_{\mathrm{S}}$ and $\Xi^{\pm}$ efficiencies are computed using a MC with a different dependence of the material budget on the radial distance from the interaction point. This MC is anchored to minimum bias pp collisions at $\sqrt{\mathrm{s}} = 13$ TeV. The relative semi-difference between the efficiency such obtained and the default one is taken as a systematic uncertainty. For $\mathrm{K}^0_{\mathrm{S}}$, it decreases with p_{T} from a maximum of 5% at low p_{T} down to values $< 1\%$ at high p_{T}, and it shows a similar trend in all multiplicity classes. The systematic uncertainty computed in the 0-100% multiplicity class is assigned to all multiplicity classes of pp collisions at $\sqrt{\mathrm{s}} = 5.02$ TeV, and the one computed in the 0-5% multiplicity class is assigned to the spectra measured in high multiplicity pp collisions at $\sqrt{\mathrm{s}} = 13$ TeV. The difference between the $\Xi^{\pm}$ efficiencies computed with the two MC simulations does not depend on the multiplicity class and on p_{T}, and is approximately equal to 2%. A systematic uncertainty of 2% is added in quadrature to the $\Xi^{\pm}$ p_{T} spectra.

Finally, the systematic uncertainties related to pile-up rejection are inherited from the analysis of (multi-)strange hadron production in pp collisions at $\sqrt{\mathrm{s}} = 13$ TeV [57]. Pile-up collisions occurring within the same bunch crossing are removed by rejecting events with multiple vertices reconstructed in the SPD (see Section 4.3). The effect of residual contamination from in-bunch pile-up events is estimated in Ref. [57] by varying the pile-up rejection criteria. In this analysis, a relative systematic uncertainty of 2% is assigned to both $\mathrm{K}^0_{\mathrm{S}}$ and $\Xi^{\pm}$ spectra. To reject $\mathrm{K}^0_{\mathrm{S}}$ and $\Xi^{\pm}$ candidates from out-of-bunch pile-up events, at least one of their daughter tracks is required to be matched in the SPD or in the TOF (see Section 4.5). In Ref. [57], the systematic uncertainty associated to out-of-bunch pile-up rejection is evaluated by changing the matching scheme with these detectors. In this analysis, a relative uncertainty of 1.2% (2%) is assigned to $\mathrm{K}^0_{\mathrm{S}}$ ($\Xi^{\pm}$) spectra in all p_{T} intervals and multiplicity classes.

Hadron	K^0_S		
p_T (GeV/c)	≈0.6	≈1.8	≈3.5
Topological selections	0.1-0.4% (2%)	0.3-1.0% (2%)	0.3-1.0% (1%)
Trigger particle DCAz selection	< 0.2% (<0.5%)	< 0.2% (<0.5%)	< 0.2% (<0.5%)
Choice of $\Delta\eta$ region	0.6% (2%)	0.6% (1.3%)	0.7% (0.6%)
Choice of $\Delta\varphi$ region	0.6% (2%)	1% (0.7%)	2% (0.3%)
Background fit function	< 0.1%	0.3%	0.5%
Monte Carlo for efficiency	1%	1%	1%
Residual in-bunch pile-up	2%	2%	2%
Out-of-bunch pile-up track rejection	1.2%	1.2%	1.2%
Material budget	2%	0.2%	0.4%

Table 4.13: Summary of the relative systematic uncertainties of K^0_S p_T spectra. The values in parentheses refer to the toward-leading spectra and are reported only when a difference from the transverse-to-leading and full spectra is observed. No significant centre-of-mass energy and multiplicity dependence is observed, with the exception of the uncertainty associated to topological selections, for which an interval which includes the spread with multiplicity and the difference between full and transverse-to-leading spectra is reported.

Hadron	$\Xi^{\pm}$		
p_T (GeV/c)	≈0.6	≈1.8	≈3.5
Topological selections	2-3%	0.5% (5%)	0.5% (3%)
Trigger particle DCAz selection	< 0.2%	< 0.2% (<0.5%)	< 0.2% (<0.5%)
Choice of $\Delta\eta$ region	-	- (2%)	- (2%)
Choice of $\Delta\varphi$ region	1%	1% (-)	1.2% (-)
Background fit function	0.5%	0.5%	0.5%
Fake $\Xi^{\pm}$ subtraction	0.8%	0.4% (2.5%)	0.3% (1.2%)
Out-of-jet subtraction	-	5-10%	-
Residual in-bunch pile-up	2%	2%	2%
Out-of-bunch pile-up track rejection	2%	2%	2%
Material budget	2%	2%	2%

Table 4.14: Summary of the relative systematic uncertainties of $\Xi^{\pm}$ p_T spectra. The values in parentheses refer to the toward-leading spectra and are reported only when a difference from the transverse-to-leading and full spectra is observed. Since the toward-leading spectra are measured for $p_T > 1.5(2)$GeV/c, their uncertainties at $p_T > 0.6$GeV/c are not reported. No significant centre-of-mass energy and multiplicity dependence is observed, with the exception of the uncertainty associated to topological selections, for which an interval which includes the spread with multiplicity and the difference between full and transverse-to-leading spectra is reported. The uncertainty related to out-of-jet subtraction is assigned only to the spectra measured in high multiplicity classes (see text for the details).

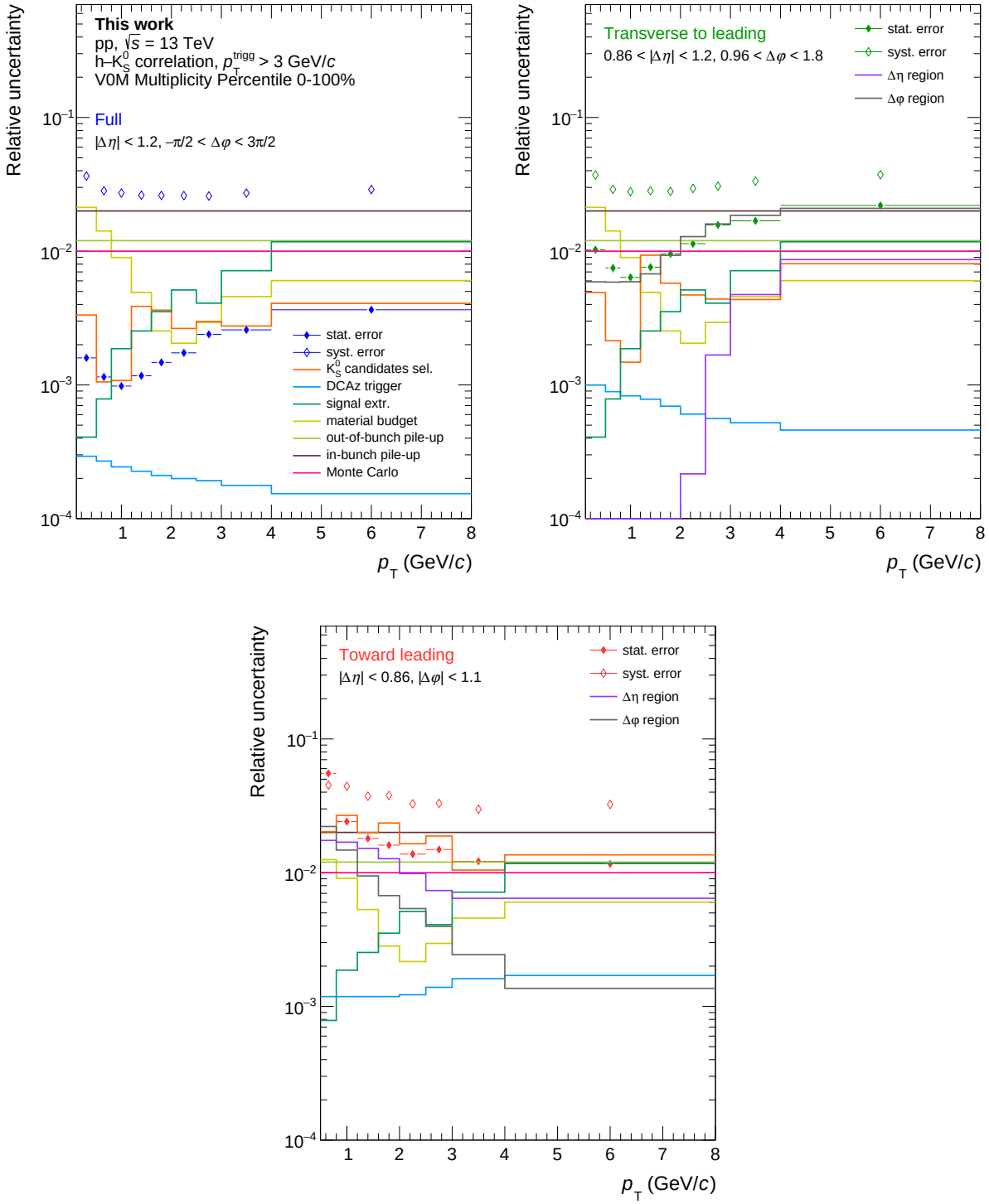

Figure 4.31: Relative uncertainties of the K^0_S p_T spectra measured in minimum bias pp collisions at $\sqrt{s} = 13$ TeV. The relative statistical error is represented by the filled markers, the total relative systematic uncertainty by the empty markers. Different colours are associated to the different systematic effects which have been considered, as indicated in the legend. See the text for details.

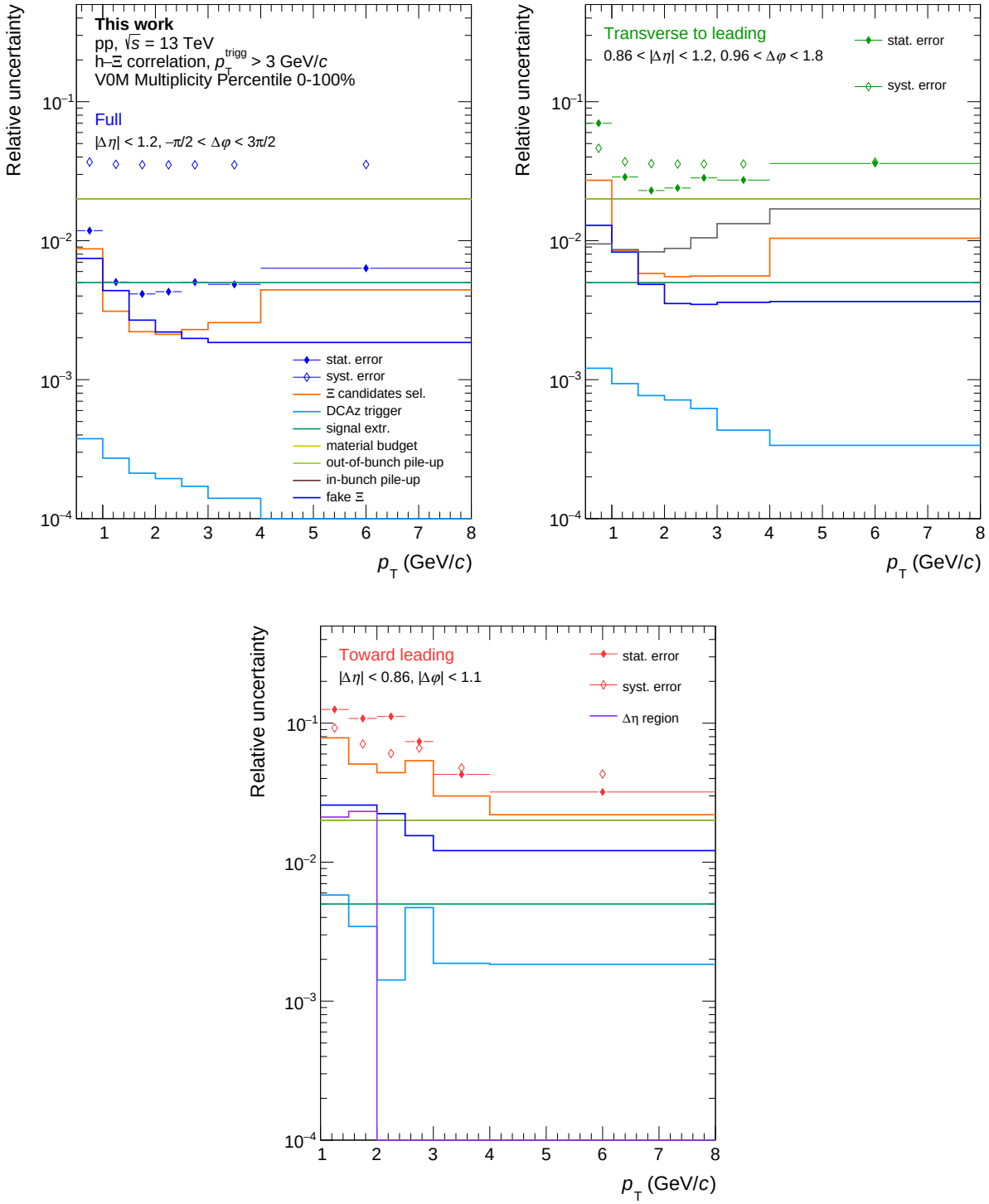

Figure 4.32: Relative uncertainties of the $\Xi^{\pm}$ p_{T} spectra measured in minimum bias pp collisions at $\sqrt{s} = 13$ TeV. The relative statistical error is represented by the filled markers, while the total relative systematic uncertainty by the empty markers. Different colours are associated to the different systematic effects which have been considered, as indicated in the legend. See the text for details.

4.7.3 Determination of the multiplicity-uncorrelated systematic uncertainty

Most of the sources of systematic uncertainties taken into account in this analysis are fully correlated across multiplicity, since they determine a variation of the yield which does not depend on the multiplicity class. Only two sources of uncertainty, namely the selections applied to identify K^0_S and $\Xi^\pm$ candidates and the choice of the $\Delta\varphi$ interval, are considered to be partially uncorrelated across multiplicity. In order to determine the fraction of uncertainty which is uncorrelated across multiplicity, the ratio R^m_{var} is computed:

$$R^m_{var} = \frac{y^m_{var}/y^m_{def}}{y^{0-100\%}_{var}/y^{0-100\%}_{def}}, \tag{4.24}$$

where y^m_{def} and $y^{0-100\%}_{def}$ are the default yields measured in a given p_T interval in the multiplicity class m and 0-100%, respectively, and y^m_{var} and $y^{0-100\%}_{var}$ are the yields obtained by applying a systematic variation. The error σ_R associated to the R^m_{var} ratio is computed taking into account the correlation between the default yield and the one obtained with a systematic variation, and the correlation between the yield in a multiplicity class and the yield measured in the 0-100% multiplicity class.

If a source of uncertainty is fully correlated across multiplicity, $R^m_{var} = 1$. The deviation of R^m_{var} from unity gives the relative uncertainty uncorrelated across multiplicity:

$$\sigma^m_{uncorr} = |R^m_{var} - 1| \tag{4.25}$$

Only variations from unity larger than two σ_R are considered statistically significant.

To evaluate the uncorrelated fraction of the systematic uncertainty associated to the topological selections, the p_T spectra are computed with the loosest and the tightest topological selections listed in Tables 4.6 and 4.7 for K^0_S and $\Xi^\pm$, respectively. These selections are expected to give the maximum possible yield variation. The R^m_{var} factors are computed for both selections, and in each p_T interval the maximum deviation from one is used to compute the uncorrelated uncertainty:

$$\sigma^{m,p_\mathrm{T}}_{uncorr} = |R^m_{var} - 1|_{max} \times 2/\sqrt{12}, \tag{4.26}$$

where the factor $2/\sqrt{12}$ is applied since it is assumed that R^m_{var} is uniformly distributed between the maximum values obtained with the loosest and the tightest selections. For K^0_S, the fraction of uncorrelated uncertainty increases with p_T from 0.15 up to 0.9 and does not show any significant dependence on the multiplicity class. For $\Xi^\pm$, the fraction of uncorrelated uncertainty covers the range 0.1 to 0.5 and shows a decrease with multiplicity for $p_\mathrm{T} < 3$ GeV/c. For both particles, the fractions evaluated for the full p_T spectra are also applied to the transverse-to-leading and toward-leading spectra, whose statistical uncertainties are too large to provide a statistically significant variation of R^m_{var} from unity.

To evaluate the uncorrelated fraction of the systematic uncertainty associated to the $\Delta\varphi$ selections, the R^m_{var} factors are computed for all the possible variations listed in Table 4.12, and the uncorrelated uncertainty is computed considering the maximum deviation of R^m_{var} from unity:

$$\sigma^{m,p_\mathrm{T}}_{uncorr} = |R^m_{var} - 1|_{max} \times 1/2. \tag{4.27}$$

The factor 1/2 is applied since the total systematic uncertainty associated to the $\Delta\varphi$ selection is given by the half-difference between the maximum variation of the yield and the

default yield. For the toward-leading production the fraction of uncorrelated uncertainty is zero for both particles, whereas for the transverse-to-leading production the fraction increases with multiplicity.

On average, the uncorrelated fraction of the total systematic uncertainty amounts to approximately 3%(5%), 10%(20%) and 25%(25%) for the full, transverse-to-leading and toward-leading production of $\mathrm{K}^0_{\mathrm{S}}$ ($\Xi^{\pm}$).

4.8 Final corrections applied to the p_{T} spectra

A final correction factor is applied to the p_{T} spectra in order to take into account the efficiency with which events with a trigger particle are selected. Indeed, due to track inefficiencies, a reconstructed trigger particle satisfying the selections reported in Table 4.1 might not be found in a fraction of the events which actually contain a charged primary particle with $p_{\mathrm{T}} > 3$ GeV/c, i.e. a generated trigger particle. To take this effect into account, a correction factor is computed using a MC simulation. The correction factor depends on the efficiency of trigger particle reconstruction and on the possible difference between the $\mathrm{K}^0_{\mathrm{S}}$ ($\Xi^{\pm}$) spectra measured in events with a reconstructed trigger particle and those measured in events with a generated trigger particle.

The corrected spectra are given by:

$$\frac{1}{\Delta\eta\Delta\varphi}\frac{1}{N_{trigg}}\frac{\mathrm{d}N}{\mathrm{d}p_{\mathrm{T}}} = \frac{1}{\Delta\eta\Delta\varphi}\frac{1}{N^{reco}_{trigg}}\frac{\mathrm{d}N}{\mathrm{d}p_{\mathrm{T}}} \times \frac{\epsilon_{trigg\ event}}{\epsilon_{part}(p_{\mathrm{T}})}, \tag{4.28}$$

where

$$\epsilon_{trigg\ event} = \frac{N^{reco}_{trigg}}{N^{gen}_{trigg}} \tag{4.29}$$

and

$$\epsilon_{part}(p_{\mathrm{T}}) = \frac{\frac{\mathrm{d}N^{gen}}{dp_{\mathrm{T}}}(\text{events with reconstructed trigger particle})}{\frac{\mathrm{d}N^{gen}}{\mathrm{d}p_{\mathrm{T}}}(\text{events with generated trigger particle})}, \tag{4.30}$$

where $\epsilon_{trigg\ event}$ is the efficiency of events with a trigger particle, that is the fraction of events with a generated trigger particle in which a reconstructed trigger particle is found. Figure 4.33 shows $\epsilon_{trigg\ event}$ as a function of the multiplicity class. It is approximately 85% and it shows an increase with multiplicity of about 2% due to the larger probability of finding a charged particle with $p_{\mathrm{T}} > 3$ GeV/c in events characterised by larger multiplicity. It can also be observed that $\epsilon_{trigg\ event}$ measured in pp collisions at $\sqrt{\mathrm{s}} = 13$ TeV is $\sim 2\%$ larger than in pp collisions at $\sqrt{\mathrm{s}} = 5.02$ TeV, since for the same V0M percentile values the charged particle multiplicity is larger in collisions with a larger centre-of-mass energy. $\epsilon_{part}(p_{\mathrm{T}})$ is the ratio between the spectra of generated $\mathrm{K}^0_{\mathrm{S}}$ ($\Xi^{\pm}$) measured in events with a reconstructed trigger particles and the spectra of generated $\mathrm{K}^0_{\mathrm{S}}$ ($\Xi^{\pm}$) measured in events with a generated trigger particle. $\epsilon_{part}(p_{\mathrm{T}})$ is computed by repeating the full h-$\mathrm{K}^0_{\mathrm{S}}$(h-$\Xi^{\pm}$) correlation analysis using MC events, considering as associated particles the generated particles labelled as true $\mathrm{K}^0_{\mathrm{S}}$ ($\Xi^{\pm}$) in the MC, and as trigger particles the reconstructed ones for the numerator and the generated ones for the denominator. The generated trigger particles are required to be pions, kaons or protons, in order to consider only the particle species which are taken as reconstructed trigger particles in the data: indeed, multi-strange hadrons are not tracked with the ALICE detector. $\epsilon_{part}(p_{\mathrm{T}})$ is evaluated separately for full, transverse-to-leading and toward-leading spectra.

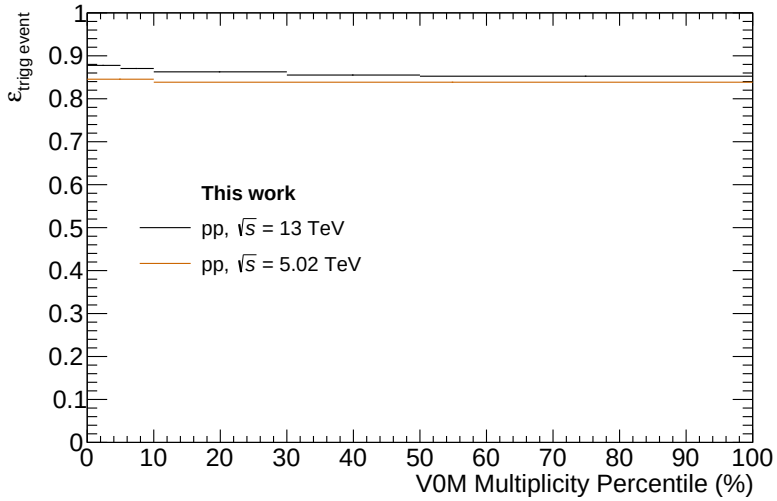

Figure 4.33: $\epsilon_{trigg\ event}$ as a function of the multiplicity class. $\epsilon_{trigg\ event}$ is defined in equation 4.29.

The ratio $\epsilon_{part}(p_{\mathrm{T}})/\epsilon_{Trigg\ event}$, called from now on correction factor, is shown in Figures 4.34 and 4.35 for the full, transverse-to-leading and toward-leading spectra of $\mathrm{K}^0_{\mathrm{S}}$ and $\Xi^{\pm}$ produced in minimum bias pp collisions at $\sqrt{\mathrm{s}} = 13$ TeV. Overall, the correction factors differ from one by less than 3%. The full and transverse-to-leading correction factors increase with p_{T}. On the contrary, the toward-leading correction factors do not show any p_{T} dependence. For this reason, they are fitted with a zero degree polynomial and the parameters of the fit are used as correction factors in all p_{T} intervals, in order to reduce the statistical uncertainty. The correction factors obtained in different multiplicity classes are compatible within uncertainties. Therefore, the p_{T} spectra measured in the high multiplicity sample are corrected with the correction factors measured in the 0-100% multiplicity class. This allows to reduce the statistical uncertainty, as the MC anchored to the high multiplicity sample contains less events. Finally, the correction factors computed in pp collisions at $\sqrt{\mathrm{s}} = 5.02$ TeV are compared to those measured in minimum bias pp collisions at $\sqrt{\mathrm{s}} = 13$ TeV. Since no energy dependence is observed, the latter are used to correct the spectra measured in pp collisions at $\sqrt{\mathrm{s}} = 5.02$ TeV, since they have a smaller statistical uncertainty.

To check if the correction factors are affected by any systematic effect related to the choice of the $\Delta\eta$ and $\Delta\varphi$ intervals, the correction factors obtained with different choices of $\Delta\eta$ and $\Delta\varphi$ are compared. The variations are found not to be significant according to the Barlow prescription [156].

To test if all the correction factors applied in the analysis, such as the $\mathrm{K}^0_{\mathrm{S}}$ ($\Xi^{\pm}$) efficiency and the $\epsilon_{trigg\ event}/\epsilon_{part}(p_{\mathrm{T}})$ factor, have been properly computed, a Monte Carlo closure test is performed by comparing the $\mathrm{K}^0_{\mathrm{S}}$ ($\Xi^{\pm}$) spectra obtained by analysing the MC as if it were the data to the spectra of generated $\mathrm{K}^0_{\mathrm{S}}$ ($\Xi^{\pm}$) in events with a generated trigger particle. This procedure is summarised by the ratio R:

$$R = \frac{1}{\Delta\eta\Delta\varphi}\frac{1}{N^{reco}_{trigg}}\frac{\mathrm{d}N}{\mathrm{d}p_{\mathrm{T}}} \times \frac{\epsilon_{trigg\ event}}{\epsilon_{part}(p_{\mathrm{T}})} \Bigg/ \frac{1}{\Delta\eta\Delta\varphi}\frac{1}{N^{gen}_{trigg}}\frac{\mathrm{d}N^{gen}}{\mathrm{d}p_{\mathrm{T}}}, \tag{4.31}$$

where both the numerator and the denominator are computed using a MC simulation based on PYTHIA8 [84]. If all the correction factors applied to the spectra are computed in the correct way, the ratio R should be compatible with one within the statistical uncertainty.

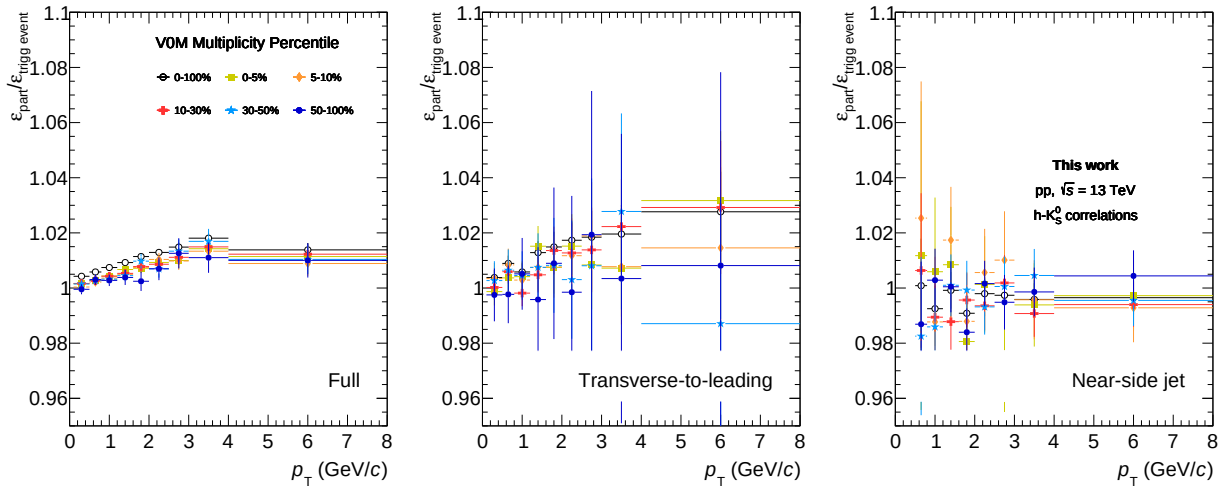

Figure 4.34: Correction factors $\epsilon_{part}(p_{\mathrm{T}})/\epsilon_{Trigg\ event}$ for full (left panel), transverse-to-leading (central panel) and toward-leading (right panel) p_{T} spectra of $\mathrm{K}^0_{\mathrm{S}}$ in minimum bias pp collisions at $\sqrt{s} = 13$ TeV. Different colours refer to different multiplicity classes, as indicated in the legend.

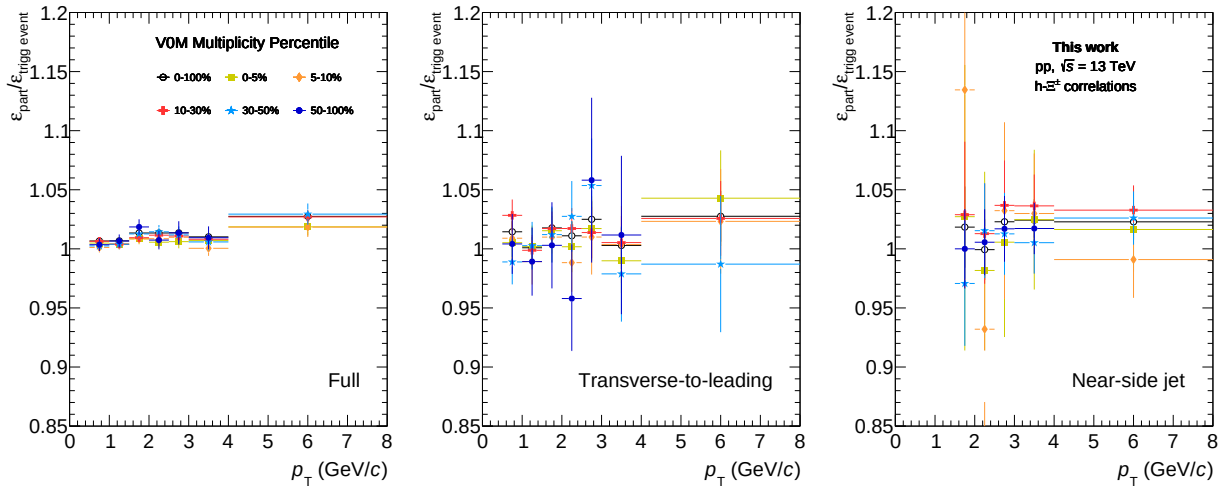

Figure 4.35: Correction factors $\epsilon_{part}(p_{\mathrm{T}})/\epsilon_{Trigg\ event}$ for full (left panel), transverse-to-leading (central panel) and toward-leading (right panel) p_{T} spectra of $\Xi^{\pm}$ in minimum bias pp collisions at $\sqrt{s} = 13$ TeV. Different colours refer to different multiplicity classes, as indicated in the legend.

Figure 4.36 shows the p_{T} dependence of R for the full, transverse-to-leading and toward-leading spectra of $\mathrm{K}^0_{\mathrm{S}}$ in simulated pp collisions at $\sqrt{s} = 13$ TeV on the left, central and right panels, respectively. The error bars show the statistical uncertainty of R, which is calculated taking into account the fact that the numerator is partially correlated with the denominator.

The closure test is verified not only when the correction factor $\epsilon_{trigg\ event}/\epsilon_{part}(p_{\mathrm{T}})$ is computed using a MC simulation based on PYTHIA8 [84] (dark blue markers), but also when it is computed with a MC simulation based on a different model, i.e. EPOS LHC [87] (light blue markers). This indicates that all the corrections applied to the spectra have been correctly computed and show that $\epsilon_{trigg\ event}/\epsilon_{part}(p_{\mathrm{T}})$ does not depend on the model on which the MC simulation is based.

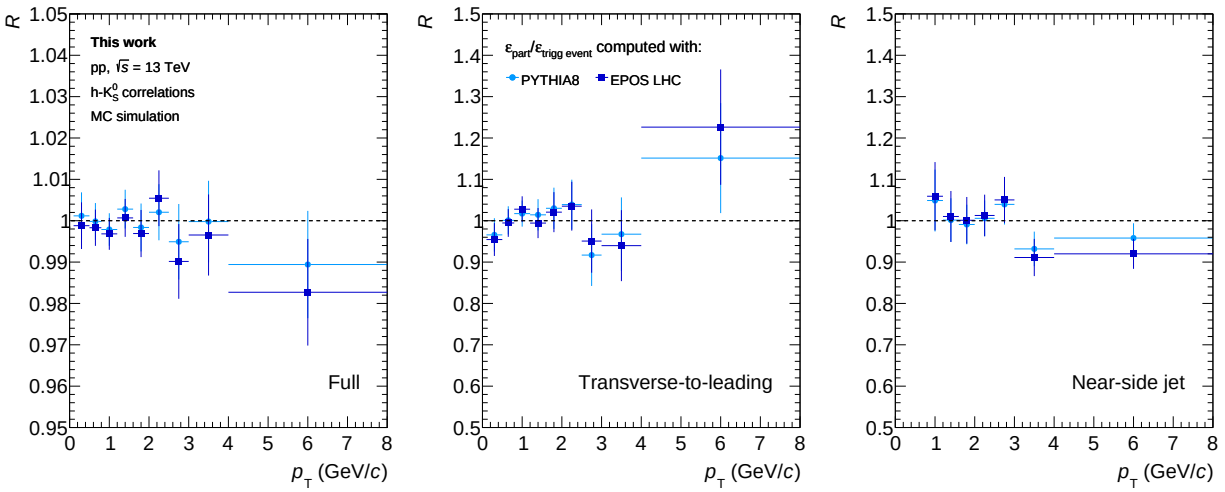

Figure 4.36: Monte Carlo closure test for full (left), transverse-to-leading (centre) and toward-leading (right) spectra of $\mathrm{K}^0_{\mathrm{S}}$ in pp collisions at $\sqrt{s} = 13$ TeV simulated with a MC based on PYTHIA8 [84]. The plots show R (see equation 4.31) as a function of the $\mathrm{K}^0_{\mathrm{S}}$ transverse momentum p_{T}. The error bars represent the statistical uncertainty. The correction factor $\epsilon_{trigg\ event}/\epsilon_{part}(p_{\mathrm{T}})$ used in the calculation of R is computed using a MC simulation based on PYTHIA8 [84] (dark blue markers) or on EPOS LHC [87] (light blue markers). See the text for details.

Chapter 5

K^0_S and $\Xi^\pm$ production in and out of jets in pp collisions at $\sqrt{s} = 13$ TeV and $\sqrt{s} = 5.02$ TeV

This chapter is dedicated to the description of the analysis of the full, transverse-to-leading and toward-leading p_T spectra and p_T-integrated yields of K^0_S and $\Xi^\pm$ produced in pp collisions at $\sqrt{s} = 13$ TeV and in pp collisions at $\sqrt{s} = 5.02$ TeV. The ratios between the $\Xi^\pm$ and the K^0_S spectra and p_T-integrated yields are also discussed, as they provide insight into the strangeness enhancement effect.

5.1 Full, transverse-to-leading and toward-leading p_T spectra of K^0_S and $\Xi^\pm$

The full, transverse-to-leading and toward-leading p_T spectra of K^0_S and $\Xi^\pm$ produced in pp collisions at $\sqrt{s} = 13$ TeV are shown in Figure 5.1 and 5.5. The plots show the spectra obtained from the analysis of minimum bias collisions, as well as those obtained by analysing events collected with the high multiplicity trigger. The spectra measured in pp collisions at $\sqrt{s} = 5.02$ TeV are shown in Figures 5.3 and 5.7 for K^0_S and $\Xi^\pm$, respectively.

In all multiplicity classes and for both centre-of-mass energies, the toward-leading spectra are harder than transverse-to-leading and full spectra, indicating that K^0_S ($\Xi^\pm$) produced in the near-side jet have a larger average transverse momentum than K^0_S ($\Xi^\pm$) produced out of jets. This observation is expected since the near-side jet production is associated to the hardest partonic scattering in the collision. This effect can be more clearly observed in the left (right) panel of Figure 5.9, which shows in the same plot the full, transverse-to-leading and toward-leading spectra of K^0_S ($\Xi^\pm$) measured in minimum bias pp collisions at $\sqrt{s} = 13$ TeV in the 0-100% multiplicity class. It can also be observed that full spectra have very similar characteristics to transverse-to-leading spectra, suggesting that the full production is dominated by the transverse-to-leading one, as will be more clearly shown in Section 5.3.

The ratios between the K^0_S ($\Xi^\pm$) spectra measured in the different multiplicity classes and the one measured in the 0-100% multiplicity classes are shown in Figure 5.2 (Figure 5.6) for the analysis of pp collisions at $\sqrt{s} = 13$ TeV, and in Figure 5.4 (Figure 5.8) for the analysis of pp collisions at $\sqrt{s} = 5.02$ TeV. The transverse-to-leading and full yields increase with the multiplicity in all p_T intervals and at both centre-of-mass energies. The increase

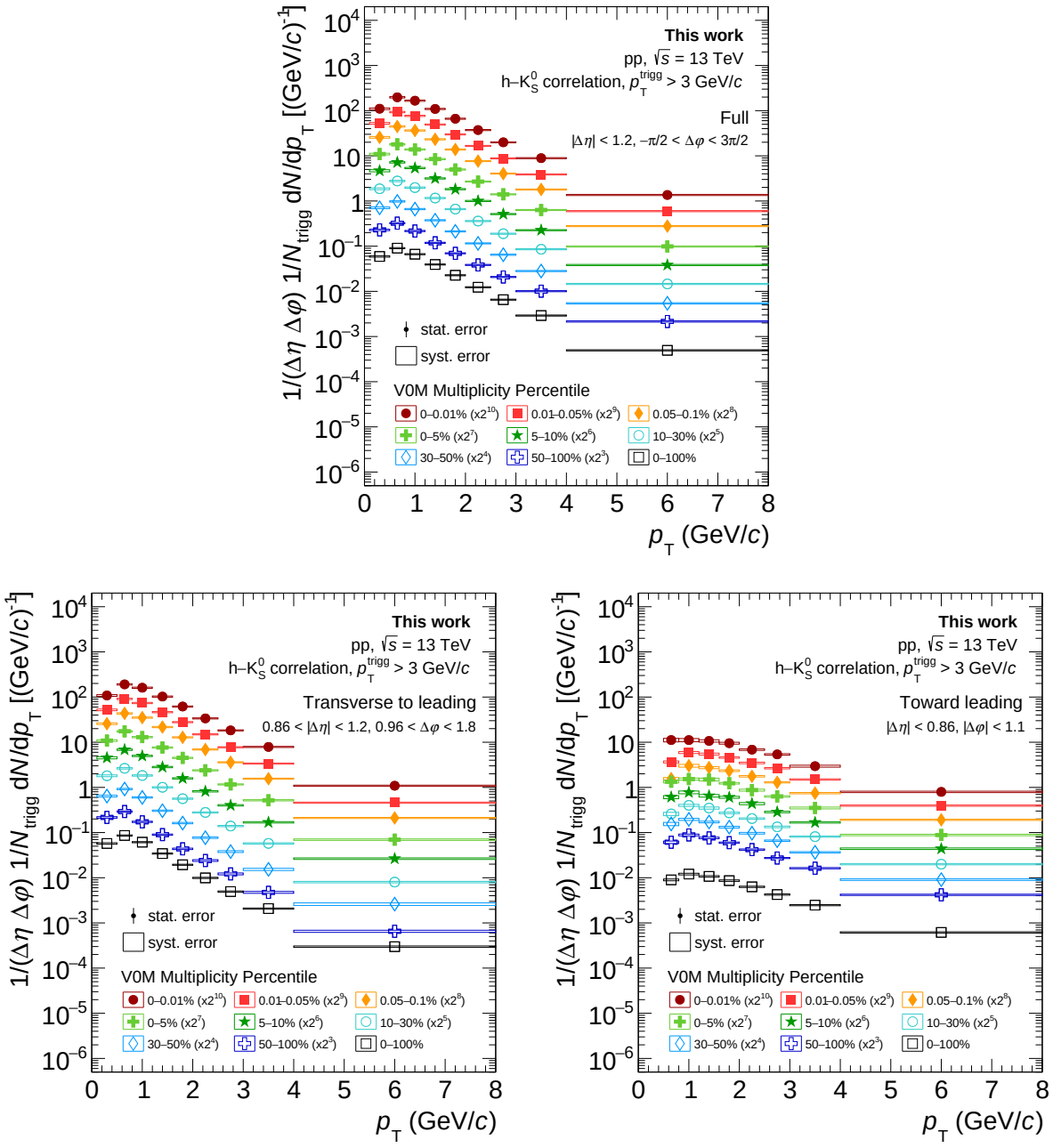

Figure 5.1: Transverse momentum spectra of $\mathrm{K}^0_{\mathrm{S}}$ in pp collisions at $\sqrt{s}$ = 13 TeV. The upper, bottom left and bottom right plots refer to full, transverse-to-leading and toward-leading production, respectively. Different colours refer to different multiplicity classes as indicated in the legend. The statistical errors are represented by the error bars, the systematic uncertainties by the empty boxes.

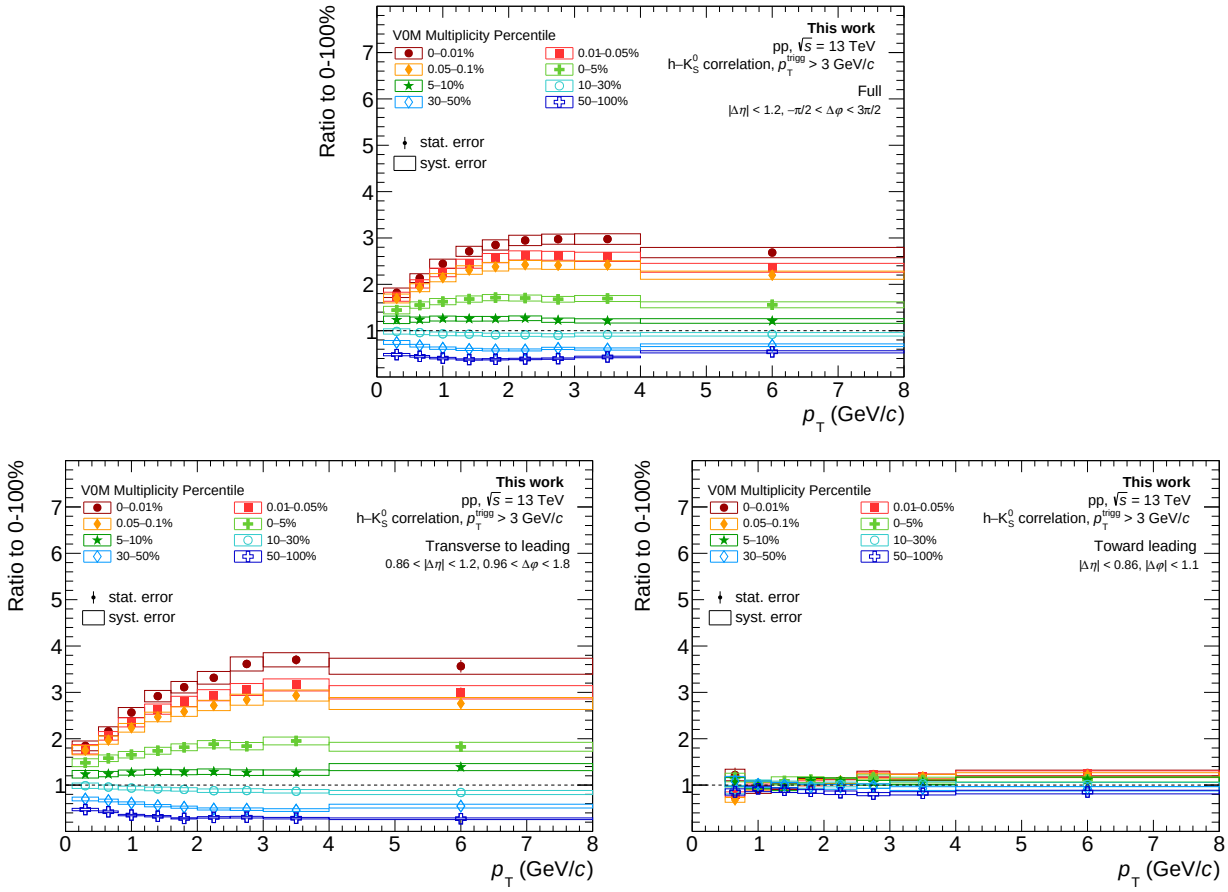

Figure 5.2: Ratios between the $\mathrm{K}^0_{\mathrm{S}}$ spectra in the different multiplicity classes and the $\mathrm{K}^0_{\mathrm{S}}$ spectra in the 0-100% multiplicity class in pp collisions at $\sqrt{s} = 13$ TeV. The upper, bottom left and bottom right plots refer to full, transverse-to-leading and toward-leading production, respectively. Different colours refer to different multiplicity classes as indicated in the legend. The statistical errors are represented by the error bars, the systematic uncertainties by the empty boxes.

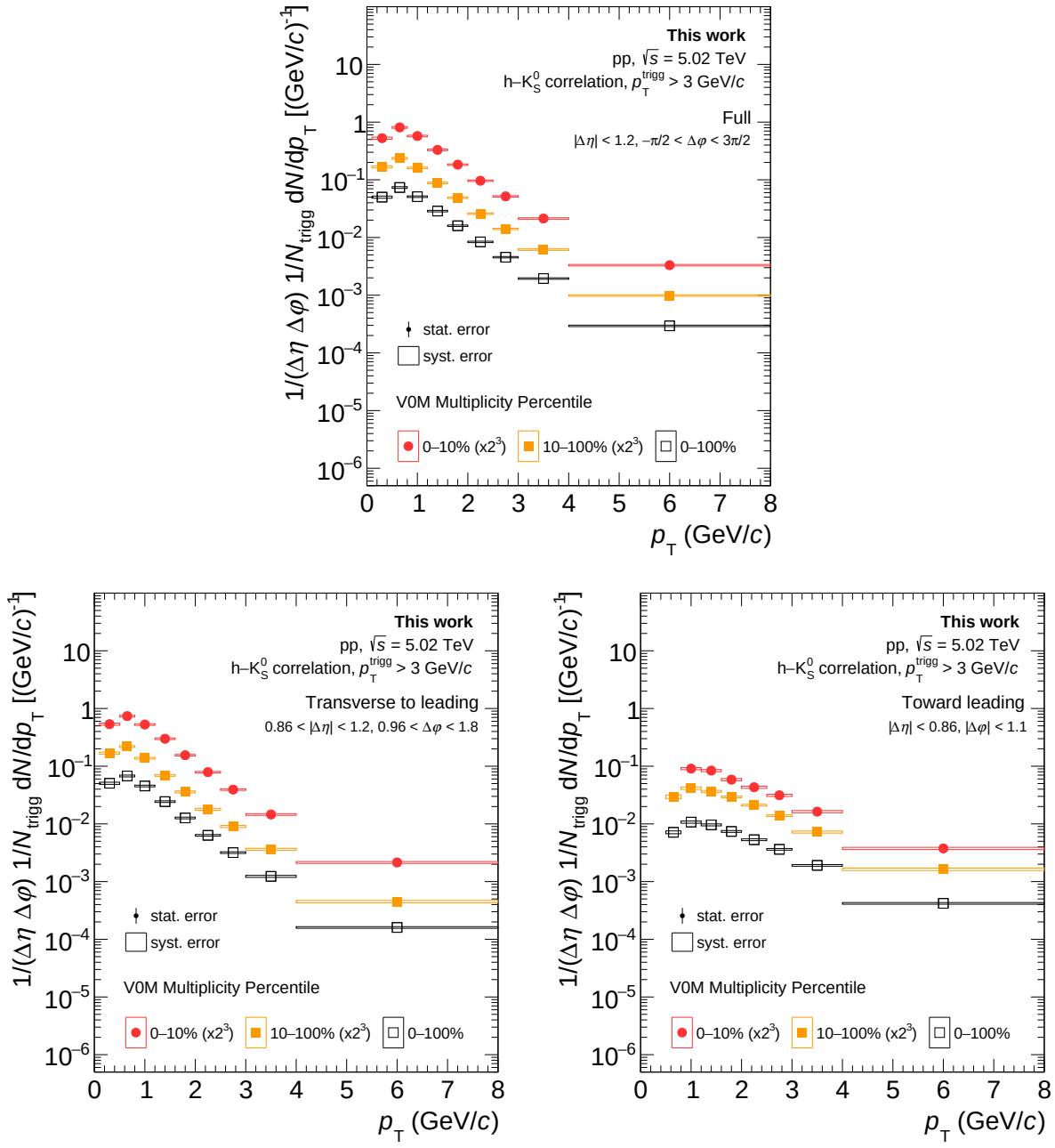

Figure 5.3: Transverse momentum spectra of $\mathrm{K}^0_{\mathrm{S}}$ in pp collisions at $\sqrt{s} = 5.02$ TeV. The upper, bottom left and bottom right plots refer to full, transverse-to-leading and toward-leading production, respectively. Different colours refer to different multiplicity classes as indicated in the legend. The statistical errors are represented by the error bars, the systematic uncertainties by the empty boxes.

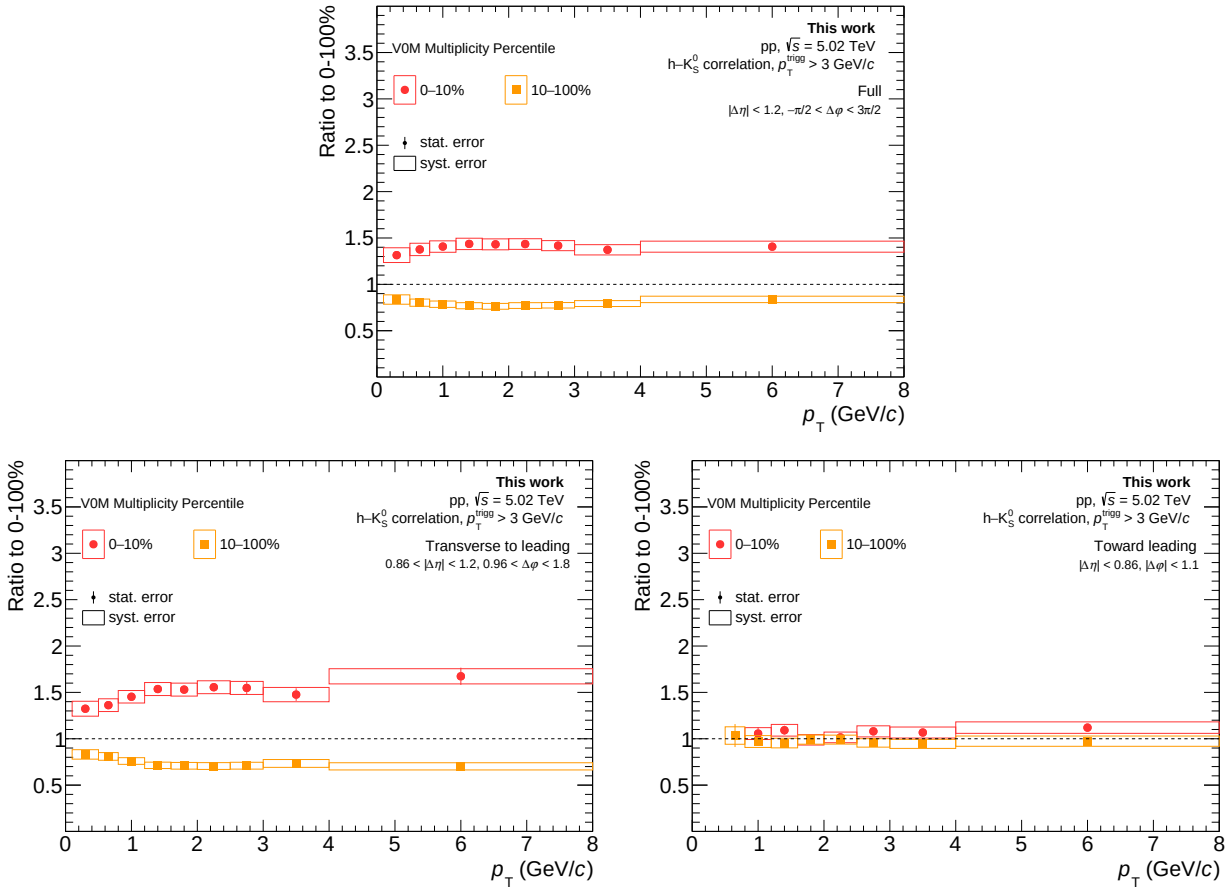

Figure 5.4: Ratios between the $\mathrm{K}^0_{\mathrm{S}}$ spectra in the different multiplicity classes and the $\mathrm{K}^0_{\mathrm{S}}$ spectra in the 0-100% multiplicity class in pp collisions at $\sqrt{s} = 5.02$ TeV. The upper, bottom left and bottom right plots refer to full, transverse-to-leading and toward-leading production, respectively. Different colours refer to different multiplicity classes as indicated in the legend. The statistical errors are represented by the error bars, the systematic uncertainties by the empty boxes.

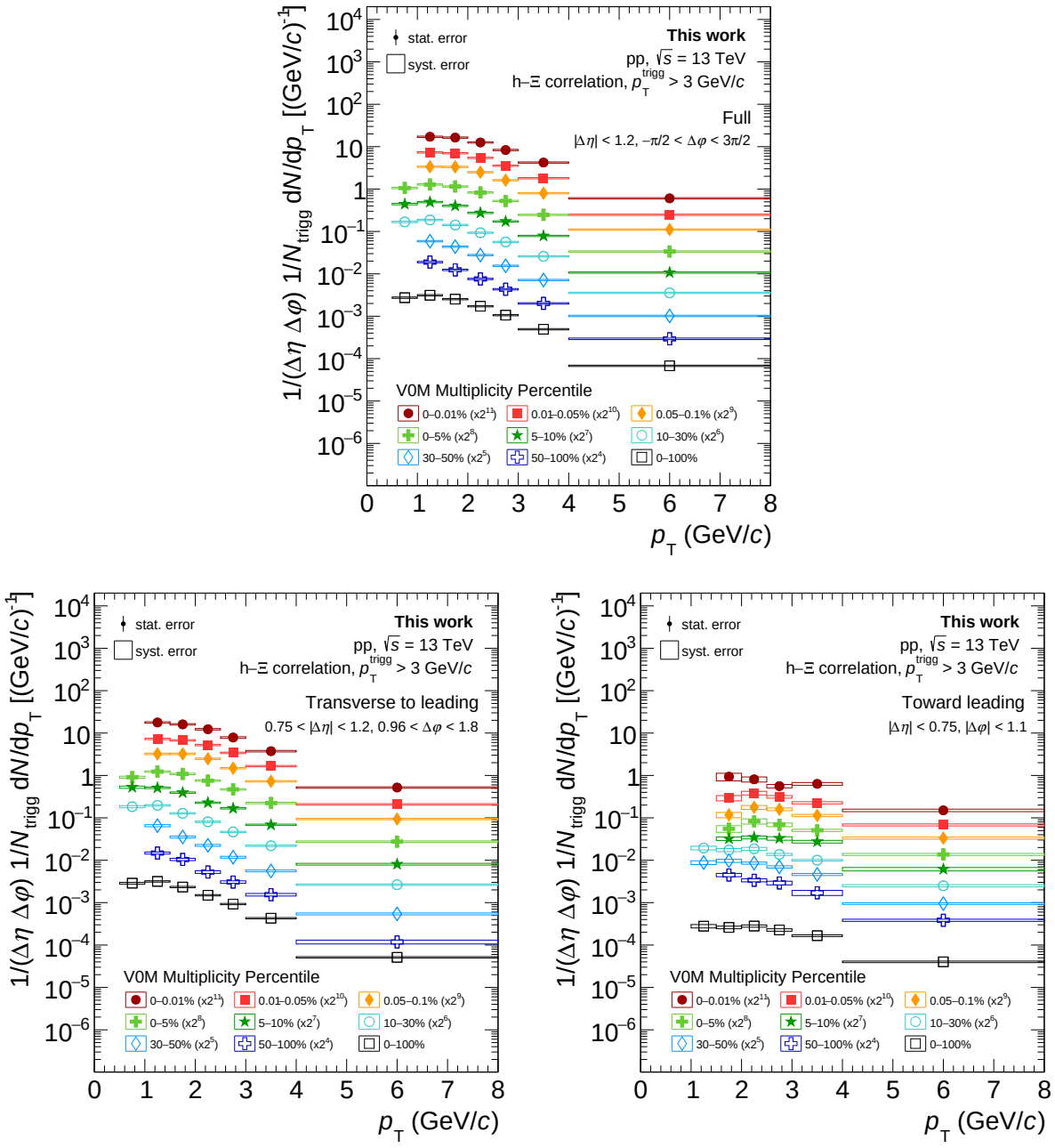

Figure 5.5: Transverse momentum spectra of $\Xi^{\pm}$ in pp collisions at $\sqrt{s}$ = 13 TeV. The upper, bottom left and bottom right plots refer to full, transverse-to-leading and toward-leading production, respectively. Different colours refer to different multiplicity classes as indicated in the legend. The statistical errors are represented by the error bars, the systematic uncertainties by the empty boxes.

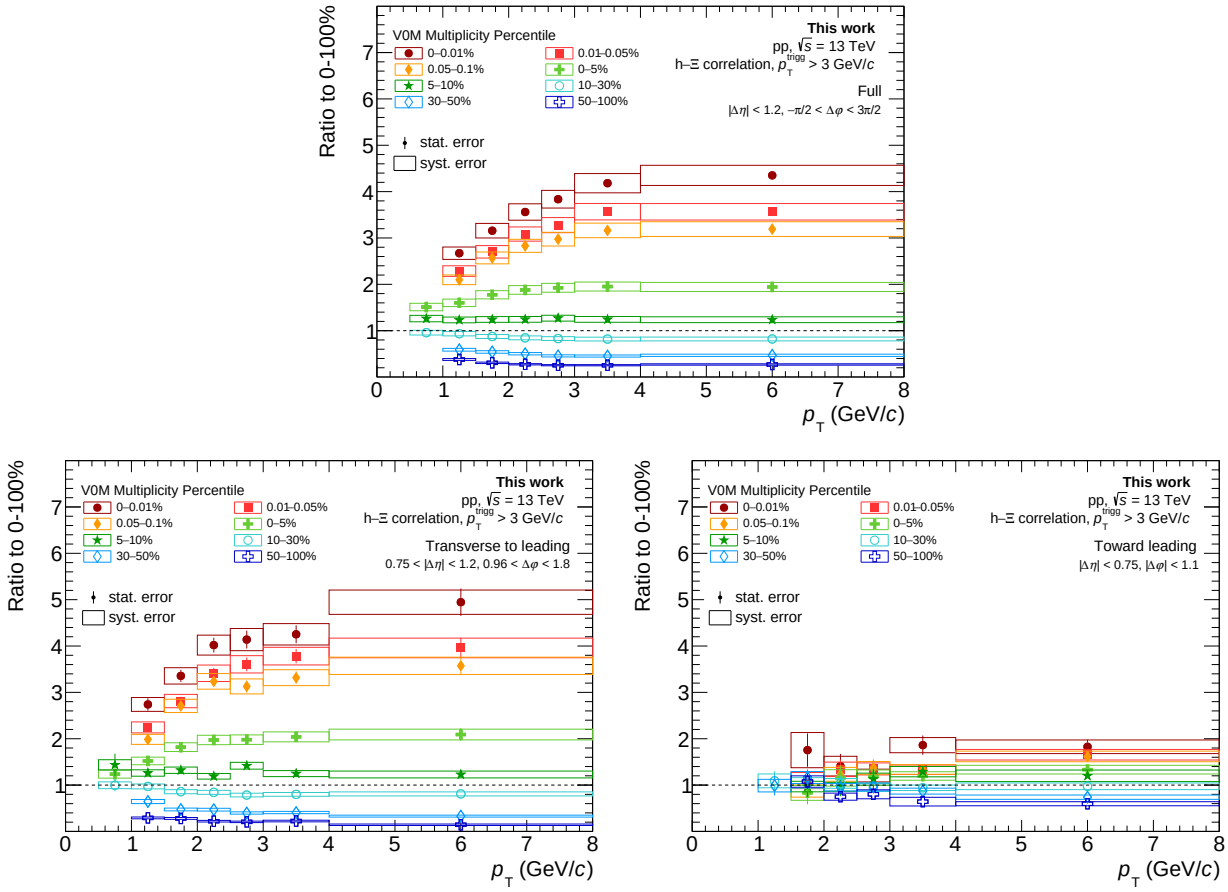

Figure 5.6: Ratios between the $\Xi^{\pm}$ spectra in the different multiplicity classes and the $\Xi^{\pm}$ spectra in the 0-100% multiplicity class in pp collisions at $\sqrt{s} = 13$ TeV. The upper, bottom left and bottom right plots refer to full, transverse-to-leading and toward-leading production, respectively. Different colours refer to different multiplicity classes as indicated in the legend. The statistical errors are represented by the error bars, the systematic uncertainties by the empty boxes.

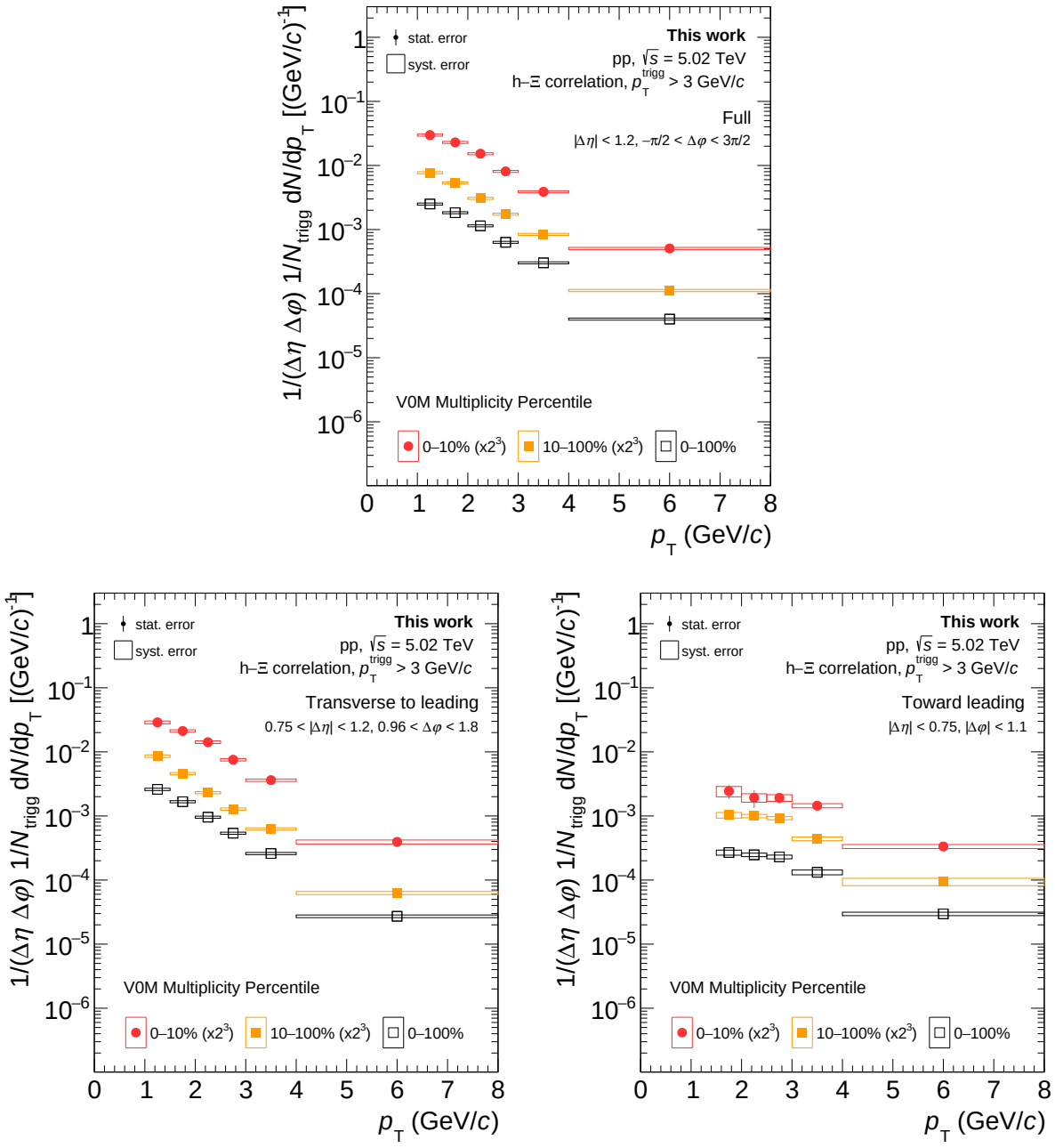

Figure 5.7: Transverse momentum spectra of $\Xi^{\pm}$ in pp collisions at $\sqrt{s} = 5.02$ TeV. The upper, bottom left and bottom right plots refer to full, transverse-to-leading and toward-leading production, respectively. Different colours refer to different multiplicity classes as indicated in the legend. The statistical errors are represented by the error bars, the systematic uncertainties by the empty boxes.

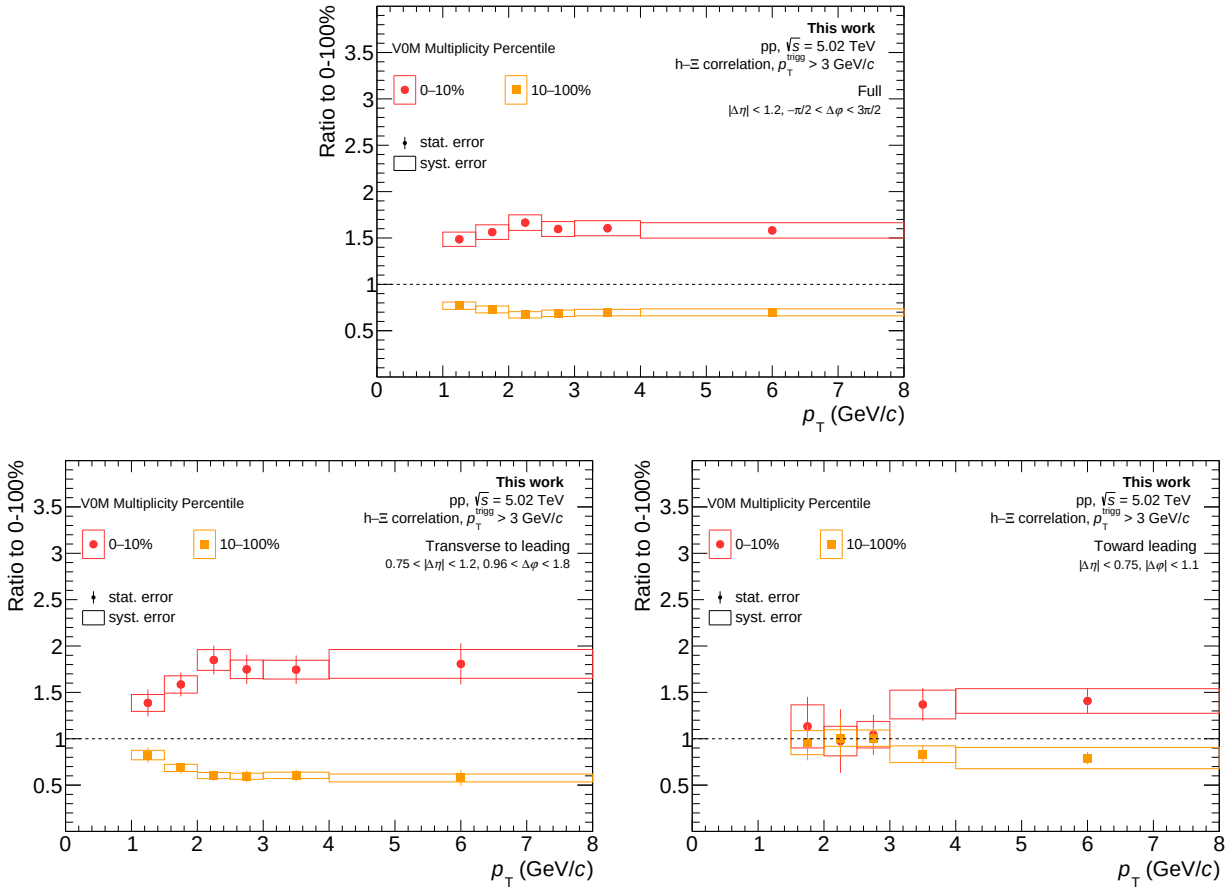

Figure 5.8: Ratios between the $\Xi^{\pm}$ spectra in the different multiplicity classes and the $\Xi^{\pm}$ spectra in the 0-100% multiplicity class in pp collisions at $\sqrt{\mathrm{s}} = 13$ TeV. The upper, bottom left and bottom right plots refer to full, transverse-to-leading and toward-leading production, respectively. Different colours refer to different multiplicity classes as indicated in the legend. The statistical errors are represented by the error bars, the systematic uncertainties by the empty boxes.

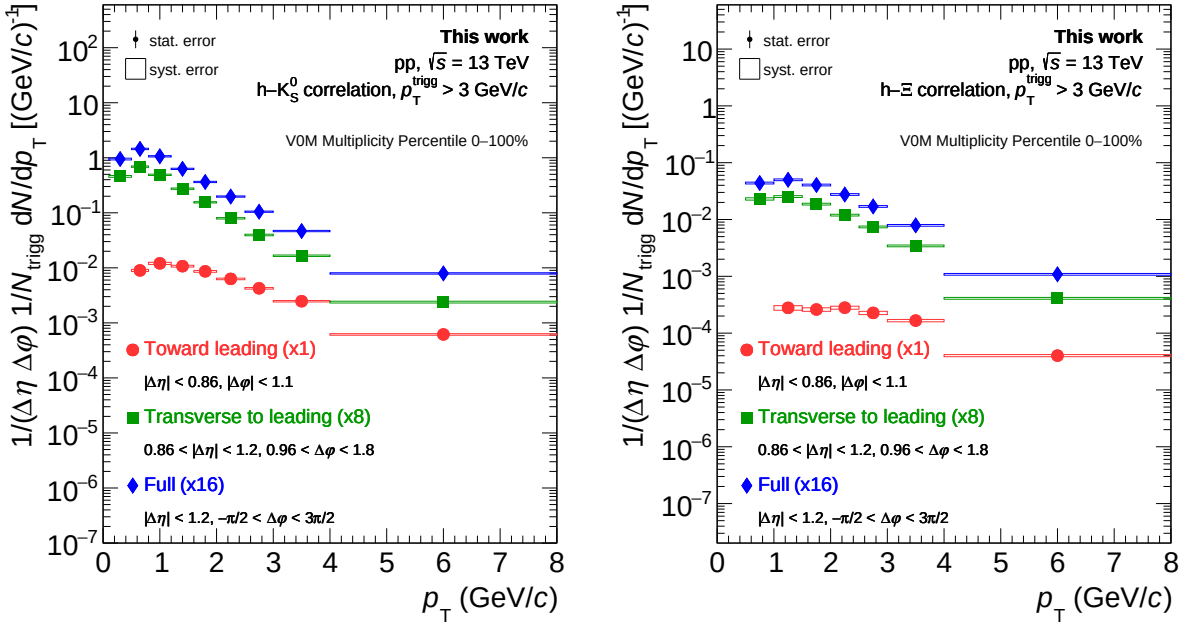

Figure 5.9: Transverse momentum spectra of $\mathrm{K}^0_{\mathrm{S}}$ (left panel) and $\Xi^{\pm}$ (right panel) in minimum bias pp collisions at $\sqrt{s} = 13$ TeV. The blue, green and red distributions are the full, transverse-to-leading and toward-leading p_{T} spectra, respectively. The statistical errors are represented by the error bars, the systematic uncertainties by the empty boxes.

with multiplicity is larger at higher p_{T} values, implying that the spectra are harder at larger multiplicity. This behaviour is also observed for the spectra of strange hadrons measured in all events (inclusive production), in Pb-Pb [59], p-Pb [58] and pp collisions [56, 57]. The trend is more pronounced in Pb-Pb collisions than in small collision systems, and is interpreted as an indication of the presence of radial flow. The toward-leading spectra show instead a much smaller dependence on the multiplicity, suggesting that particles produced in jets are not sensitive to the radial flow.

The ratios between $\Xi^{\pm}$ and $\mathrm{K}^0_{\mathrm{S}}$ spectra are shown in Figure 5.10 and in the top panel of Figure 5.11 for the analysis of pp collisions at $\sqrt{s} = 13$ TeV, and in the top panel of Figure 5.12 for the analysis of pp collisions at $\sqrt{s} = 5.02$ TeV. The different colours refer to the different multiplicity classes, as indicated in the legend. For better visibility, the top panel of Figure 5.11 shows only the $\Xi^{\pm}/\mathrm{K}^0_{\mathrm{S}}$ ratios in the highest (0-0.01%), the lowest (50-100%) and the 0-100% multiplicity classes. The left, central and right plots refer to toward-leading, transverse-to-leading and full spectra, respectively. For $p_{\mathrm{T}} < 2$ GeV/c, where the p_{T} intervals of the $\mathrm{K}^0_{\mathrm{S}}$ spectra have a smaller width than the $\Xi^{\pm}$ ones, the ratio is computed by dividing the $\Xi^{\pm}$ yield in a given p_{T} interval by the value of the spline of the $\mathrm{K}^0_{\mathrm{S}}$ spectra in the centre of the same p_{T} interval. In both Figure 5.11 and Figure 5.12, the bottom panel shows the $\Xi^{\pm}/\mathrm{K}^0_{\mathrm{S}}$ ratios measured in the highest and lowest multiplicity classes divided by the one measured in the 0-100% multiplicity class.

The full and transverse-to-leading $\Xi^{\pm}/\mathrm{K}^0_{\mathrm{S}}$ ratios show similar features, while the toward-leading ratios are smaller in all p_{T} intervals, suggesting that the relative production of $\Xi^{\pm}$ with respect to $\mathrm{K}^0_{\mathrm{S}}$ is favoured in out of jet processes than in hard scattering events. The ratios increase with p_{T}: this indicates that $\Xi^{\pm}$ spectra are harder than $\mathrm{K}^0_{\mathrm{S}}$ ones, and is a consequence of the fact that the $\Xi^{\pm}$ is heavier than the $\mathrm{K}^0_{\mathrm{S}}$. A hint of decrease is shown in the full and transverse-to-leading ratios at $p_{\mathrm{T}} > 4$ GeV/c. This behaviour is reminiscent of

the p_{T} evolution of the $\Lambda/\mathrm{K}^0_{\mathrm{S}}$ yield ratio, described in Section 1.4.

The transverse-to-leading and full double ratios (bottom panels of Figures 5.11 and 5.12) increase with multiplicity. A hint of increase with multiplicity is also shown by the toward-leading ratios, which are systematically larger in the 0-0.1% multiplicity than in 50-100% one, even though for $p_{\mathrm{T}} < 3$ GeV/c they are compatible within statistical and systematic uncertainties. The increase with multiplicity observed for full production can be interpreted as strangeness enhancement and can be ascribed to the larger strangeness content of $\Xi^{\pm}$ ($|S| = 2$) with respect to $\mathrm{K}^0_{\mathrm{S}}$ ($|S| = 1$). The similar increase with multiplicity shown by the transverse-to-leading ratios indicates that the strangeness enhancement effect is a feature of transverse-to-leading processes, and the toward-leading ratios hint at the presence of strangeness enhancement also in hard scattering processes.

The features highlighted above will be further discussed in the next Section, where the $\mathrm{K}^0_{\mathrm{S}}$ and $\Xi^{\pm}$ p_{T}-integrated yields are shown as a function of the charged particle multiplicity measured at midrapidity.

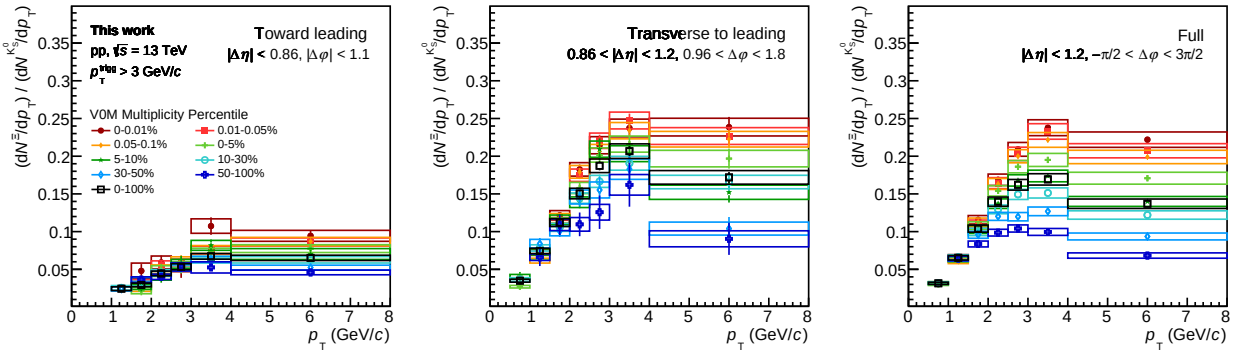

Figure 5.10: Ratios between $\Xi^{\pm}$ and $\mathrm{K}^0_{\mathrm{S}}$ transverse momentum spectra in pp collisions at $\sqrt{s} = 13$ TeV. The different colours refer to different multiplicity classes, as indicated in the legend. The left plot refers to toward-leading production, the central one to transverse-to-leading production and the right one to the full production. The statistical errors are represented by the error bars, the total systematic uncertainty by the empty boxes.

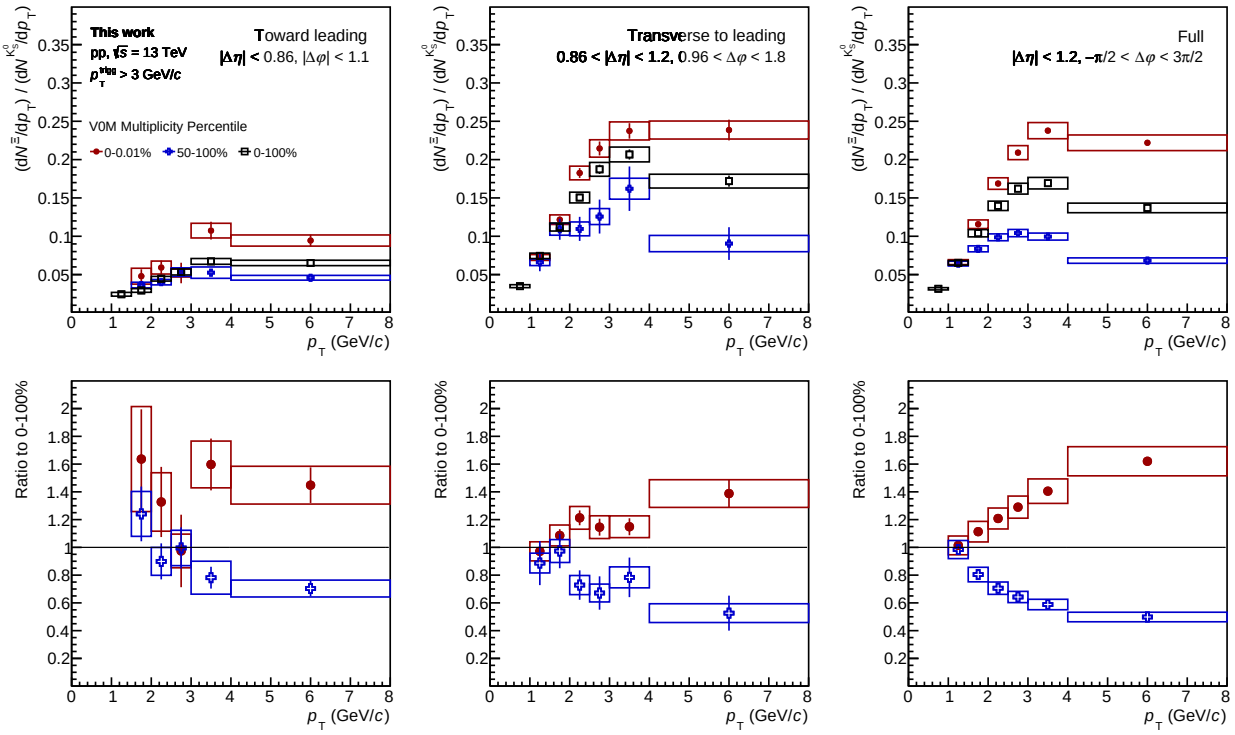

Figure 5.11: (top panel) Ratios between $\Xi^{\pm}$ and $\mathrm{K}^0_{\mathrm{S}}$ transverse momentum spectra in pp collisions at $\sqrt{\mathrm{s}} = 13$ TeV. For better visibility, the ratios are shown only in the highest (red markers) and lowest (blue markers) multiplicity classes and in the 0-100% multiplicity class (black markers). (bottom) $\Xi^{\pm}/\mathrm{K}^0_{\mathrm{S}}$ ratios in the largest and the smallest multiplicity classes divided by the $\Xi^{\pm}/\mathrm{K}^0_{\mathrm{S}}$ ratio in the 0-100% multiplicity class. The left plots refer to toward-leading production, the central ones to transverse-to-leading production and the right ones to the full production. The statistical errors are represented by the error bars, the total systematic uncertainty by the empty boxes.

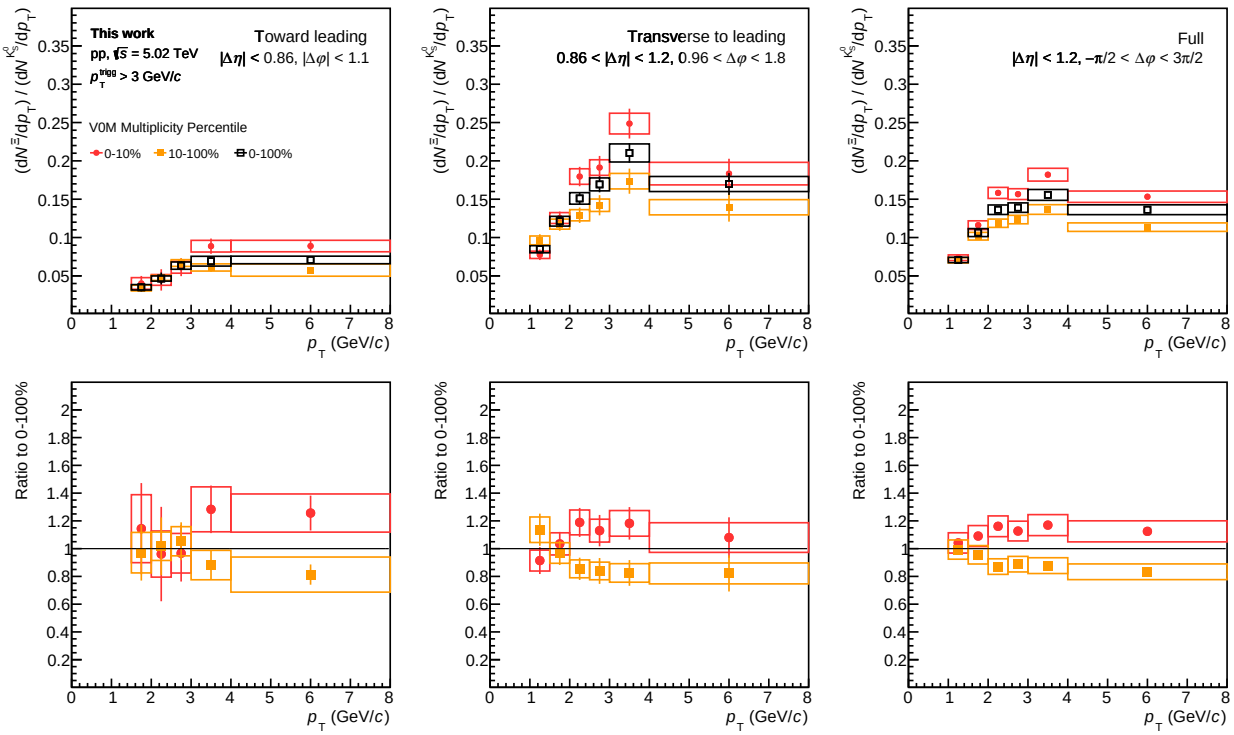

Figure 5.12: (top panel) Ratios between $\Xi^{\pm}$ and $\mathrm{K}^0_{\mathrm{S}}$ transverse momentum spectra in pp collisions at $\sqrt{\mathrm{s}} = 5.02$ TeV. The different colours refer to different multiplicity classes, as indicated in the legend. (bottom) $\Xi^{\pm}/\mathrm{K}^0_{\mathrm{S}}$ ratios in the largest and the smallest multiplicity classes divided by the $\Xi^{\pm}/\mathrm{K}^0_{\mathrm{S}}$ ratio in the 0-100% multiplicity class. The left plots refer to toward-leading production, the central ones to transverse-to-leading production and the right ones to the full production. The statistical errors are represented by the error bars, the total systematic uncertainty by the empty boxes.

5.2 Computation of the p_{T}-integrated yields

To obtain the p_{T}-integrated yield, an extrapolation in the p_{T} interval where the yield cannot be measured has to be performed. For this purpose, four different functions are fitted to the spectra, and the average extrapolated yields at low and high p_{T} are added to the integral of the measured spectrum in order to obtain the p_{T}-integrated yield. The four different fit functions are the Lévi-Tsallis, the Boltzmann, the Fermi-Dirac, and the m_{T}-exponential function. The Lévi-Tsallis function is defined as:

$$\frac{\mathrm{d}N}{\mathrm{d}p_{\mathrm{T}}} = \frac{N(n-1)(n-2)}{nC(nC+m(n-2))}\left(1+\frac{m_{\mathrm{T}}-m}{nC}\right)^{-n}, \tag{5.1}$$

where m is the $\mathrm{K}^0_{\mathrm{S}}$ ($\Xi^{\pm}$) mass, $m_{\mathrm{T}} = \sqrt{m^2+p_{\mathrm{T}}^2}$ is the transverse mass, and n, C and N are free fit parameters.

The other three fit functions have only two free fit parameters A and T. The Fermi-Dirac function is defined as:

$$\frac{\mathrm{d}N}{\mathrm{d}p_{\mathrm{T}}} = A\cdot p_{\mathrm{T}}\cdot\frac{1}{e^{\frac{\sqrt{p_{\mathrm{T}}^2+m^2}}{T}}+1}, \tag{5.2}$$

the Boltzmann function as:

$$\frac{\mathrm{d}N}{\mathrm{d}p_{\mathrm{T}}} = A\cdot p_{\mathrm{T}}\cdot\sqrt{p_{\mathrm{T}}^2+m^2}\cdot e^{\frac{-\sqrt{p_{\mathrm{T}}^2+m^2}}{T}}, \tag{5.3}$$

and finally, the m_{T}-exponential is defined as:

$$\frac{\mathrm{d}N}{\mathrm{d}p_{\mathrm{T}}} = A\cdot p_{\mathrm{T}}\cdot e^{\frac{-\sqrt{p_{\mathrm{T}}^2+m^2}}{T}}. \tag{5.4}$$

An example of fit to the $\mathrm{K}^0_{\mathrm{S}}$ and $\Xi^{\pm}$ spectra is shown in Figures 5.13 and 5.14, respectively. Different fit functions are drawn with different colours, as indicated in the legend.

The extrapolated fraction of the $\mathrm{K}^0_{\mathrm{S}}$ yield amounts to approximately 1% of the total yield for full and transverse-to-leading production, and to approximately 8% for toward-leading production, where the p_{T} interval in which the yield cannot be measured is larger. The extrapolated fraction for $p_{\mathrm{T}} > 8$ GeV/c is negligible. The extrapolated fraction of the $\Xi^{\pm}$ yield varies between 15% and 35% of the total yield, depending on the multiplicity class. Indeed, the p_{T} interval where the yield cannot be measured depends on the multiplicity class. The extrapolated fraction for $p_{\mathrm{T}} > 8$ GeV/c is smaller than 0.1% for full and transverse-to-leading production, and smaller than 2% for toward-leading production, and it is included in the computation of the total yield.

The statistical uncertainty of the p_{T}-integrated yield is computed by shifting the yields measured in each p_{T} interval by a random value extracted from a Gaussian distribution centred in zero and with standard deviation equal to the statistical uncertainty of the data points. This procedure is repeated 1000 times. The p_{T}-integrated yields extracted from the shifted spectra have a Gaussian distribution, whose standard deviation gives the statistical uncertainty of the p_{T}-integrated yield.

The systematic uncertainty of the extrapolated yield is calculated by shifting the spectra by $\pm 1\sigma^{p_{\mathrm{T}}}_{SYS}$, where $\sigma^{p_{\mathrm{T}}}_{SYS}$ represents the systematic uncertainty of the p_{T} spectra, and by repeating the fitting procedure. This procedure is followed since the systematic uncertainties are observed to be correlated across p_{T} (see Section 4.7). The half-difference between the two extrapolated yields gives the systematic uncertainty σ_{extr} of the extrapolated yield.

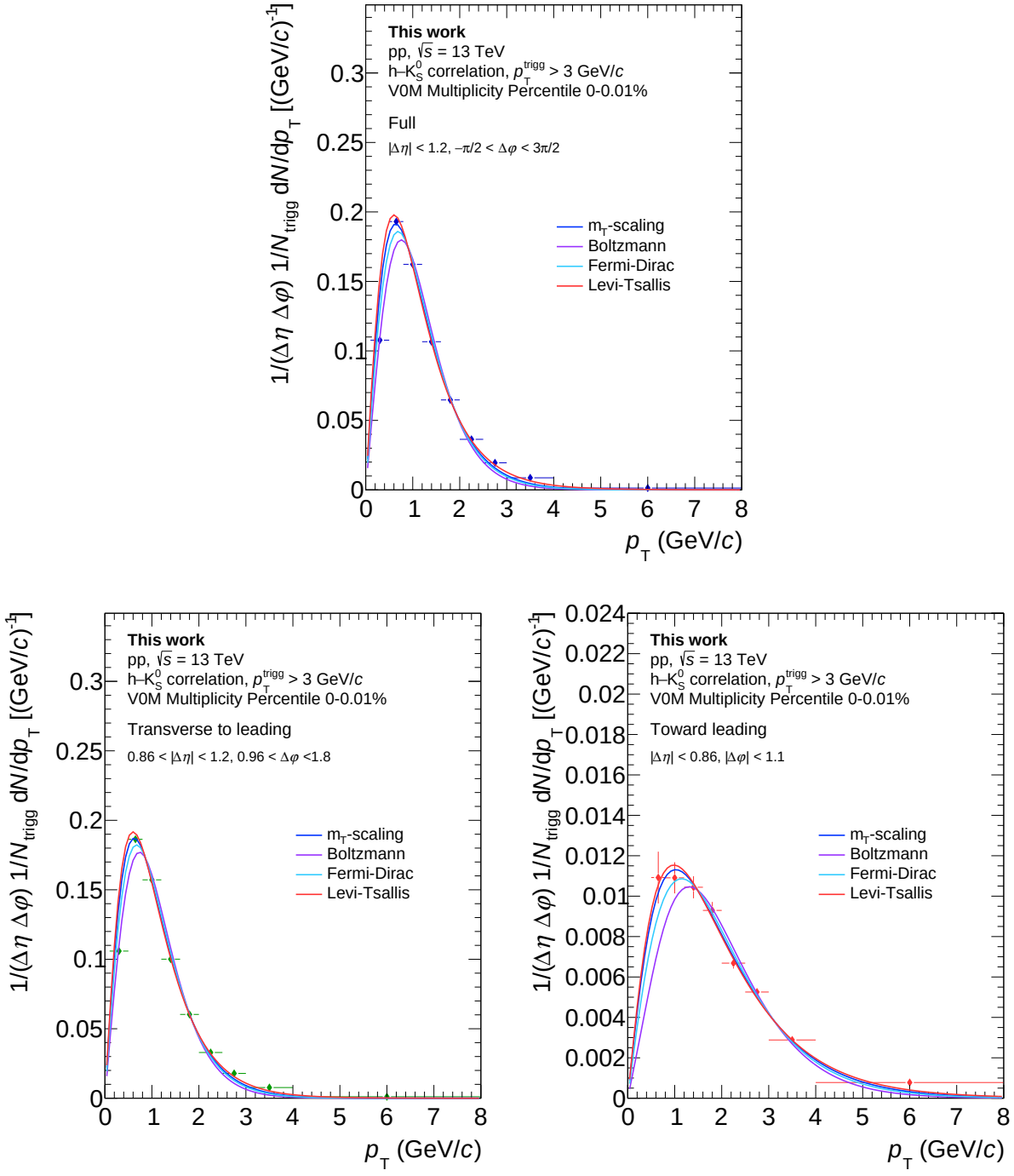

Figure 5.13: Transverse momentum spectra of K^0_S measured in high multiplicity pp collisions at $\sqrt{s}$ = 13 TeV in the multiplicity class 0-0.01%. The upper, bottom left and bottom right plots refer to full, transverse-to-leading and toward-leading production, respectively. Statistical errors are represented by the error bars. The spectra are fitted with four different fit functions, as indicated in the legend, in order to extrapolate the yield at low and high p_{T}.

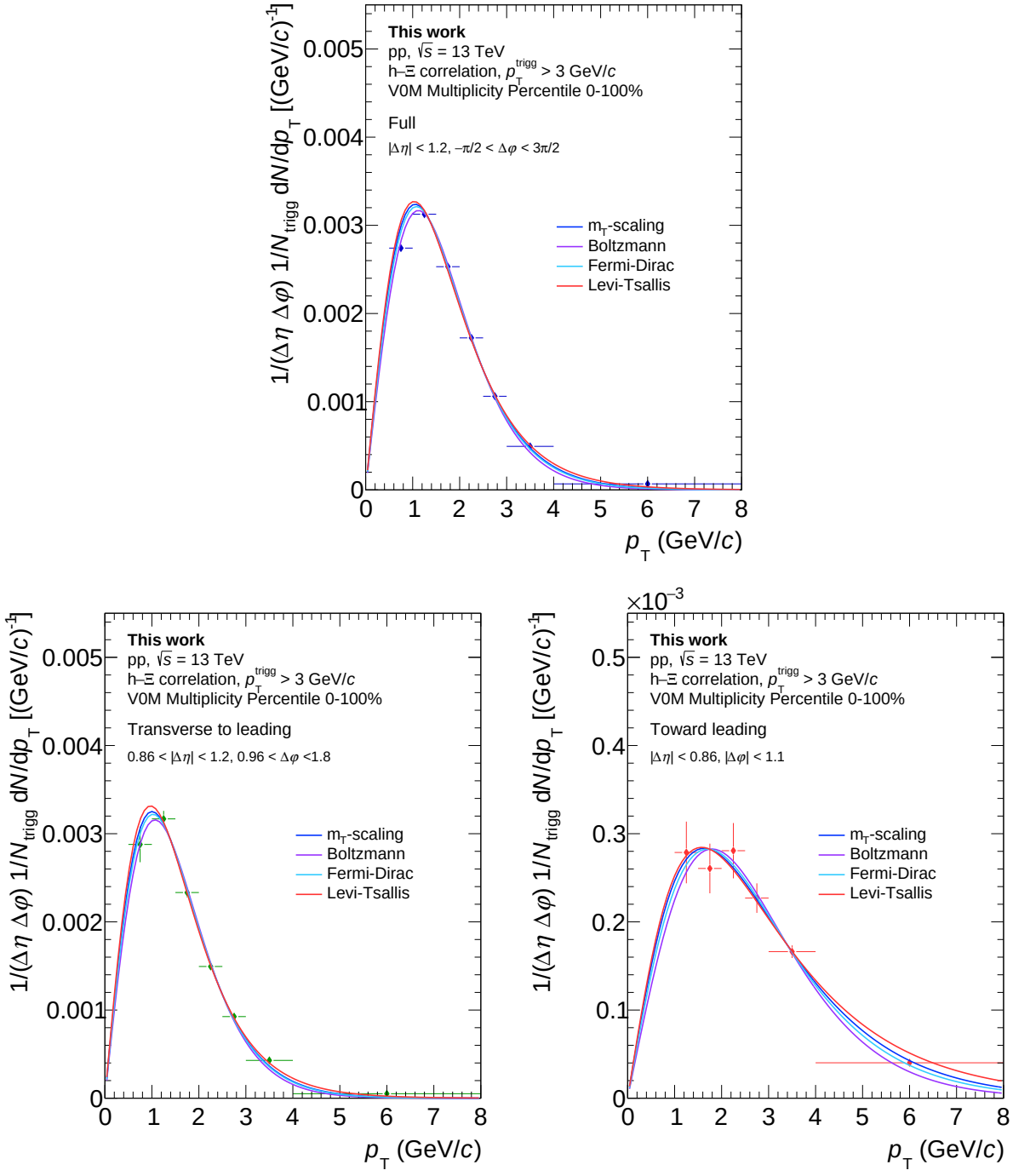

Figure 5.14: Transverse momentum spectra of $\Xi^{\pm}$ measured in minimum bias pp collisions at $\sqrt{s} = 13$ TeV in the multiplicity class 0-100%. The upper, bottom left and bottom right plots refer to full, transverse-to-leading and toward-leading production, respectively. Statistical errors are represented by the error bars. The spectra are fitted with four different fit functions, as indicated in the legend, in order to extrapolate the yield at low and high p_{T}.

Another source of systematic uncertainty of the p_T-integrated yield is associated to the choice of the fit function, and is given by the difference between the maximum extrapolated yield and the minimum extrapolated yield, separately for the low and high p_T intervals.

The total systematic uncertainty σ_{SYS} of the p_T-integrated yield is obtained by summing linearly all the systematic uncertainties but the one associated to the choice of the fit functions σ_{fit}, which is summed in quadrature since it is uncorrelated with the other sources. The systematic uncertainties σ_{p_T} of the p_T-spectra are summed linearly because most of the sources are correlated with p_T, as described in Section 4.7.

$$\sigma_{SYS} = \sqrt{\left[\sum_{p_T} \sigma_{p_T} + \sigma_{extr}\right]^2 + \sigma^2_{fit}} \tag{5.5}$$

The systematic uncertainty uncorrelated across multiplicity $\sigma_{SYS,uncorr}$ is given by:

$$\sigma_{SYS,uncorr} = \sum_{p_T} \sigma^{uncorr}_{p_T} + \sigma^{uncorr}_{extr}, \tag{5.6}$$

where $\sigma^{uncorr}_{p_T}$ represents the systematic uncertainty of the p_T spectra uncorrelated with multiplicity, and σ^{uncorr}_{extr} is estimated with the formula:

$$\sigma^{uncorr}_{extr} = \frac{\sum_{p_T} \sigma^{uncorr}_{p_T}}{\sum_{p_T} \sigma_{p_T}} \times \sigma_{extr} \tag{5.7}$$

The systematic uncertainty σ_{fit} associated to the choice of the fit functions is observed to be fully correlated with multiplicity, and therefore is not included in the computation of $\sigma_{SYS,uncorr}$.

5.3 Full, transverse-to-leading and toward-leading yields of K^0_S and $\Xi^{\pm}$ as a function of multiplicity

The full, transverse-to-leading and toward-leading yields of K^0_S ($\Xi^{\pm}$) per unit $\Delta\eta\Delta\varphi$ area are shown in Figure 5.15 (5.17) as a function of the charged particle multiplicity measured at midrapidity in events with a trigger particle $\langle dN/d\eta \rangle_{|\eta|<0.5,\ p_{T,trigg}>3\ \mathrm{GeV}/c}$. The toward-leading yields are also shown for better visibility in Figures 5.16 and 5.18 for K^0_S and $\Xi^{\pm}$, respectively. The plots report both the yields measured in pp collisions at $\sqrt{s} = 5.02$ TeV, shown with light coloured markers, and the ones measured in pp collisions at $\sqrt{s} = 13$ TeV, displayed by darker coloured markers.

The full and transverse-to-leading yields of both particles increase with multiplicity faster than the toward-leading yields, which show a much milder multiplicity dependence.

This indicates that the contribution of transverse-to-leading production mechanisms relative to toward-leading ones increases with the multiplicity.

The full and transverse-to-leading yields of both particles show no centre-of-mass energy dependence. For what concerns the toward-leading production, the K^0_S yields measured in pp collisions at $\sqrt{s} = 5.02$ TeV are systematically smaller than those measured in pp collisions at $\sqrt{s} = 13$ TeV (see Figure 5.16). However, considering the total systematic uncertainty, the yields measured at similar multiplicity values at the two centre-of-mass energies are compatible within 2σ. This feature is not observed for the $\Xi^{\pm}$ baryons, whose yields measured

in pp collisions at $\sqrt{s} = 5.02$ TeV follow the same trend observed in pp collisions at $\sqrt{s} = 13$ TeV (see Figure 5.18).

The K^0_S and $\Xi^\pm$ toward-leading yields measured in pp collisions at $\sqrt{s} = 13$ TeV were fitted with polynomials of zero and first degree in order to evaluate their dependence on the multiplicity. Both statistical errors and systematic uncertainties uncorrelated across multiplicity were taken into account in the fit procedure. For both particles, a flat behaviour with multiplicity can be excluded. The $\Xi^\pm$ yield can be described by a first degree polynomial ($\chi^2/\text{ndf} = 6.3/6$), whereas the K^0_S yields are not compatible with a linear increase with multiplicity.

The ratios between $\Xi^\pm$ and K^0_S yields as a function of $\langle dN/d\eta \rangle_{|\eta|<0.5,\ p_{T,trigg}>3\ \text{GeV}/c}$ are shown in the top panel of Figure 5.19. The ratio of full yields increases with multiplicity: this can be attributed to the larger strangeness content of the $\Xi^\pm$ with respect to the K^0_S. Indeed, the strangeness enhancement with multiplicity was observed to be larger for particles with larger strangeness content [56, 57]. The ratio of transverse-to-leading yields increases with the multiplicity and is compatible with the ratio of full yields. This is a consequence of the fact that the full yield is dominated by transverse-to-leading production, as shown in Figures 5.15 and 5.17. Also the toward-leading ratio shows an increase with multiplicity: a flat behaviour with multiplicity can be excluded since the zero degree polynomial fit to the ratio measured in pp collisions at $\sqrt{s} = 13$ TeV gives a $\chi^2/\text{ndf} = 6.7$. Instead, the toward-leading ratio is well described by a first degree polynomial ($\chi^2/\text{ndf} = 1.02$). In both cases the fit procedure was performed considering the sum in quadrature of the statistical errors and the systematic uncertainties uncorrelated across multiplicity.

The bottom plot of Figure 5.19 displays the double ratio between the toward-leading and the transverse-to-leading $\Xi^\pm/K^0_S$ ratios. The double ratio is smaller than one, suggesting that the production of $\Xi^\pm$ with respect to K^0_S is favoured in transverse-to-leading processes. The double ratio is well described by a zero degree polynomial, indicating that the transverse-to-leading and toward-leading yield ratios increase with multiplicity in a compatible way, and that the production of $\Xi^\pm$ with respect to K^0_S is favoured in transverse-to-leading processes in a similar way throughout the whole multiplicity interval where the measurement was performed.

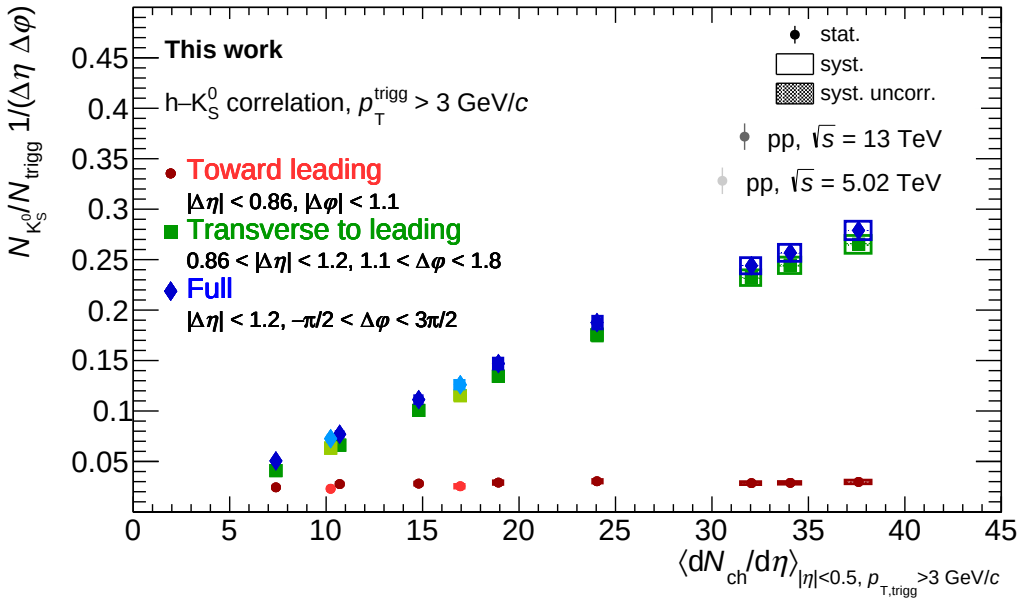

Figure 5.15: Full (blue), transverse-to-leading (green) and toward-leading (red) yields of K^0_S per unit $\Delta\eta\Delta\varphi$ area as a function of the charged particle multiplicity measured at midrapidity in events with a trigger particle. Statistical and systematic uncertainties are shown by error bars and empty boxes, respectively. Shadowed boxes represent the systematic errors uncorrelated across multiplicity.

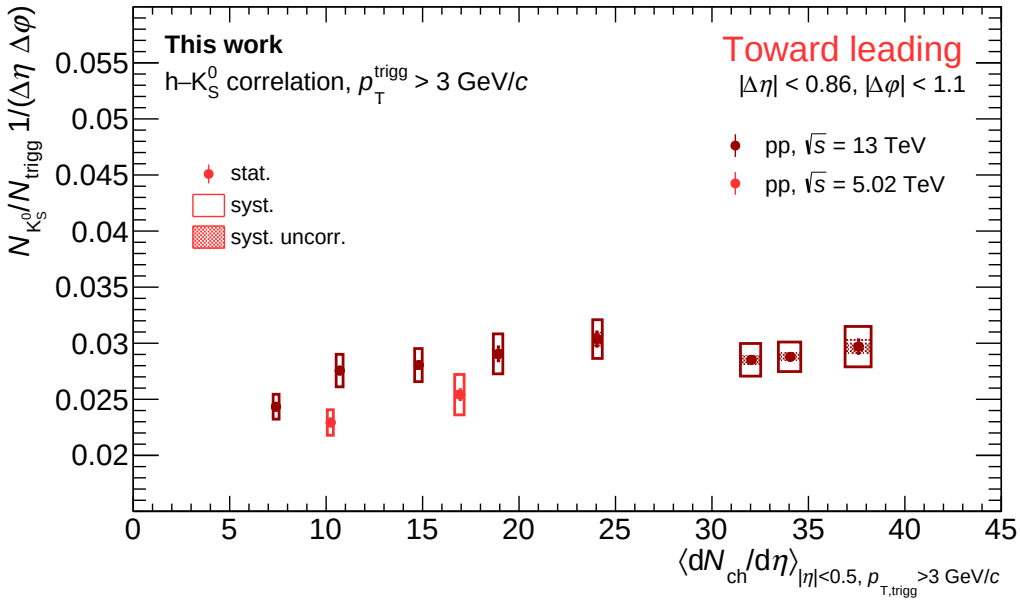

Figure 5.16: Toward-leading yield of K^0_S per unit $\Delta\eta\Delta\varphi$ area as a function of the charged particle multiplicity measured at midrapidity in events with a trigger particle. Statistical and systematic uncertainties are shown by error bars and empty boxes, respectively. Shadowed boxes represent the systematic errors uncorrelated across multiplicity.

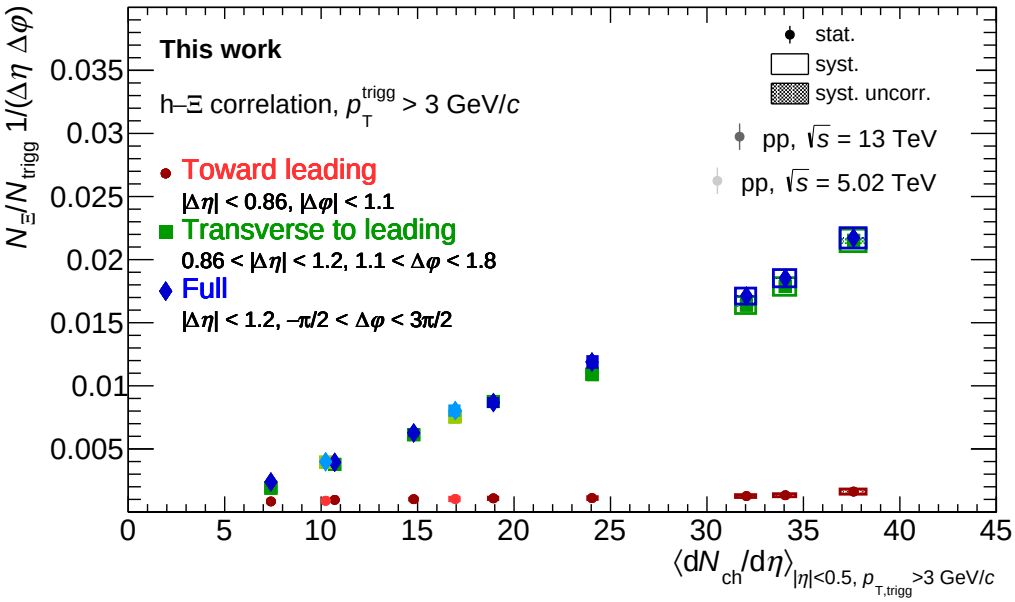

Figure 5.17: Full (blue), transverse-to-leading (green) and toward-leading (red) yields of $\Xi^{\pm}$ per unit $\Delta\eta\Delta\varphi$ area as a function of the charged particle multiplicity measured at midrapidity in events with a trigger particle. Statistical and systematic uncertainties are shown by error bars and empty boxes, respectively. Shadowed boxes represent the systematic errors uncorrelated across multiplicity.

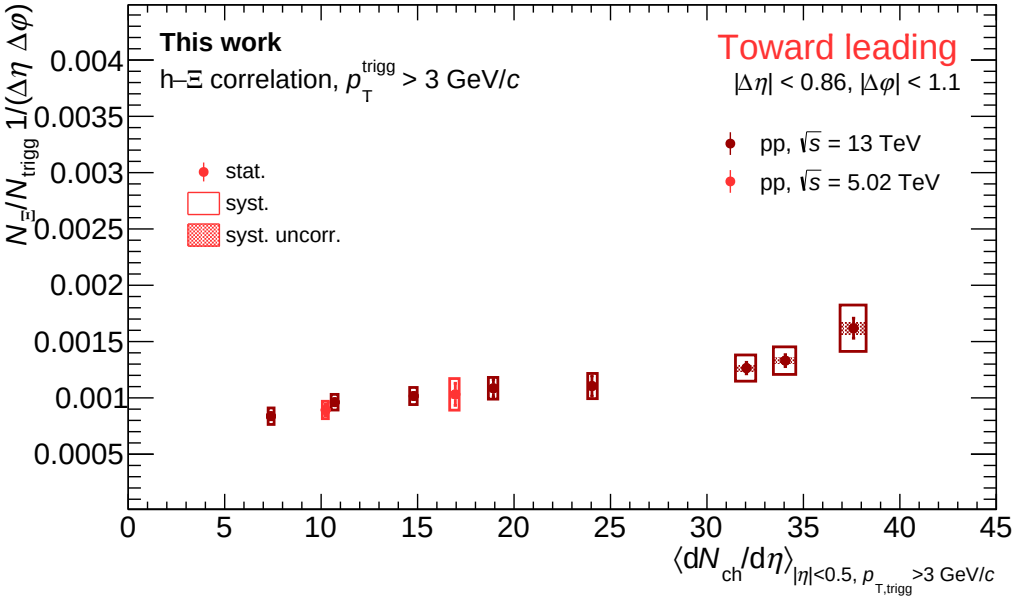

Figure 5.18: Toward-leading yield of $\Xi^{\pm}$ per unit $\Delta\eta\Delta\varphi$ area as a function of the charged particle multiplicity measured at midrapidity in events with a trigger particle. Statistical and systematic uncertainties are shown by error bars and empty boxes, respectively. Shadowed boxes represent the systematic errors uncorrelated across multiplicity.

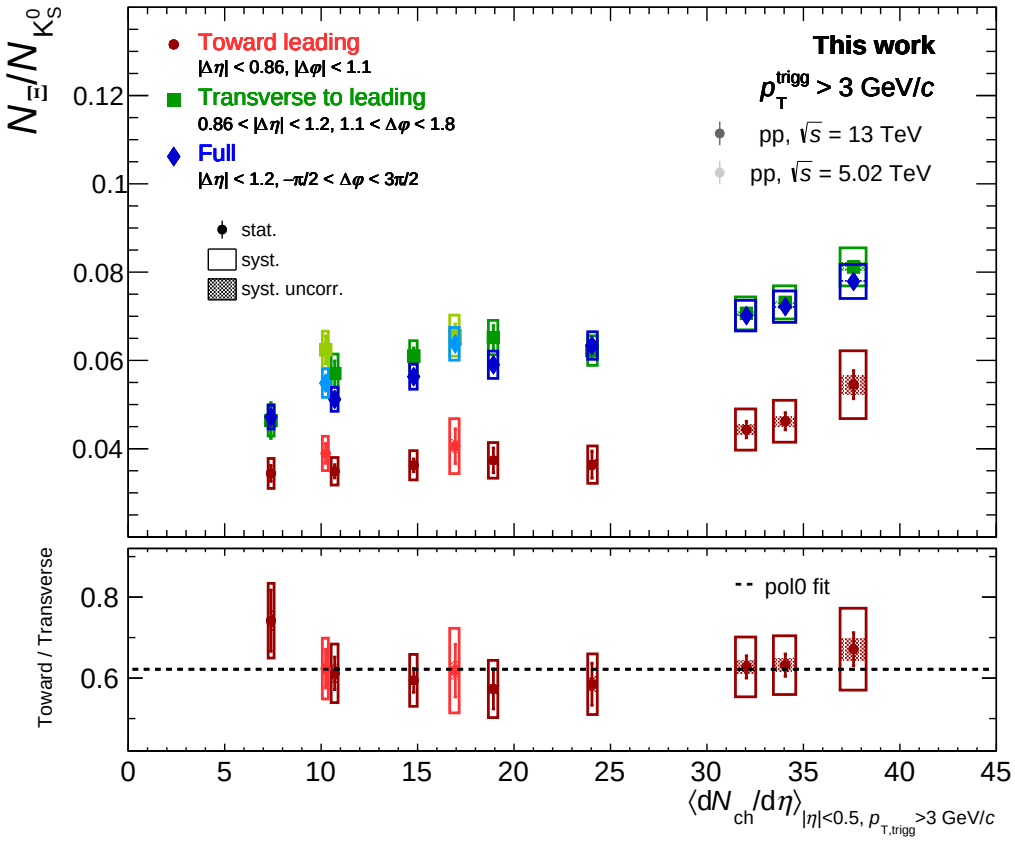

Figure 5.19: (top panel) Full (blue), transverse-to-leading (green) and toward-leading (red) $\Xi^{\pm}/K^0_S$ yield ratios as a function of the charged particle multiplicity measured at midrapidity in events with a trigger particle. Statistical and systematic uncertainties are shown by error bars and empty boxes, respectively. Shadowed boxes represent the systematic errors uncorrelated across multiplicity. (bottom panel) Toward-leading $\Xi^{\pm}/K^0_S$ ratio divided by the transverse-to-leading $\Xi^{\pm}/K^0_S$ ratio.

5.4 Comparison of the results with predictions of phenomenological models

The K^0_S and $\Xi^{\pm}$ yields are compared to the predictions of three different phenomenological models, namely PYTHIA8.2 with the standard Monash tune [84], PYTHIA8.2 with ropes [157] and EPOS LHC [87]. The three event generators are embedded into the ALICE framework, which provides an interface for the generation and the analysis of the events. The analysis of the generated events is performed at the generator level, i.e. using only the kinematic information of the generated particles, without simulating their passage through the ALICE detector and reconstructing each event as it is done for the real collisions.

5.4.1 Analysis strategy

The analysis of generated events is performed using the same angular correlation technique applied to the analysis of the data. The sample used for h-K^0_S (h-$\Xi^{\pm}$) correlation consists of 4×10^9 (8×10^9) events.

As for the analysis of the data, the trigger particle is defined as the highest-p_{T} charged particle found in the event with $p_{\mathrm{T}} > 3$ GeV/c and $|\eta| < 0.8$. In order to allow for a proper comparison with the data, only primary charged particles identified as protons, pions, kaons, electrons and muons are considered. K^0_S and $\Xi^{\pm}$ are identified using the MC truth information, and they are selected in the same acceptance interval used for the analysis of the data ($|\eta| < 0.8$).

The analysis is performed by dividing the generated events containing a trigger particle into ten multiplicity classes based on the number of charged particles produced in the acceptance of the V0A and V0C detector ($2.8 < |\eta| < 5.1$ and $-3.7 < |\eta| < -1.7$). For each of these multiplicity classes, the average number of charged particles produced at midrapidity $\langle \mathrm{d}N/\mathrm{d}\eta \rangle_{|\eta|<0.5,\ p_{\mathrm{T,trigg}}>3\ \mathrm{GeV}/c}$ is computed. In the following, $\langle \mathrm{d}N/\mathrm{d}\eta \rangle_{|\eta|<0.5,\ p_{\mathrm{T,trigg}}>3\ \mathrm{GeV}/c}$ will be abbreviated with $\langle \mathrm{d}N/\mathrm{d}\eta \rangle$. An example of the correlation between the number of charged particles in the V0 acceptance and the number of charged particles produced at midrapidity in events with a trigger particle is shown in Figure 5.20. The ten multiplicity classes allow to span the multiplicity range $7 \lesssim \langle \mathrm{d}N/\mathrm{d}\eta \rangle \lesssim 31$, which extends up approximately to the value associated with the multiplicity class 0.05-0.1% of the data. Indeed, the total number of generated events is not sufficient to reach larger values of multiplicity: a MC sample of events at least a hundred times larger than the analysed one would be needed to extend the analysis to the highest value of $\langle \mathrm{d}N/\mathrm{d}\eta \rangle$ reached in the data ($\langle \mathrm{d}N/\mathrm{d}\eta \rangle \sim 38$).

The procedure followed in order to measure the full, transverse-to-leading and toward-leading p_{T} spectra is the same described for the data, with the exception of the steps related to the reconstruction of real collisions, which are not needed since the MC analysis is performed at the generator level. In particular, the correction by the K^0_S and $\Xi^{\pm}$ efficiency is not applied, as well as the correction to take into account the efficiency of events with a trigger particle (see Section 4.8). The correction by the pair acceptance is applied in order to take into account the η distributions of trigger and associated particles. To extract the full, transverse-to-leading and toward-leading yields, the same $\Delta\eta$ and $\Delta\varphi$ intervals used for the analysis of the data are used. To assess the systematic uncertainties associated to the choice of these intervals, the procedure described in Section 4.7 was followed. For both the transverse-to-leading and the toward-leading production, the variations of the yield are not significant according to the Barlow check.

While the full and transverse-to-leading spectra of both K^0_S and $\Xi^{\pm}$can be measured

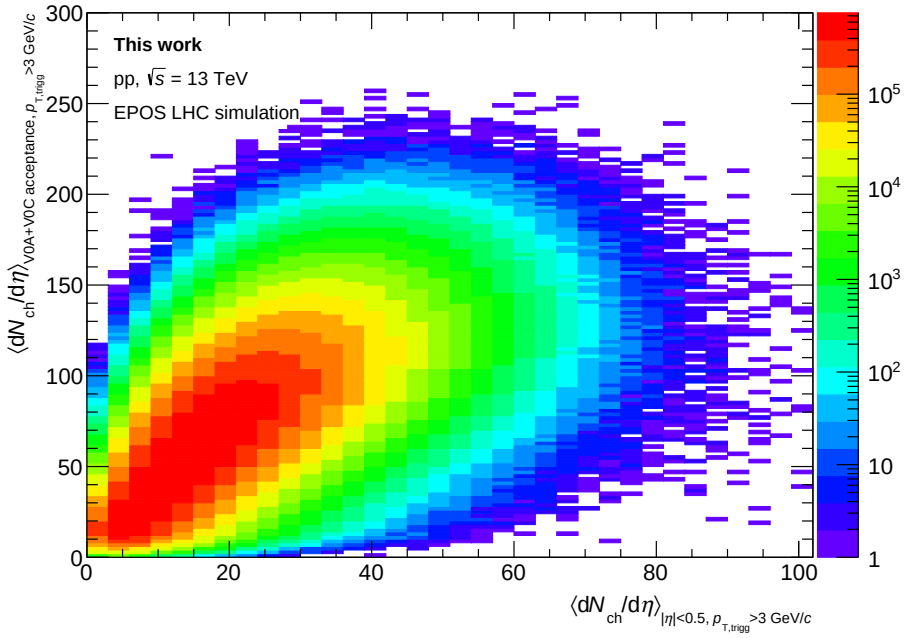

Figure 5.20: Distribution of the number of charged particles in the V0A and V0C acceptance as a function of the number of charged particles produced at midrapidity in events with a trigger particle simulated with EPOS LHC event generator.

in the interval $0 < p_{\mathrm{T}} < 8$ GeV/c, the toward-leading yield can only be measured for $p_T > 0.5(1.0)$ GeV/c, since the near-side jet peak is not visible at lower p_{T} values. Therefore, the p_{T} spectra are interpolated in order to extrapolate the yield at low p_{T}. As for the analysis of data, four different fit functions are used (see Section 5.3) and the half difference between the maximum and the minimum extrapolated yields is assigned as a systematic uncertainty. The choice of the fit function represents the only significant source of systematic uncertainty.

5.4.2 Comparison of the $\mathrm{K}^0_{\mathrm{S}}$ and $\Xi^{\pm}$ yields to the model predictions

The comparison between the measured p_{T} spectra and the model predictions is performed in three multiplicity classes characterised by similar values of $\langle \mathrm{d}N/\mathrm{d}\eta \rangle$ in the data and in the MC ($\langle \mathrm{d}N/\mathrm{d}\eta \rangle \sim 15$, 19 and 25). The comparison of the transverse-to-leading and toward-leading spectra measured in the multiplicity classes characterised by $\langle \mathrm{d}N/\mathrm{d}\eta \rangle \sim 19$ is reported in Figures 5.21 and 5.22 for $\mathrm{K}^0_{\mathrm{S}}$ and $\Xi^{\pm}$, respectively. The left plots show the p_{T} spectra, the right ones the ratios between the model predictions and the data points.

The $\mathrm{K}^0_{\mathrm{S}}$ transverse-to-leading yields (top plots of Figure 5.21) are underestimated by all the three models. The underestimation worsens with increasing p_{T}, especially for PYTHIA8 with ropes and EPOS LHC, indicating that the models predict softer spectra than the measured ones. These features are observed in all the three multiplicity classes in which the comparison between the data and the model predictions was performed.

Also the predicted $\mathrm{K}^0_{\mathrm{S}}$ toward-leading spectra (bottom plots of Figure 5.21) are softer than the measured ones, as indicated by the fact that the ratios between the models and the data points decrease with p_{T}. Both PYTHIA8 tunes predict larger yields, especially at low p_{T}, while EPOS LHC underestimates the yield for $p_{\mathrm{T}} \gtrsim 1$ GeV/c.

The $\Xi^{\pm}$ transverse-to-leading spectra predicted by PYTHIA8 Monash (top plots of Fig-

ure 5.22) underestimate the yield of about 60% in all the three considered multiplicity classes. However, PYTHIA8 Monash can fairly well reproduce the p_{T} dependence of the measured yield. On the contrary, PYTHIA8 with ropes cannot describe the p_{T} dependence of the yield: the ratios between model predictions and data points decrease with p_{T}, indicating that the spectra predicted by the model are softer. EPOS LHC can better describe the data, but the description worsens at lower and higher multiplicities: for $\langle \mathrm{d}N/\mathrm{d}\eta \rangle_{|\eta|<0.5,\ p_{\mathrm{T,trigg}}>3\ \mathrm{GeV}/c} \sim 15$ the model over data ratio decreases with p_{T} and is smaller than one, while for $\langle \mathrm{d}N/\mathrm{d}\eta \rangle \sim 25$ the model overestimates the yield by about 20% in all p_{T} intervals.

Finally, the $\Xi^{\pm}$ toward-leading spectra (bottom plots of Figure 5.22) are overestimated at low p_{T} ($p_{\mathrm{T}} \lesssim 3$ GeV/c) by both PYTHIA8 with ropes and EPOS LHC. For all the three considered values of multiplicity, the toward-leading spectra predicted by PYTHIA8 with ropes and EPOS LHC are softer than the measured ones. PYTHIA8 Monash describes the yields fairly well in all p_{T} intervals. However, its description gets worse at larger multiplicity values: for $\langle \mathrm{d}N/\mathrm{d}\eta \rangle \sim 25$ the yield is underestimated of about 20%, but the p_{T} dependence is still reproduced fairly well.

The issues in the model description of the p_{T} spectra can also be observed when comparing the p_{T}-integrated yields. The comparison between the full, transverse-to-leading and toward-leading p_{T}-integrated yields measured in the data and the model predictions are shown as a function of $\langle \mathrm{d}N/\mathrm{d}\eta \rangle$ in Figures 5.23 and 5.25 for $\mathrm{K}^0_{\mathrm{S}}$ and $\Xi^{\pm}$, respectively. The data points are drawn with markers, the model predictions with lines of different styles, as indicated in the legend. Statistical and systematic uncertainties of the data points are shown by error bars and empty boxes, respectively. To show the discrepancy between the data and the model predictions, the sum in quadrature of statistical and systematic uncertainties of the model predictions is displayed with error bars. The bottom panels display the ratios between the model predictions and the data points. Since the $\langle \mathrm{d}N/\mathrm{d}\eta \rangle_{|\eta|<0.5,\ p_{\mathrm{T,trigg}}>3\ \mathrm{GeV}/c}$ values associated to the data and the MC multiplicity classes are different, a fit with a spline to the data points was performed in order to compute the ratios. The shaded band around one represents the sum in quadrature of the statistical and systematic uncertainties of the data points. For better visibility, the comparison between the toward-leading yields measured in the data and the model predictions are also shown in Figures 5.24 and 5.26 for $\mathrm{K}^0_{\mathrm{S}}$ and $\Xi^{\pm}$, respectively.

All the models underestimate the full and the transverse-to-leading $\mathrm{K}^0_{\mathrm{S}}$ yields (Figure 5.23). The underestimation is larger at low multiplicity ($\langle \mathrm{d}N/\mathrm{d}\eta \rangle \sim 10$), where all models underestimate the yields of about 30%. At high multiplicity ($\langle \mathrm{d}N/\mathrm{d}\eta \rangle \sim 30$) the PYTHIA8 tunes underestimate the yields of about 15%, while EPOS LHC predicts values compatible with the measured ones.

None of the three models can describe the increase with multiplicity of the toward-leading yield of $\mathrm{K}^0_{\mathrm{S}}$ (Figure 5.24). Both PYTHIA8 tunes overestimate the yields and show a hint of decrease with multiplicity, while EPOS LHC overpredicts the yield at low multiplicity and underpredicts it at large multiplicity, showing a clear decrease with multiplicity.

The model description of the full and transverse-to-leading $\Xi^{\pm}$ yields (Figure 5.25) is worse than the $\mathrm{K}^0_{\mathrm{S}}$ one. Both PYTHIA8 tunes underestimate the yields: PYTHIA8 Monash underestimates them by approximately 70% over the whole multiplicity interval, whereas PYTHIA8 with ropes underestimates them of about 50% at low multiplicity and 20% at high multiplicity. EPOS LHC underestimates the yield at low multiplicity of about 50%, and overestimates it of about 20% at high multiplicity, predicting an increase of the yield with multiplicity larger than the one observed in the data.

The increase with multiplicity of the $\Xi^{\pm}$ toward-leading yield is qualitatively reproduced

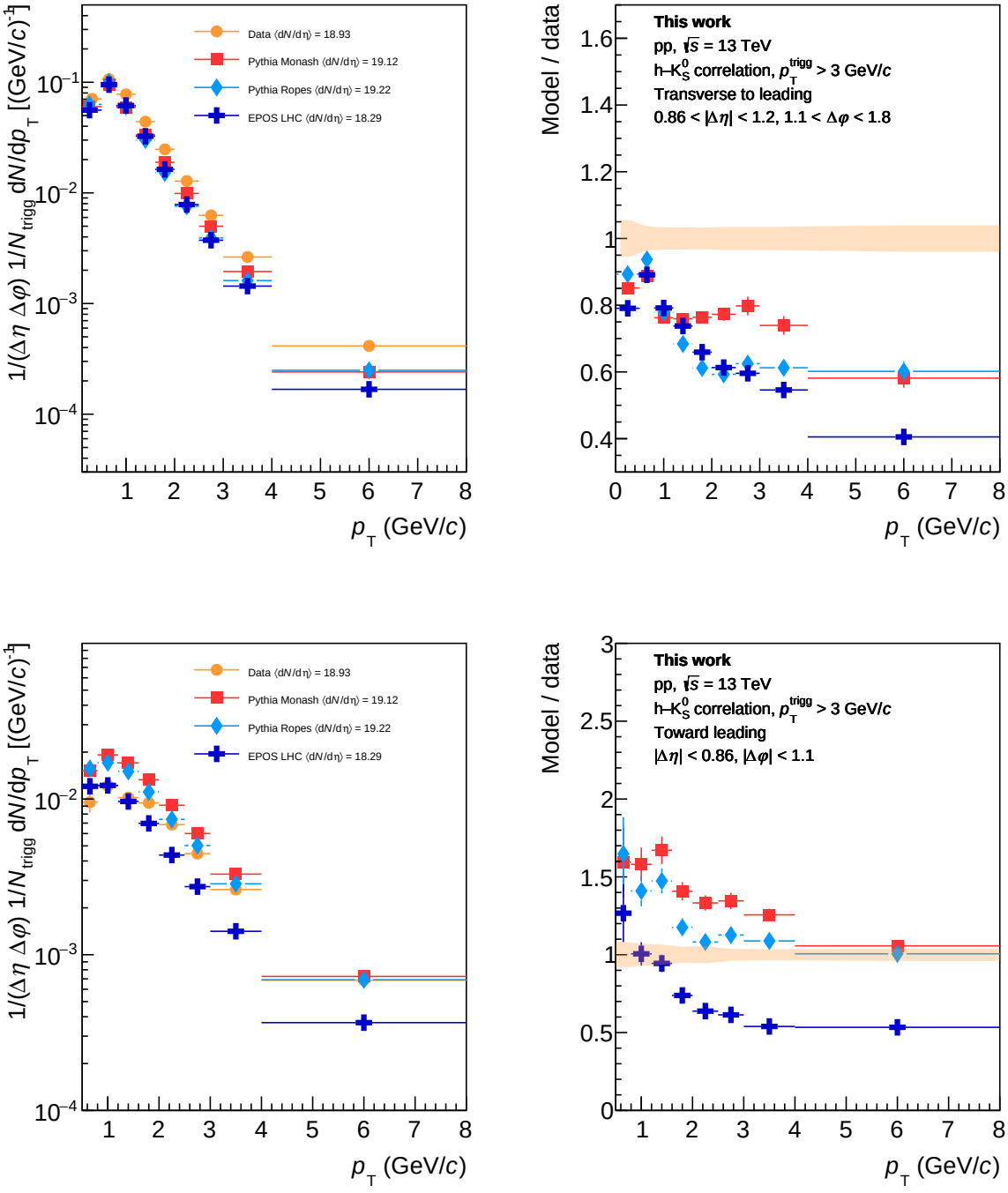

Figure 5.21: (left plots) Transverse-to-leading (top) and toward-leading (bottom) transverse momentum spectra of K^0_S in pp collisions at $\sqrt{s} = 13$ TeV. Data points are shown with orange markers, model predictions with different colours as indicated in the legend. The spectra are obtained in multiplicity classes characterised by $\langle dN/d\eta \rangle \sim 19$. Only statistical errors are shown. (right plots) Ratios between the model predictions and the data points. The error bars show the statistical uncertainties, the orange band around one represents the systematic uncertainties of the data points.

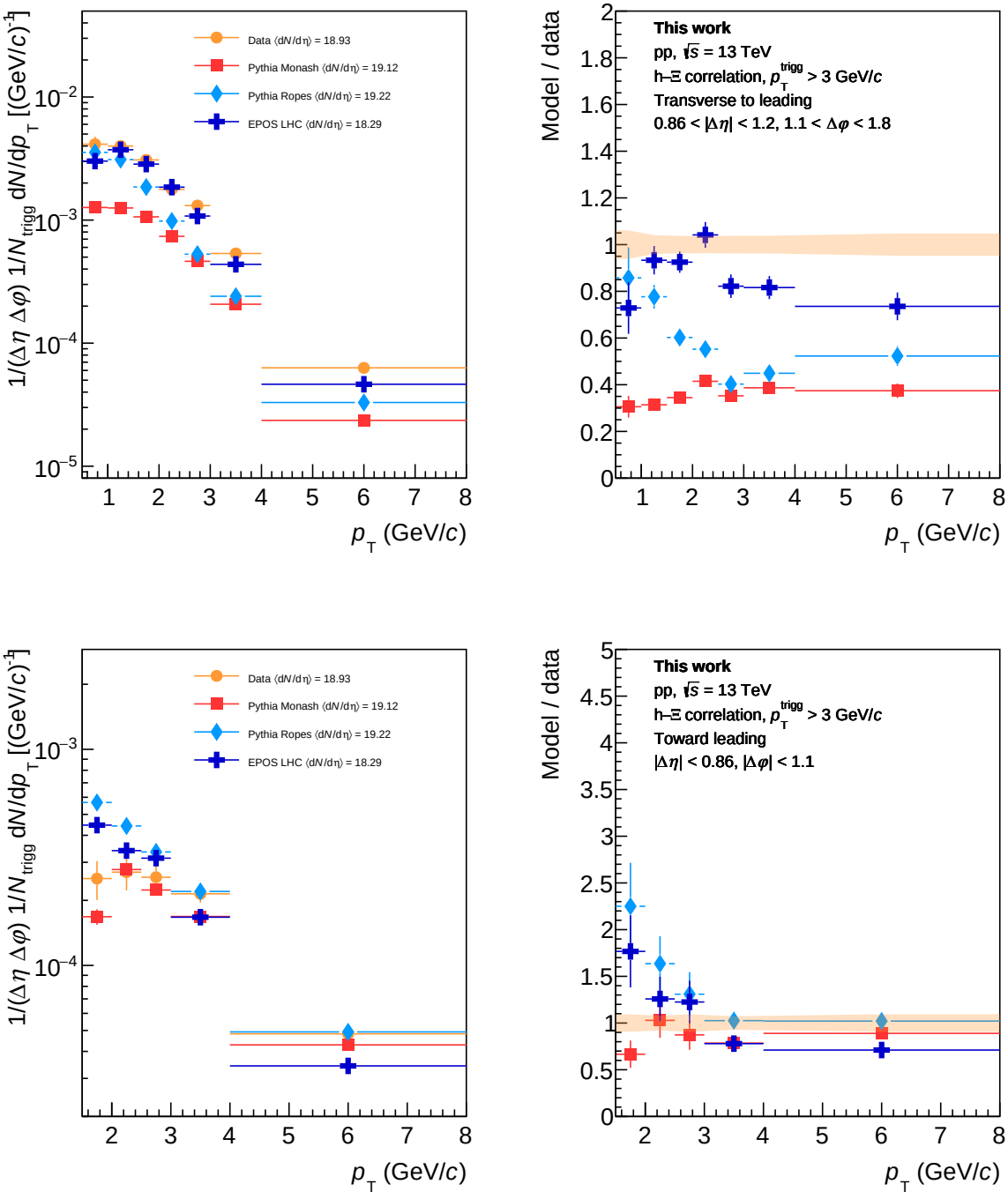

Figure 5.22: (left plots) Transverse-to-leading (top) and toward-leading (bottom) transverse momentum spectra of $\Xi^{\pm}$ in pp collisions at $\sqrt{s} = 13$ TeV. Data points are shown with orange markers, model predictions with different colours as indicated in the legend. The spectra are obtained in multiplicity classes characterised by $\langle dN/d\eta \rangle \sim 19$. Only statistical errors are shown. (right plots) Ratios between the model predictions and the data points. The error bars show the statistical uncertainties, the orange band around one represents the systematic uncertainties of the data points.

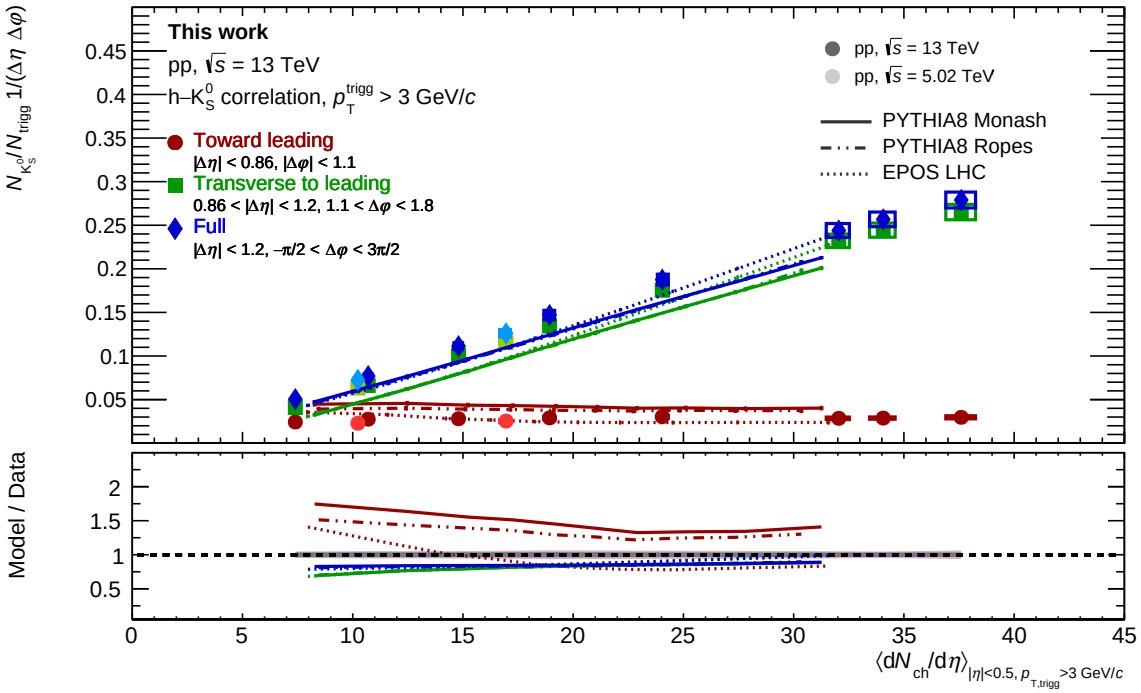

Figure 5.23: (upper panel) K^0_S full (blue), transverse-to-leading (green) and toward-leading (red) yields per unit $\Delta\eta\Delta\varphi$ area as a function of the charged particle multiplicity measured in events with a trigger particle. The data points are drawn with markers, the model predictions with lines of different styles, as indicated in the legend. Statistical and systematic uncertainties of the data points are shown by error bars and empty boxes, respectively. The sum in quadrature of statistical and systematic uncertainties of the model predictions are shown by error bars. (bottom panel) Ratio between the model predictions and the spline fitted to the data points. The shaded band around one represents the sum in quadrature of the statistical and systematic uncertainties of the data points.

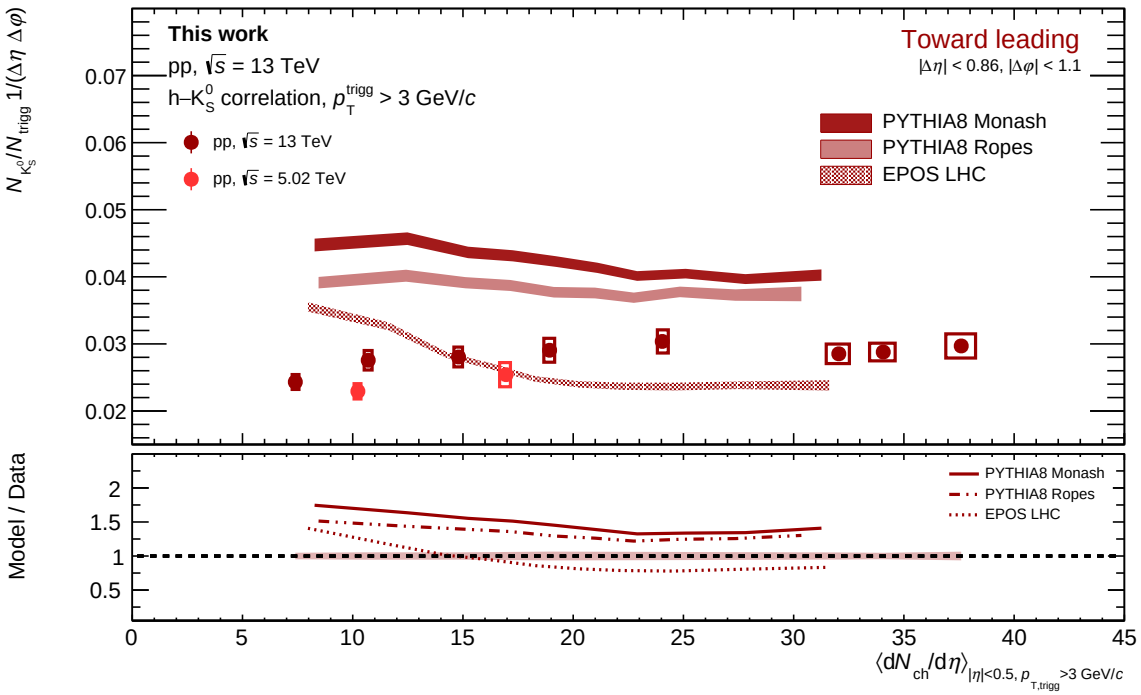

Figure 5.24: (upper panel) K^0_S toward-leading yield per unit $\Delta\eta\Delta\varphi$ area as a function of the charged particle multiplicity measured in events with a trigger particle. The data points are drawn with markers, and their statistical and systematic uncertainties are shown by error bars and empty boxes, respectively. The model predictions are drawn with bands of different styles, as indicated in the legend. The width of the band represents the sum in quadrature of statistical and systematic uncertainties. (bottom panel) Ratio between the model predictions and the spline fitted to the data points. The shaded band around one represents the sum in quadrature of the statistical and systematic uncertainties of the data points.

by PYTHIA8 with ropes and EPOS LHC. These models, however, overestimate the yields over the whole multiplicity interval. PYTHIA8 Monash cannot describe the increase of the toward-leading yield observed in the data, as it predicts a flat trend with multiplicity.

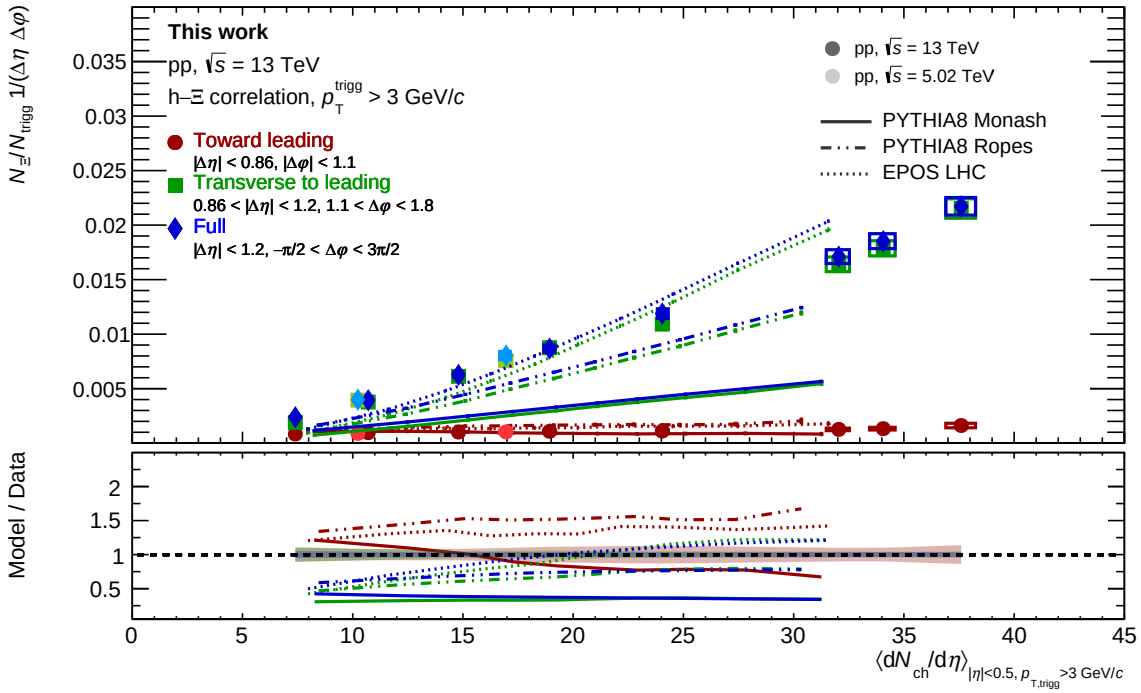

Figure 5.25: (upper panel) $\Xi^{\pm}$ full (blue), transverse-to-leading (green) and toward-leading (red) yields per unit $\Delta\eta\Delta\varphi$ area as a function of the charged particle multiplicity measured in events with a trigger particle. The data points are drawn with markers, the model predictions with lines of different styles, as indicated in the legend. Statistical and systematic uncertainties of the data points are shown by error bars and empty boxes, respectively. The sum in quadrature of statistical and systematic uncertainties of the model predictions are shown by error bars. (bottom panel) Ratio between the model predictions and the spline fitted to the data points. The shaded band around one represents the sum in quadrature of the statistical and systematic uncertainties of the data points.

The comparison between the measured $\Xi^{\pm}/K^0_S$ ratios and the model predictions is shown in Figure 5.27. PYTHIA8 Monash underestimates the ratios in the whole multiplicity interval. This is a consequence of the large underestimation of the $\Xi^{\pm}$ full and transverse-to-leading yields, and of the overestimation of the K^0_S toward-leading yield. The toward-leading ratio shows a hint of decrease with multiplicity, in contrast to the increase observed in the data. The full and transverse-to-leading ratios show instead an increase with multiplicity which is, however, smaller than the one observed in the data, as shown by the fact that the ratios between the model predictions and the data points decrease from about 0.5 at low multiplicity to about 0.4 at high multiplicity.

PYTHIA8 with ropes can qualitatively describe the increase of the ratios with multiplicity observed in the data. However, the full and transverse-to-leading ratios are underestimated in the whole multiplicity interval, and in particular at low multiplicity, where the underestimation of the $\Xi^{\pm}$ yields is larger. The toward-leading ratio is in qualitative agreement with the data, but its increase with multiplicity is slightly overestimated. This fair agreement is however resulting from the overestimation of the both the K^0_S and the $\Xi^{\pm}$ toward-leading

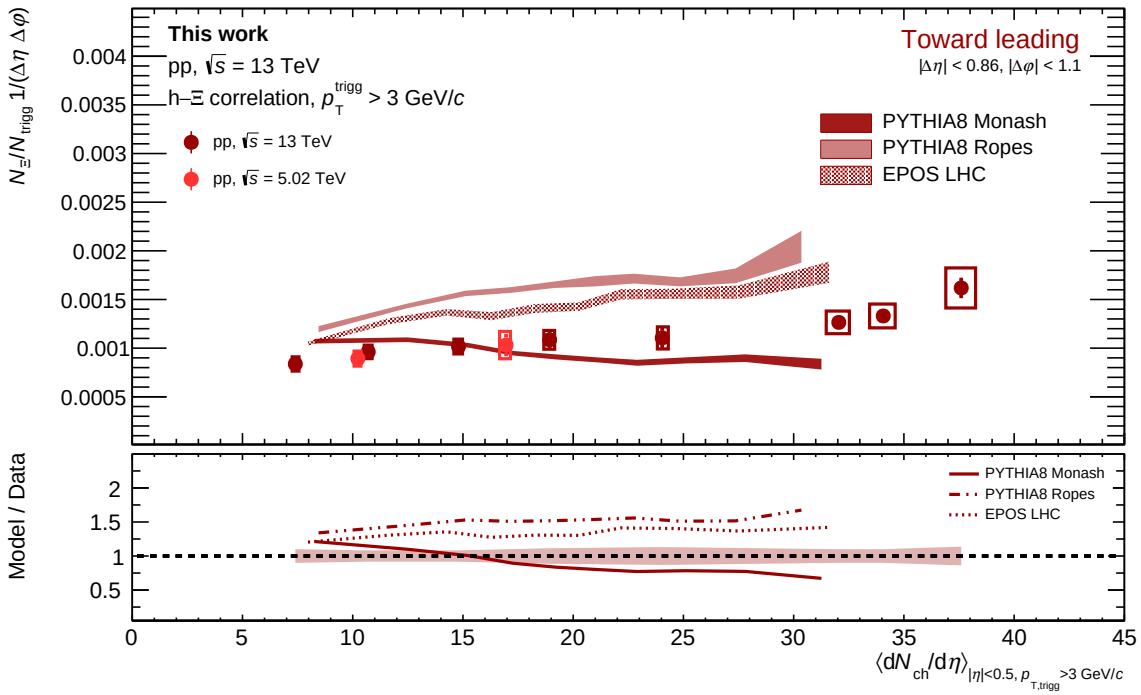

Figure 5.26: (upper panel) $\Xi^{\pm}$ toward-leading yield per unit $\Delta\eta\Delta\varphi$ area as a function of the charged particle multiplicity measured in events with a trigger particle. The data points are drawn with markers, and their statistical and systematic uncertainties are shown by error bars and empty boxes, respectively. The model predictions are drawn with bands of different styles, as indicated in the legend. The width of the band represents the sum in quadrature of statistical and systematic uncertainties. (bottom panel) Ratio between the model predictions and the spline fitted to the data points. The shaded band around one represents the sum in quadrature of the statistical and systematic uncertainties of the data points.

yields (see Figures 5.24 and 5.26).

Finally, EPOS LHC overestimates the increase with multiplicity of the full and transverse-to-leading ratios, as a consequence of the overestimation of the increase of $\Xi^{\pm}$ yields. In particular, the full and transverse-to-leading ratios are underestimated of about 30% at low multiplicity, and overestimated of about 20% at high multiplicity. The toward-leading ratio is instead overestimated in the whole multiplicity interval, mainly as a consequence of the overestimation of the $\Xi^{\pm}$ toward-leading yield. Moreover, its increase with multiplicity is larger than the one observed in the data: this is mainly related to the fact that the K^0_S toward-leading yields predicted by EPOS LHC decreases with multiplicity.

The bottom panel of Figure 5.27 shows the double ratios between the toward-leading and the transverse-to-leading $\Xi^{\pm}/K^0_S$ ratios, for both data and model predictions. All the three models predict a larger double ratio than the one measured in the data. The double ratios predicted by PYTHIA8 with ropes and EPOS LHC are smaller than one and can be described with a zero degree polynomial if both statistical and systematic uncertainties are taken into account. This is in agreement with the flat dependence with multiplicity observed in the data, and indicates that also in these two models the production of $\Xi^{\pm}$ with respect to K^0_S is favoured in transverse-to-leading processes in a similar way throughout the whole multiplicity interval where the measurement was performed. On the contrary, the double ratio predicted by PYTHIA8 Monash is compatible with one in the lowest multiplicity class and decreases to about 0.8 in the highest multiplicity class. Therefore, PYTHIA8 Monash predicts that $\Xi^{\pm}/K^0_S$ production is equally favoured in transverse-to-leading and toward-leading processes at low multiplicity, whereas the $\Xi^{\pm}/K^0_S$ production becomes more favoured in transverse-to-leading processes at larger values of multiplicity.

In conclusion, none of the models can quantitatively describe the full, transverse-to-leading and toward-leading yields of both K^0_S and $\Xi^{\pm}$. All the three models predict softer K^0_S spectra than the measured ones. PYTHIA8 with ropes predict softer spectra for the $\Xi^{\pm}$ as well, whereas PYTHIA Monash can fairly well describe the p_T dependence of both the toward-leading and the transverse-to-leading spectra of $\Xi^{\pm}$, but it largely underestimates the transverse-to-leading p_T-integrated yield. For what concerns the p_T-integrated yields, all models underestimate the full and the transverse-to-leading K^0_S yields, and none of them can describe the increase with multiplicity of the toward-leading yield of K^0_S. Both PYTHIA8 tunes also underestimate the transverse-to-leading and full $\Xi^{\pm}$ yields: the underestimation is worse than for K^0_S, especially the one provided by PYTHIA8 Monash. EPOS LHC, instead, predict an increase with multiplicity of the $\Xi^{\pm}$ full and transverse-to-leading yields larger than the measured one. As a consequence of the described behaviour, PYTHIA8 Monash underestimates the $\Xi^{\pm}/K^0_S$ ratios in the whole multiplicity interval, while PYTHIA8 with ropes and EPOS LHC can qualitatively, but not quantitatively, describe the increase of the ratios with multiplicity observed in the data.

The comparison with the models suggests that both the mechanisms associated with strange hadron production in jets and the ones associated with the production of strange particles out of jets are not properly described in the considered models.

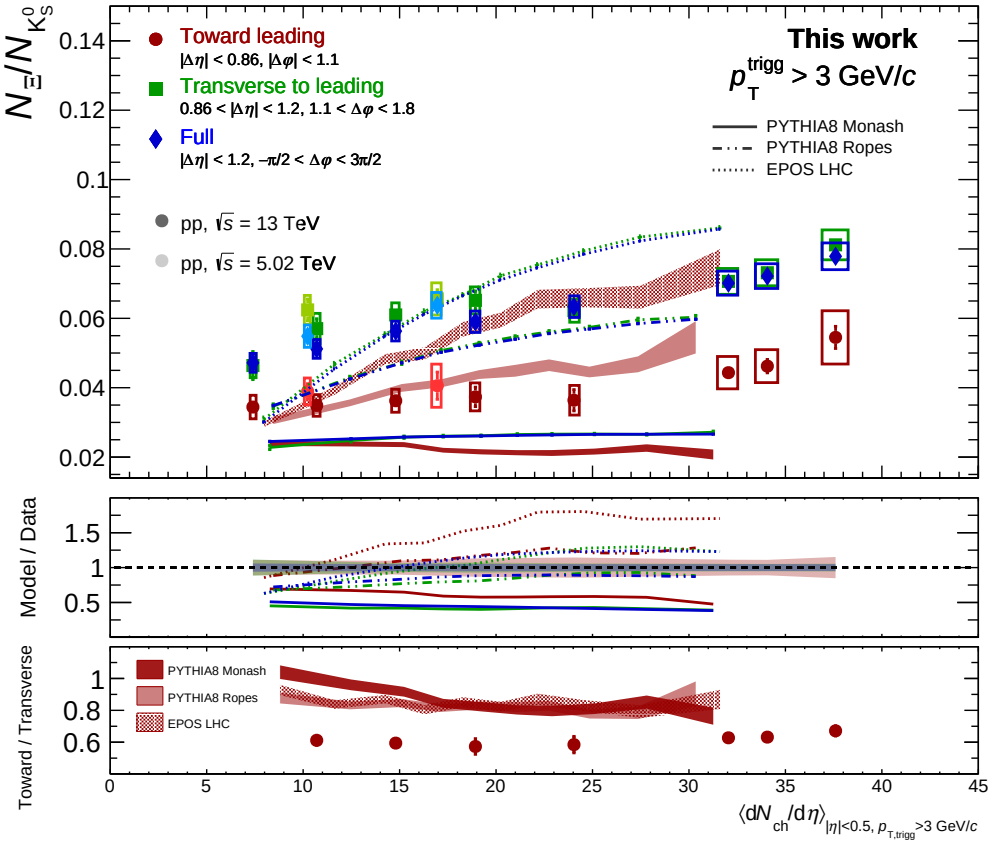

Figure 5.27: (top panel) Full (blue), transverse-to-leading (green) and toward-leading (red) $\Xi^{\pm}/K^0_S$ yield ratios as a function of the charged particle multiplicity measured at midrapidity in events with a trigger particle. The data points are drawn with markers, and their statistical and systematic uncertainties are shown by error bars and empty boxes, respectively. The model predictions are drawn with lines of different styles. The width of the band represents the sum in quadrature of statistical and systematic uncertainties, and is visible only for toward-leading production. (central panel) Ratio between the model predictions and the spline fitted to the data points.The shaded band around one represents the sum in quadrature of the statistical and systematic uncertainties of the data points. (bottom panel) Toward-leading $\Xi^{\pm}/K^0_S$ ratio divided by the transverse-to-leading $\Xi^{\pm}/K^0_S$ ratio.

Chapter 6

Perspectives and conclusions

6.1 Future prospects for strangeness production studies in pp collisions with the ALICE experiment

The results shown in this thesis were obtained by exploiting the full pp data sample collected in Run 2. Further multi-differential studies of strangeness production will be performed with Run 3 data and will profit from a huge increase of the number of collected events.

As mentioned in Section 3, in view of the Run 3 data taking the ALICE detector underwent a major upgrade which increased its readout speed capabilities, making it able to cope with the higher interaction rates provided by the LHC. This improvement will allow for a substantial increase of the number of recorded proton-proton collisions with respect to the Run 2 data taking. Indeed, the foreseen integrated luminosity of pp collisions collected during Run 3 and Run 4 is $L_{int} \approx 200\text{pb}^{-1}$, corresponding to about 14×10^{12} inelastic collisions, approximately three orders of magnitude larger than the minimum bias sample collected in Run 2. This implies an increase of the integrated luminosity of three orders of magnitude for those measurements which were performed using the minimum bias sample collected during Run 2, and of a factor 5 to 20 for those measurements which used dedicated triggers for rare events [127].

Since this huge amount of data cannot be fully stored, a selection to retain the events of interest will be performed. In order to cope with the available computing resources, the fraction of selected events should be of the order of 0.1% of the total [127]. Since the Run 3 data taking applies a *continuous readout* mode, as described in Section 4.4, the event selection is not based on hardware triggers. Instead, it will be performed at the software level, by applying software triggers taking advantage of the full reconstruction of each event.

Several software triggers (or *filters*) have been discussed within the ALICE collaboration, with the purpose of studying rare probes with high precision. I have contributed to the development of dedicated filters for future multi-differential studies of strangeness production. These filters will allow for the selection of the following types of events:

- **Events with at least one $\Omega^{\pm}$ baryon**
  Considering an integrated luminosity of 200pb^{-1}, a sample of about 1×10^9 $\Omega^{\pm}$ baryons will be available. Such a sample will allow for the study of the $\Omega^{\pm}$ yield as a function of the charged particle multiplicity produced at midrapidity up to values of multiplicity of about 100, which is comparable to the most peripheral Pb–Pb collision where the measurement has been performed so far. These studies will reveal if the $\Omega^{\pm}/\pi^{\pm}$ ratio reaches, in high-multiplicity pp collisions, the thermal limit observed in Pb–Pb

collisions, or if instead it increases above the Pb–Pb values. Moreover, such a large $\Omega^{\pm}$ sample will allow for the application of the angular correlation technique to study the transverse-to-leading and toward-leading production of $\Omega^{\pm}$ as a function of multiplicity. This study was not feasible with the events collected during Run 2.

- **Events with a high-p_{T} charged hadron and a $\Xi^{\pm}$ baryon candidate**
  This trigger will allow for further developments of the analysis presented in this thesis. The huge amount of collisions to be recorded during Run 3 will allow for an increase of the minimum p_{T} of the trigger particle to values larger than 3 GeV/c, in order to reduce the contamination from particles not originating from hard scattering processes. This trigger will be discussed in more detail in Section 6.1.1.

- **Events with two or more $\Xi^{\pm}$ baryon candidates**
  These events will be useful to study exotic states decaying into two $\Xi^{\pm}$ baryons as well as the correlation in space and momentum between two $\Xi^{\pm}$ baryons produced in the same event.

- **Events with a $\Xi^{\pm}$ baryon candidate with large decay radius for hyperon-nucleon interaction measurement**
  To improve the current knowledge of the $\Xi^{\pm}$-nucleon elastic cross section, which is based on low-statistics measurements performed at low transverse momentum ($p_{\mathrm{T}} \lesssim 1$ GeV/c) [158, 159], the elastic interaction of $\Xi^{\pm}$ produced in pp collisions at the LHC with the material of the ALICE Inner Tracking System (ITS) can be exploited. To measure the elastic cross-section as a function of the scattering angle θ, the momentum of the $\Xi^{\pm}$ must be determined before and after the scattering event occurs. The momentum after the scattering process can be determined from the topological reconstruction of $\Xi^{\pm}$ (see Section 4.5), whereas the momentum before the scattering event can be directly measured by tracking the $\Xi^{\pm}$ with the innermost ITS layers, making use of a novel reconstruction technique called *strangeness tracking* [160]. To allow for a good momentum resolution of $\Xi^{\pm}$ tracked before their decay, $\Xi^{\pm}$ are required to traverse at least four layers of the ITS.

The selection of these events will be performed by applying kinematic and topological selections to the variables describing the decay of the $\Xi^{\pm}$ and the $\Omega^{\pm}$ baryons into charged hadrons: $\Xi^{-} \rightarrow \pi^{-}\Lambda(\rightarrow \mathrm{p}\pi^{-})$, $\Omega^{-} \rightarrow K^{-}\Lambda(\rightarrow \mathrm{p}\pi^{-})$ and their charge conjugates. As mentioned above, the possibility to apply software triggers based on topological and kinematic selections is due to the fact that all recorded events are fully reconstructed and buffered until the event skimming is performed.

In order to cope with the available computing resources, each of the filters should select a fraction of events of the order of 10^{-5}, corresponding to a *rejection factor* of 10^{5}. The rejection factors associated to the aforementioned filters have been estimated using Run 2 data. I have estimated the rejection factor for the trigger selecting events with a high-p_{T} hadron and a $\Xi^{\pm}$ candidate, as described in Section 6.1.1.

I have contributed to the implementation of the software triggers in the new analysis framework O^2 [137] of the ALICE experiment, and I am currently working on their validation using Monte Carlo samples and pp collisions collected during Run 3. Once validated, the event filtering software will be applied to the sample of pp collisions at $\sqrt{s} = 13.6$ TeV recorded during 2022, which amounts to an integrated luminosity of about 15 pb^{-1}. Rejected events will be deleted, in order to free disk space for the 2023 pp and Pb–Pb data taking, while the selected ones will be stored for subsequent data analyses.

6.1.1 Estimates of the rejection factor for events with a high-p_{T} charged hadron and a $\Xi^{\pm}$ candidate

I have estimated the fraction of events containing a high-p_{T} charged hadron and a $\Xi^{\pm}$ baryon as a function of the minimum transverse momentum of the charged track $p_{\mathrm{T}}^{\mathrm{th}}$ using pp collisions recorded during Run 2. Charged tracks are required to satisfy the selections reported in Table 4.1, and $\Xi^{\pm}$ baryon candidates are selected by applying the topological selections reported in Table 4.5 and an additional selection on the invariant mass of the $\Xi^{\pm}$ candidate, which is required to differ from the nominal mass of the $\Xi^{\pm}$ by less than 3σ, with σ representing the resolution of the $\Xi^{\pm}$ invariant mass. The fraction of events containing a high-p_{T} charged track and a $\Xi^{\pm}$ baryon (called from now on h-$\Xi^{\pm}$events) is shown in the top left panel of Figure 6.1 for $p_{\mathrm{T}}^{\mathrm{th}}$ values ranging from 3 to 10 GeV/c. The estimates are shown as a function of the V0M multiplicity class. As expected, the fraction of h-$\Xi^{\pm}$ events decreases with decreasing multiplicity and with increasing $p_{\mathrm{T}}^{\mathrm{th}}$. The top right plot of Figure 6.1 shows the ratios between the fraction of h-$\Xi^{\pm}$ events for different $p_{\mathrm{T}}^{\mathrm{th}}$ values and the fraction of h-$\Xi^{\pm}$ events for $p_{\mathrm{T}}^{\mathrm{th}} = 3$ GeV/c, whereas the bottom panel shows the ratio between the fraction of h-$\Xi^{\pm}$ events with a charged track with $p_{\mathrm{T}} >$ x, where x can assume the values displayed in the legend in the top left panel, and the fraction of h-$\Xi^{\pm}$ events containing a charged hadron with $p_{\mathrm{T}} >$ (x $-$ 1) GeV/c. This plot shows that the fraction of h-$\Xi^{\pm}$ events decreases by about 40% to 60% when $p_{\mathrm{T}}^{\mathrm{th}}$ is increased of 1 GeV/c, with the decrease being larger at low $p_{\mathrm{T}}^{\mathrm{th}}$.

The fraction of h-$\Xi^{\pm}$ events computed in the 0-100% multiplicity class varies from 3.5×10^{-4} for $p_{\mathrm{T}}^{\mathrm{th}} = 3$ GeV/c to 4.8×10^{-6} for $p_{\mathrm{T}}^{\mathrm{th}} = 10$ GeV/c. A rejection factor of about 10^5, which satisfies the requirements imposed by the available computing resources, is achieved for $p_{\mathrm{T}}^{\mathrm{th}} = 7$ GeV/c. Considering a total integrated luminosity of 200 pb^{-1}, the number of selected h-$\Xi^{\pm}$ events with $p_{\mathrm{T}}^{\mathrm{th}} = 7$ GeV/c would be about 140×10^6, approximately 400 times larger than the sample used for the analysis presented in this thesis.

Currently, the rejection factors are being calculated using a Monte Carlo simulation of pp collisions at $\sqrt{s} = 13.6$ TeV which implements the description of the ALICE detector in the Run 3 configuration, and using the pp collisions at $\sqrt{s} = 13.6$ TeV collected during 2022. These studies will allow for the definition of the value of $p_{\mathrm{T}}^{\mathrm{th}}$ which provides a rejection factor of about 10^5 in pp collisions at $\sqrt{s} = 13.6$ TeV. Some difference with respect to the Run 2 estimates are expected since the tracking efficiency and the efficiency of cascade reconstruction might be different, as a consequence of the major hardware and software upgrade of the ALICE detector.

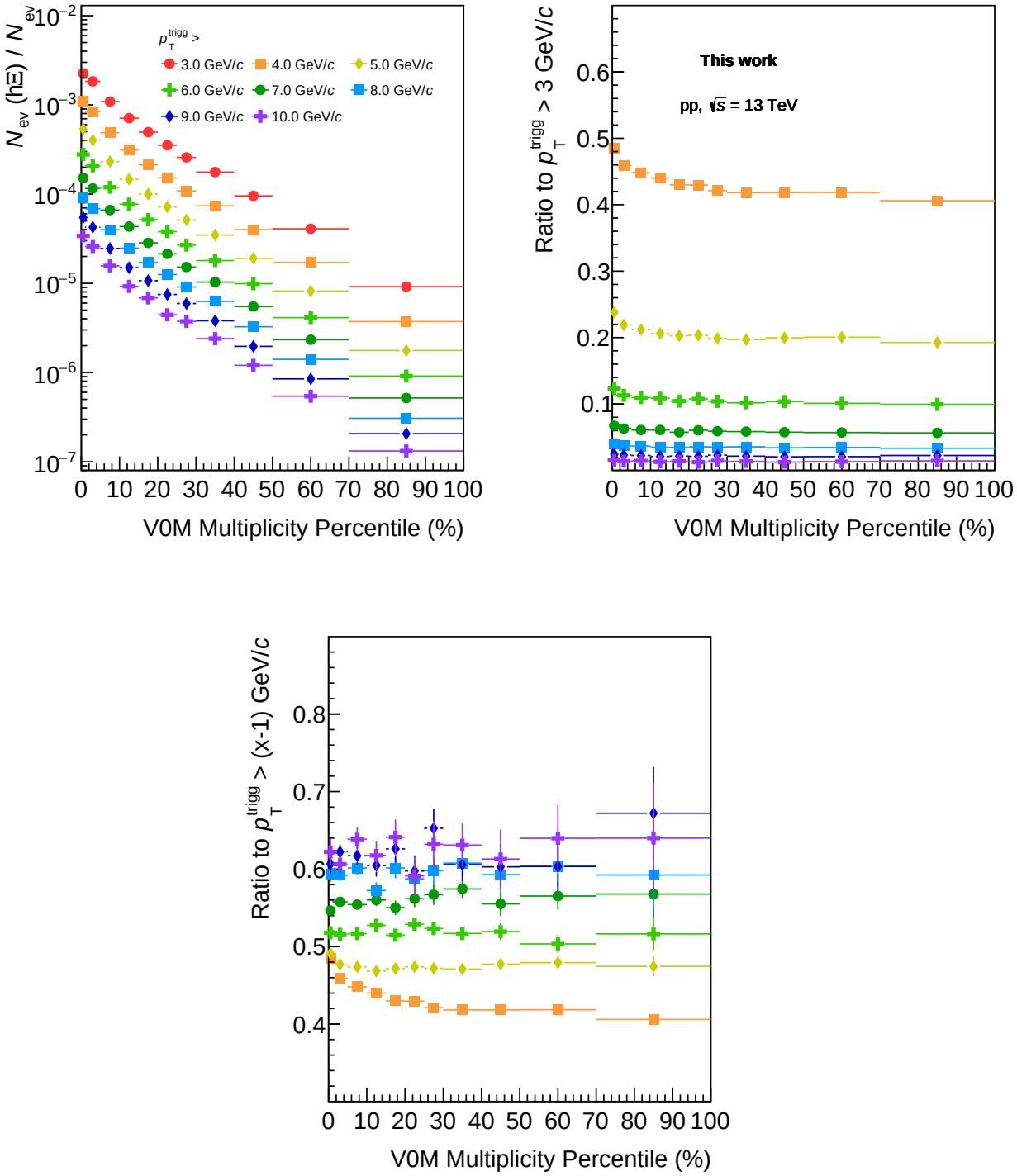

Figure 6.1: (top left) Fraction of pp collisions at $\sqrt{s} = 13$ TeV containing a charged hadron with p_T above a specified threshold, as indicated in the legend, and a $\Xi^{\pm}$ baryon candidate, as a function of the V0M multiplicity class. (top right) Ratios between the fraction of events containing a charged hadron with p_T above a specified threshold, and the fraction of events containing a charged hadron with $p_T > 3$ GeV/c. (bottom) Ratios between the fraction of events containing a charged hadron with $p_T >$ x, where x can assume the different values reported in the legend in the top left panel, and the fraction of events containing a charged hadron with $p_T > (x - 1)$ GeV/c.

6.1.2 A first look at strange hadrons in pp collisions at $\sqrt{s} = 13.6$ TeV collected in 2022

About 10% of the pp collisions at $\sqrt{s} = 13.6$ TeV collected by the ALICE experiment in 2022 have already been reconstructed and are available for analysis purposes. This sample consists of about 7×10^{10} events, more than 30 times the number of minimum bias pp collisions recorded during Run 2.

A first look at K^0_S, $\Lambda(\overline{\Lambda})$ and $\Xi^\pm$ invariant mass distributions in Run 3 data was performed using the V^0 and cascades reconstruction algorithm implemented in the new analysis framework O^2 [137] of the ALICE experiment. The reconstruction of V^0 and cascades is performed by exploiting their weak decay into charged hadrons:

$$\mathrm{K}^0_\mathrm{S} \to \pi^+\pi^-$$

$$\Lambda \to \mathrm{p}\pi^-(\overline{\Lambda} \to \overline{\mathrm{p}}\pi^+)$$
$$\Xi^- \to \Lambda\pi^- \to \mathrm{p}\pi^-\pi^-(\Xi^+ \to \overline{\Lambda}\pi^+ \to \overline{\mathrm{p}}\pi^+\pi^+)$$
$$\Omega^- \to \Lambda\mathrm{K}^- \to \mathrm{p}\pi^-\mathrm{K}^-(\Omega^+ \to \overline{\Lambda}\mathrm{K}^+ \to \overline{\mathrm{p}}\pi^+\mathrm{K}^+)$$

Topological and kinematic selections are applied to the variables describing these decays in order to reject the combinatorial background. Figure 6.2 shows the invariant masses of K^0_S (top panel), Λ and $\overline{\Lambda}$ (left and right central panels, respectively), and Ξ^- and Ξ^+ (left and right bottom panels, respectively) measured at midrapidity ($|y| < 0.5$) in the transverse momentum interval $0 < p_\mathrm{T} < 10$ GeV/c. The applied topological and kinematic selections are very similar to those used in the analysis described in the thesis and reported in Tables 4.4 and Tables 4.5 for K^0_S and $\Xi^\pm$, respectively. For Λ ($\overline{\Lambda}$) identification, the same topological selections applied to identify K^0_S are used. The invariant mass distributions are fitted with a fit function (red line) given by the sum of a Gaussian function, which describes the signal, and of a polynomial (dotted black line) used to describe the combinatorial background. For all particles, the mean and σ values of the Gaussian functions are comparable to those measured in Run 2. Further studies of the invariant mass properties as a function of the transverse momentum will be carried out. Moreover, a systematic study of the purity of the strange hadron samples will be performed by varying the topological and kinematic selections.

The studies carried out so far have provided important information about the quality of the collected data and the performance of the V^0 and cascade reconstruction algorithm implemented in the new analysis framework O^2.

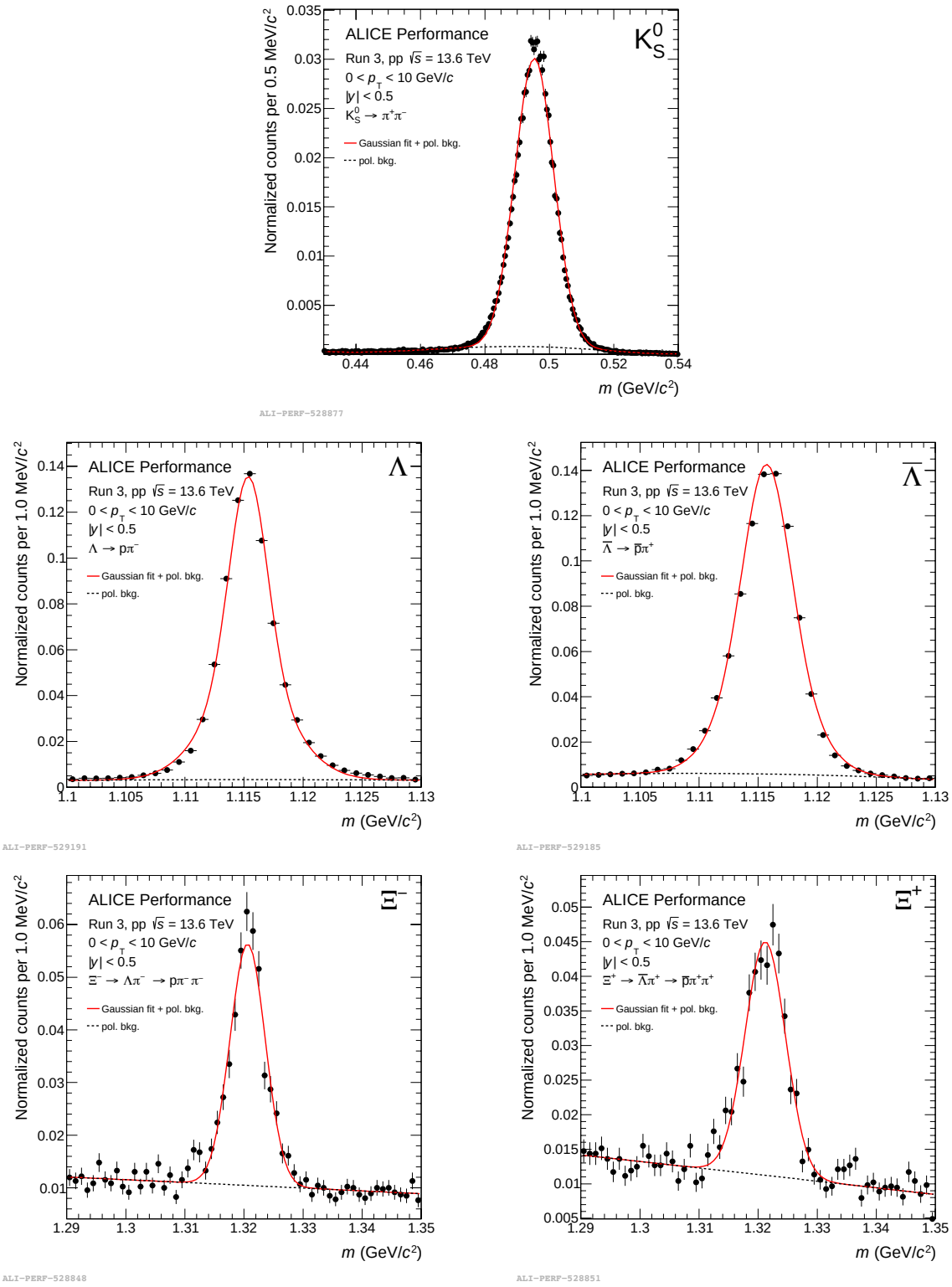

Figure 6.2: Invariant mass distributions of K^0_S (top panel), Λ and $\overline{\Lambda}$ (left and right central panel, respectively), and Ξ^- and Ξ^+ (left and right bottom panels, respectively) measured at midrapidity ($|y| < 0.5$) in the transverse momentum interval $0 < p_T < 10$ GeV/c in pp collisions at $\sqrt{s} = 13.6$ TeV. The invariant mass distributions are fitted with the sum of a Gaussian function, used to describe the signal, and of a polynomial function (dotted line), used to describe the background. The global fit is displayed with a red line. Figures taken from the ALICE repository.

6.2 Conclusions

The study of strange hadron production in different hadronic collisions (pp, p–Pb, Pb–Pb) at the LHC energies has revealed a smooth increase of the ratios of strange to non-strange hadron yields as a function of the multiplicity of charged particles produced in the collision. This behaviour, commonly referred to as "strangeness enhancement", is striking, as different particle production mechanisms are expected to be involved in the different collision systems. Indeed, the larger ratio of (multi-)strange hadron to pion yields observed in central Pb–Pb collisions with respect to minimum bias pp collision was historically interpreted as a signature of quark-gluon plasma formation, which however is not expected to form in small collision systems.

To understand the origin of this behaviour, which suggests the presence of collective effects in small collision systems, multi-differential analyses are being carried out within the ALICE collaboration. The analysis work described in this thesis focuses on the contributions to strange hadron production in pp collisions given by the mechanisms associated to hadron production in jets (hard processes) and out of jets.

This topic was addressed by performing the first analysis of the production of the K^0_S meson and the $\Xi^\pm$ baryon in jets and out of jets as a function of the charged-particle multiplicity at midrapidity in pp collisions at $\sqrt{s} = 13$ TeV and $\sqrt{s} = 5.02$ TeV collected by the ALICE experiment. The angular correlation between the trigger particle, i.e. the highest-p_T charged particle with $p_\mathrm{T} > 3$ GeV/c, and the K^0_S ($\Xi^\pm$) hadrons was exploited to separate K^0_S ($\Xi^\pm$) produced in the leading jet from those produced out of jets. The former are produced in the direction of the trigger particle (toward-leading production), the latter are selected in an angular region transverse to the trigger particle direction (transverse-to-leading production).

The results, presented in Chapter 5, show that the toward-leading p_T spectra are harder than the transverse-to-leading ones, indicating that K^0_S ($\Xi^\pm$) produced in jets have a larger average transverse momentum than K^0_S ($\Xi^\pm$) produced out of jets, as expected from the fact that jets are associated to hard scattering processes. For both K^0_S and $\Xi^\pm$, the p_T-integrated yields are dominated by transverse-to-leading production and increase with the multiplicity of charged-particles produced at midrapidity. The toward-leading yields show instead a much milder dependence on the multiplicity, indicating that the contribution of transverse-to-leading processes relative to toward-leading ones increases with the multiplicity.

The ratio between the $\Xi^\pm$ and the K^0_S yields provides insight into the strangeness enhancement effect, since the strangeness content of the $\Xi^\pm$ ($|S|$=2) is larger than the K^0_S one ($|S|$=1). Both the transverse-to-leading and the toward-leading $\Xi^\pm/\mathrm{K}^0_\mathrm{S}$ yield ratios increase with the multiplicity of charged particles. The transverse-to-leading ratio is larger than the toward-leading one, suggesting that the relative production of $\Xi^\pm$ with respect to K^0_S is favoured in transverse-to-leading processes. Moreover, the yield ratios do not show any centre-of-mass energy dependence, as expected.

The results were compared with the predictions of PYTHIA8 Monash tune, PYTHIA8 with ropes and EPOS LHC. None of the models can quantitatively describe the transverse-to-leading and toward-leading yields of K^0_S and $\Xi^\pm$. The comparison with the models suggests that both the mechanisms associated with in-jet and out-of-jet strange hadron production are not properly described in the considered models.

Future multi-differential analyses of strange hadron production with Run 3 data will allow for further investigation of the origin of strangeness enhancement in pp collisions. Thanks to the development of software filters for the selection and storage of pp collisions containing strange hadron candidates, a huge sample of $\Xi^\pm$ and $\Omega^\pm$ baryon will be available at the

end or Run 3. The measurement of the toward-leading and transverse-to-leading $\Omega^{\pm}$ yields as a function of the charged-particle multiplicity and the study of the dependence of the toward-leading and transverse-to-leading $\Xi^{\pm}$ yields on the minimum p_{T} of the trigger particle will become feasible and will help improve the current understanding of particle production mechanisms.

Bibliography

1. Thomson, M. *Modern Particle Physics* (Cambridge University Press, 2013).
2. Greiner, W., Schramm, S. & Stein, E. *Quantum chromodynamics* (Springer, 2002).
3. Aoki, S. *et al.* Review of lattice results concerning low-energy particle physics. *Eur. Phys. J.* **C77,** 112. arXiv: 1607.00299 (2017).
4. Workman, R. L. *et al.* Review of Particle Physics. *PTEP* **2022,** 083C01 (2022).
5. Braun-Munzinger, P., Koch, V., Schäfer, T. & Stachel, J. Properties of hot and dense matter from relativistic heavy ion collisions. *Physics Reports* **621.** Memorial Volume in Honor of Gerald E. Brown, 76–126 (2016).
6. Gross, D. J. & Wilczek, F. Ultraviolet Behavior of Non-Abelian Gauge Theories. *Phys. Rev. Lett.* **30,** 1343–1346 (1973).
7. Politzer, H. D. Reliable Perturbative Results for Strong Interactions? *Phys. Rev. Lett.* **30,** 1346–1349 (1973).
8. Wilson, K. G. Confinement of quarks. *Phys. Rev. D* **10,** 2445–2459 (1974).
9. Pasechnik, R. & Šumbera, M. Phenomenological Review on Quark–Gluon Plasma: Concepts vs. Observations. *Universe* **3,** 7. arXiv: 1611.01533 (2017).
10. Baldo, M. *et al.* Neutron stars and the transition to color superconducting quark matter. *Phys. Lett.* **B562,** 153–160. arXiv: nucl-th/0212096 (2003).
11. Bazavov, A. *et al.* Chiral crossover in QCD at zero and non-zero chemical potentials. *Phys. Lett.* **B795,** 15–21. arXiv: 1812.08235 (2019).
12. Stephanov, M. A. QCD phase diagram and the critical point. *Prog. Theor. Phys. Suppl.* **153** (eds Muller, B. & Tan, C. I.) 139–156. arXiv: hep-ph/0402115 (2004).
13. Gavai, R. V. & Gupta, S. The Critical end point of QCD. *Phys. Rev. D* **71,** 114014. arXiv: hep-lat/0412035 (2005).
14. Bzdak, A. *et al.* Mapping the phases of quantum chromodynamics with beam energy scan. *Physics Reports* **853,** 1–87 (2020).
15. Kapishin, M. The fixed target experiment for studies of baryonic matter at the Nuclotron (BM@N). *The European Physical Journal A* **52** (2016).
16. Golovatyuk, V., Kekelidze, V., Kolesnikov, V., Rogachevsky, O. & Sorin, A. The Multi-Purpose Detector (MPD) of the collider experiment. *Eur. Phys. J. A* **52,** 212 (2016).
17. Ablyazimov, T. *et al.* Challenges in QCD matter physics –The scientific programme of the Compressed Baryonic Matter experiment at FAIR. *Eur. Phys. J. A* **53,** 60. arXiv: 1607.01487 (2017).

18. Dahms, T., Scomparin, E. & Usai, G. *Expression of Interest for a new experiment at the CERN SPS: NA60+* tech. rep. (CERN, Geneva, 2019). https://cds.cern.ch/record/2673280.
19. Aprahamian, A. *et al.* Reaching for the horizon: The 2015 long range plan for nuclear science (2015).
20. Gustafsson, H. A. *et al.* Collective Flow Observed in Relativistic Nuclear Collisions. *Phys. Rev. Lett.* **52,** 1590–1593 (1984).
21. Koch, P., Müller, B. & Rafelski, J. From strangeness enhancement to quark–gluon plasma discovery. *Int. J. Mod. Phys.* **A32,** 1730024. arXiv: 1708.08115 (2017).
22. ALICE collaboration. The ALICE experiment - A journey through QCD. arXiv: 2211.04384 (2022).
23. Bazavov, A. *et al.* Equation of state in (2+1)-flavor QCD. *Phys. Rev. D* **90,** 094503. arXiv: 1407.6387 (2014).
24. Gale, C., Jeon, S. & Schenke, B. Hydrodynamic Modeling of Heavy-Ion Collisions. *Int. J. Mod. Phys.* **A28,** 1340011. arXiv: 1301.5893 (2013).
25. Miller, M. L., Reygers, K., Sanders, S. J. & Steinberg, P. Glauber modeling in high energy nuclear collisions. *Ann. Rev. Nucl. Part. Sci.* **57,** 205–243. arXiv: nucl-ex/0701025 (2007).
26. Abbas, E. *et al.* Performance of the ALICE VZERO system. *JINST* **8,** P10016. arXiv: 1306.3130 (2013).
27. Abelev, B. B. *et al.* Performance of the ALICE Experiment at the CERN LHC. *Int. J. Mod. Phys.* **A29,** 1430044. arXiv: 1402.4476 (2014).
28. Adam, J. *et al.* Centrality Dependence of the Charged-Particle Multiplicity Density at Midrapidity in Pb-Pb Collisions at $\sqrt{s_{\mathrm{NN}}} = 5.02$ TeV. *Phys. Rev. Lett.* **116,** 222302. arXiv: 1512.06104 (2016).
29. Wheaton, S., Cleymans, J. & Hauer, M. THERMUS. arXiv: 1108.4588 (2011).
30. Petrán, M., Letessier, J., Petráček, V. & Rafelski, J. Hadron production and quark-gluon plasma hadronization in Pb-Pb collisions at $\sqrt{s_{NN}} = 2.76$ TeV. *Phys. Rev.* **C88,** 034907. arXiv: 1303.2098 (2013).
31. Vovchenko, V. & Stoecker, H. Thermal-FIST: A package for heavy-ion collisions and hadronic equation of state. *Comput. Phys. Commun.* **244,** 295–310. arXiv: 1901.05249 (2019).
32. Andronic, A., Braun-Munzinger, P. & Stachel, J. Thermal hadron production in relativistic nuclear collisions: The hadron mass spectrum, the horn, and the QCD phase transition. *Physics Letters B* **673,** 142–145 (2009).
33. Aamodt, K. *et al.* Midrapidity antiproton-to-proton ratio in pp collisions at $\sqrt{s} = 0.9$ and 7˜TeV measured by the ALICE experiment. *Phys. Rev. Lett.* **105,** 072002. arXiv: 1006.5432 (2010).
34. Acharya, S. *et al.* Production of charged pions, kaons, and (anti-)protons in Pb-Pb and inelastic *pp* collisions at $\sqrt{s_{NN}} = 5.02$ TeV. *Phys. Rev. C* **101,** 044907. arXiv: 1910.07678 (2020).

35. Schnedermann, E., Sollfrank, J. & Heinz, U. W. Thermal phenomenology of hadrons from 200-A/GeV S+S collisions. *Phys. Rev.* **C48,** 2462–2475. arXiv: nucl-th/9307020 (1993).

36. Abelev, B. B. *et al.* Multiplicity Dependence of Pion, Kaon, Proton and Lambda Production in p-Pb Collisions at $\sqrt{s_{NN}}$ = 5.02 TeV. *Phys. Lett.* **B728,** 25–38. arXiv: 1307.6796 (2014).

37. Nagle, J. L. & Zajc, W. A. Small System Collectivity in Relativistic Hadronic and Nuclear Collisions. *Ann. Rev. Nucl. Part. Sci.* **68,** 211–235. arXiv: 1801.03477 (2018).

38. Molnar, D. & Voloshin, S. A. Elliptic flow at large transverse momenta from quark coalescence. *Phys. Rev. Lett.* **91,** 092301. arXiv: nucl-th/0302014 (2003).

39. Kovtun, P., Son, D. T. & Starinets, A. O. Viscosity in strongly interacting quantum field theories from black hole physics. *Phys. Rev. Lett.* **94,** 111601. arXiv: hep-th/0405231 (2005).

40. Bernhard, J. E., Moreland, J. S. & Bass, S. A. Bayesian estimation of the specific shear and bulk viscosity of quark–gluon plasma. *Nature Phys.* **15,** 1113–1117 (2019).

41. Acharya, S. *et al.* Anisotropic flow of identified particles in Pb-Pb collisions at $\sqrt{s}_{\mathrm{NN}}$ = 5.02 TeV. *JHEP* **09,** 006. arXiv: 1805.04390 (2018).

42. Aamodt, K. *et al.* Suppression of Charged Particle Production at Large Transverse Momentum in Central Pb-Pb Collisions at $\sqrt{s_{NN}}$ = 2.76 TeV. *Phys. Lett. B* **696,** 30–39. arXiv: 1012.1004 (2011).

43. Chatrchyan, S. *et al.* Study of high-pT charged particle suppression in PbPb compared to *pp* collisions at $\sqrt{s_{NN}}$ = 2.76 TeV. *Eur. Phys. J. C* **72,** 1945. arXiv: 1202.2554 (2012).

44. Abelev, B. B. *et al.* Transverse momentum dependence of inclusive primary charged-particle production in p-Pb collisions at $\sqrt{s_{\mathrm{NN}}}$ = 5.02 TeV. *Eur. Phys. J. C* **74,** 3054. arXiv: 1405.2737 (2014).

45. Lee, Y.-J. Measurement of isolated photon production in pp and PbPb collisions at $sqrtsNN$ = 2.76 TeV with CMS. *Nucl. Phys. A* **910-911** (eds Antinori, F. *et al.*) 376–378. arXiv: 1208.6156 (2013).

46. Chatrchyan, S. *et al.* Study of Z boson production in PbPb collisions at $\sqrt{s_{NN}}$ = 2.76 TeV. *Phys. Rev. Lett.* **106,** 212301. arXiv: 1102.5435 (2011).

47. Chatrchyan, S. *et al.* Study of W boson production in PbPb and *pp* collisions at $\sqrt{s_{NN}}$ = 2.76 TeV. *Phys. Lett. B* **715,** 66–87. arXiv: 1205.6334 (2012).

48. Alessandro, B. *et al.* A New measurement of J/psi suppression in Pb-Pb collisions at 158-GeV per nucleon. *Eur. Phys. J. C* **39,** 335–345. arXiv: hep-ex/0412036 (2005).

49. Adam, J. *et al.* Measurement of inclusive J/ψ suppression in Au+Au collisions at $\sqrt{s_{NN}}$ = 200 GeV through the dimuon channel at STAR. *Phys. Lett. B* **797,** 134917. arXiv: 1905.13669 (2019).

50. $\psi(2S)$ suppression in Pb-Pb collisions at the LHC. arXiv: 2210.08893 (Oct. 2022).

51. Sirunyan, A. M. *et al.* Relative Modification of Prompt ψ(2S) and J/ψ Yields from pp to PbPb Collisions at $\sqrt{s_{NN}}$ = 5.02 TeV. *Phys. Rev. Lett.* **118,** 162301. arXiv: 1611.01438 (2017).

52. Acharya, S. *et al.* Υ production and nuclear modification at forward rapidity in Pb–Pb collisions at $\sqrt{s_{\mathrm{NN}}} = 5.02$ TeV. *Phys. Lett. B* **822,** 136579. arXiv: 2011.05758 (2021).
53. Sirunyan, A. M. *et al.* Measurement of nuclear modification factors of Υ(1S), Υ(2S), and Υ(3S) mesons in PbPb collisions at $\sqrt{s_{\mathrm{NN}}} = 5.02$ TeV. *Phys. Lett. B* **790,** 270–293. arXiv: 1805.09215 (2019).
54. Observation of a Centrality-Dependent Dijet Asymmetry in Lead-Lead Collisions at $\sqrt{s_{\mathrm{NN}}} = 2.76$ TeV with the ATLAS Detector at the LHC. *Phys. Rev. Lett.* **105,** 252303 (2010).
55. Havener, L. & on behalf of the ATLAS Collaboration. Dijet asymmetries in Pb+Pb and pp collisions with the ATLAS detector. *Journal of Physics: Conference Series* **832,** 012007. https://dx.doi.org/10.1088/1742-6596/832/1/012007 (2017).
56. Adam, J. *et al.* Enhanced production of multi-strange hadrons in high-multiplicity proton-proton collisions. *Nature Phys.* **13,** 535–539. arXiv: 1606.07424 (2017).
57. Acharya, S. *et al.* Multiplicity dependence of (multi-)strange hadron production in proton-proton collisions at $\sqrt{s} = 13$ TeV. arXiv: 1908.01861 (2019).
58. Adam, J. *et al.* Multi-strange baryon production in p-Pb collisions at $\sqrt{s_{\mathrm{NN}}} = 5.02$ TeV. *Phys. Lett.* **B758,** 389–401. arXiv: 1512.07227 (2016).
59. Abelev, B. B. *et al.* Multi-strange baryon production at mid-rapidity in Pb-Pb collisions at $\sqrt{s_{\mathrm{NN}}} = 2.76$ TeV. *Phys. Lett.* **B728.** [Erratum: Phys. Lett.B734,409(2014)], 216–227. arXiv: 1307.5543 (2014).
60. Observation of Long-Range Elliptic Azimuthal Anisotropies in $\sqrt{s} = 13$ and 2.76 TeV *pp* Collisions with the ATLAS Detector. *Phys. Rev. Lett.* **116,** 172301 (2016).
61. Abelev, B. *et al.* Long-range angular correlations on the near and away side in *p*-Pb collisions at $\sqrt{s_{NN}} = 5.02$ TeV. *Phys. Lett. B* **719,** 29–41. arXiv: 1212.2001 (2013).
62. Abelev, B. B. *et al.* Long-range angular correlations of π, K and p in p-Pb collisions at $\sqrt{s_{\mathrm{NN}}} = 5.02$ TeV. *Phys. Lett. B* **726,** 164–177. arXiv: 1307.3237 (2013).
63. Acharya, S. *et al.* Investigations of Anisotropic Flow Using Multiparticle Azimuthal Correlations in pp, p-Pb, Xe-Xe, and Pb-Pb Collisions at the LHC. *Phys. Rev. Lett.* **123,** 142301. arXiv: 1903.01790 (2019).
64. Acharya, S. *et al.* Long- and short-range correlations and their event-scale dependence in high-multiplicity pp collisions at $\sqrt{s} = 13$ TeV. *JHEP* **05,** 290. arXiv: 2101.03110 (2021).
65. Abelev, B. B. *et al.* Multiplicity dependence of the average transverse momentum in pp, p-Pb, and Pb-Pb collisions at the LHC. *Phys. Lett.* **B727,** 371–380. arXiv: 1307.1094 (2013).
66. Acharya, S. *et al.* Multiplicity dependence of light-flavor hadron production in pp collisions at $\sqrt{s} = 7$ TeV. *Phys. Rev. C* **99,** 024906. arXiv: 1807.11321 (2019).
67. Rafelski, J. & Müller, B. Strangeness Production in the Quark-Gluon Plasma. *Phys. Rev. Lett.* **48,** 1066–1069 (1982).
68. Koch, P., Rafelski, J. & Greiner, W. Strange hadrons in hot nuclear matter. *Physics Letters B* **123,** 151–154 (1983).
69. Koch, P., Müller, B. & Rafelski, J. Strangeness in relativistic heavy ion collisions. *Physics Reports* **142,** 167–262 (1986).

70. NA35 Collaboration. Neutral strange particle production in sulphur-sulphur and proton-sulphur collisions at 200 GeV/nucleon. *Zeitschrift für Physik C Particles and Fields* **48,** 191–200 (1990).

71. Andersen, E. *et al.* Strangeness enhancement at mid-rapidity in Pb–Pb collisions at 158 A GeV/c. *Physics Letters B* **449,** 401–406 (1999).

72. Antinori, F. *et al.* Enhancement of hyperon production at central rapidity in 158-A-GeV/c Pb-Pb collisions. *J. Phys.* **G32,** 427–442. arXiv: nucl-ex/0601021 (2006).

73. Antinori, F. *et al.* Strangeness enhancements at central rapidity in 40 A GeV/cPb–Pb collisions. *Journal of Physics G: Nuclear and Particle Physics* **37,** 045105 (2010).

74. Alt, C. *et al.* Omega- and anti-Omega+ production in central Pb + Pb collisions at 40-AGeV and 158-AGeV. *Phys. Rev. Lett.* **94,** 192301. arXiv: nucl-ex/0409004 (2005).

75. Alt, C., Anticic, *et al.* Energy dependence of Λ and Ξ production in central Pb + Pb collisions at $20A, 30A, 40A, 80A$, and $158A$ GeV measured at the CERN Super Proton Synchrotron. *Phys. Rev. C* **78,** 034918 (2008).

76. Anticic, T. *et al.* System-size dependence of Λ and Ξ production in nucleus-nucleus collisions at $40A$ and $158A$ GeV measured at the CERN Super Proton Synchrotron. *Phys. Rev. C* **80,** 034906 (2009).

77. Adams, J., Adler, C., *et al.* Multistrange Baryon Production in Au-Au Collisions at $\sqrt{s_{NN}} = 130$ GeV. *Phys. Rev. Lett.* **92,** 182301 (2004).

78. Adams, J., Adler, C., *et al.* Identified Particle Distributions in *pp* and Au+Au Collisions at $\sqrt{s_{NN}} = 200$ GeV. *Phys. Rev. Lett.* **92,** 112301 (2004).

79. Abelev, B. I., Aggarwal, M., *et al.* Enhanced strange baryon production in Au+Au collisions compared to $p + p$ at $\sqrt{s_{NN}} = 200$ GeV. *Phys. Rev. C* **77,** 044908 (2008).

80. Acharya, S. *et al.* Multiplicity dependence of π, K, and p production in pp collisions at $\sqrt{s} = 13$ TeV. *Eur. Phys. J. C* **80,** 693. arXiv: 2003.02394 (2020).

81. Acharya, S. *et al.* Production of light-flavor hadrons in pp collisions at $\sqrt{s} = 7$ and $\sqrt{s} = 13$ TeV. *Eur. Phys. J. C* **81,** 256. arXiv: 2005.11120 (2021).

82. Cleymans, J., Kraus, I., Oeschler, H., Redlich, K. & Wheaton, S. Statistical model predictions for particle ratios at $\sqrt{s_{NN}} = 5.5$ TeV. *Phys. Rev. C* **74,** 034903. arXiv: hep-ph/0604237 (2006).

83. Acharya, S. *et al.* Production of pions, kaons, (anti-)protons and ϕ mesons in Xe–Xe collisions at $\sqrt{s_{\mathrm{NN}}} = 5.44$ TeV. *Eur. Phys. J. C* **81,** 584. arXiv: 2101.03100 (2021).

84. Sjöstrand, T. *et al.* An Introduction to PYTHIA 8.2. *Comput. Phys. Commun.* **191,** 159–177. arXiv: 1410.3012 (2015).

85. Bahr, M. *et al.* Herwig++ Physics and Manual. *Eur. Phys. J. C* **58,** 639–707. arXiv: 0803.0883 (2008).

86. Bellm, J. *et al.* Herwig 7.0/Herwig++ 3.0 release note. *Eur. Phys. J. C* **76,** 196. arXiv: 1512.01178 (2016).

87. Pierog, T., Karpenko, I., Katzy, J. M., Yatsenko, E. & Werner, K. EPOS LHC: Test of collective hadronization with data measured at the CERN Large Hadron Collider. *Phys. Rev.* **C92,** 034906. arXiv: 1306.0121 (2015).

88. Kanakubo, Y., Tachibana, Y. & Hirano, T. Unified description of hadron yield ratios from dynamical core-corona initialization. *Phys. Rev. C* **101,** 024912. arXiv: 1910.10556 (2020).

89. Kanakubo, Y., Tachibana, Y. & Hirano, T. Interplay between core and corona components in high-energy nuclear collisions. *Phys. Rev. C* **105,** 024905. arXiv: 2108.07943 (2022).

90. Sjostrand, T., Mrenna, S. & Skands, P. Z. A Brief Introduction to PYTHIA 8.1. *Comput. Phys. Commun.* **178,** 852–867. arXiv: 0710.3820 (2008).

91. Andersson, B. *The Lund model* (Cambridge University Press, July 2005).

92. Skands, P., Carrazza, S. & Rojo, J. Tuning PYTHIA 8.1: the Monash 2013 Tune. *Eur. Phys. J. C* **74,** 3024. arXiv: 1404.5630 (2014).

93. Bierlich, C. & Christiansen, J. R. Effects of color reconnection on hadron flavor observables. *Phys. Rev. D* **92,** 094010. arXiv: 1507.02091 (2015).

94. Werner, K. Core-Corona Separation in Ultrarelativistic Heavy Ion Collisions. *Phys. Rev. Lett.* **98,** 152301 (2007).

95. Aichelin, J. & Werner, K. Centrality Dependence of Strangeness Enhancement in Ultrarelativistic Heavy Ion Collisions: A Core-Corona Effect. *Phys. Rev.* **C79.** [Erratum: Phys. Rev.C81,029902(2010)], 064907. arXiv: 0810.4465 (2009).

96. Bierlich, C., Gustafson, G., Lönnblad, L. & Shah, H. The Angantyr model for Heavy-Ion Collisions in PYTHIA8. *JHEP* **10,** 134. arXiv: 1806.10820 (2018).

97. Kanakubo, Y., Okai, M., Tachibana, Y. & Hirano, T. *Strangeness Enhancement in p + p, p + Pb, and Pb + Pb Collisions at LHC Energies* in *Proceedings of the 8th International Conference on Quarks and Nuclear Physics (QNP2018)* (Journal of the Physical Society of Japan, Nov. 2019). https://doi.org/10.7566%2Fjpscp.26.031021.

98. Rafelski, J. & Letessier, J. Importance of reaction volume in hadronic collisions: Canonical enhancement. *J. Phys. G* **28** (ed Tennant, J.) 1819–1832. arXiv: hep-ph/0112151 (2002).

99. Redlich, K. & Tounsi, A. Strangeness enhancement and Energy dependence in Heavy Ion Collisions. *Eur. Phys. J. C* **24,** 589–594 (2001).

100. Hamieh, S., Redlich, K. & Tounsi, A. Canonical description of strangeness enhancement from p-A to Pb Pb collisions. *Phys. Lett.* **B486,** 61–66. arXiv: hep-ph/0006024 (2000).

101. Vovchenko, V., Dönigus, B. & Stoecker, H. Canonical statistical model analysis of p-p , p–Pb, and Pb–Pb collisions at energies available at the CERN Large Hadron Collider. *Phys. Rev. C* **100,** 054906. arXiv: 1906.03145 (2019).

102. Wheaton, S., Cleymans, J. & Hauer, M. THERMUS—a thermal model package for ROOT. *Computer Physics Communications* **180,** 84–106 (2009).

103. Chatrchyan, S. *et al.* Measurement of the underlying event in the Drell-Yan process in proton-proton collisions at $\sqrt{s} = 7$ TeV. *Eur. Phys. J.* **C72,** 2080. arXiv: 1204.1411 (2012).

104. Acharya, S. *et al.* Production of Λ and K^0_s in jets in p–Pb collisions at $\sqrt{s_{NN}}$=5.02 TeV and pp collisions at $\sqrt{s}$=7 TeV. *Phys. Lett. B* **827,** 136984. arXiv: 2105.04890 (2022).

105. Production of K^0_S, Λ ($\bar{\Lambda}$), $\Xi^{\pm}$ and $\Omega^{\pm}$ in jets and in the underlying event in pp and p−Pb collisions. arXiv: 2211.08936 (Nov. 2022).

106. Cacciari, M., Salam, G. P. & Soyez, G. The anti-k_t jet clustering algorithm. *JHEP* **04,** 063. arXiv: 0802.1189 (2008).

107. Cacciari, M., Salam, G. P. & Soyez, G. FastJet User Manual. *Eur. Phys. J. C* **72,** 1896. arXiv: 1111.6097 (2012).

108. Evans, L. & Bryant, P. LHC Machine. *JINST* **3,** S08001 (2008).

109. *LEP design report* http://cds.cern.ch/record/102083 (CERN, Geneva, 1984).

110. Aad, G. *et al.* The ATLAS Experiment at the CERN Large Hadron Collider. *JINST* **3,** S08003. 437 p (2008).

111. Chatrchyan, S. *et al.* The CMS experiment at the CERN LHC. *JINST* **3,** S08004. 361 p (2008).

112. Aamodt, K. *et al.* The ALICE experiment at the CERN LHC. *JINST* **3,** S08002 (2008).

113. Alves, A. *et al.* The LHCb Detector at the LHC. *JINST* **3,** S08005 (2008).

114. Aad, G. *et al.* Observation of a new particle in the search for the Standard Model Higgs boson with the ATLAS detector at the LHC. *Phys. Lett.* **B716,** 1–29. arXiv: 1207.7214 (2012).

115. Chatrchyan, S. *et al.* Observation of a New Boson at a Mass of 125 GeV with the CMS Experiment at the LHC. *Phys. Lett.* **B716,** 30–61. arXiv: 1207.7235 (2012).

116. Lopienska, E. The CERN accelerator complex, layout in 2022. Complexe des accélérateurs du CERN en janvier 2022. General Photo. http://cds.cern.ch/record/2800984 (2022).

117. Linear accelerator 2. https://cds.cern.ch/record/1997427 (2012).

118. Vretenar, M. *et al. Linac4 design report* https://cds.cern.ch/record/2736208 (CERN, Geneva, 2020).

119. The Proton Synchrotron Booster. https://cds.cern.ch/record/1997372 (2012).

120. *The Proton Synchrotron* https://home.cern/science/accelerators/proton-synchrotron. Accessed: 2022-10-08.

121. *The Super Proton Synchrotron* https://home.cern/science/accelerators/super-proton-synchrotron. Accessed: 2022-10-08.

122. Linear accelerator 3. http://cds.cern.ch/record/1997426 (2012).

123. The Low Energy Ion Ring. https://cds.cern.ch/record/1997352 (2012).

124. Noferini, F. ALICE results from Run-1 and Run-2 and perspectives for Run-3 and Run-4. *J. Phys.: Conf. Ser.* **1014,** 012010. 13 p (2018).

125. Apollinari, G., Brüning, O., Nakamoto, T. & Rossi, L. High Luminosity Large Hadron Collider HL-LHC. *CERN Yellow Rep.,* 1–19. arXiv: 1705.08830 (2015).

126. Abelev, B. *et al.* Upgrade of the ALICE Experiment: Letter Of Intent. *J. Phys.* **G41,** 087001 (2014).

127. Acharya, S. *et al.* Future high-energy pp programme with ALICE. ALICE-PUBLIC-2020-005, CERN-LHCC-2020-018. https://cds.cern.ch/record/2724925 (2020).

128. Dellacasa, G. *et al.* ALICE technical design report of the inner tracking system (ITS). CERN-LHCC-99-12. https://cds.cern.ch/record/1625842 (1999).

129. Abelev, B. *et al.* Technical Design Report for the Upgrade of the ALICE Inner Tracking System. *J. Phys.* **G41,** 087002 (2014).

130. Reidt, F. Upgrade of the ALICE ITS detector. *Nuclear Instruments and Methods in Physics Research Section A: Accelerators, Spectrometers, Detectors and Associated Equipment* **1032,** 166632 (2022).

131. Dellacasa, G. *et al.* ALICE: Technical design report of the time projection chamber. CERN-OPEN-2000-183, CERN-LHCC-2000-001. https://cds.cern.ch/record/451098 (2000).

132. Cortese, P. *et al.* ALICE: Physics performance report, volume I. *J. Phys. G* **30,** 1517–1763 (2004).

133. Adolfsson, J. *et al.* The upgrade of the ALICE TPC with GEMs and continuous readout. *Journal of Instrumentation* **16,** P03022 (2021).

134. Dellacasa, G. *et al.* ALICE technical design report of the time-of-flight system (TOF). CERN-LHCC-2000-012. https://cds.cern.ch/record/430132 (2000).

135. Trzaska, W. H. New Fast Interaction Trigger for ALICE. *Nuclear Instruments and Methods in Physics Research Section A: Accelerators, Spectrometers, Detectors and Associated Equipment* **845.** Proceedings of the Vienna Conference on Instrumentation 2016, 463–466 (2017).

136. Fabjan, C. W. *et al.* ALICE Technical Design Report: Trigger, Data Acquisition, High Level Trigger and Control System. CERN-LHCC-2003-062. https://cds.cern.ch/record/684651 (2004).

137. Buncic, P., Krzewicki, M. & Vande Vyvre, P. Technical Design Report for the Upgrade of the Online-Offline Computing System. CERN-LHCC-2015-006, ALICE-TDR-019. https://cds.cern.ch/record/2011297 (2015).

138. Lamanna, M. The LHC computing grid project at CERN. *Nuclear Instruments and Methods in Physics Research Section A: Accelerators, Spectrometers, Detectors and Associated Equipment* **534.** Proceedings of the IXth International Workshop on Advanced Computing and Analysis Techniques in Physics Research, 1–6 (2004).

139. Bagnasco, S. *et al.* AliEn: ALICE environment on the GRID. *Journal of Physics: Conference Series* **119,** 062012 (2008).

140. Cortese, P., Carminati, F., Fabjan, C. W., Riccati, L. & de Groot, H. ALICE technical design report of the computing. CERN-LHCC-2005-018. http://cds.cern.ch/record/832753 (2005).

141. Brun, R., Bruyant, F., Maire, M., McPherson, A. C. & Zanarini, P. *GEANT 3: user's guide Geant 3.10, Geant 3.11; rev. version* https://cds.cern.ch/record/1119728 (CERN, Geneva, 1987).

142. Agostinelli, S. *et al.* GEANT4: A Simulation toolkit. *Nucl. Instrum. Meth.* **A506,** 250–303 (2003).

143. Battistoni, G. *et al.* Overview of the FLUKA code. *Annals of Nuclear Energy* **82.** Joint International Conference on Supercomputing in Nuclear Applications and Monte Carlo 2013, SNA + MC 2013. Pluri- and Trans-disciplinarity, Towards New Modeling and Numerical Simulation Paradigms, 10–18 (2015).

144. *AliPhysics: the ALICE software repository* https://github.com/alisw/AliPhysics. Accessed: 2022-10-18.

145. *ALICE online-offline software repository* https://github.com/AliceO2Group/AliceO2. Accessed: 2022-10-18.

146. *ALICE O2 analysis repository* https://github.com/AliceO2Group/O2Physics. Accessed: 2022-10-18.

147. Frühwirth, R. Application of Kalman filtering to track and vertex fitting. *Nuclear Instruments and Methods in Physics Research Section A: Accelerators, Spectrometers, Detectors and Associated Equipment* **262,** 444–450 (1987).

148. Maire, A. *Production des baryons multi-étranges au LHC dans les collisions proton-proton avec l'expérience ALICE* Presented 13 Oct 2011 (2011). https://cds.cern.ch/record/1490315.

149. Rolandi G., R. W. & W., B. *Particle detection with drift chambers* (Springer Berlin, Heidelberg, 2008).

150. Andres, Y. *et al.* R&D in ALICE: The CsI-based RICH high momentum particle identification detector. *Eur. Phys. J. direct* **4,** 25 (2002).

151. Cortese, P. ALICE transition-radiation detector: Technical Design Report. CERN-LHCC-2001-021, ALICE-TDR-9. http://cds.cern.ch/record/519145 (2001).

152. Cormier, T., Fabjan, C. W., Riccati, L. & de Groot, H. ALICE electromagnetic calorimeter: addendum to the ALICE technical proposal. CERN-LHCC-2006-014, CERN-LHCC-96-32-ADD-3. http://cds.cern.ch/record/932676 (2006).

153. Man'ko, V. I., Klempt, W., Leistam, L., De Groot, J. & Schükraft, J. ALICE Photon Spectrometer (PHOS): Technical Design Report. CERN-LHCC-99-004, ALICE-TDR-2. http://cds.cern.ch/record/381432 (1999).

154. Breakstone, A. *et al.* High p_T hadrons as leading particles in jets produced at the ISR: 1, momentum distribution of secondaries in the trigger jet. *Z. Phys. C* **23,** 9–18. 33 p (1983).

155. Tanabashi, M. *et al.* Review of Particle Physics. *Phys. Rev.* **D98,** 030001 (2018).

156. Barlow, R. *Systematic errors: Facts and fictions* in *Advanced Statistical Techniques in Particle Physics. Proceedings, Conference, Durham, UK, March 18-22, 2002* (2002), 134–144. arXiv: hep-ex/0207026.

157. Bierlich, C., Gustafson, G., Lönnblad, L. & Tarasov, A. Effects of Overlapping Strings in pp Collisions. *JHEP* **03,** 148. arXiv: 1412.6259 (2015).

158. Majka, R. *et al.* Sigma- p, xi- p, and pi- p Elastic Scattering at 23-GeV/c. *Phys. Rev. Lett.* **37,** 413–416 (1976).

159. Ahn, J. K. *et al.* Measurement of the Xi-p scattering cross sections at low energy. *Phys. Lett. B* **633,** 214–218. arXiv: nucl-ex/0502010 (2006).

160. Dobrigkeit Chinellato, D. Charm and multi-charm baryon measurements via strangeness tracking with the upgraded ALICE detector. *EPJ Web Conf.* **259,** 09004. arXiv: 2110.00955 (2022).